THE ROLE OF FLOW DISORDER IN THE NONINVASIVE DETECTION OF ATHEROSCLEROSIS

A THESIS

Presented to

The Faculty of the Division of Graduate Studies

By

Adel M. A. Khalifa

In Partial Fulfillment

of the Requirements for the Degree

Doctor of Philosophy in Mechanical Engineering

Georgia Institute of Technology

November, 1978

THE ROLE OF FLOW DISORDER IN THE NONINVASIVE DETECTION

OF ATHEROSCLEROSIS

Approved:

Don P. Giddens, Chairman

R. P. Vito

P. V. Desai

James H. Rust

R. F. Mabon

John M. Mills

Date approved by Chairman 11/21/78

ACKNOWLEDGMENTS

Praise be to the God, "Allah", for lightening my life with faith.

I wish to express my sincere appreciation to my advisor, Prof. Don P. Giddens, for his generous contributions of time. His effort to generate interest in the field as well as his advice and encouragement during experimental studies made my research work a most pleasurable and rewarding experience.

I am obliged to Dr. R. A. Cassanova for his help and cooperation during various phases of the experimental study. Also, I wish to thank Drs. R. P. Vito, P. V. Desai, J. H. Rust, R. F. Mabon, and J. M. Mills, members of the reading committee, for their useful suggestions.

Assistance given by V. Saxena in using the mass storage system of the Fourier analyzer is gratefully appreciated.

The financial assistance given by the School of Mechanical Engineering and both the NSF and NIH grants during my course of study is gratefully acknowledged.

Finally, I am grateful to my parents and brother Osama for their encouragement in my academic pursuits. I dedicate this work in the memory of my father.

TABLE OF CONTENTS

TABLE OF CONTENTS (Continued)

LIST OF TABLES

LIST OF ILLUSTRATIONS

LIST OF ILLUSTRATIONS (Continued)

LIST OF ILLUSTRATIONS (Continued)

LIST OF ILLUSTRATIONS (Continued)

LIST OF ILLUSTRATIONS (Continued)

LIST OF ILLUSTRATIONS (Continued)

LIST OF ILLUSTRATIONS (Continued)

SUMMARY

The flow field in the neighborhood of a subtotal vascular stenosis is of great interest in clinical medicine and represents a challenging problem in fluid mechanics. The flow disorder created in the poststenotic field has been shown to be an important feature of the flow.

In the present study a theory has been established for the analysis of flow disorder in pulsatile flow. The motivation is to describe the disorder and study the possibility of using it as a diagnostic tool to detect atherosclerosis noninvasively. The theory characterizes the disturbance velocity as a function of time in the velocity cycle and suggests several digital techniques to describe flow disorder which includes computation of the ensemble average waveforms, energy spectra and autocorrelation functions, and the rms disturbance velocity.

The theory has been applied to in vivo hot film measurements that were taken at one axial position distal to several degrees of occlusion ranging from zero to severe. The stenoses were formed by placing bands about the aorta of an anesthetized dog. The analysis shows that the flow disorder is a sensitive indicator of mild to moderate stenoses which implies the possibility of using it to detect the location and size of arterial stenoses in their early stages, particularly before becoming clinically significant. The disturbance velocity of these data was nonstationary for mild to moderate stenoses, so that results for rms disturbance velocities and energy spectra depend strongly upon the interval

being studied. However under certain conditions dynamic similarity of the disturbance energy spectra existed. The ensemble average waveforms demonstrate the appearance of split systolic peaks for mild to moderate stenosis and suppression of the pulsatility nature of the flow for severe stenoses.

To study the disordered flow field distal to arterial constriction and to identify the fluid mechanics phenomena associated with it, three models of arterial stenosis were constructed to represent mild, moderate, and severe occlusions. A specially designed flow system was made to provide pulsatile flow with sinusoidal velocity oscillations proximal to the stenoses models. The upstream velocity waveform has a frequency of 1 Hz and Reynolds number range from 500 to 2400. The laser Doppler velocimeter was used to measure the centerline velocity at several axial positions downstream of the constriction. The flow disorder analysis applied to these data shows that this complex flow field is characterized by the existence of three major classes of disturbances, namely, shed vortices, periodic instabilities that break down to turbulence, and turbulent fluctuations. The existence and interaction between these disturbances depend on the degree of constriction, Reynolds number, and the frequency parameter.

The flow field distal to the mild stenosis (25 percent area reduction) is characterized by several vortices being shed during the acceleration phase at the near poststenotic field which then propagate downstream. Interaction between vortices was also noticed. As vortices move distal to the stenosis they lose their strength and decay by viscous dissipation.

There was no significant turbulence observed for this mild stenosis distal flow field.

The flow field distal to a mild stenosis (50 percent area reduction) is characterized by shed vortices leading periodic instabilities that break down to turbulent fluctuations and forming the turbulent front. Both vortices and the turbulent fluctuations decay and dissipate their energy as they move downstream.

The severe stenosis (75 percent area reduction) poststenotic field is more violent. Both the vortices and the turbulent front are formed in a similar way to the 50 percent occlusion. However, the turbulent front is able to overtake the leading vortices breaking them into high amplitude turbulent fluctuations. This region of turbulence is convected downstream and decays because production of turbulence is not balancing dissipation.

Spectral similarity was obtained between in vivo and in vitro data provided that the most turbulent parts of the cycle are examined. The ensemble average waveforms for the in vitro data show split peaks similar to those of the in vivo results. This can be caused either by a vortex or a turbulent front passing through this position while flow is reaching its maximum velocity.

Thus, results obtained from the in vitro study add to the understanding of physiological turbulence, its development and decay and explain some of the phenomena observed in the in vivo data. The use of the development of the disturbance velocity with time to identify and follow the vortices and the turbulent front provided a good method of

flow description.

Finally, a direct comparison between the pulsed Doppler velocimeter (PD) and the laser Doppler velocimeter (LDV) was conducted in a water flow system to determine the capability and limitations of the PD as a noninvasive detector of the flow disorder. A modified technique was used to process the Doppler audio signal of the PD by employing the phase lock loop (PLL). The flow disorder analysis was also applied to these measurements. Average velocities, turbulent spectra, and intensities as measured by the PD/PLL system in steady pipe flow agree very well with data from LDV and hot film measurements. This implies that very useful turbulence information may be obtained with ultrasound. Measurements in pulsatile flow show very good agreement between the ensemble average velocities measured by PD and LDV. The poststenotic flow measurements of turbulence using the PD/PLL system at an angle to the flow is still difficult to interpret because of the severe nonisotropy of the turbulent fluctuations.

The present study has demonstrated that mild constrictions in the dog aorta can be readily identified by disordered flow analysis. The in vitro model studies disclosed information on the nature and source of poststenotic flow disorder, and a method of obtaining turbulence measurements noninvasively was verified.

CHAPTER I

INTRODUCTION

The physician is interested in diseases of the arteries because it is probable that if his patients (and he himself) do not die of cancer, they will die of arterial disease. This is only natural because the arteries, since they are under continuous stress, are the tissues which begin to degenerate soonest with the possibility of a future complication from involvement of the heart or brain (1).

Of all arterial lesions ARTERIOSCLEROSIS is the most common, the most important, and the most obscure. The word literally means hardening (sclerosis) of the arteries. The very name is enigmatic. It is really an omnibus term including three distinct conditions, namely atherosclerosis, Mönckeberg's sclerosis, and arteriolesclerosis (1).

ATHEROSCLEROSIS or atheroma is responsible for more disabilities and death than any other disease. This form of disease is characterized by the occurrence of localized obstruction or plaques. It is the cause of about 95 percent of deaths from coronary artery disease and about 50 percent of deaths from cerebrovascular disease. In some ways it presents the same kind of dark mystery as does cancer, for its etiology and pathogenesis are matters of endless and sometimes furious debate. On the clinical side at the present time convincing evidence is lacking that something can be done with respect either to prevention or treatment, although clues are not lacking.

Atherosclerosis is commonly seen and most readily studied in the aorta and aortic arch, but it is also frequently found in other arteries such as the coronaries, the cerebrals, and the carotids. It may also be found in the common iliac and femoral arteries. It is most noticed at branches and bifurcations. The earliest lesions may take the form of yellow linear streaks at first hardly raised above the inner surface of the blood vessel. These represent fatty deposits in the depth of the intima (the tissue just below the endothelium, the inner lining of the arterial wall). As the process advances the intima over the patch of fatty deposits gradually becomes raised, thickened, and more hyaline. After that, the intima loses its continuity and a stenosis or constriction is formed. On the resulting roughened surface, thrombosis or clotting occurs and may form the starting point of a future embolus, or abnormal particle. The embolus may be large enough to cause total arterial occlusion and in turn death to the part fed by this artery. The deposition of limesalt in the fatty material may convert the lesion into a calcified plaque with the brittleness of a shell, and this may be cracked across due to vibrations and stresses caused by turbulent flow of blood in the region of the stenosis (1). The cracked brittle parts may form the starting point of a dissecting aneurysm, or bulge in the arterial wall.

The possibility that hemodynamic factors may participate in the genesis and proliferation of atherosclerosis has fostered increased study during the past decade. Suspicions were aroused by the clinical observations of a predilection for atherosclerotic plaques to form at particular sites of the vascular tree, most notably regions of vessel branching and

bifurcation. Continuing investigations into blood flow patterns have contributed important data, but at the present time the precise relationship of hemodynamics to possible causative mechanisms have not been established.

Fry (2,3) has emphasized the interaction of local flow with the arterial lining (the endothelium) as a possible precursor to plaque formation. He suggests that high rates of wall shear can actually tear away the endothelial cells which line arterial walls and that damaged sites thus produced are preferential for the deposit of lipids carried in the blood stream. He also mentioned that an unstable and unsteady stress pattern (like that associated with flow separation) tends to increase the permeability of the endothelium to lipoprotein and may in turn lead to fat deposition in the intima.

Caro et al. (4,5), on the other hand, advanced a hypothesis based on the general proportionality between wall shear and mass transport. They suggested that fatty deposits accumulate at locations where the mass transport rate of cholesterol away from the wall into the blood stream is insufficient to balance the rate at which it is manufactured in the vessel wall. Since mass transport rate correlated with shear rates, they argue that sites of preferential buildup of fatty deposits will be those having low shear rates. The controversy between Caro's approach and that of Fry has not yet been resolved.

Regardless of the exact initiating factors of the atherosclerotic plaques, it is clear that once an obstruction has developed, the flow of blood will be disturbed and hemodynamic factors must play an increasingly

important role as the stenosis continues to develop. This phenomenon created a new and very interesting research area in the hemodynamic studies of atherosclerosis.

The flow field created by arterial stenoses has attracted many research workers. The reason is the complications and challenges associated with the actual flow conditions in partially occluded arteries, such as the complex pulsatile nature of the flow, extensibility, and viscoelastic properties of arterial walls, the nonuniformity of the stenoses, branching, curvature, and geometric taper in the arteries, in addition to the fact that the blood is a non Newtonian fluid.

In spite of all of these complications, there are some theoretical approaches and modeling to study the flow through the stenosis such as those of Lee and Fung (6); Morgan and Young (7); Daly (8); Kozman and Forrester (9); and Deshpande and Giddens (10). These authors and others tried to start with simplified models of steady or pulsating flow through axisymmetric stenoses in rigid tubes as a step to understand and clarify the characteristics of the complicated actual flow field.

Experimental investigations, on the other hand, have rapidly developed and spread to study specific factors and parameters of the actual flow field in the region of arterial stenoses that have medical significance. Some of these experiments are in vitro, others are in vivo. The main parameters and factors that have been studied are:

(1) The resistance or impedence of the constriction as characterized by the relationship between the pressure drop and flow (11,12,13,14).

(2) The distribution of pressure and shear stress through the

constriction (2,4,15,16).

(3) The nature and extent of localized separated regions of flow distal to the stenosis (11,19).

(4) The velocity distribution in the region of the arterial stenosis (17,18,19,20,21).

(5) The nature and intensity of turbulence and flow disorder developed at the stenosis.

Among all of the factors relating to the flow field in the region of arterial stenoses, the study of the nature and intensity of turbulence and flow disorders is proving to be one of the most important. Roach (22) has proposed that turbulence is a probable mechanism in the production of poststenotic dilatation. Fry (2,3) has suggested that turbulence and unstable stress patterns may affect the normal endothelial barrier to lipid accumulation. Giddens et al. (23) have demonstrated that disordered flow patterns occur for rather mild stenoses emplaced about the descending thoracic aortas of dogs. Turbulence has been shown to exist in regions of aortic ball valves situated in vitro by Bellhouse (24). Stein and Sabbah (25) have recorded disturbed flow patterns and turbulence in the ascending aorta of human subjects with normal and diseased aortic valves. These references are simply a few examples of the widespread interest in disturbed blood flow in the arterial system.

The ability to describe and detect flow disorders caused by the arterial stenoses adds to the insight needed to solve the puzzle of the pathology of atherosclerosis. Beyond that, there is keen interest in determining whether the disordered flow patterns can be used to detect

the location and size of arterial stenoses in their early stages, particularly before becoming clinically significant.

There are two phenomena of interest in studying flow disorder, the sound field (26,27,28) and the velocity field. Although several investigators (29,30,31,32) have attempted to relate the power spectra of pseudo sound produced by the turbulent fluctuations to the degree of vessel constriction, these methods are useful only for fairly severe disease states.

It is believed by the group of investigators at Georgia Institute of Technology (33) that the more sensitive indicator of flow disorder and also the more fundamental phenomenon occurring is the disturbance to the velocity field as opposed to pressure or sound field. The velocity fluctuations are the basic mechanism creating sounds and are therefore the primary entity to be studied. The velocity field is very complex and may have profound effects upon both the vessel intima and upon the transport of materials into and from the wall. Furthermore, the experiments done by this group (23,34,35,38) indicated that the velocity field is a much more sensitive indicator of mild to moderate stenoses than is the sound field. Thus, there appeared to be a need for well-defined methods of analysis of turbulence and flow disorder in arterial flows utilizing direct measurements of the velocity waveform.

It should be stressed that several factors combine to create complexities in approaching the problem in this way. The most dominant of these factors is the pulsatility of the flow. Because of this, the traditional approach of averaging quantities for a long time to obtain

mean values must be modified In arterial flows, the "mean" velocity of interest may not be the average over a long time, but rather the basic pulsatile waveform itself. Further, this waveform is not of a particularly convenient shape for engineering analysis. The sharp increase in velocity during systole is often followed by a reverse flow phase and a subsequent secondary forward flow peak. The general shape is such that many harmonics other than the fundamental heart rate are present, so that flow disorder or turbulence which occurs at, say ten Hertz, may be difficult to distinguish from harmonics of the basic waveform. Finally, an additional complication is the presence of biological variability. The basic velocity waveform is not strictly periodic since each heartbeat may differ slightly (or significantly) from all others. Coupled with this is the fact that it is often difficult to maintain a biological subject in a relatively constant state for a time sufficiently long to allow a reliable description of flow disorder.

There are several measurements which characterize flow disorder. Among them are the one dimensional energy spectrum $E(f)$ and the autocorrelation function $R(\tau)$, which are related by inverse Fourier transformation (36). In principle, these measurements are equivalent if the velocity is a stationary random variable.

Winter et al. (37) have used correlation functions to describe the degree of flow disorder in arteries. Their results were categorized as "undisturbed" or "highly disturbed." Several investigators have independently tried to analyze turbulence and flow disorders using the energy spectrum technique (39,41,42). The earliest approaches were to compute

energy spectra of the entire velocity waveform without regard to time history of the disturbance velocity component (38).

The motivation for studying the time history of the developing disturbance in pulsating flow is to describe the onset of the disorder and to monitor its development in the cycle. In addition, it can be a very sensitive indicator of the existence of localized occlusions in the arteries. Examples of these approaches are Nerem et al. (4), McEvory et al. (43), Falsetti et al. (44), Pawell (45), Parker (46), and Giddens et al. (23).

Pawell (45) has studied the problem of turbulence produced by velocity pulsations in an elastic tube of constant cross sectional area using a hot film anemometer to measure velocities. He divided the simulated heart cycle into several segments and determined a temporal development of the disturbance energy spectra. The data showed short bursts of turbulence during and immediately after systole for a pulse rate of 71 beats per minute and a more developed turbulence at a higher rate of 112 beats per minute. These findings were very sensitive to the values of the Reynolds number, frequency parameter, and the harmonic composition of the periodic velocity waveform.

In a related study, McEvory et al.(43) report a similar attempt at in vivo measurements in the canine aorta. The cardiac cycle was divided into seven segments and corresponding energy spectra were calculated. Chemical stimulants were administered in an effort to induce a disturbed aortic flow. This study indicated that the time segment which covered the acceleration phase of systole contained the greatest high

frequency flow disorder. This is directly contrary to the results presented by Giddens et al. (23). The difference is likely due to the fact that McEvory et al. attributed what is actually a stimulant-induced physiologic disorder to flow disorder.

Parker (46) has given results taken from in vivo data in the descending thoracic aorta of dogs which show instabilities during the initial deceleration phase of systole.

Giddens et al. (23) have reported on the temporal development of the energy spectrum of the total velocity in the cardiac cycle for flows distal to varying degrees of stenoses. The results indicated substantial flow disorder during flow deceleration.

Additional work is needed to extend these efforts in that the disturbance velocity should be characterized at various stages in the cardiac cycle and for degrees of occlusion ranging from zero to severe. Also, the relationship of the energy spectra of flow disturbances distal to vascular stenoses to the degree of occlusion should be investigated.

Knowledge of the nature of flow disorder caused by the vascular stenosis is also essential. Cassanova (38) illustrated that the pulsatile flow field distal to axisymmetric stenosis is characterized by two phenomena, namely the vortex shedding mechanism and turbulent velocity fluctuations. Further experiments with the application of new techniques to analyze the data are required especially for the cases where the turbulence is not persisting during the entire velocity cycle.

One of the difficulties associated with the application of the techniques of relating the flow disturbance to the degree of occlusion developed in the human arterial system is the method of measuring the

blood velocity. At present, only two methods have been successfully applied for velocity profile measurement in arteries of living animals: hot film and the ultrasonic Doppler techniques.

To measure the blood velocity with a thermal anemometer system (47,48), a hot film probe is placed directly into the flow stream either by vessel puncture or with the aid of a catheter. Velocity profiles may be constructed from time-varying velocity waveforms obtained at various locations in the lumen cross section as the probe is transversed across the vessel diameter. When the hot film is positioned near the vessel wall, the normal flow pattern in that region is altered and the corresponding velocity waveforms do not represent those of the undisturbed system. The hot film also does not intrinsically distinguish forward from backward flow. This causes loss of information of the flow in arteries during the interval of reversed flow that may exist during diastole. Although the hot film has the disadvantage of being an invasive technique that cannot be applied to human arteries, it has the advantage of high frequency response and can be used for turbulence studies.

The ultrasound Doppler velocimeter provides a non traumatic measurement of blood velocity, since it is possible to monitor the velocity of blood extraluminally or transcutaneously. This measuring technique is noninvasive in the sense that blood vessel walls remain intact, and it has the additional advantage of not disrupting the normal blood velocity patterns.

The work of Satomura (49) and Kaneko (50) in Japan and of Rushmer et al. (51,52) in the U.S. has made it possible to obtain signals indicative

of blood velocity in the arteries and veins from transcutaneous measurements with ultrasound. Since then the Continuous Wave (CW) ultrasonic flowmeters have been increasingly improved and used widely to measure the velocity patterns from normal subjects and patients with arteriosclerosis (53,54,55,56). Almost in parallel with the development of more effective instruments, clinicians began to ask for a more sophisticated diagnostic tool.

The CW Doppler flowmeters did not have any range perception, everything moving within the reach of the ultrasound beam scattered it and thus contributed towards the final signal received. Thus vessel wall motion or the presence of two arteries in the beam leads to confusing results. As a result of these limitations, the use of CW devices was rather qualitative, whether the Doppler signal was processed and recorded as analog waveforms or the clinician based his conclusions on listening to the Doppler signals through an audio amplifier.

Many of the problems associated with the continuous wave system can be overcome if the ultrasound is pulsed. The pulsed, range-gated ultrasonic Doppler velocimeter operates in a radar-like mode (57) and measures the average velocity of blood cells is a small sample volume within a blood vessel by sensing the change in frequency of the ultrasound waves scattered by the moving particles. Velocity waveforms from sample volumes located at increments across the vessel lumen are obtained by an electronic range gating circuit and velocity profiles at specific instants of the cardiac cycle can then be constructed. Several investigators have described this device, such as Baker (58,59), Wells (60), Peronneou (61),

and McLeod (62,63). The new versions of pulsed Doppler ultrasonic devices are able to sense direction of the flow (63,64) and yield instantaneous values of velocity at several depths simultaneously (62).

More recently, the emphasis of research has been on the theoretical understanding of the actual Doppler process. Reid et al. (65) and Thomson et al. (66) studied how the blood cells scatter ultrasound. Brody (67) and Flax et al. (68,69) give a very comprehensive statistical analysis of the noise distorted Doppler signal and how it affects the instrument output. Baker et al. (70,71,72,73) studied the sample volume very thoroughly, theoretically as well as experimentally, in order to define the interaction of the ultrasound pulse and the flow as three dimensional convolution process. They also predicted the distorted velocity profiles from the assumed true ones. Jorgensen et al. (74) also modeled the Doppler process as a convolution integral, incorporating the physical characteristics of the flowmeter and those of the flow field. Distortion of the measured velocity profile was corrected by deconvolution using discrete Fourier transform and the true velocity profile was obtained.

To measure velocity and turbulent quantities directly using the pulsed Doppler ultrasonic velocimeter (PD), it is necessary to process the Doppler signal. Various techniques have been used to convert the Doppler signal spectrum to a voltage proportional to the average velocity within the sample volume. These techniques are:

1. The zero crossing frequency meter (74,75,90,91),
2. The phase lock loop, and
3. Digital processing of the Doppler signal using the Doppler spectrum to calculate the moments.

The first method has been unsatisfactory for turbulence measurements. Employing the phase lock loop of the laser Doppler velocimeter (LDV) is promising and the preliminary experiments (76) show that there is a possibility of utilizing this method to measure the turbulent quantities in addition to accurate measurements of the instantaneous velocity. A second group at the School of Aerospace Engineering, Georgia Institute of Technology is working in the digital treatment of the Doppler signal.

In summary, the flow field in the neighborhood of a subtotal vascular stenosis is of great interest in clinical medicine and represents a challenging problem in fluid mechanics. A thorough understanding of the flow characteristics, coupled with a reliable means of noninvasive measurement, would be of significant benefit.

In the present research a theory has been established for the analysis of a disorder in pulsatile flow. The theory characterizes the disturbance velocity at different stages of the velocity cycle and suggests several digital techniques to describe the flow disorder. This theory is applied to in vivo hot film measurements at one axial position downstream of several degrees of occlusion ranging from zero to severe to study the nature of the flow disorder and its relation to the degree of constriction. It is also applied to in vitro measurements of the centerline velocity for modeled rigid stenoses at different axial positions in the poststenotic flow field. This second application facilitates the study of flow disorder under controlled flow conditions, also the different phenomena associated with the flow can be investigated. Finally, the theory is applied to experimental investigation to improve the

frequency response of the Doppler ultrasonic velocimeter and to compare it with the laser Doppler velocimeter.

CHAPTER II

ANALYSIS OF FLOW DISORDER

2.1 Theory

Most fluid dynamic studies of turbulence deal with flows which have steady mean values. That is, if time averages are formed of any particular variable, this average value is a constant. This is best illustrated by consideration of a velocity measurement at a fixed point in a turbulent flow. The output of an anemometer might look like that shown in Figure (2-1a). If the average reading is formed, by determining the integral

$$\frac{1}{T}\int_0^T u(t)dt = U \qquad (2\text{-}1)$$

where u(t) is the instantaneous velocity and t is time, then one finds that for large time T, the value of U approaches a constant. This is then termed the mean velocity of the flow at that point in space. Typically, then, one writes

$$u(t) = U + u'(t) \qquad (2\text{-}2)$$

as a representation of the instantaneous velocity at a point. The quantity $u'(t)$ is a disturbance velocity, and by definition its time

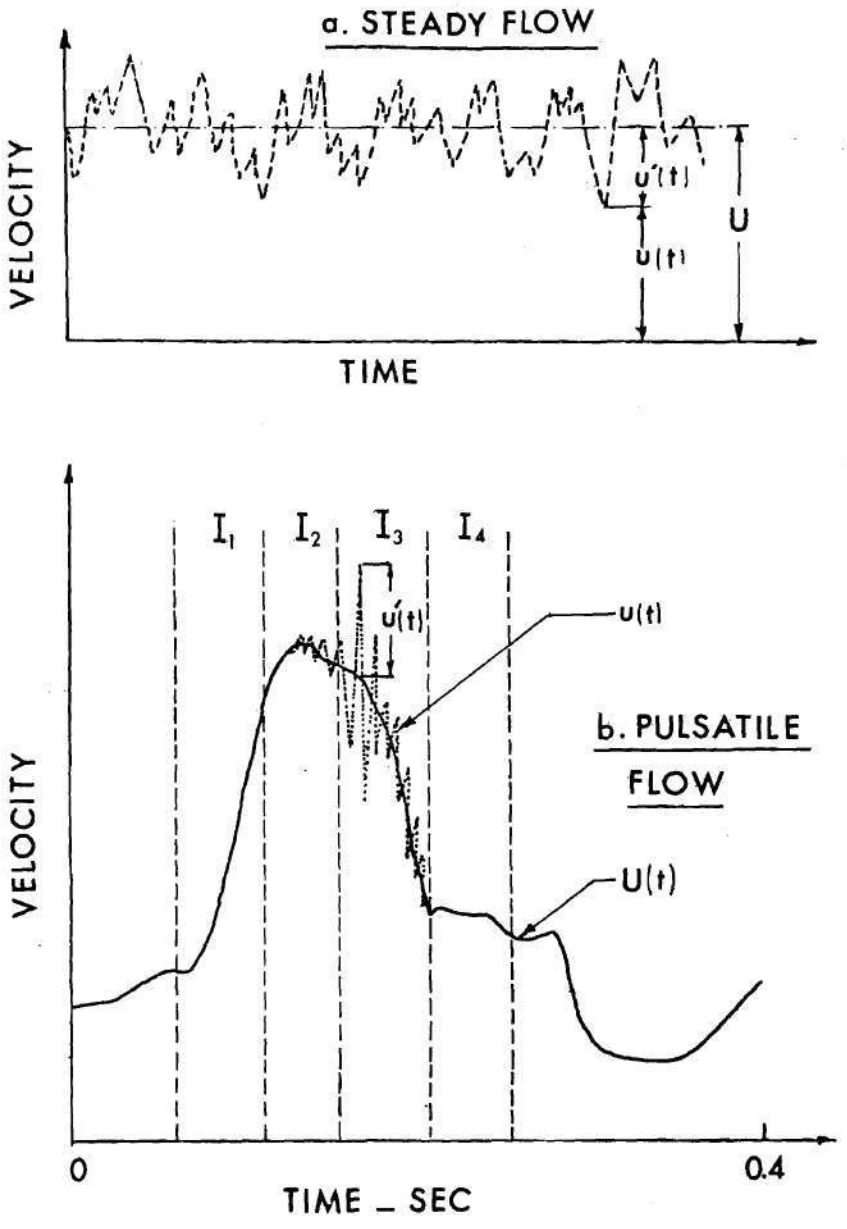

Figure 2-1. Illustration of Disturbances in "Steady" and Pulsatile Flow, and Intervals Used for Analysis of Time-Development of Disorder

average is zero. This same representation may be used for other flow variables such as pressure, temperature, and additional velocity components. Furthermore, in most treatments of turbulent flows the magnitude of $u'(t)$ is considerably less than that of U.

In studies of ordered structures in a turbulent flow a further breakdown of contributions to the velocity is prescribed. For such flows a velocity is considered to be composed of mean, periodic, and turbulent components. The periodic disturbance is often "buried" in the turbulence and an important problem is to extract the ordered structure from a seemingly random pattern. Examples of this approach are given by Hussain and Reynolds (77).

When the problem of arterial flows is considered, immediate complications arise. First of all, only at the crudest level of description--namely, mean blood flow delivered--is it useful to define a mean velocity such as that of Equation (2-1). The flow is essentially periodic rather than essentially steady. Furthermore, the heart is not a perfectly reproducible pump. Each heartbeat may be slightly different from all others so that a "biological disorder" is present, as described earlier. Fortunately, in a carefully controlled experiment, heart rates and ejection characteristics which are reasonably periodic can be maintained. It is thus possible, under proper conditions, to define a time-varying ensemble average waveform by

$$U(t) = \lim_{N\to\infty} \frac{1}{N} \sum_{n=0}^{N-1} u(t + nP) \qquad (2\text{-}3)$$

where P is the period of the waveform or inverse of the fundamental heart rate. Note that if every heartbeat produced exactly the same waveform (i.e., no biological disorder) and if there were no fluid dynamic disorder, then $u(t) = u(t + nP)$ for all values of the integer n.

Having defined such a deterministic ensemble average waveform given by $U(t)$, it is possible to describe disturbance or deviations from this. For any given waveform the velocity may be expressed as

$$u(t) = U(t) + u'(t) \qquad (2\text{-}4)$$

where $u'(t)$ is the disturbance velocity, to be treated as a random variable. This is illustrated in Figure (2-1b). It is not a straightforward matter to define turbulence, in the strictest sense, for such a flow. For example, to achieve a developed turbulent flow the time scale over which $U(t)$ varies significantly should be much longer than that over which $u'(t)$ varies. Also, a condition for maintaining turbulence throughout most of a cycle is that the instantaneous Reynolds number be sufficiently high. If the dissipation time is short in comparison with the heart rate period, any so-called turbulence which is generated during systole, for example, would not persist throughout diastole. Furthermore, in the case of stenoses in particular, periodic low frequency disturbances such as vortex shedding may be generated and then break up as they proceed downstream. In cases of steady flow such periodic component will appear only in the disturbance velocity, while in the case of pulsating flow this periodic component, ideally, would appear only in the ensemble average

waveform.

For situations in which the disturbances exist over only a part of the cycle there is the additional complication that $u'(t)$ is not a stationary random variable. Therefore, computations of energy spectra, correlation functions, and rms disturbance velocities depend upon the time intervals selected for analysis. In fact, it is precisely this dependence which provides information on the development of disorder. Although the concept of energy spectra which are time-varying is perhaps unusual, there is precedent for such a notion, given by Priestly (80).

For these reasons, the flow through a stenosis in a relatively large vessel is such that it is frequently misleading to term it turbulent. Thus, we have chosen to call these "disturbed" or "disordered" flows. Turbulence falls, of course, under such a definition, as do vortex shedding and transitional flows. However, the existence of a disturbance velocity $u'(t)$ in an arterial blood velocity waveform can by no means be construed as signifying turbulence. Simple deviations from perfect reproducibility among heartbeats may give u' results which, upon superficial analysis, seem to resemble flow disturbance. In fact, separation of biological disorder from fluid dynamic disorder is a most difficult problem, particularly when dealing with an awake, unanesthetized subject.

Several types of analyses are useful in describing disordered flows. Among these are

a) determination of time-varying ensemble average waveforms,

b) computation of energy spectra and autocorrelation function for the disturbance velocity component, $u'(t)$,

c) analysis of (b) as a function of the time interval within the cycle (evolution of energy spectra and autocorrelation functions),

d) determination of rms values for the disturbance velocity component and the variation of this quantity with time,

e) spectral analysis of the time-varying ensemble average waveform.

It is inappropriate to select any one of these as the most significant method for analysis. Each has information to offer, and together they complement each other to form a total description of the flow.

2.2 The Autocorrelation Function

The autocorrelation $\bar{R}(t_1, t_2)$ of a random process $\vec{x}(t)$ is the joint moment of the random variables $\vec{x}(t_1)$ and $\vec{x}(t_2)$ (78)

$$\bar{R}(t_1, t_2) = \int_{-\infty}^{+\infty} x_1 x_2 \, f(x_1, x_2; t_1, t_2) dx_1 dx_2 \qquad (2\text{-}5)$$

where $f(x_1, x_2; t_1, t_2)$ is the joint probability distribution,

$$x_1 = \vec{x}(t_1) \quad \text{and} \quad x_2 = \vec{x}(t_2)$$

Using the "expectation" notation this may be written as

$$\bar{R}(t_1, t_2) = \{\vec{x}(t_1) \, \vec{x}(t_2)\} \qquad (2\text{-}6)$$

If the random process is stationary, then the autocorrelation is a function only of $\tau = t_2 - t_1$ and can be written as

$$\bar{R}(\tau) = E\{\vec{x}(t)\ \vec{x}(t+\tau)\} \tag{2-7}$$

For ergodic processes which satisfy the sufficient condition that $\tau\bar{R}(\tau)$ is absolutely integral over the infinite time domain, the autocorrelation may be expressed as

$$\bar{R}(\tau) = \lim_{T\to\infty} \frac{1}{2T} \int_{-T}^{T} x(t)\ x(t+\tau)\ dt \tag{2-8}$$

and the energy spectrum is its inverse Fourier transform given by

$$E(f) = 2 \int_{-\infty}^{+\infty} d\tau \bar{R}(\tau)\ e^{-12\pi f\tau} \tag{2-9}$$

or

$$\bar{R}(\tau) = \frac{1}{2} \int_{-\infty}^{+\infty} df\ E(f)\ e^{12\pi f\tau}$$

In a stationary turbulent flow the autocorrelation function

$$R(\tau) = \frac{\bar{R}(\tau)}{\bar{R}(o)} \tag{2-10}$$

is often used and the process $x(t)$ is taken to be the value of the disturbance velocity $u'(t)$. Thus equation (2-10) becomes

$$R(\tau) = \frac{\int_{-\infty}^{\infty} u'(t)u'(t+\tau)dt}{u'^2} \tag{2-11}$$

where $u'^2 = R(o)$

$$= \int_{-\infty}^{\infty} [u'(t)]^2 \, dt \tag{2-12}$$

This coefficient function may be used to define the integral time scale (36)

$$\tau_E = \int_0^{\infty} R(\tau) \, d\tau \tag{2-13}$$

and also the dissipation time scale

$$\frac{1}{\lambda_E^2} = \frac{1}{2} \left\{ \frac{\partial^2 R(\tau)}{\partial T^2} \right\}_{\tau=0} \tag{2-14}$$

Figure (2-2) shows a sketch of an autocorrelation function for turbulent flow. By expanding $R(\tau)$ in Taylor series about the origin for small τ, $R(\tau)$ can be written as

$$R(\tau) = 1 - \tau^2/\lambda^2 \tag{2-15}$$

The dissipation time scale of turbulence is thus the intercept of the parabola that matches $R(\tau)$ at the origin.

The autocorrelation function provides information about the turbulence structure and is used to calculate the time scale for the largest and smallest eddies. As flow becomes turbulent there is a tendency for the disturbance velocity to be randomized and thus less correlated. This causes the autocorrelation function to go to zero more rapidly and

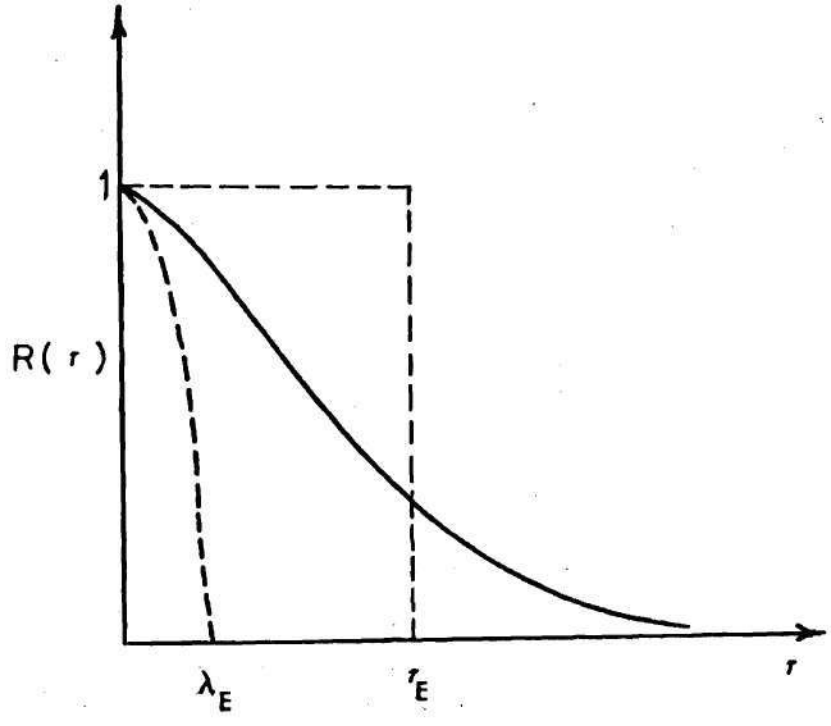

Figure 2-2. A Sketch for an Autocorrelation Function $R(\tau)$

smaller values for τ_E and λ_E are obtained.

Unfortunately, for arterial flows, the velocity is pulsating and the disturbance velocity is not a stationary random variable as previously explained in Section (2.1). If the R.M.S. of the disturbance velocity is not varying rapidly with time, and by properly dividing the velocity cycle into time intervals each of duration (T), the disturbance velocity can be treated approximately as a stationary variable within each interval and the previously described analysis can be applied. One limitation for this approach is the error involved in considering a finite integration time (T) to calculate $R(\tau)$. The concept of an evolutionary energy spectrum, which is a companion function to the quasi-stationary autocorrelation function, has been discussed by Priestly (80). The evolution of these calculated functions during the velocity cycle, can give information on the development of disturbances with time.

From the clinical application point of view, the autocorrelation curves calculated in this way may give an indication of the degree of flow disorder at the location where velocity is measured and hence some indication of the degree of constriction.

2.3 Energy Spectrum

The energy spectrum provides a method to analyze the kinetic energy of the turbulence fluctuations according to distribution over the various frequencies occurring in these fluctuations.

Consider for instance, the disturbance velocity at a fixed point in a flow field. It is assumed that this field has a zero mean velocity,

so that it is statistically homogeneous with respect to time. Then, there exists a constant average value of $\overline{u'^2}$ which can be considered to consist of the sum of the contributions of all frequencies f.

Let E(f) df be the contribution to $\overline{u'^2}$ of the frequencies between f and f + df. Then the energy spectrum function E(f) has to satisfy the condition (36)

$$\int_0^\infty df\ E(f) = \overline{u'^2} \tag{2-16}$$

At a stationary point in this flow field the largest eddies will tend to cause fluctuations of low frequencies where as the smallest eddies will lead to fluctuations of high frequencies.

The energy spectrum and the autocorrelation are related by the equation (2-9) which indicates that energy spectrum is an alternative and equivalent approach to the autocorrelation function, but presented in the frequency domain.

In the present treatment of the nonstationary disturbance velocity during a pulsatile flow, it is assumed that the process occurring during time (to, to + Δt) is but a single realization of an experiment and that other realizations of the same experiment are obtained for (to + nT, to + nT + ΔT), where n is an integer and T is the period of the pulsatile flow. Thus, each cycle is assumed to produce the same random process during the prescribed time interval, so that an ensemble is created for which the statistics are quasi-stationary. According to the Shannon sampling theorem, the maximum frequency (F_{max}) and the frequency resolution

(Δf) obtained for the energy spectrum are related to the sampling time (T) by the relation

$$\Delta f = \frac{1}{T}$$

and

$$F_{max} = \frac{L}{2} \Delta f \qquad (2\text{-}17)$$

where L is the number of sample points in the time domain. Equation (2-17) imposes a limit on the sample time if a reasonable frequency resolution is to be maintained.

The approach used for energy spectrum estimation is known as Bartlett's procedure (97). In this approach the energy spectrum estimator E(f) is considered to be the average over a number of independent estimates. For N time segments (time windows) of L digitized points each, the energy spectrum $E^{(i)}(f)$ can be calculated for each time segment using the fast Fourier transform (FTT) technique. Then, the energy spectrum estimator according to Bartlett's procedure is simply

$$E(f) = \frac{1}{N} \sum_{i=1}^{N} E^{(i)}(f) \qquad (2\text{-}18)$$

Since the estimation of the spectrum is based upon a finite segment of time, different time segments should give different estimates of the spectrum. Moreover, being calculated from a finite number of random

variables (the digitized disturbance velocity signal), the spectrum estimator is also a random variable and, therefore, has a probability distribution function (PDF). It is reasonable to characterize the estimator of being good if there is a high probability that the estimator E(f) will be close to the true value of the spectrum P(f).

It can be proved that (97) the variance value of the estimator is given by

$$\text{Var}\ [E(f)] \cong \frac{1}{N} P^2(f)\ \{1 + [\frac{\sin(2\pi fL)}{L\sin(2\pi f)}]^2\} \qquad (2\text{-}19)$$

It is clear that the variance of E(f) is inversely proportional to the number of energy spectra averaged, and as N gets large, the variance approaches zero, so Bartlett estimate is a consistent estimate.

One way of characterizing the concentration of the probability density function of an estimator is in terms of a confidence interval. By examining equation (2-19) for large values of L, say over 100 points, this equation can be approximated to

$$\text{Var}\ [E(f)] \cong \frac{1}{N} P^2(f) \qquad (2\text{-}20)$$

Hence, the standard deviation σ is given by

$$\sigma\ [E(f)] = \frac{1}{\sqrt{N}} P(f) \qquad (2\text{-}21)$$

According to the central limit theorem (98) for large N, the probability

distribution function (PDF) of the spectrum estimates approaches the PDF of a Gaussian random variable. Thus, using the standard tables of Gaussian distribution, it is possible to say that with 68.2 percent confidence, the estimator of the spectrum will be plus or minus 0.1 of the true value if a hundred energy spectra were used (N = 100) to calculate the estimator.

The energy spectra can be used to study the distribution of the disturbance energy for different frequencies. From the clinical application point of view, the energy spectra curves tend to show higher energy content for higher degrees of occlusion.

The theory stated in this chapter for the method of analysis will be the basis for different applications introduced in the following chapters.

CHAPTER III

APPLICATION OF THE FLOW DISORDER ANALYSIS TO IN VIVO MEASUREMENTS

In this chapter the digital techniques proposed to obtain and analyze the disturbance velocity will be applied to poststenotic flow field measurements which were previously performed in dogs. The data employed for these studies were available on FM tape and were recorded in a series of animal experiments reported earlier (Giddens et al. (23)). The methods of obtaining the measurements are described in that reference. Briefly, the velocity studies were conducted with a hot film anemometer located approximately at the centerline of the descending thoracic aorta of anesthetized mongrel dogs. Stenoses were created by flexible, plastic, constricting bands whose circumference could be varied rapidly during a procedure.

It should be emphasized that hot film measurements under these conditions have several restrictions. These were discussed in detail by Giddens et al. (23). The ECG signal and electromagnetic flowmeter measurement of volume flow rate were also recorded. For the specific set of data analyzed here, the velocity was measured at the center line of the aorta of a dog 2 cm distal to the plan of minimum area of the imposed constriction. The measurements were taken first without a constriction imposed. Then several constrictions with 25, 40, 58, 74, and 88 percent area reduction were applied and measurements were then taken and recorded.

All of the digital computations were carried out with a Hewlett-Packard Model 5451A Fourier Analyzer.

3.1 Data Analysis

3.1.1 Time Ensemble Average Waveforms

Equation (3-1) is used to calculate a digital representation of the ensemble average velocity waveform, U(t). The digitization is always begun at a specific point in the cardiac cycle, say t_o, using the recorded ECG signal as a reference. Thus, $U(t_\ell)$ is computed as

$$U(t_\ell) = \frac{1}{N} \sum_{n=0}^{N-1} u(t_\ell + nP) \qquad (3\text{-}1)$$

where

$t_\ell = t_o + \ell\Delta t, \quad \ell = 0, 1, 2, \ldots, L-1$

Δt = time between digitized points

L = number of digitized points in one sample record

t_o = initial time in the sampling interval.

The time duration of one sample is equal to $L\Delta t$. The ensemble average waveforms reported here were obtained by taking N = 200 analog sample records, each of duration T = 1 second. The number of points per sample, L, was 512. For the heart rates of the dogs under study, each complete velocity waveform is represented by over 200 digitized points.

The onset of the QRS complex of the ECG is used as the triggering signal. This activates a variable delay circuit which is set to give a one microsecond pulse at any desired time subsequent to the trigger. This

pulse, in turn, is used to initiate the analog-to-digital conversion process. The velocity waveform itself as a trigger is not sufficiently reliable due to a greater variability in the velocity signal, particularly once disorder develops in a poststenotic flow. It should be emphasized that it is difficult to maintain a regular heartbeat for the time required to obtain 200 samples, even under general anesthesia. Also, any introduction of cardiac stimulants tends to produce subtle variations in both waveform shape and heart rate which make it difficult to obtain meaningful average waveforms. This problem will be of even greater importance in dealing with awake humans.

For analyses to determine the temporal development of disturbance velocities a shorter sampling time was necessary. Four intervals each of 0.05 second duration were chosen. Figure (2-1b) shows these intervals with respect to the velocity waveform for the case of zero occlusion. The initiation of interval I_1 is just prior to the sharp velocity increase caused by the onset of systole. This interval continues for 0.05 sec, terminating before the peak systolic velocity is attained. Interval I_2 encompasses the region in the neighborhood of peak systolic velocity and thus the region of highest instantaneous Reynolds number. The subsequent deceleration phase is included in I_3, while I_4 starts at the beginning of a jump in velocity which corresponds, for the case of no occlusion, to the dicrotic notch in the pressure waveform. These time intervals were established for the case with no stenosis present. The actual triggering signal, however, was the corresponding ECG recording since the velocity itself is unreliable as a timing standard when flow disorder

occurs. Thus, the same time locations on the ECG were used as the time base for all degrees of occlusion.

The procedure for each interval was to digitize 100 samples of 0.05 seconds duration. Each of these samples was represented by 128 points. After that, the same procedure was followed to take 100 samples of 0.20 second duration that includes the four intervals together. Each sample was represented by 512 points. For the above mentioned cases the average waveform segment was calculated according to equation (3-1).

3.1.2 Energy Spectra

Spectral analyses were performed on the HP5451A Fourier Analyzer using fast Fourier transform techniques. The disturbance velocity was found by applying the digital counterpart of Equation (2-4) once the average $U(t_\ell)$ was obtained. Thus,

$$u'(t_\ell) = u(t_\ell) - U(t_\ell); \qquad \ell = 0, 1, 2, \ldots, L - 1 \qquad (3\text{-}2)$$

where t_ℓ represents a specific value of time corresponding to the sampling points and

t_o is the initial time in the interval.

Again, 100 sample intervals were employed to obtain the spectral results. Since the frequency bandwidth resolution is the inverse of the sample time, the value of Δf for a sampling record of 0.05 second is 20 Hertz, while for $T = 0.2$ second, the resultant Δf is 5 Hertz.

3.1.3 The Root Mean Square of the Disturbance Velocity

The rms value of the disturbance velocity was found by analog-to-digital conversion of $u'(t)$, employing the same sampling parameter values

as for the energy spectra, and then squaring, integrating over the time interval, and taking the square root. As a check on the numerical accuracy of the fast Fourier transform techniques utilized within the Fourier analyzer, the rms disturbance velocity was also determined from the integral under the energy spectrum. The direct method and the energy spectrum integration gave good agreement if the turbulence level was not low. However, for mild to moderate stenoses, the fact that the relatively high energy, low frequency content below 20 Hz is approximated by points only at 0 and 20 Hz leads to some error in obtaining u'_{rms} from the spectral integration. The values reported here were all obtained from the direct calculation technique.

3.1.4 Autocorrelation Functions

The autocorrelation functions for the disturbance velocity were calculated according to equation (2-9) and (2-10) using the HP5451A Fourier Analyzer. Again, the same sampling parameters used to calculate u' and the energy spectrum of the disturbance velocity were also used here. Because of the wrap around error, the autocorrelation function can only be presented for delay times between zero and one-fourth of the sampling time. For the time history analysis, the maximum time for the autocorrelation function plot is .0125 second.

3.2 Results

This section summarizes the results obtained from the study of one of the in vivo experiments selected to characterize flow disturbances. The measurements were made with a right angle hot film probe stationed at the centerline of the descending thoracic aorta of a dog. The sensing

element was located 2 cm distal to the application of the constricting band. Relevant data for this experiment are tabulated in Table (3-1).

3.2.1 Velocity Waveforms

Figure (3-1) illustrates the velocity waveform results obtained for several degrees of stenosis (23). The percent occlusion is given as a reduction in the internal cross-sectional area of the vessel. The appearance of flow disorder created by the stenosis is readily observed in the waveforms. Instabilities first appear in the region of peak systolic velocity, but preferentially occurring in the deceleration phase of systole. As the degree of stenosis increases, so does the duration of flow disorder, first into a larger segment of deceleration and then moving into the acceleration phase. The severest stenosis created a flow in which little pulsatility could be seen and turbulence persisted throughout the entire cycle. All other experiments showed the same trends as did these data. In particular, in every animal experiment performed, a relatively mild stenosis on the order of 20 percent occlusion always yielded flow disorder immediately downstream of the constriction.

It can be seen that no negative velocities were recorded in these results. Although the corresponding electromagnetic flowmeter waveforms, Figure (3-2), likewise showed no overall flow reversal, it is entirely possible that localized regions of the aorta experienced reversed velocities which could not be measured with the hot film probes. It is for this reason that analysis of the late diastolic phase was not attempted.

The ensemble average waveforms for the total cardiac cycle are given in Figure (3-3) and show several features of interest. First,

Table 3-1. Parameters for Stenosis Experiment

Percent Occlusion (reduction in area)	Constriction diameter (cm)	Peak Local Velocity (U_p ~ cm/sec)	Mean Volume Flow Rate (Q ~ ml/sec)	Peak Reynolds Number ($\rho U_p D/\eta_\infty$)	Mean Reynolds Number ($4\rho Q/\pi\eta_\infty D$)
0	1.2	59	31	2500	1200
20	1.1	50	29	2100	1100
40	0.9	45	31	1900	1200
58	0.8	41	30	1700	1100
74	0.6	48	29	2000	1100
88	0.4	57	27	2400	1000

Frequency parameter: $\alpha = 13.8$ ($\omega = 15.0$ rad/sec, $\eta_\infty = 0.030$ poise).

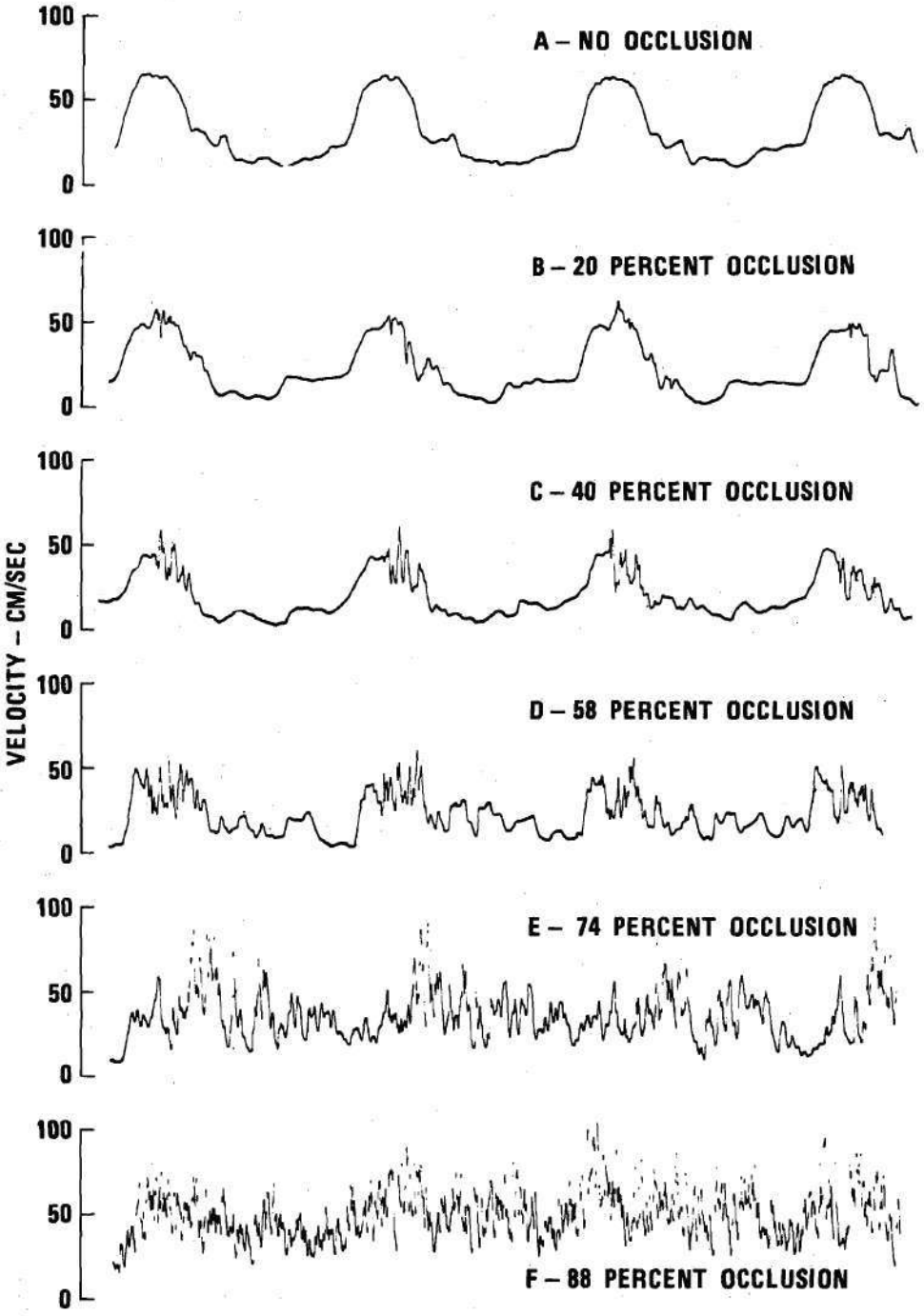

Figure 3-1. Velocity Waveforms Distal to Aortic Stenoses in the Descending Thoracic Aorta of a Dog

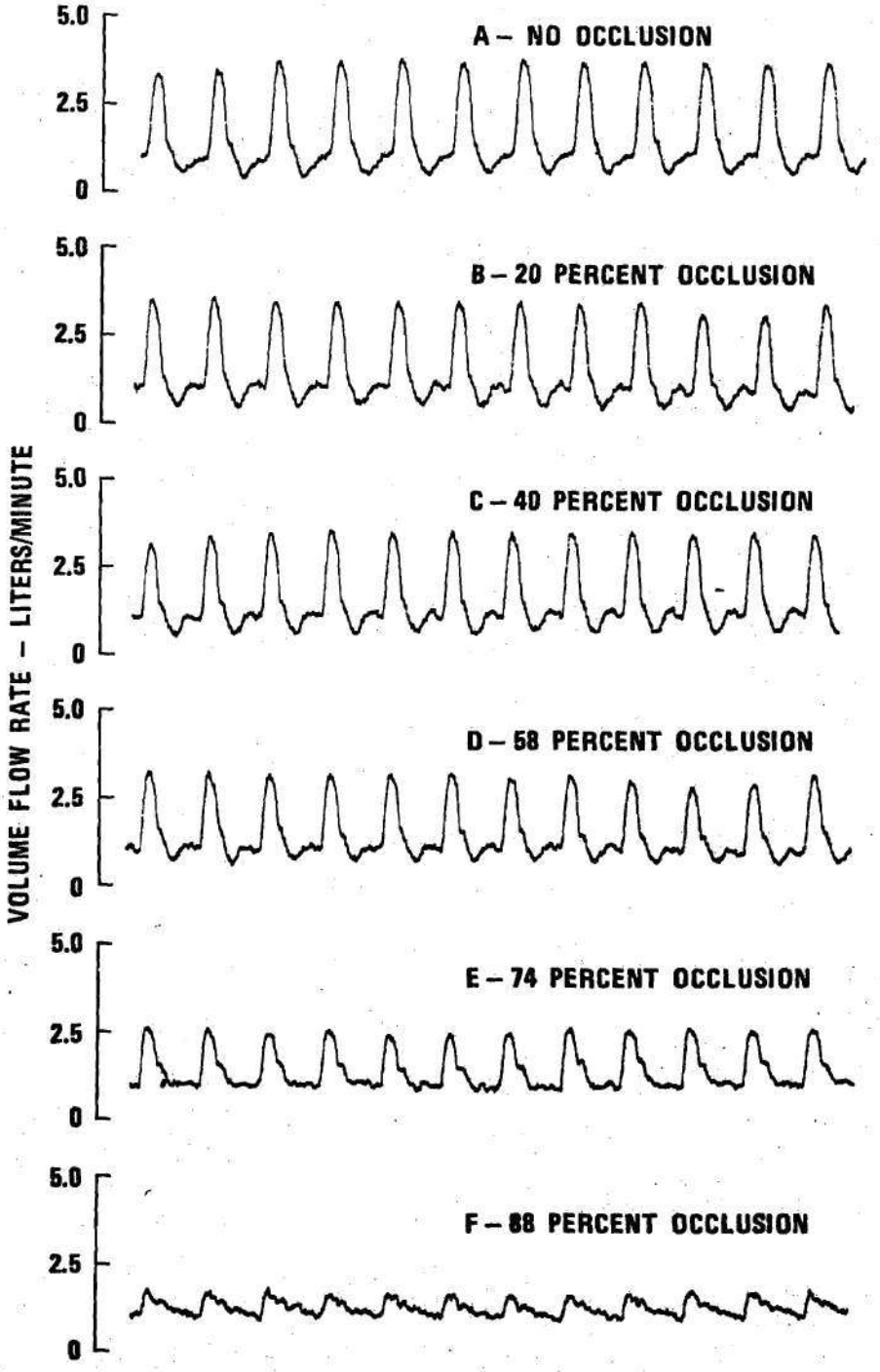

Figure 3-2. Instantaneous Flow Rate Recorded Distal to Partial Occlusions in Aorta, Experiment 102974

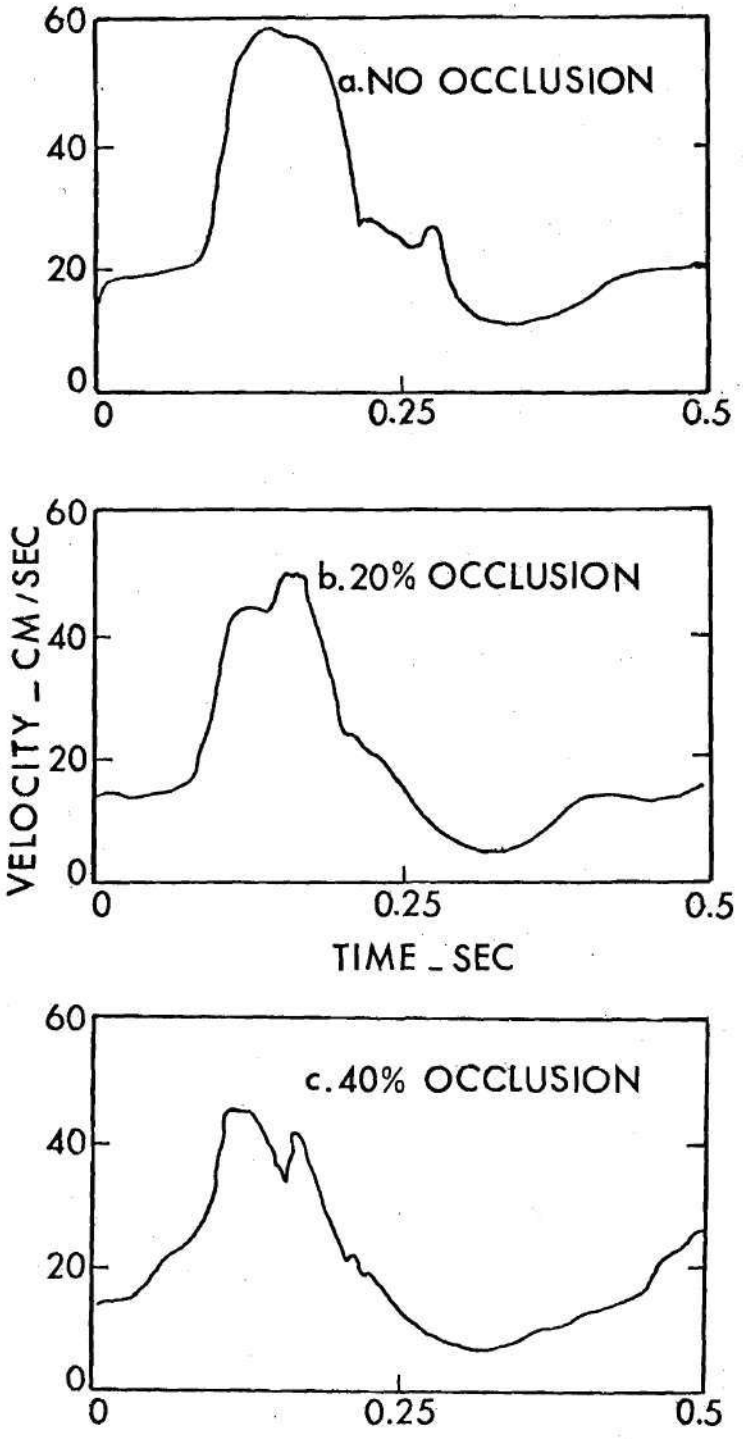

Figure 3-3. Ensemble Average Waveforms for the Total Cardiac Cycle

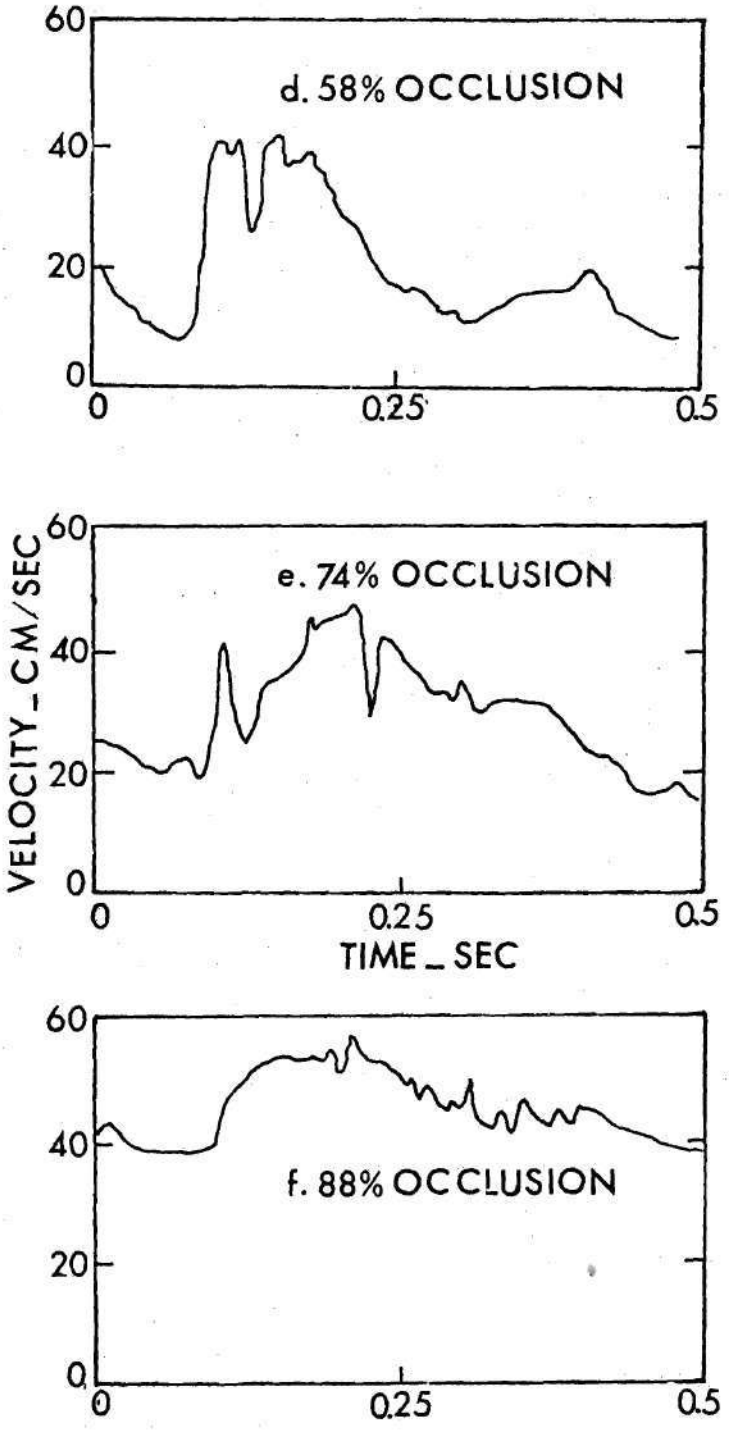

Figure 3-3. (Continued) Ensemble Average Waveforms for the Total Cardiac Cycle

consider the mild to moderate stenoses (20, 40, and 58 percent). The disturbances viewed in Figure (3-1) for these waveforms appear upon first inspection to be somewhat random. However, the ensemble averaging process reveals that, in the region near maximum velocity, there is a periodicity which occurs and results in split systolic peaks which are not at all random. In fact, this feature can be detected in the average waveform for the 74 percent stenosis although it is not seen in the 88 percent case. Second, although the individual waveforms for the cases of severe stenoses (74 and 88 percent) did not appear to give a distinguishably pulsatile shape, the average waveforms do display definite pulsatile features. Third, the pulsatility index, defined as the ratio of the amplitude envelope to the mean value of the velocity waveform (for example, see Gosling and King (56)), decreases as the degree of stenosis increases. This is due to the compliant nature of the vessels. Flow approaching the stenosis senses a relatively high resistance path so that substantial wave reflection occurs. This is manifested in the immediately proximal segment acting as a temporary "reservoir." The fluid cannot pass through the constriction as rapidly as before, and the proximal segment expands momentarily. Then with the vessel now in an expanded state, during diastole this "stored" blood will be released through the narrowing, resulting in a waveform which is considerably flatter than for the case of zero or mild stenosis.

It must be pointed out, however, that due to the inability of the hot film to measure reverse velocity, the values of this index for the mild to moderate stenoses, where there is a possibility of backflow

occurring, are likely to appear lower than the true value. This index also can be calculated from the measurements of volume flow rate using the electromagnetic flowmeter results, shown in Figure (3-2). The cuff-type probe was placed proximal to the renal arteries and the instantaneous volume flow rates were recorded from which a mean value was computed by integration. Table (3-2) summarizes the pulsatility index,

$$PI = \frac{\text{(maximum waveform value) - (minimum waveform value)}}{\text{mean waveform value}}$$

for both the hot film and electromagnetic flowmeter measurements.

Although the data in Table (3-2) demonstrate the effect of a stenosis-induced damping of the velocity waveform, an attempt to relate these index values to published clinical data has not been made since the conditions under which the results were obtained are quite different, both anatomically and from the standpoint of measurement technique and location.

Figures (3-4) show samples of the disturbance velocity development during the four intervals for the different degrees of occlusion investigated. The disturbance starts to develop for the case of 20 percent occlusion during the peak phase (I_2) and continues during the deceleration phase (I_3). As the degree of occlusion increases the disturbance becomes more extensive in time until it reaches the acceleration phase (I_1) for the case of 58 and 74 percent occlusion.

One can notice also the high level of disturbance velocity for the cases of severe occlusion as compared to the corresponding ensemble

Table 3-2. Pulsatility Index

Percent Occlusion	PI, Hot Film Anemometer	PI, EM Flowmeter
0	1.53	1.72
20	1.85	1.72
40	1.77	1.51
58	1.56	1.33
74	.86	.92
88	.39	.43

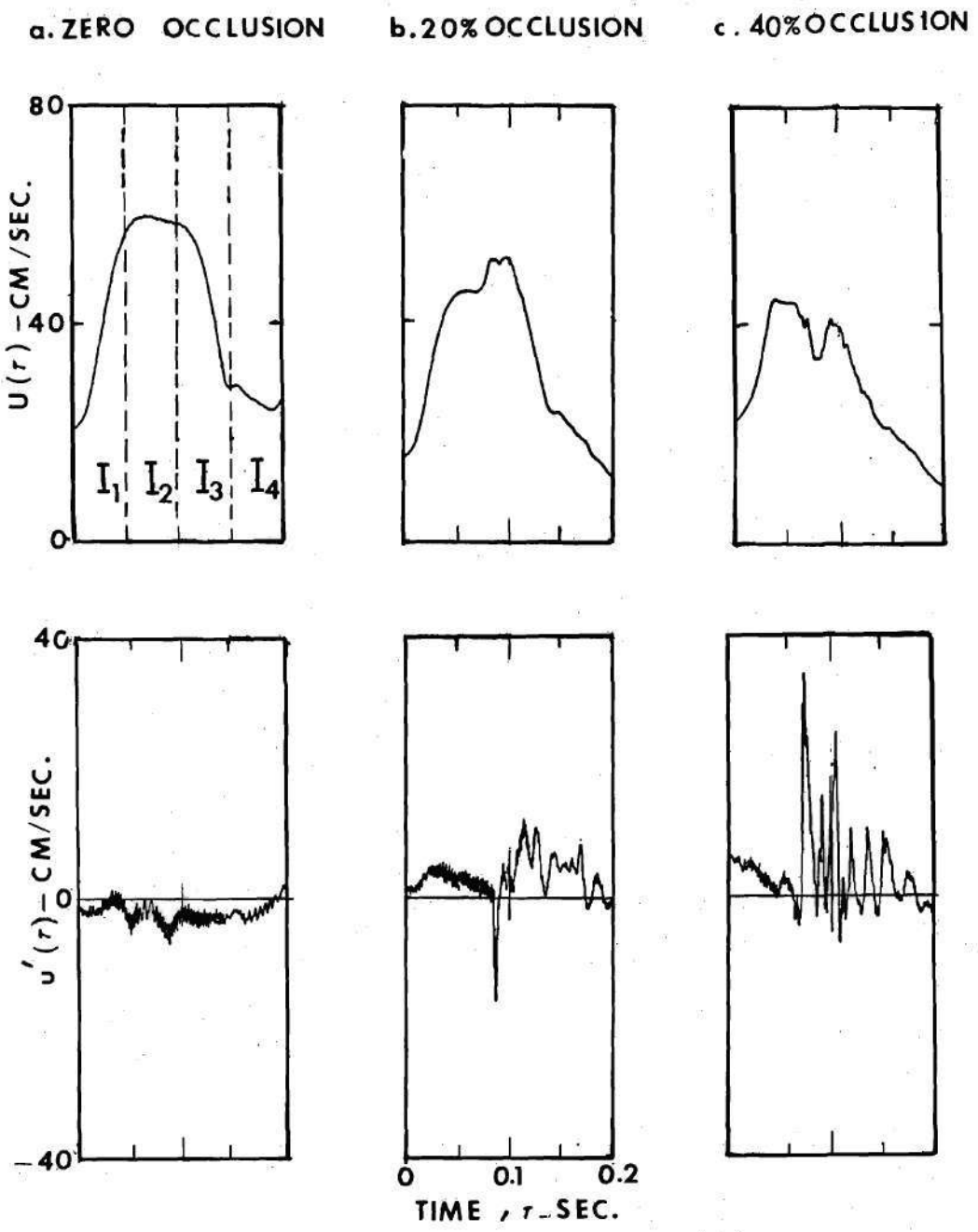

Figure 3-4. Disturbance Velocity Development During the Four Intervals

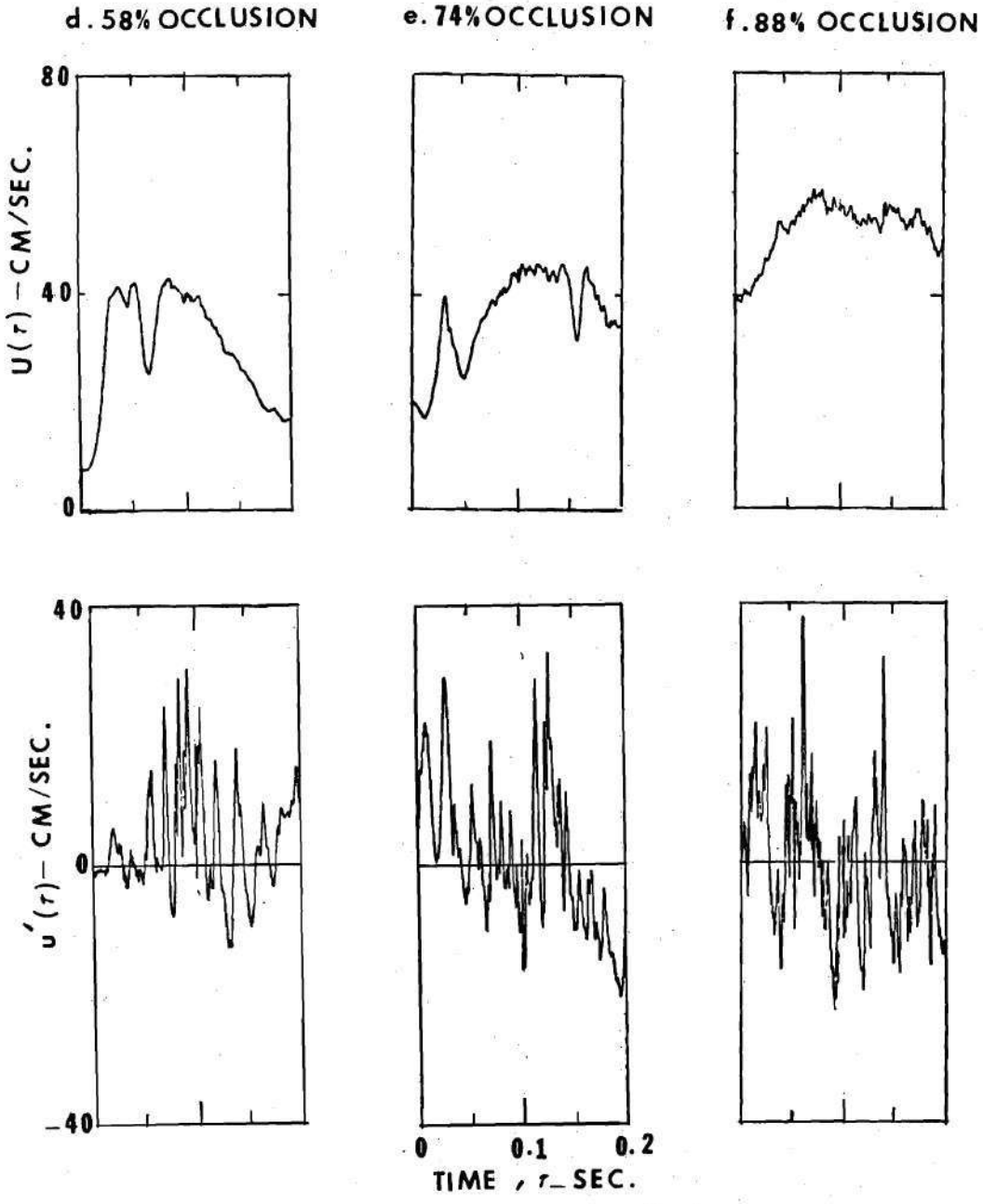

Figure 3-4. (Continued) Disturbance Velocity Development During the Four Intervals

average velocities, demonstrating that these poststenotic fields are severely turbulent. This finding is in agreement with the laser Doppler velocimeter in vitro measurements of Deshpande (81) and with data taken in vitro in the present study (see Chapter V).

3.2.2 Energy Spectra

Figures (3-5) illustrate the results for disordered flow development as the degree of stenosis is increased. These curves show energy spectra for the disturbance velocity u', as calculated from Equation (3-2). The case for no occlusion is given in Figure (3-5a). The energy spectra for all four time intervals are very nearly the same, indicating little disorder in the velocity waveforms during systole.

Figure (3-5b) gives the energy spectra for a 20 percent stenosis. Interval I_1 is very similar to that for zero occlusion and shows a very low energy content. However, even for such a mild blockage, the spectra for I_2 through I_4 show a substantial increase in disorder.

The development of disorder is seen to be quite rapid. It begins within the peak velocity region, persists throughout the deceleration phase of systole and then starts to decay within the I_4 interval, subsequent to aortic valve closure. The spectrum for I_4 indicates a reduction in amplitude but is still markedly greater than for I_4 with no stenosis. Since the spectra for I_1 at zero and 20 percent occlusion are virtually identical, the disorder created during one heartbeat for the mild stenosis decays sufficiently rapidly that it is no longer present at the onset of the next beat.

Energy spectra for the disturbance velocity for a 40 percent

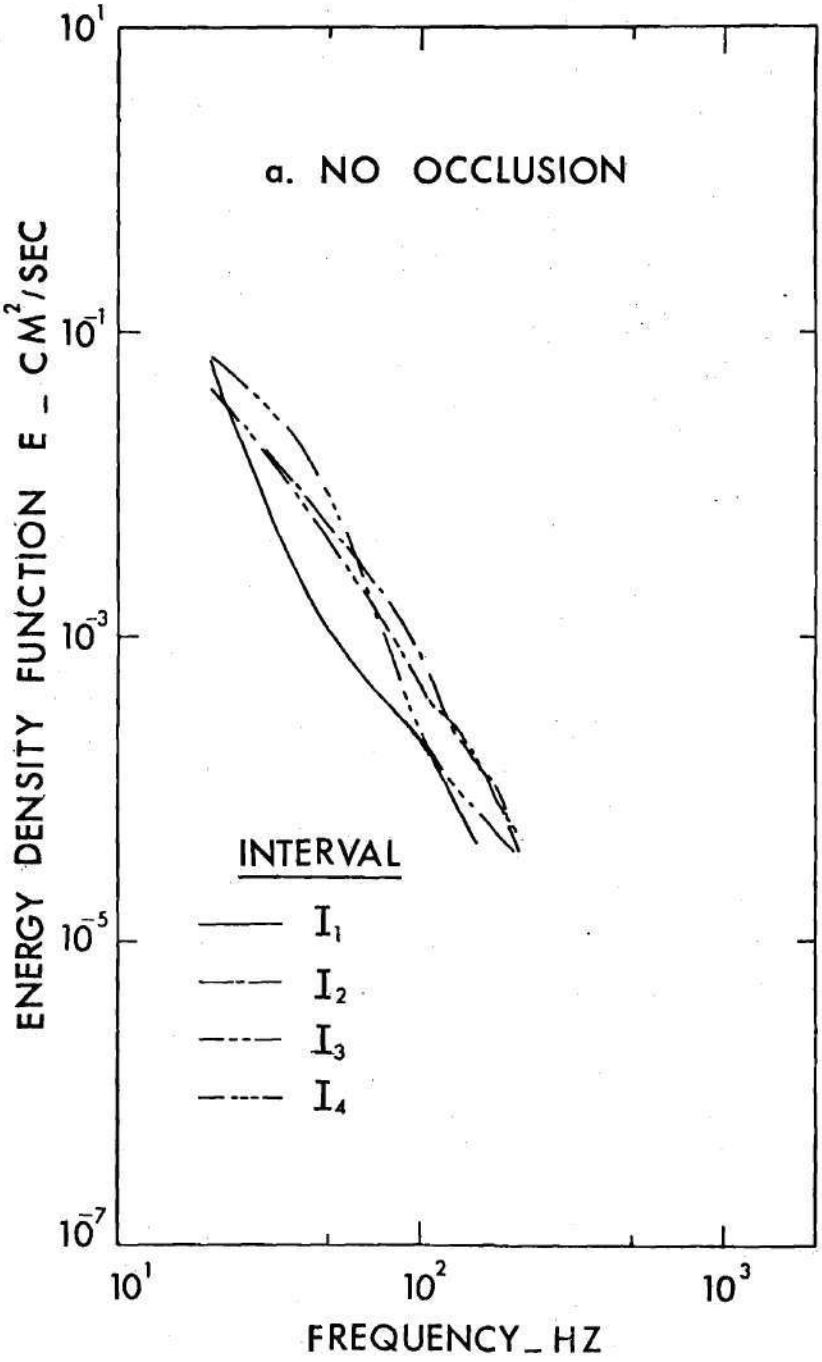

Figure 3-5a. Development with Time of the Disturbance Energy Spectrum for the Case of No Occlusion

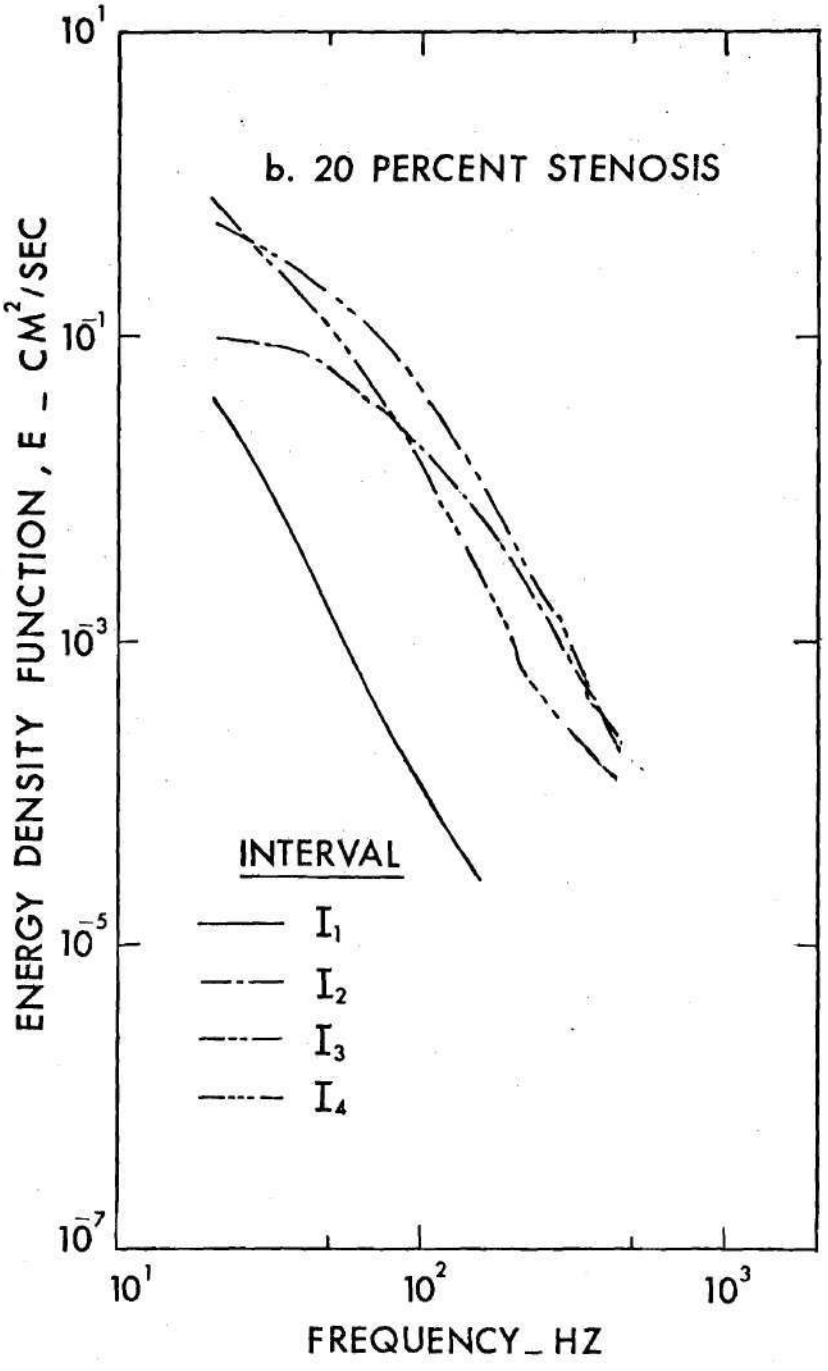

Figure 3-5b. Development with Time of the Disturbance Energy Spectrum for the Case of 20 Percent Stenosis

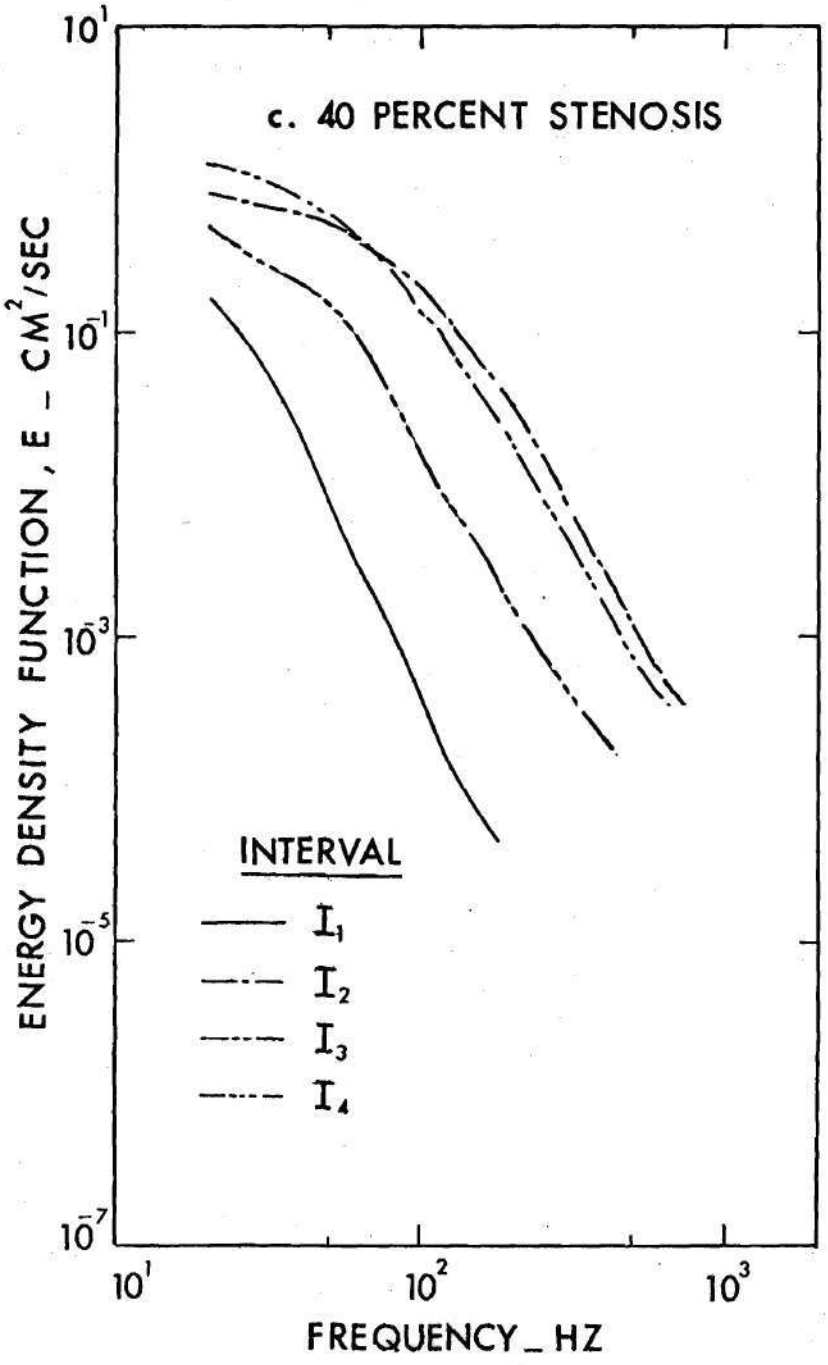

Figure 3-5c. Development with Time of the Disturbance Energy Spectrum for the Case of 40 Percent Stenosis

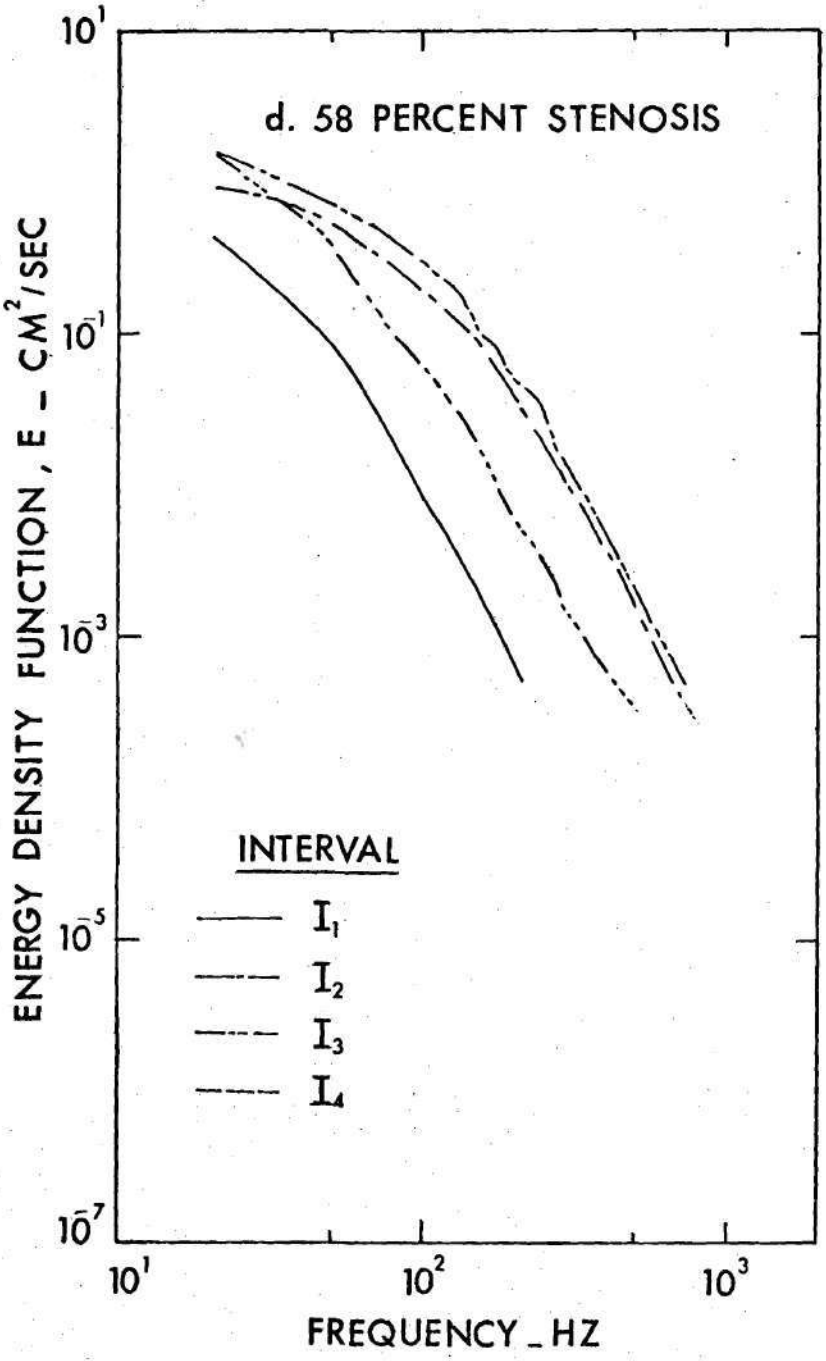

Figure 3-5d. Development with Time of the Disturbance Energy Spectrum for the Case of 58 Percent Stenosis

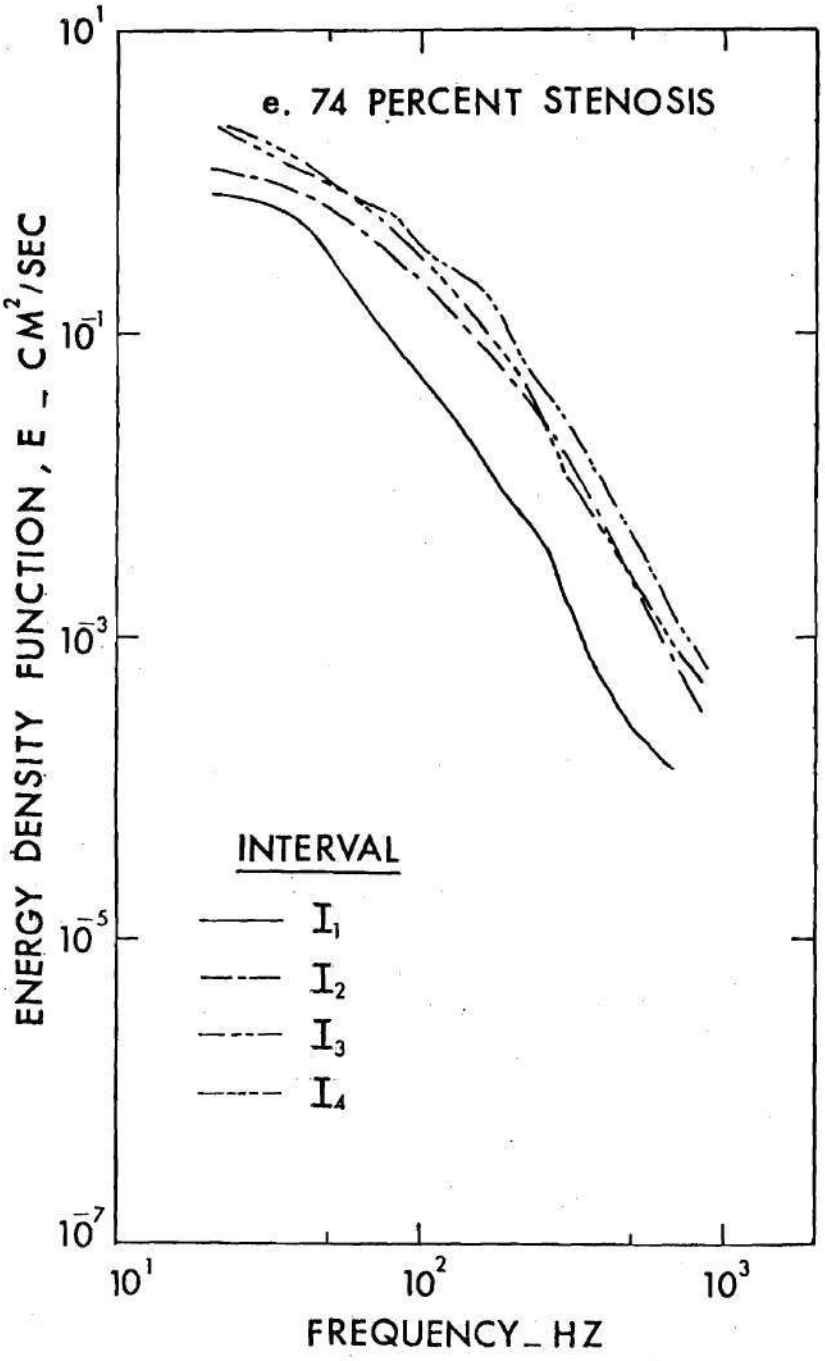

Figure 3-5e. Development with Time of the Disturbance Energy Spectrum for the Case of 74 Percent Stenosis

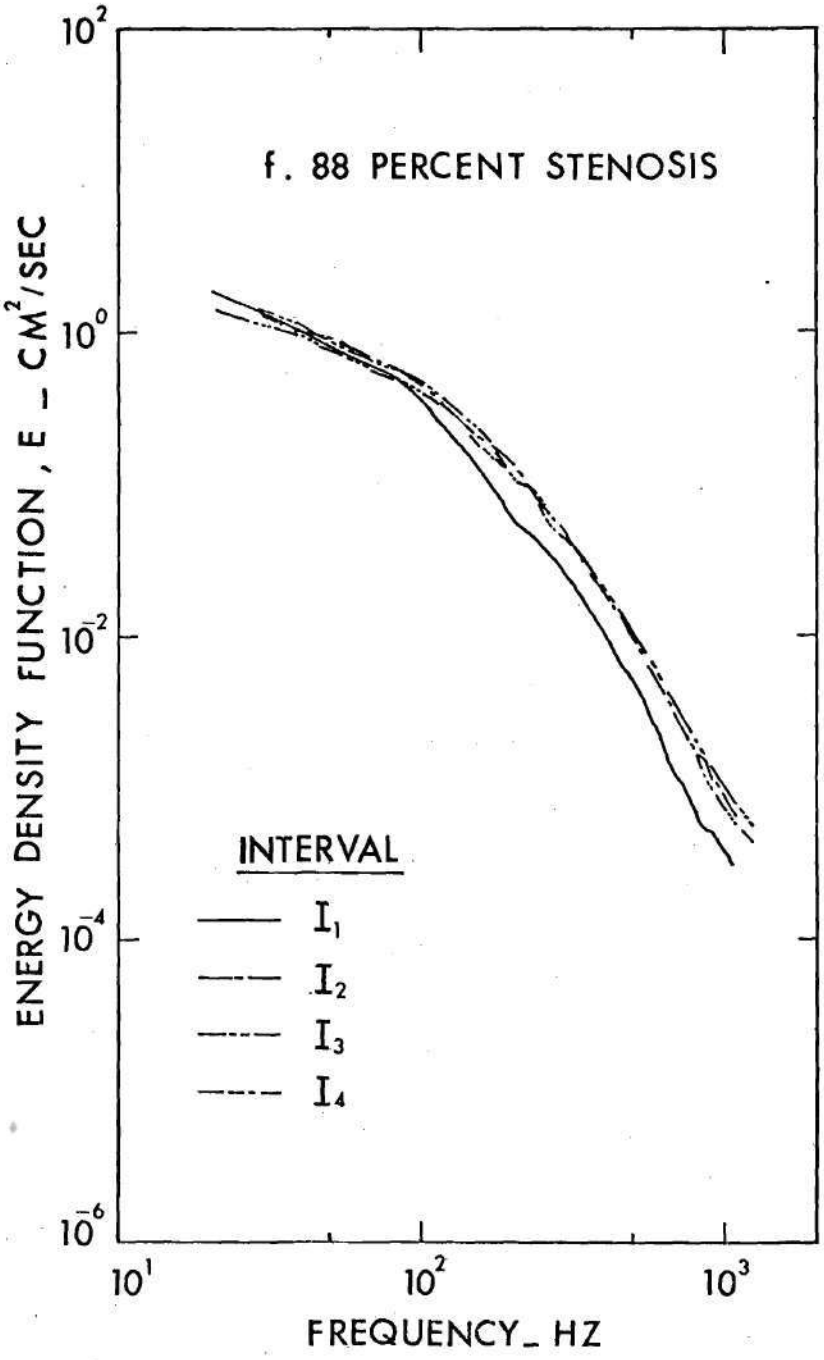

Figure 3-5f. Development with Time of the Disturbance Energy Spectrum for the Case of 88 Percent Stenosis

stenosis are given in Figure (3-5c). At this degree of occlusion there is some flow disorder throughout the waveform. Even the acceleration phase (interval I_1) shows considerably higher energy content than for the corresponding interval with no stenosis present. Intervals I_2 and I_3 have a high degree of disorder which decays during I_4. The remaining Figures (3-5d, e, f) illustrate how the flow disorder continues to spread throughout the cardiac cycle. Although I_2 and I_3 consistently show higher energy content, it becomes less easy to distinguish among spectra from the various intervals. Certainly, for the severest stenosis (88 percent) the time interval taken for analysis makes little difference; the flow is turbulent throughout.

An informative manner of presenting the results is to graph the energy spectra for various degrees of occlusion at the same time interval. Although it is useful to employ nondimensional variables in doing this, selection of the appropriate characteristic length and velocity is not straightforward. Since the mean velocity, U(t), varies with time, it would seem that a reasonable characteristic velocity is the "average" velocity over a given interval of analysis which can be defined, for this experiment, to be

$$\overline{U}_i = \frac{1}{T} \int_{t_i}^{t_i+T} U(t)dt \qquad (3\text{-}4)$$

where

t_i is the initial time of the i^{th} interval and

T is the duration of that interval.

This average velocity may not be the best for situations in which there is a sharp variation in U(t) over the interval, since disorder may only be produced at times corresponding to large U(t); and the averaging process would not give proper weighting to the higher velocities. Such may be the case for interval I_1 in these experiments.

The choice of a characteristic length must take into account the location of the measurement point with respect to the stenosis. This problem has been discussed by Cassanova (38), Giddens et al. (23), and Clark (42). For the probe location in the data presented here the appropriate length is the diameter of the constricted opening, rather than the unoccluded vessel diameter, because of the proximity of the velocity sensor to the minimum area of constriction. Thus, the stenosis diameter, d, tabulated in Table (3-1) is employed as the proper characteristic length.

Finally, since the u'_{rms} values are nonstationary, it is appropriate to use the normalized spectrum for an interval as

$$F(f) = \frac{E(f)}{\overline{u'^2}} \tag{3-5}$$

where

E(f) is the energy (actually, velocity-squared) content per unit frequency, and

$\overline{u'^2}$ is the mean square velocity fluctuation averaged over the interval.

The frequency is denoted by f in Hz. This quantity $\overline{u'^2}$ is related to E(f) by

$$\overline{u'^2} = \int_0^\infty E(f)df \tag{3-6}$$

Thus, the dimensionless variables

$$E^* = \frac{F\bar{U}}{2\pi d} \qquad \text{and} \qquad N_s^* = \frac{2\pi f d}{\bar{U}} \tag{3-7}$$

may be formed and the energy spectra graphed in these coordinates.

The results for intervals I_1, I_2, and I_3 are given in Figures (3-6). It can be seen that during the interval I_1, the spectra fall into two distinct groups in Figure (3-6a); the cases of zero, 20, and 40 percent occlusion merge together as do those of 58, 74, and 88 percent occlusion. However, the two sets of curves are distinctly separate. For the intervals I_2 and I_3 all degrees of occlusion other than zero fall reasonably well into a single group as shown in Figures (3-6b and c). The case for no occlusion stands clearly apart. The interpretation of these results is that, for the first interval, there is very little flow disorder for the zero, 20, and 40 percent constrictions and thus the spectra are similar. For the larger degrees of stenosis, however, considerable disorder is present; and the behavior of these spectra is again similar. For the intervals I_2 and I_3 all but the zero occlusion case show marked flow disturbances and the postulated similarity coordinates tend to collapse the data reasonably well. Thus, even though the rms values are quite different, it appears that the disorder has spectral similarity.

Care is required in comparing these spectra with a "typical"

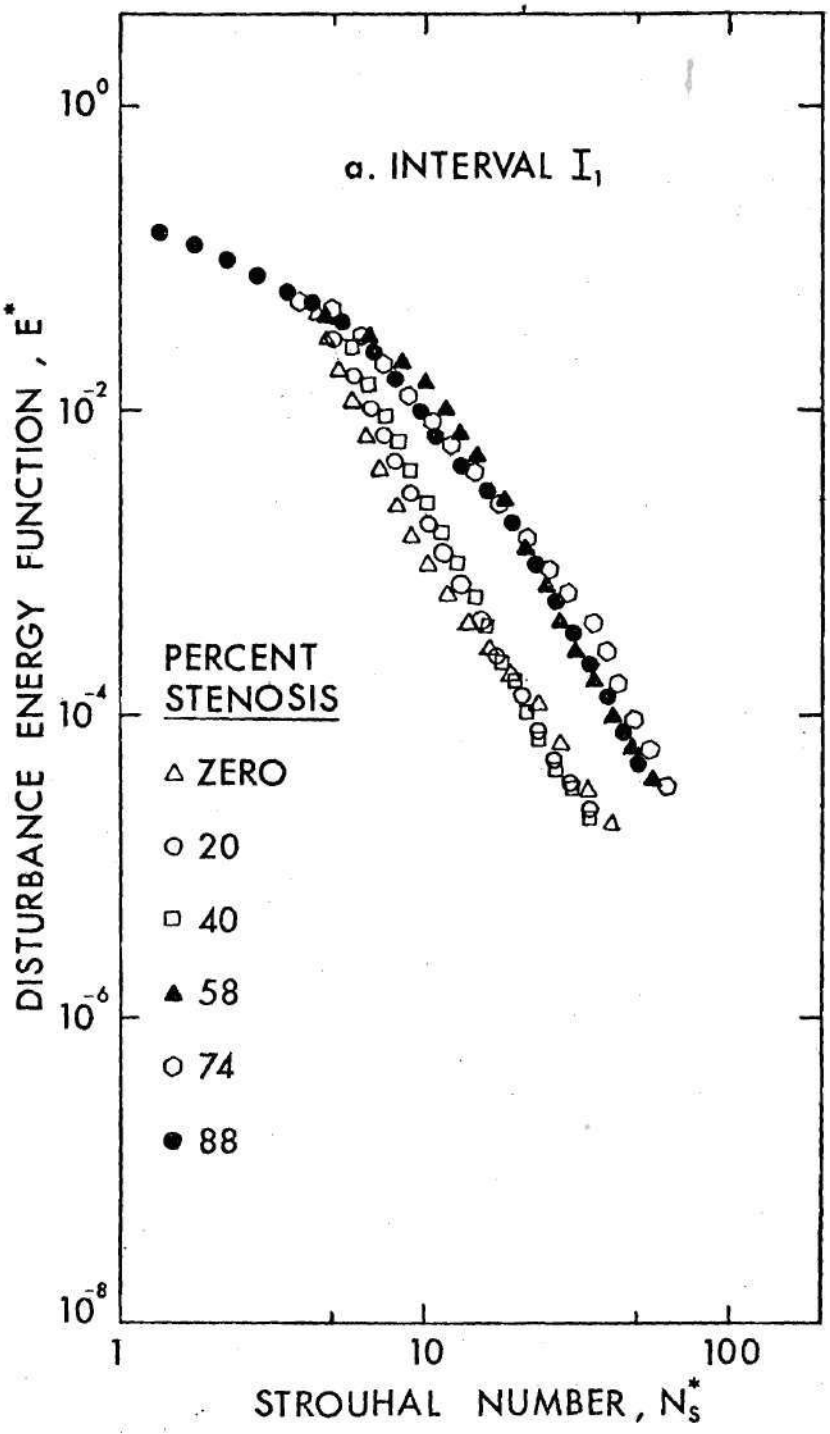

Figure 3-6a. Nondimensionalized Energy and Frequency Correlation for the Acceleration Phase

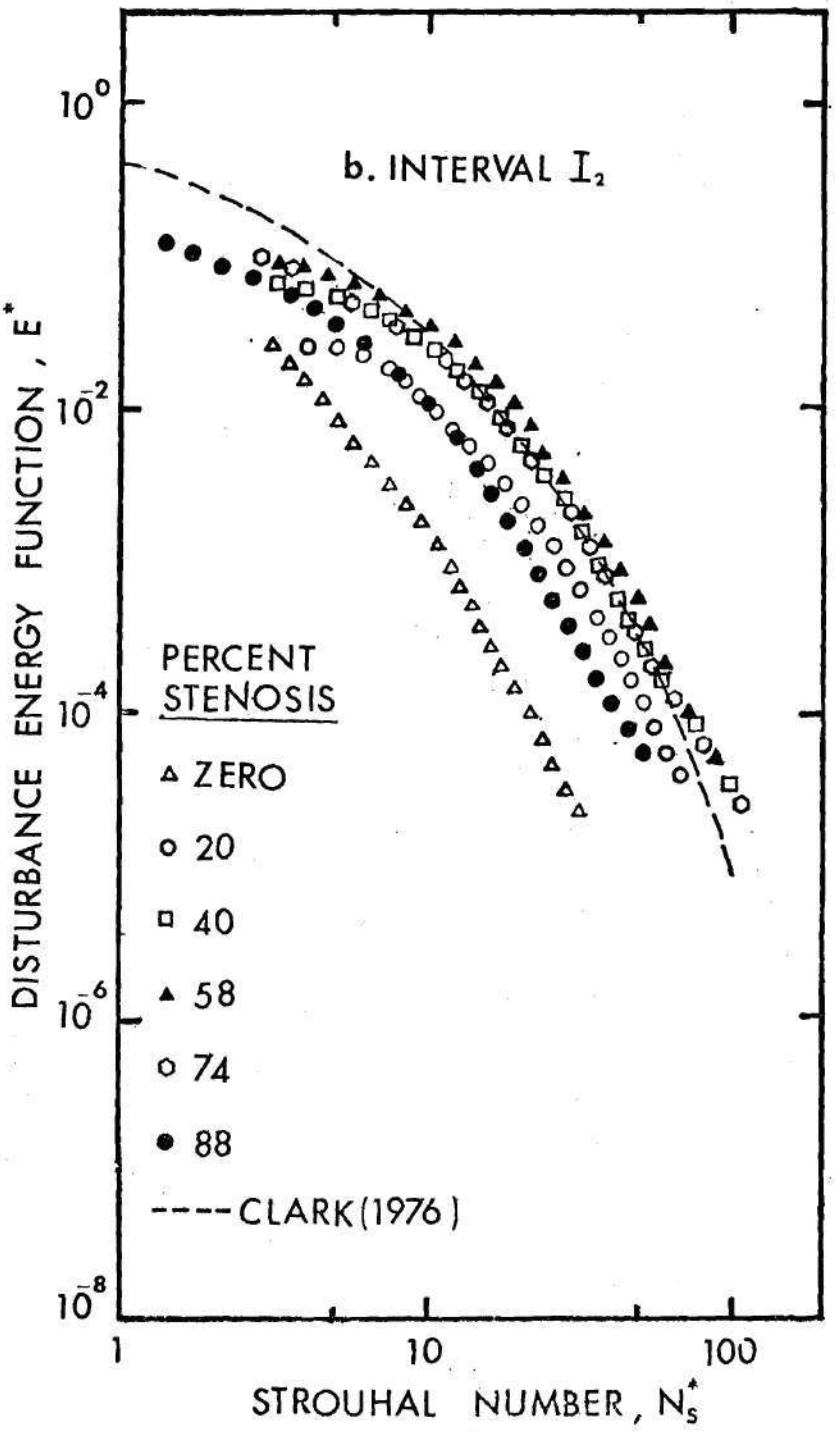

Figure 3-6b. Nondimensionalized Energy and Frequency Correlation for the Peak Phase

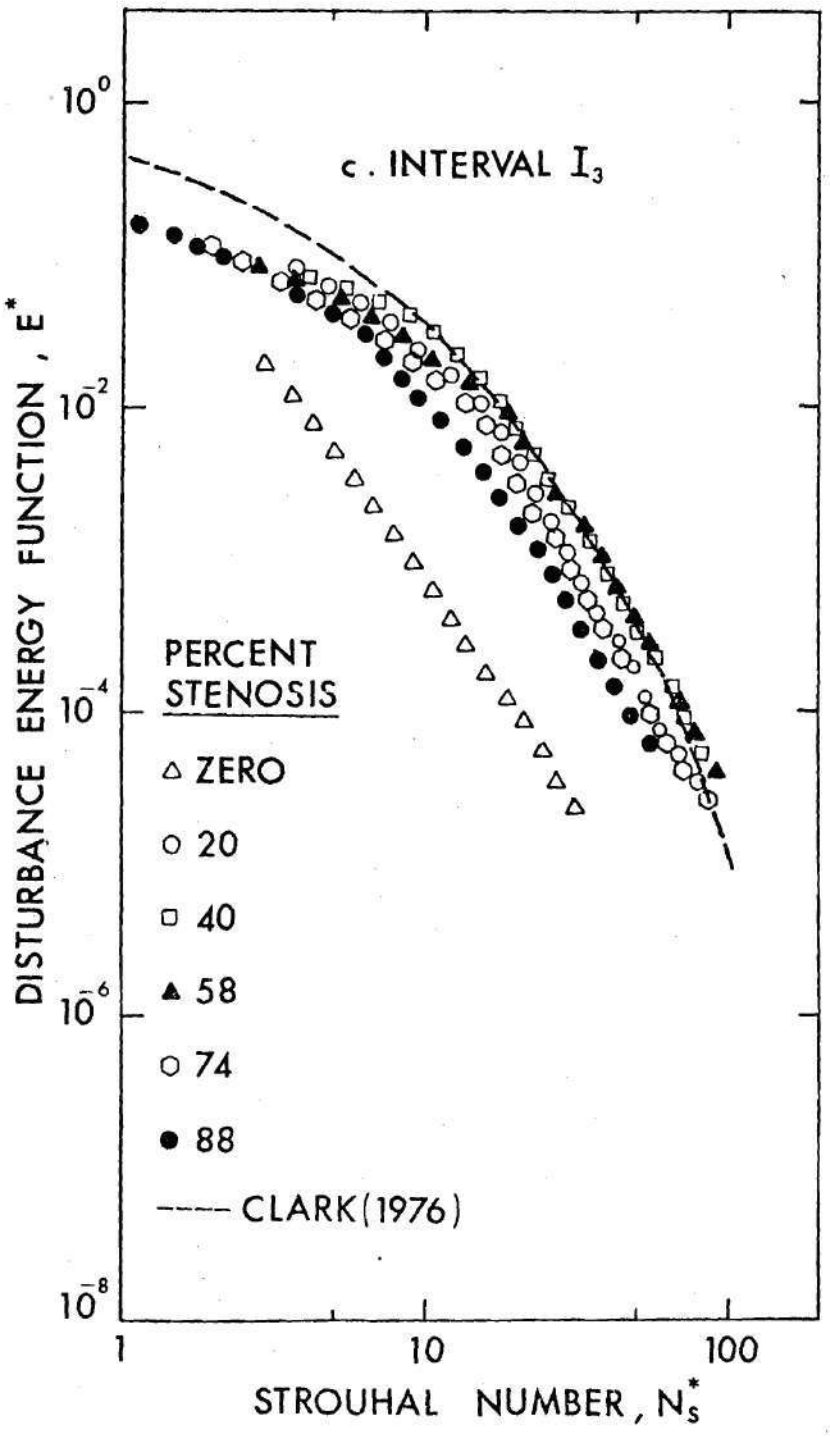

Figure 3-6c. Nondimensionalized Energy and Frequency Correlation for the Deceleration Phase

turbulent energy spectrum since it is rather difficult to decide just what spectral shape is typical. For example, Resch (82) has demonstrated that the shapes of energy spectra for turbulent flow in a cylindrical pipe show a Reynolds number dependence in the range from 6,000 to 140,000. Clark (42) has given energy spectra for poststenotic flow fields in laboratory models of stenoses, using velocity measurements obtained with a hot film probe. For the presentation of his data frequencies below 22.4 Hertz were excluded in the calculation of $\overline{u'^2}$, so that his definition is not quite the same as that employed in this study. However, a curve has been drawn through the data reported in Figure (7b) of that reference, and this is plotted in Figures (3-6b and c) for the purposes of comparison with the present results. The data reported by Clark in that particular figure represent energy spectra obtained distal to stenoses of 88.9 percent area reduction, at an axial location corresponding to maximum turbulence energy. The range of Reynolds number was from 2600 to 27,000 and the flow was steady. The agreement between those results and the present spectra is reasonably good. As a check the 0-20 Hz contribution was removed from the present data and a further comparison was made which is not presented here. With this low frequency contribution removed, the agreement between Clark's results and the present one is quite good.

An alternative approach to illustrate adequately the trend as the constriction is increased and to examine the flow disorder is to consider a sampling time that includes the four intervals (I_1, I_2, I_3, and I_4) together. Figure (3-7) presents the energy density function for different degrees of occlusion. Very little disorder is observed for the case of

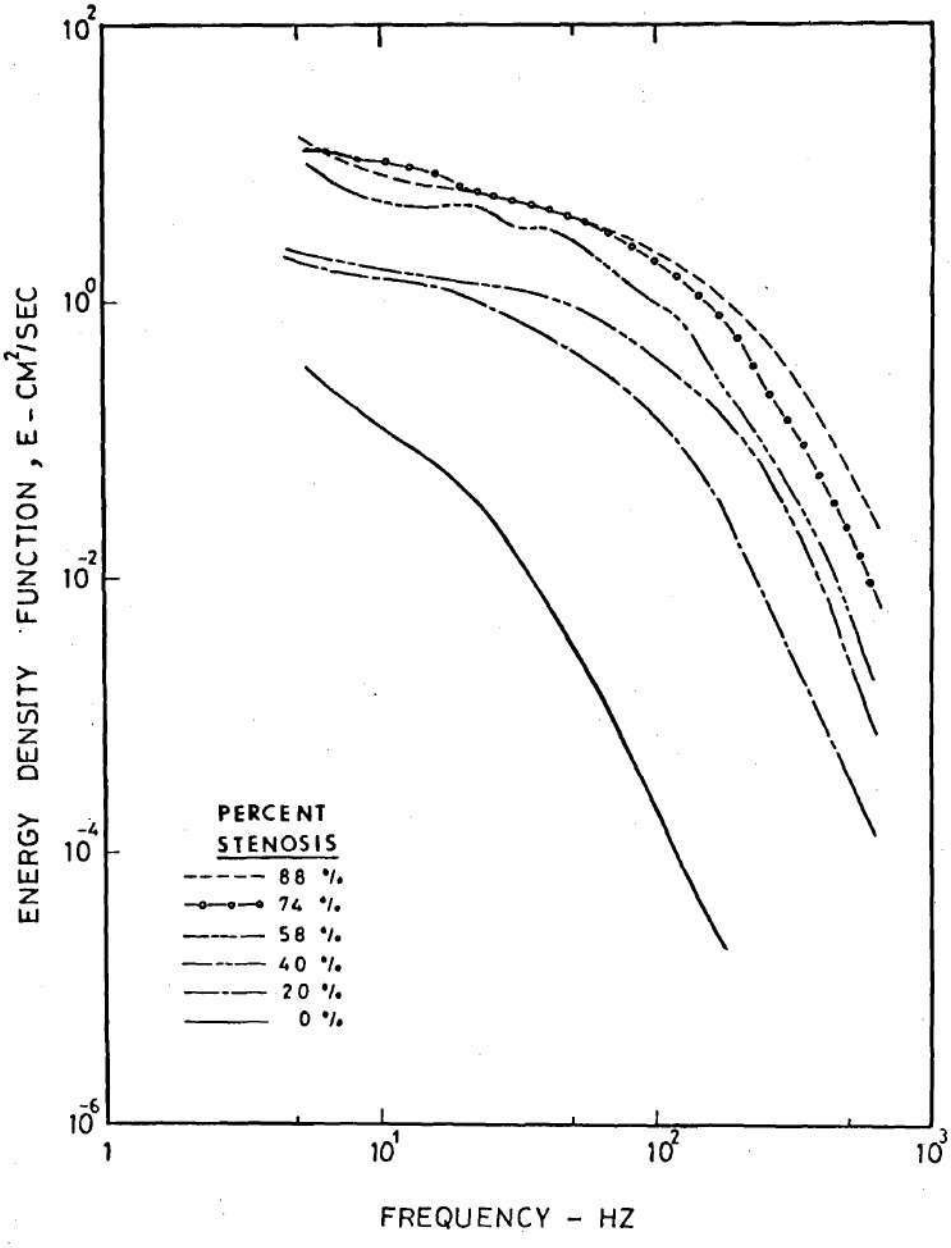

Figure 3-7. Energy Spectra for Different Degrees of Occlusion Considering the Four Intervals Together

zero occlusion. However, once there exists a mild stenosis (20 percent area reduction) a considerable increase in the disturbance energy, especially at high frequencies is observed. The level of the energy spectra increases for higher degrees of occlusion.

3.2.3 RMS Velocity Fluctuations

Figure (3-8) gives the results for the rms velocity fluctuation as a function of the degree of stenosis and the time period within the cardiac cycle. The nonstationary behavior can be clearly seen. It can be noted that the case for zero occlusion has relatively low values for u'_{rms}. Since the velocity waveforms for this case appeared to be generally smooth, it is suspected that the corresponding values in Figure (3-8) are, in fact, an indication of the biological disorder induced upon the flow. The first time period for 20 percent stenosis likewise has a low rms fluctuating velocity value. However, during time period I_2, the value has increased sharply and is indicative of a contribution arising from flow disorder created by the stenosis. The magnitude of u'_{rms} then rises slightly during I_3, followed by a mild decline in I_4. For the 40 percent occlusion a similar pattern is seen; that is, a fairly low rms disturbance velocity occurs during the onset of systole followed by a substantial increase near peak systolic velocity and in the deceleration phase. The remaining occlusions exhibit high disturbance velocities throughout the time periods studied. It is interesting that all stenoses studied, except the most severe, gave maximum turbulence levels during I_3, the deceleration phase of the waveform. Also, except for cases where u'_{rms} was relatively low, the similarity correlations discussed previously

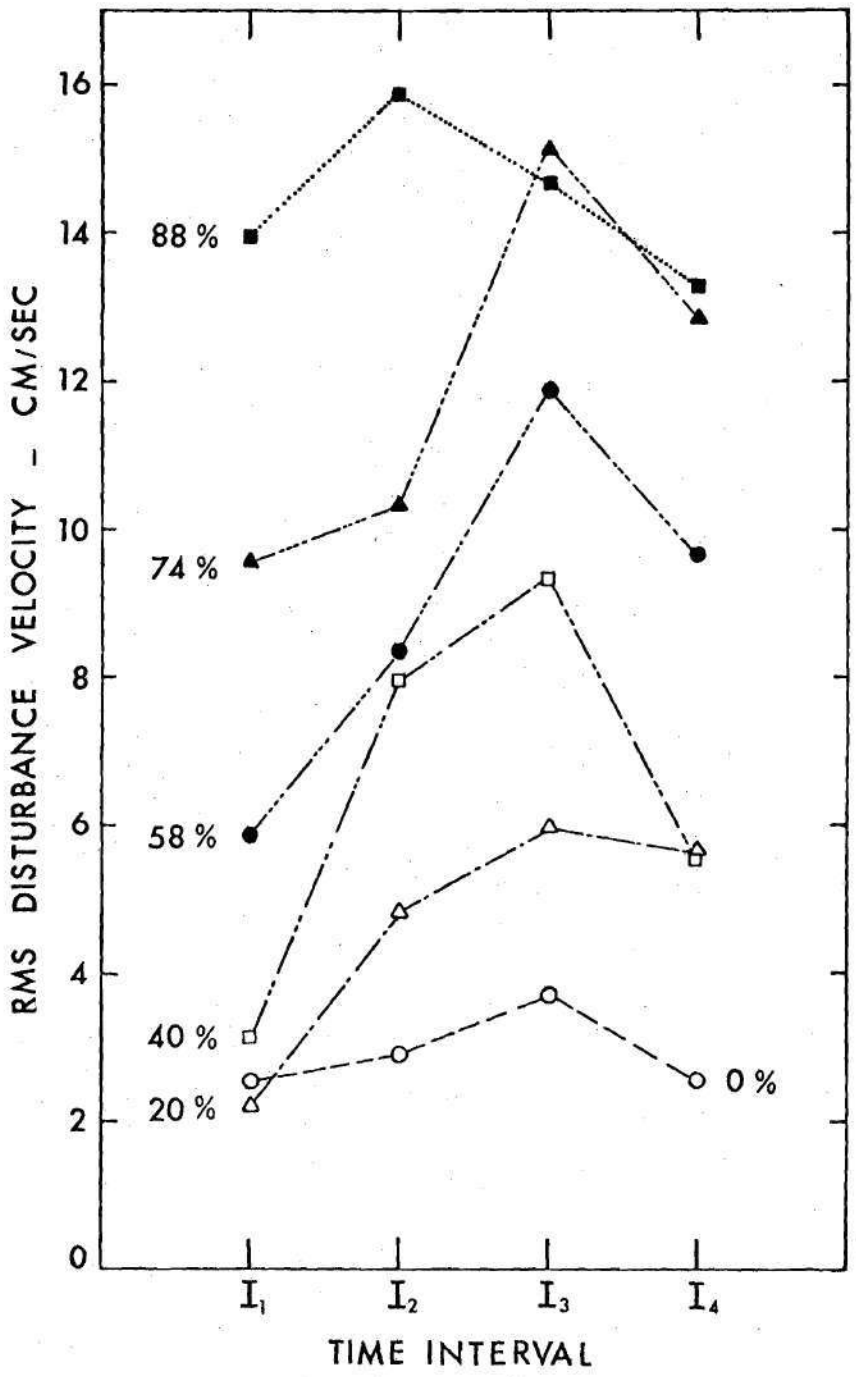

Figure 3-8. Variation of R.M.S. Disturbance Velocity as a Function of Time Interval

succeeded reasonably well in merging the energy spectra into a closely grouped set.

Many of the values reported in Figure (3-8) are much greater than those reported by Stein and Sabbah (25) for turbulence measured in human aortas with normal and stenosed values. One probable reason is that the measurements reported here are taken just distal to the stenoses; and, for moderate to severe obstructions, the flow field is violently disturbed. Also, their analysis was for the entire velocity waveform so that periods of low disturbance during the cycle tend to reduce the average value of u'_{rms}. However, another reason for our higher values is the manner in which the data were treated. Stein and Sabbah raported u'_{rms} based upon high pass filtering of the velocity signal at 30 Hertz under the assumption that frequencies less than this could be attributed to harmonics of the waveform. Thus, any disordered flow data at these lower frequencies is lost in their approach. The present definition of the disturbance velocity avoids this difficulty; and, in fact, the data indicate that noticeable contributions to flow disorder arise from disturbances with frequency components less than 30 Hertz. Thus, the major problem is now frequency resolution, which is entirely determined by the sampling parameters (i.e., the frequency bandwidth resolution for a sample time of 0.05 sec is equal to 20 Hertz).

3.2.4 The Autocorrelation Functions

The autocorrelation functions for different degrees of occlusion calculated for each of the four intervals are presented in Figure (3-9). Generally, the autocorrelation curves for interval I_1 show that the integral

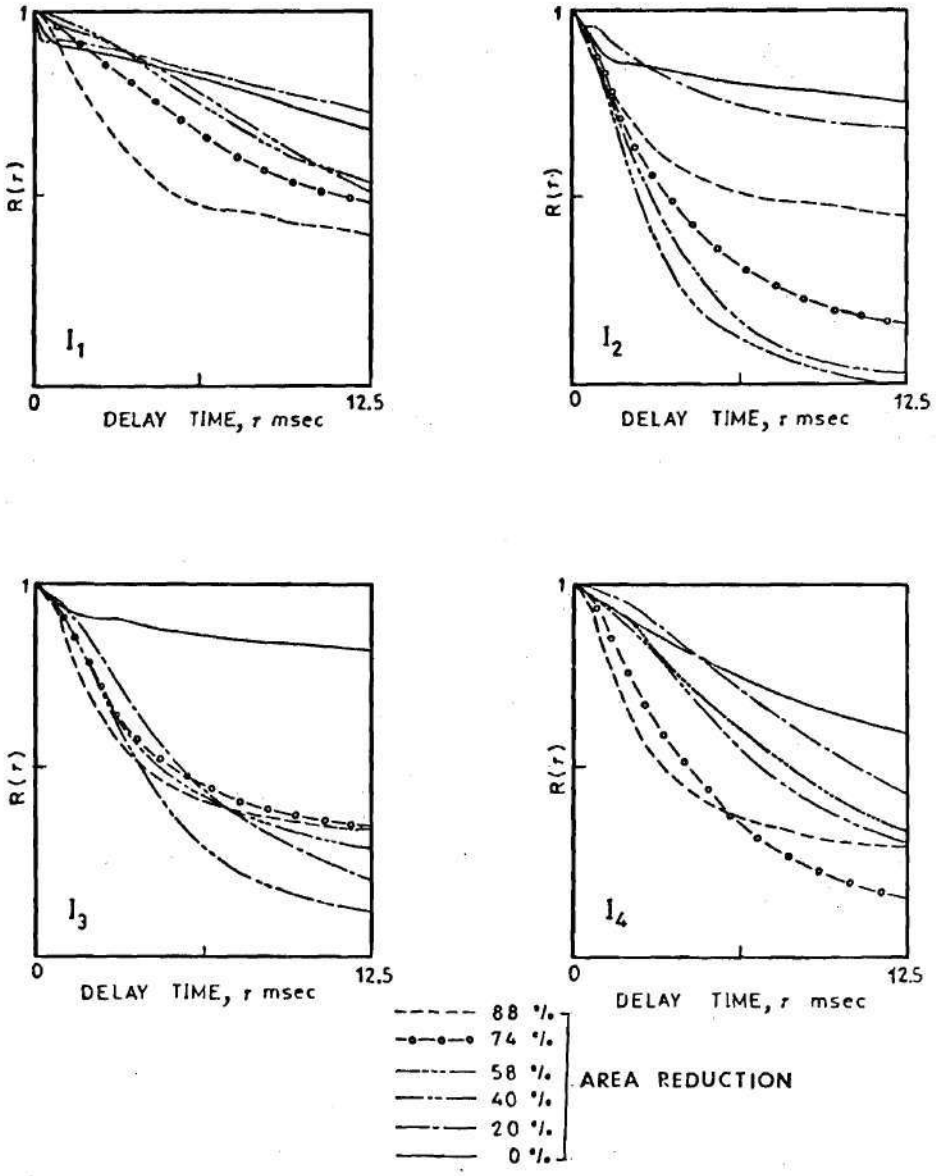

Figure 3-9. Autocorrelation Function $R(\tau)$ for Different Time Intervals

time scale of large eddies is much longer than the sampling time. Thus, the information provided by these plots is rather qualitative. The general trend is that the integral time scale decreases with the increase of the degree of occlusion for interval I_1. For interval I_2, there are two features of interest. First, by calculating the integral time scale for the case of 40 percent stenoses according to Equation (2-13), it was found to be 0.0004 second which is much smaller than the sample time (0.05 second). This indicates that calculating the corresponding autocorrelation functions gives reasonable results, despite the finite integration time. Second, the time scale for large eddies decreases with the increase of the degree of occlusion until the 58 percent stenosis; then further increases in the degree of occlusion cause an increase in the time scale. This may be due to the tremendous increase in the intensity of velocity fluctuation which in turn persists for a longer time.

Autocorrelation curves for the interval I_3 have similar features to that of I_2, except that the time scale increases with the increase of the degree of occlusion after 40 percent stenosis. Curves for interval I_4 follow trends similar to that of I_1.

The autocorrelation functions presented in this section provide an alternative approach to study the disturbance velocity in the time domain. It presents also information concerning different time scales for the occlusion cases considered. However, these results also point out the difficulty in describing the evolving integral scale because of the necessity of a finite time of observation.

From the point of view of clinical application, the autocorrelation

curves presented here do not have a monotonic trend with increasing stenosis as do the energy spectra. Recall that the spectral curves show an increase in the high frequency content with the increase of the degree of constriction which could be used as criteria for relating the degree of occlusion to the energy spectra.

3.3 Discussion

Methods for analysis of the disorder in pulsatile flows have been presented, and examples have been taken from velocity measurements obtained distal to stenoses formed by placing bands about the aortas of anesthetized dogs. The flow disturbances in these data were shown to be highly nonstationary for mild to moderate stenoses, so that results for rms disturbance velocities and energy spectra depend strongly upon the interval being studied. For the most severe case (88 percent occlusion), the disorder was stationary to a reasonable degree of approximation. The disturbance energy spectra for all degrees of stenoses, except those for which u'_{rms} were relatively low, correlated well if the average velocity during the interval, the rms disturbance velocity, and the stenosis diameter were employed in nondimensionalizing the data. This would imply that, although the amplitude of the disturbances during intervals was nonstationary, the spectral shapes in the nondimensional coordinates were similar, even for the mild stenoses, once the disturbances exceeded a certain level. It is emphasized that this may not be the case under other conditions of Reynolds number and frequency parameter.

There is certainly the need for a thorough study of the nonstationary problem from a rigorous viewpoint. This problem has many features

which have not yet been considered. One of the most important of these is the question of treating the evolution of the spectra on a more or less continuous basis rather than simply the four discrete intervals considered here.

The time ensemble average waveforms from the animal data demonstrate the appearance of split systolic peaks for mild and moderate stenoses. There was no attempt made to isolate the mechanism creating this periodicity. Two possibilities come to mind, however. The first is that of vortex shedding. In vitro studies of poststenotic flows (Cassanova (38)) indicate that the initiation of the disorder may be in the form of a "starting vortex" which then rapidly disintegrates. In addition some in vitro data presented in Chapter V exhibit split peaks due to vortices or to the beginning of turbulent front moving through this particular position of measurement. However, other possible sources are the wave reflection caused by the changing cross-sectional area presented by the constrictions and wall resonance phenomena. Further experiments specifically aimed at isolating these effects are required before any conclusions can be drawn.

The implication that measurable poststenotic flow disturbances in a major artery can be detected by the analysis methods described in Chapter II leads to the speculation that fluid dynamic studies of flow disorder may offer a valuable tool for the detection of mild to moderate localized vascular disease. The ensemble average waveforms may be descriptive of the presence of constriction, although probably not of the precise degree. A comparison of the disturbance energy spectrum and rms

velocity during the acceleration phase of systole with those measured near peak systolic velocity and the deceleration phase should show increased levels of disorder in the latter intervals for mild to moderate stenoses. Still another possibility is a comparison of the spectra obtained proximal to a suspected stenosis site with those obtained distally.

There are clearly two major obstacles to be overcome in applying these methods to a clinical setting, however. One is the need to separate biologic from fluid dynamic disorder. The biologic disorder may arise from nonreproducible heart beats or from local anatomical configurations such as vessel branching or bifurcation. A second obstacle is the invasive nature of the hot film probes. Certainly, such an instrument is not useful for a preliminary diagnosis method. A promising approach is the development of a turbulence measurement capability with Doppler ultrasound systems. If focusing and frequency response characteristics of those devices can be improved, fluid dynamic analysis of the flow disorder might be attempted noninvasively.

In the next Chapters, the fluid dynamic disorder will be studied further in the absence of biological variations by establishing stenosis models in the laboratory and applying the method of analysis to the in vitro measurements taken. Then experimental investigations to improve the frequency response of Doppler ultrasound system will be presented.

CHAPTER IV

EXPERIMENTAL ARRANGEMENTS FOR THE IN VITRO INVESTIGATIONS

To study the flow field distal to arterial constriction, it is necessary to introduce some simplifications to the actual configuration and conditions of the flow. This chapter describes the flow models, flow system, data acquisition, and processing equipment. Preliminary experiments to test the reliability of the instruments are also presented.

4.1 Models of Arterial Stenosis

An exact model of arterial stenosis would be practically impossible. The flow field created by arterial stenosis is extremely complicated due to the complex pulsatile nature of the flow, extensibility, and viscoelastic properties of the arterial walls, the nonuniformity of the stenoses, branching, curvature, and geometric taper in the arteries, in addition to the fact that blood is a non Newtonian fluid.

To study the relation between the degree of constriction and the flow disorder in the poststenotic field, the following simplifications are imposed:

1. Axisymmetric stenosis,
2. Rigid walled stenosis and tubing,
3. Simple sinusoidal flow with one frequency of oscillation,
4. No branching or curvature,
5. Newtonian fluid with viscosity approximating the high shear

rate value for blood.

These simplifications reduce the flow field and its boundaries to a simpler case which isolates the effect of the constriction on the flow field from other factors.

Three models with 25, 50, and 75 percent area reduction were used for these investigations. Figure (4-1) displays these three models and the principal dimensions. The curvature of each stenosis follows a cosine function.

At this point, it is necessary to obtain the similarity parameters which will make the model a good representation of the actual flow from the hydrodynamic point of view. According to McDonald (79) there are two parameters that should be considered for pulsating flow through a rigid tube. These are

1. Reynolds number, which is expressed as

$$Re = \frac{\rho U D}{\mu}$$

where

ρ is the density of the fluid,

μ is the viscosity,

U is the mean velocity of the flow, and

D is the diameter of the tube.

2. The frequency parameter α, defined as

$$\alpha = \frac{D}{2}\sqrt{\frac{\omega\rho}{\mu}}$$

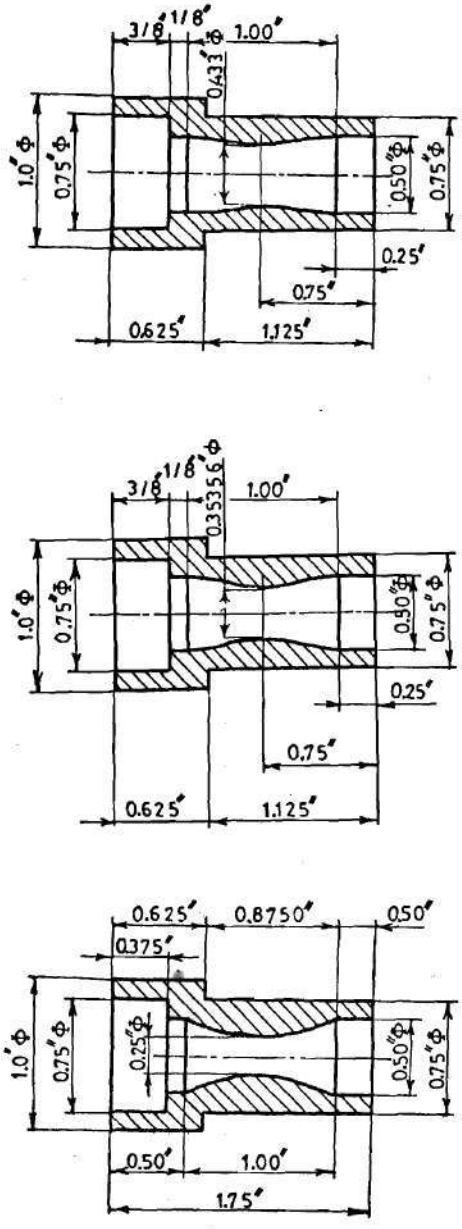

Figure 4-1. Stenoses Models

where

ω is the frequency of velocity oscillations in radians per second. This number represents the ratio of the inertia force due to flow oscillations to the viscous forces.

Giddens et al. (33) showed that for animals studied the ranges of Reynolds number based on peak velocity and the frequency parameter are

$$1{,}800 < Re < 2{,}300 \qquad \text{and} \qquad 9 < \alpha < 16.$$

One important feature for the series of the in vitro experiments performed is to work with unoccluded tube diameter similar to that of a dog's aorta. For this reason, the inner diameter of the unoccluded tube was chosen to be 0.5 inch. The frequency of velocity fluctuations was 1 Hz. A mixture of water and glycerol (concentration of pure glycerol was 40 percent of the total weight) that gave a viscosity of 3.6 centipoise was used for these experiments. The value of the viscosity was measured using a Wells-Brookfield micro viscometer. With the above mentioned values, the frequency parameter for these experiments was 16.8.

4.2 Flow System

A specially designed flow system was constructed to serve three objectives:

1. To compare the hot film anemometer with the laser Doppler velocimeter (LDV) to check and verify the capability and frequency response of the LDV,

2. To compare the LDV with the pulsed Doppler ultrasonic velocimeter. Details of this comparison are given in Chapter VII,

3. To perform in vitro studies for cases of pulsating flow through partially occluded tubes using the LDV.

The following requirements in the flow system are necessary:

1. To satisfy the first two objectives it was necessary to build the system in such a way that both steady and pulsating flows could be obtained for a wide range of Reynolds number ($0 < Re < 20,000$).

2. An easy way to insert the three models of arterial constriction with different area reduction was required.

A schematic diagram of the experimental arrangement is shown in Figure (4-2). It consists of a centrifugal pump, a pulsating pump, a settling chamber, the test section, and a constant head return tank.

The centrifugal pump (Teel Model 1P700) was used with two control valves to obtain the desired flow velocity, which was monitored by the LDV. The supply from this pump was delivered to the pulsating pump. The pulsating pump is activated by a signal generator which produces a reference signal that can be a sine wave or any other shape. This signal is amplified by using a power amplified and is used to drive a mechanical shaker which converts the reference signal to linear motion that controls the spool position, and hence the flow pulse wave. A detailed description for this pulsating pump (83) is given in Appendix A.

When the system was used for steady flow experiments, a plexiglas block of proper size was placed between the shaker face and the connecting arm so that the spool valve was at the position of maximum opening.

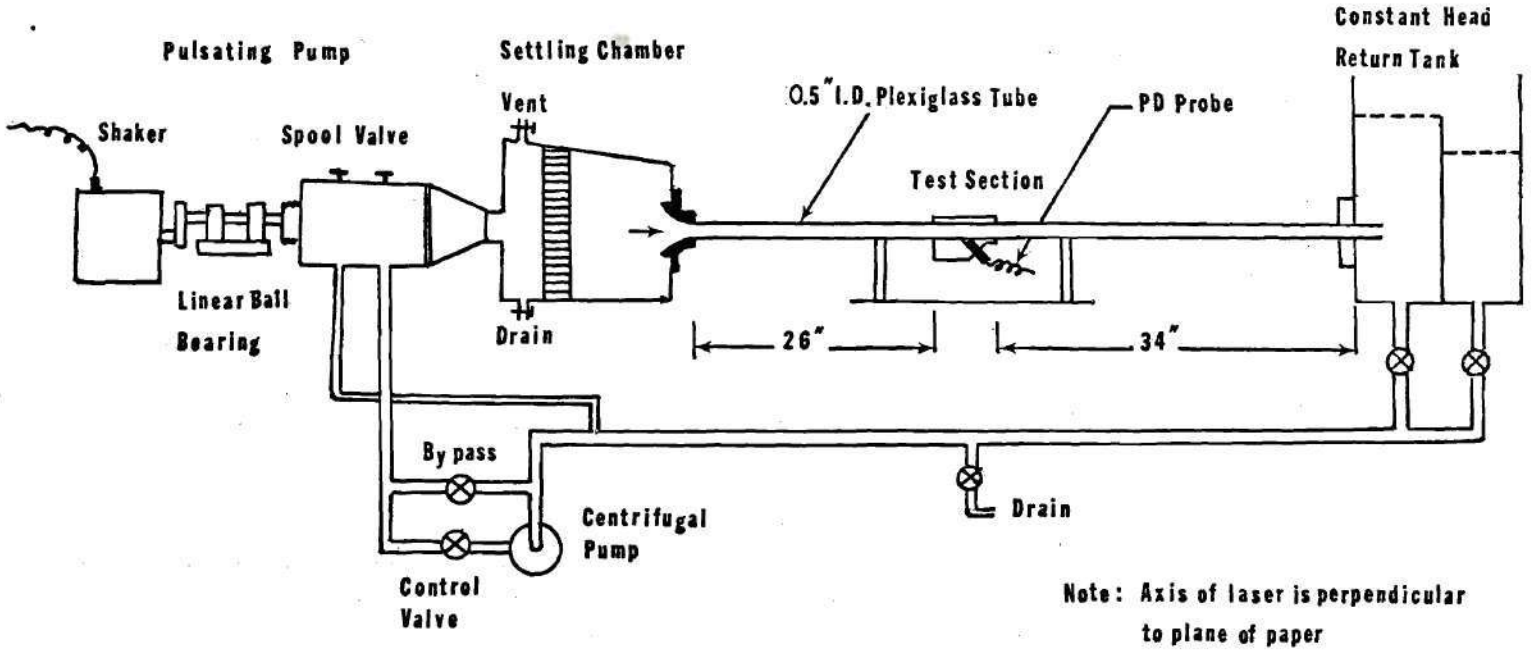

Figure 4-2. Schematic of the Flow System

The velocity was obtained by adjusting the control and bypass valves. This arrangement was used to compare the LDV and PD for steady flow situations. The comparison is explained in Chapter VII.

When the system was used for pulsating flow measurements, the plexiglas block was removed. The maximum and minimum velocities were controlled using different options, namely: the amplitude of the reference signal coming from the signal generator or its D.C. offset, the amplification ratio of the power amplifier and/or the control and bypass valves.

The discharge from the pulsating pump enters the settling chamber where a screen dampens disturbances that may exist in the flow. The settling chamber is fitted with a converging, smooth entrance which leads to a plexiglas straight tube of 0.5 inch I.D. and 0.75 inch O.D. The test section was placed 26 inches (52 diameters) from the tube entrance. This should be a sufficient length to reach fully developed condition at the point of measurement. It is also more than one wave length of the sinusoidal flow used and hence avoids wave reflection from the occlusion. The test section was constructed from plexiglas, well machined, and polished from both sides to have good optical properties required for the laser beam. Figure (4-3) shows a drawing of the test section. The PD probe was placed such that the acoustic beam axis was intersecting the tube axis at 45^{o} angle.

Preliminary experiments were necessary to compare the LDV with the hot film anemometer. For this purpose a hole was drilled in the top of the test section and two guides for the hot film probe were placed on the top to support the probe in a vertical position. However, for

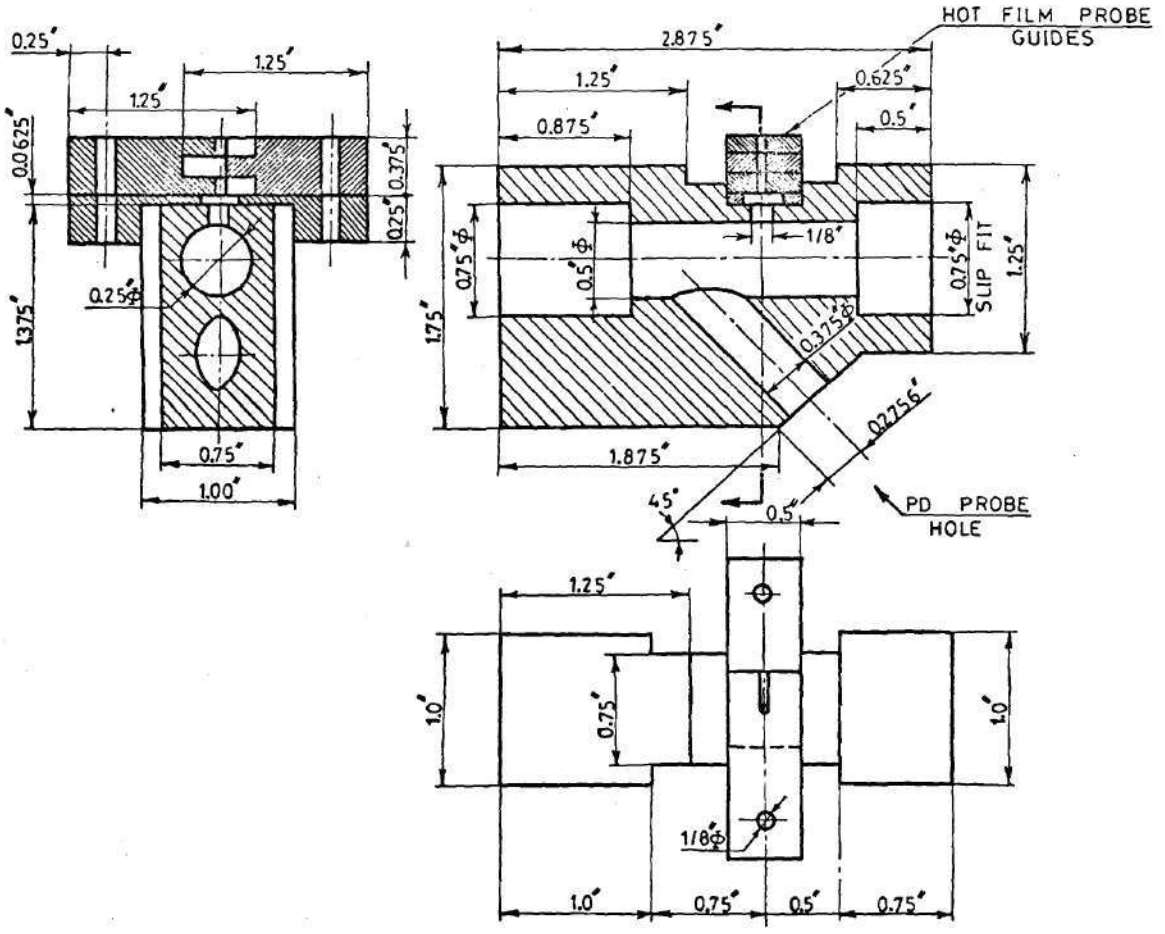

Figure 4-3. Detailed Drawing of the Test Section

comparing the LDV with the PD this arrangement was not necessary, so the guides were removed and the drilled hole was filled with RTV sealant.

When the poststenotic flow measurements were taken, the stenosis model was placed between the test section and the tube connected to the upstream settling chamber.

A tube of 34 inches length, 0.5 inch I.D., was used to convey transport the flow to the downstream constant head tank. The discharge into that tank returned to the pump through a PVC tube.

4.3 Instrumentation

The instruments used in the experiments can be subdivided into three groups, each dealing with a particular phase of this investigation: (i) data acquisition equipment, (ii) monitoring equipment, and (iii) data reduction equipment.

4.3.1 Data Acquisition Equipment

The velocity measurements at the centerline of the tube for different axial positions downstream of each of the three stenoses models were taken using the laser Doppler velocimeter (LDV) system. The major advantage of the LDV over other anemometers is that it is not dependent on the physical and thermodynamic properties of the fluid. It is, therefore, insensitive to changes in temperature or density of the fluid. The LDV is also noninvasive and hence, does not disturb the flow.

The LDV system used in the in vitro studies was DISA 55L Laser Doppler Anemometer Mark II (84). The system is composed of the following components:

1. Laser-spectra physics 120A with exciter, wave length λ = 632.8 nm and power = 15 mw.

2. Transducer-optics package

   a. Beam splitter

   b. Acousto-optic cell

   c. Focusing lens.

3. Photomultiplier with receiving lens.

4. Doppler signal processor-tracker.

5. Range translator.

A sketch for this arrangement is given in Figure (4-4). The laser light is directed into the transducer and passes through a beam splitter. One of the resulting beams passes through an acousto-optic cell (Bragg cell) where the frequency is shifted by 40 megaHertz. This shift in frequency allows measurement of both negative and positive velocity components. The second beam passes undisturbed through the optical unit. Both beams then proceed to a prism system where the beam separations of 20, 40, and 80 mm may be selected. From there the beams pass through a focusing lens (12, 30, or 60 cm focal length). At the intersection of the beams an approximately ellipsoidal geometric sampling volume is produced. The size and shape of the sampling volume depend on the selected beam separation and the focal length of the lens. In this investigation, a 40 mm beam separation with a 12 cm lens was used. The resulting sampling volume in air is 0.12 mm by 0.72 mm. Because of a difference in indices of refraction the sampling volume in water is approximately 0.12 mm by

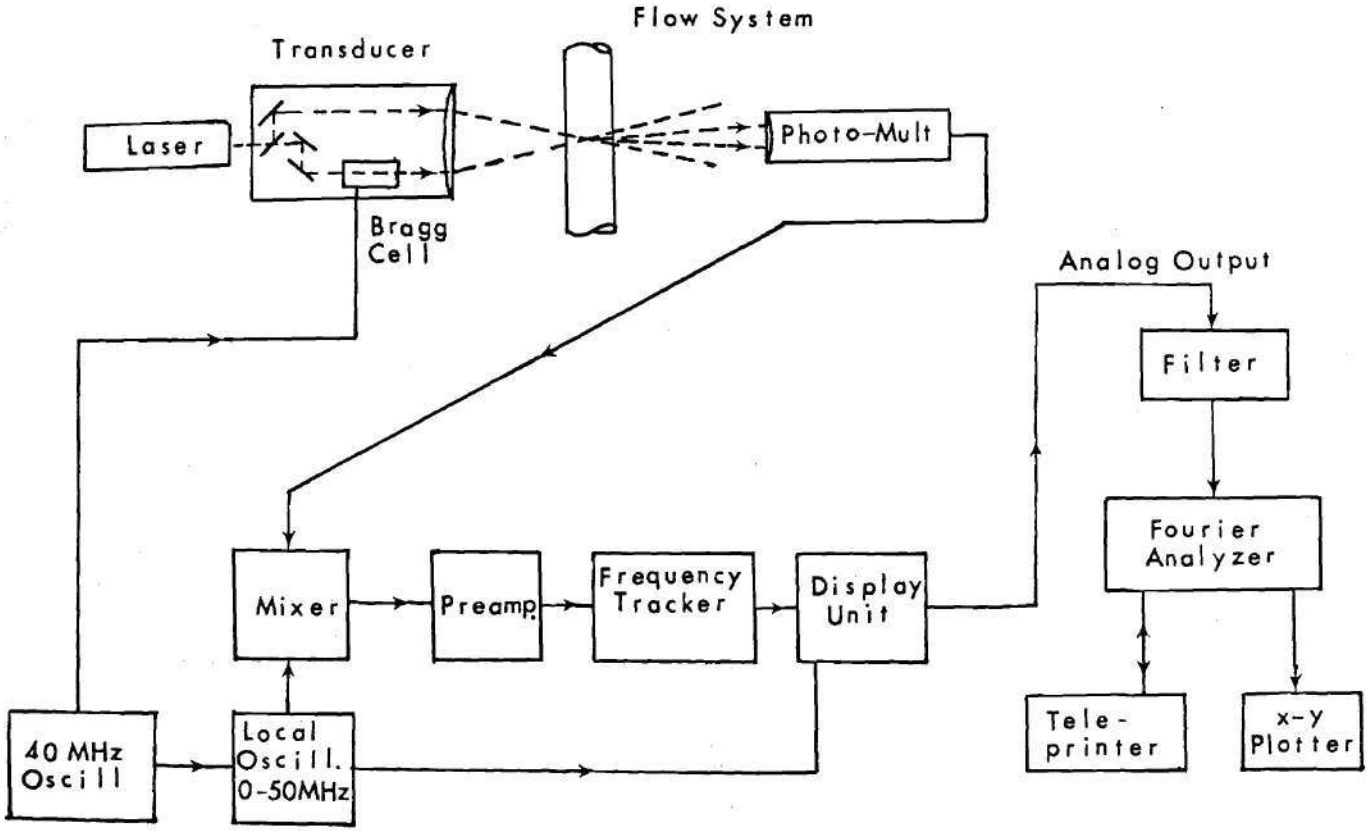

Figure 4-4. Block Diagram of the LDV and the Fourier Analyzer System

0.96 mm. In the sampling volume interference fringes are established. As a scattering particle passes through the fringes the intensity of the light entering the photomultiplier is modulated. This modulation corresponds to the shifted frequency (from the Bragg cell) minus the Doppler frequency, fd. The velocity component being measured may be determined from the relationship,

$$V = f_d \lambda / 2\sin(\theta/2)$$

where

f_d is the Doppler frequency,

λ is the wavelength of the laser light, and

θ is the beam intersection angle.

To obtain f_d, the signal processor and range translator must be used. The signal from the photomultiplier is mixed with a signal from a local oscillator and the difference is fed into a preamplifier. The preamplified signal is then mixed with the output from a voltage controlled oscillator (VCO). The resulting output frequency is kept centered in the middle of a narrow bandpass filter by means of a fast servo loop that controls the VCO output. The analog voltage of the VCO is then substracted from the translator frequency. The resulting voltage is proportional to the instantaneous velocity component. A detailed description of the Disa Tracker can be found in Appendix B.

4.3.2 Monitoring Equipments

Doppler signal strength and instantaneous velocity were monitored using a dual trace oscilloscope (Tekronix Type 556) and the LDV analog

voltage output was read on a digital voltmeter (Fluke Model 8000A). A strip chart recorder (HP Model 7702B) with two channels was used to record the analog velocity output and the driving signal to the pulsatile pump.

4.3.3 Data Reduction Equipment

The data reduction dealt primarily with analysis of the instantaneous velocity component measured by the LDV system. The signal from the LDV system was fed directly to a Hewlett-Packard Fourier Analyzer (Model 5451B). The system consists of the following units (85):

Model 180 AR/DR oscilloscope

Model 2100 Computer

Model 2752A Teleprinter

Model 5460A Display plug in unit

Model 5465A ADC plug in unit

Model 5475A Control unit.

A Hewlett-Packard Moseley 135 X-Y Recorder was used in conjunction with the Fourier Analyzer System to obtain energy spectral density graphs.

The Fourier Analyzer System performs analysis of time and frequency data containing frequencies from DC to 100 kHz. The system is capable of processing both continuous and transient data and may be programmed to perform a variety of operations on the incoming signal. The results may be displayed in a number of ways; oscilloscope, X-Y plotter, and point by point printout.

The first step in the processing is analog to digital conversion in the ADC. The rate of conversion may be chosen in one of two ways. In the first method the maximum desired frequency (F_{max}) is chosen and

the frequency resolution (Δf) is dependent on the block size (N, number of data points in the record). This frequency resolution may be calculated from the equation

$$\Delta f = 2\ F_{max}/N$$

the record length (T) may be computed by the equation

$$T = N/(2\ F_{max})$$

In the second method the desired frequency resolution (Δf) is selected and the maximum frequency is dependent on the block size chosen. The maximum frequency is calculated by the equation

$$F_{max} = \Delta f\ N/2$$

Since turbulence information for this flow system may contain frequencies as high as 500 Hz before being lost in noise, F_{max} was chosen to be 512 Hz with a block size 1024 and the frequency resolution Δf was selected to be 1 Hz. This corresponds to a record length, T, of one second.

After the signal from the LDV system was digitized by taking one hundred sample records per experiment, the data were stored on a magnetic disc for later processing and analysis. The processing of each set of data includes calculation of the time ensemble average velocity, the

ensemble average of the square of the disturbance velocity (u'^2) for hundred samples, the disturbance energy spectrum E(f) and the autocorrelation function $R(\tau)$. This analysis was done for the total velocity waveform and for the chosen time intervals. Figure (4-5) shows the flow chart of data reduction. A sample of the program utilized in this investigation is reported in Appendix C.

4.4 Preliminary Experiments

A series of preliminary experiments was conducted for the case of steady, fully developed pipe flow to compare the LDV with the hot film anemometer. The comparison was in 2 inches tube for Re = 11,000 and 22,000. The energy spectra were obtained and the results are shown in Figures (4-6) and (4-7).

Another series of experiments was conducted in the flow system previously explained in section (4.2), to compare the hot film anemometer and the LDV in pulsating flow with a sinusoidal varying velocity of fundamental frequency of one Hertz. The result of comparing the ensemble average of 100 samples of one second each, as measured by the two instruments, is shown in Figure (4-8). The same figure displays also the energy spectra of the disturbance velocity for the same experiment.

This comparison in both steady and pulsating flows should be carefully interpreted, because the quantities measured by LDV and the hot film probe are not exactly the same. This is because the hot film probe, although calibrated to measure the axial component u′ is actually subject to the effect of v′ and w′ components.

For the steady flow measurements, the noise and Doppler ambiguity

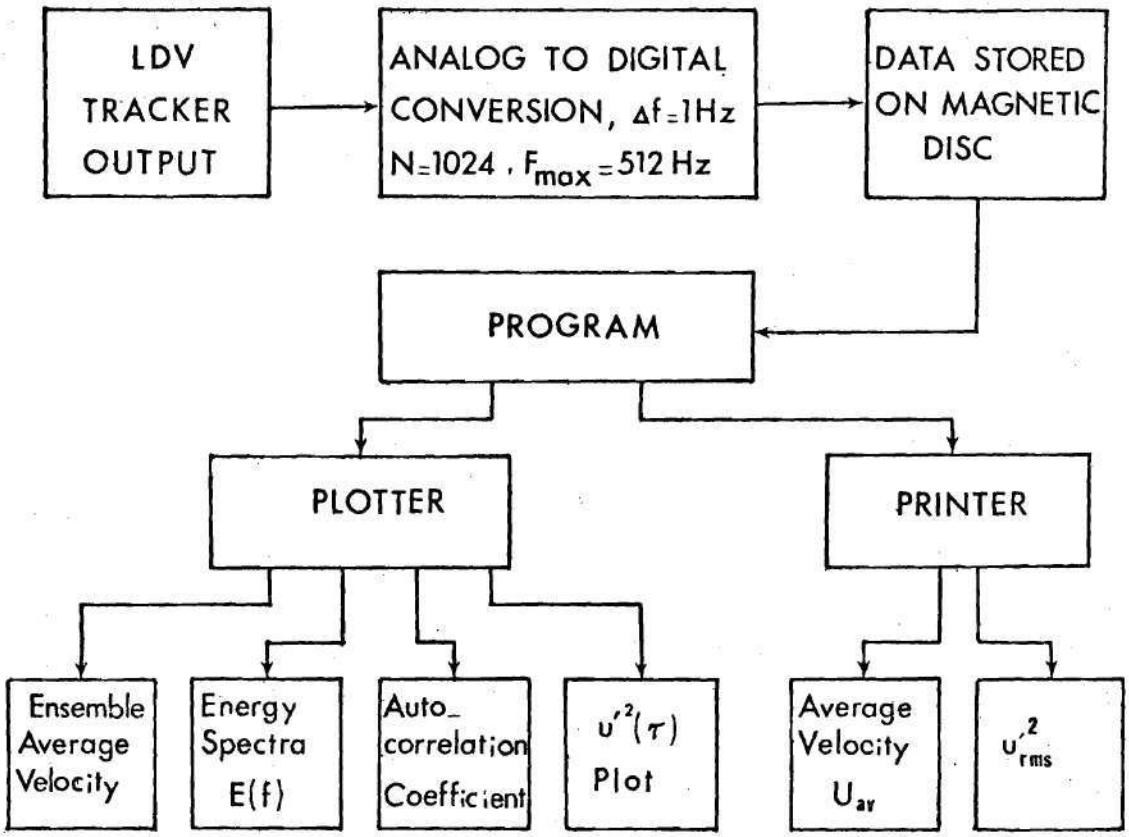

Figure 4-5. Flow Chart of Data Reduction

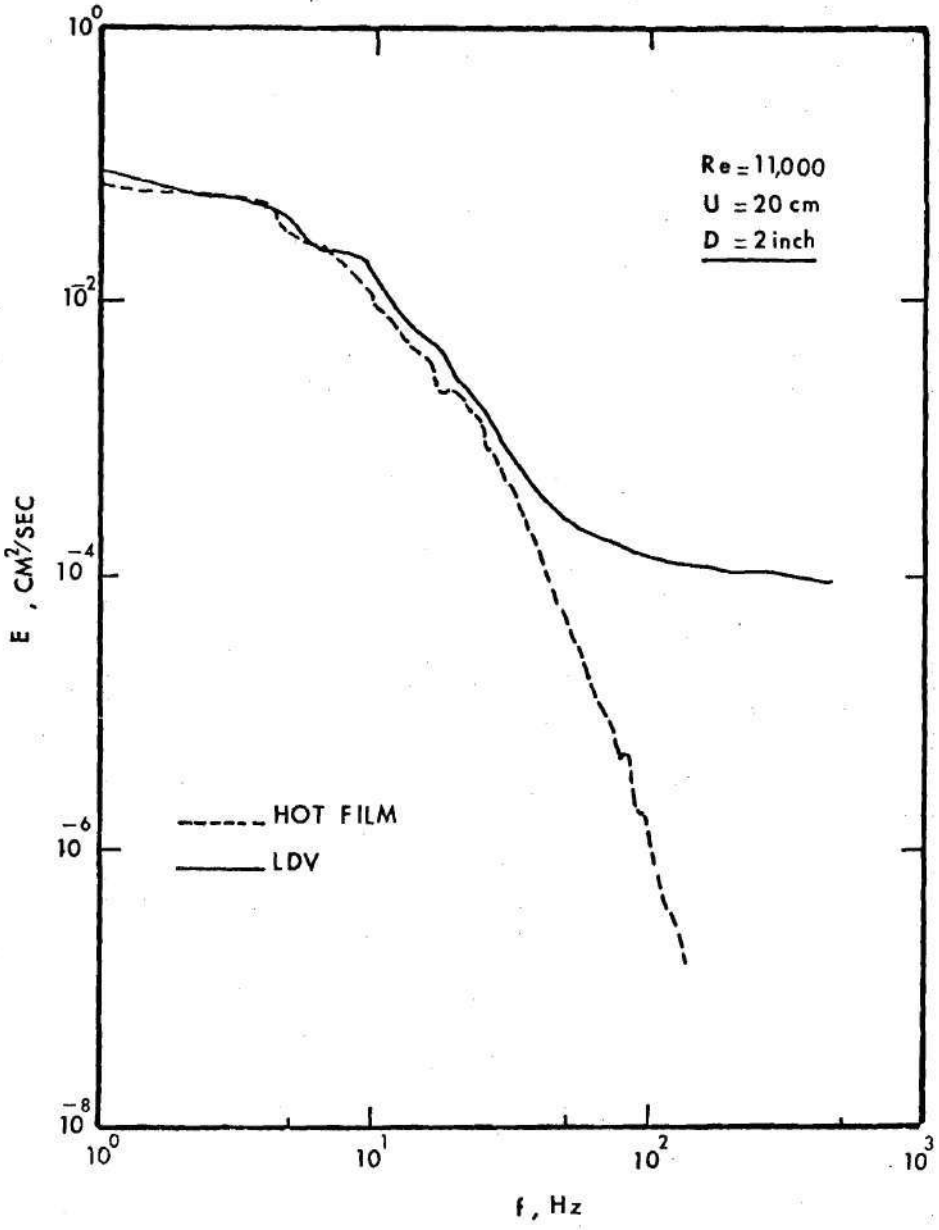

Figure 4-6. Comparison Between LDV and Hot Film for Steady Flow, Re = 11,000

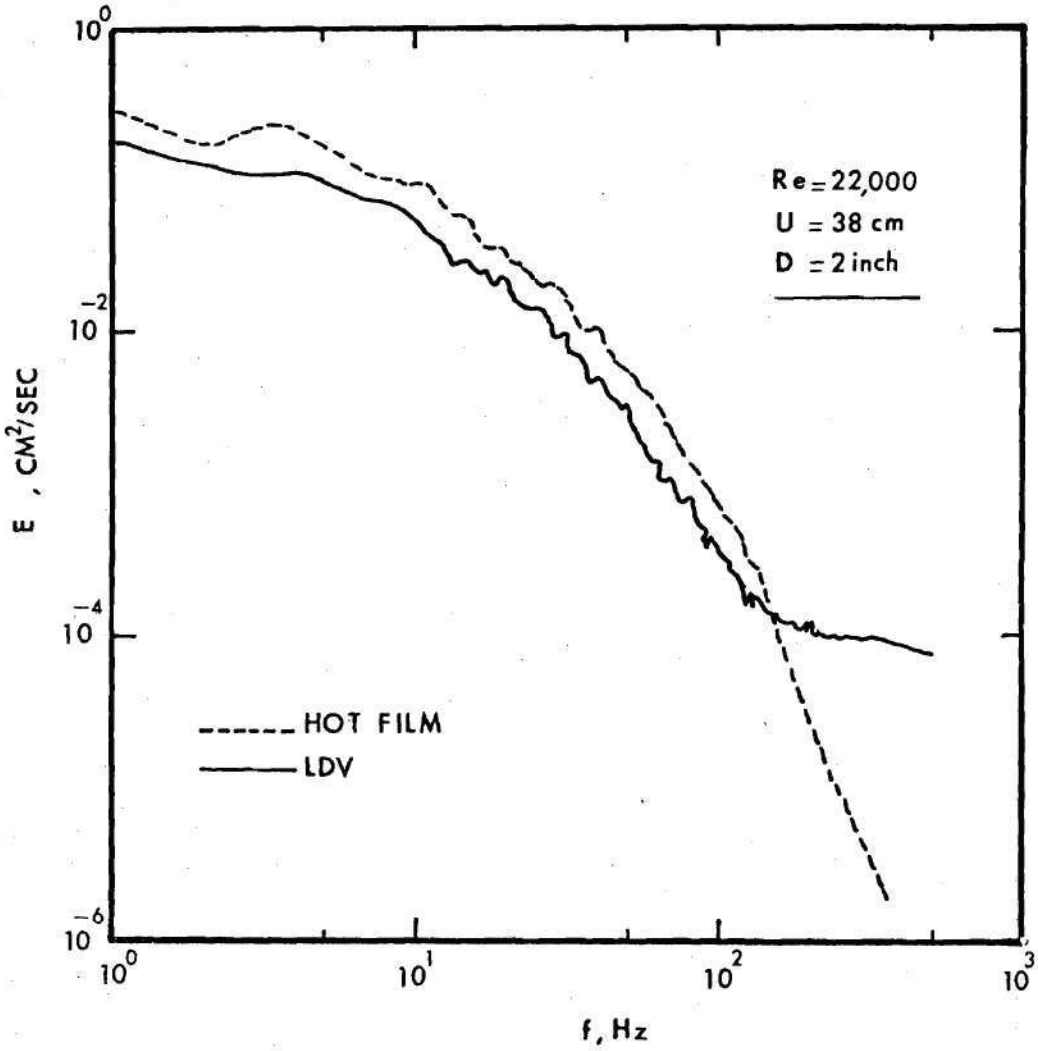

Figure 4-7. Comparison Between LDV and Hot Film for Steady Flow, Re = 22,000

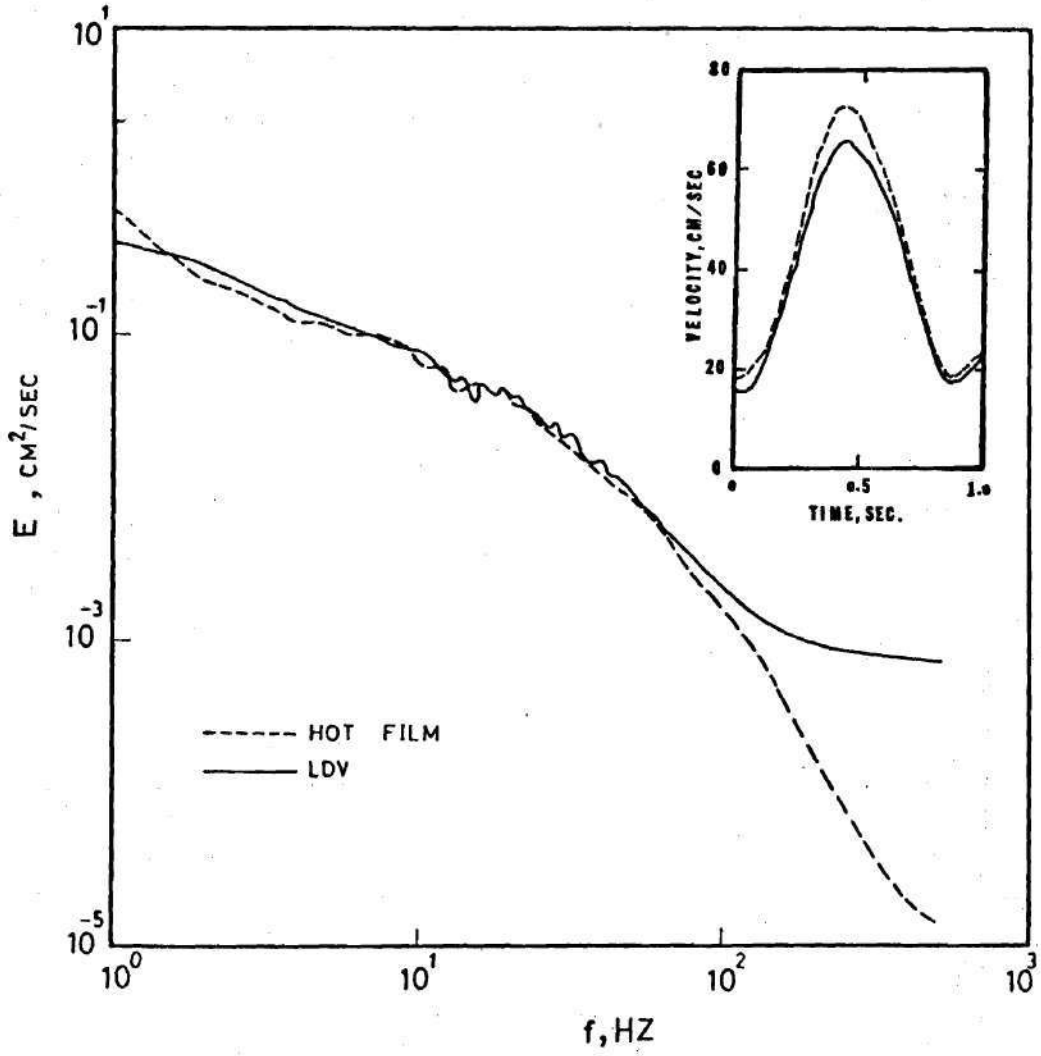

Figure 4-8. Comparison Between LDV and Hot Film for Pulsating Flow

contribute to the spectrum for frequencies above 60 Hz for Re = 11,000 and 100 Hz for Re = 22,000. For the same Reynolds number, it is expected that with smaller tube diameter (e.g., 0.5 inch) the influence of the ambiguity is at frequencies higher than that given for the 2 inches tube. This can be predicted from the analysis of George and Lumley (92).

The fundamental limitation of the LDV system is the Doppler ambiguity which is introduced by the finite transit time of particles through the scattering volume, turbulent velocity fluctuations across the scattering volume, mean velocity gradients, and electronic noise. A unified account of the effect of the Doppler ambiguity on the measurements of turbulence is given by George and Lumley (92).

For the pulsating flow, the difference in velocity magnitude measured by both instruments is believed to be due to contamination of the hot film sensor by seeding particles used for the LDV and due to variation in fluid temperature with time. This gives the LDV an advantage over the hot film anemometer because its velocity measurement does not depend on the fluid temperature or contamination. In addition, it does not disturb the flow and has a satisfactory frequency response in measuring flow disturbance. The LDV and hot film energy spectra of the disturbance velocity agree very well for frequencies up to 100 Hz and then the ambiguity is manifested by a flattening in the LDV curve. It should be mentioned that the velocity is varying with time and actually turbulence exists only during a part of the velocity cycle. During the remainder of the cycle, the disturbance velocity is very small and the signal to noise ratio is lower. This was also observed in the spectra obtained from the in vitro experiments where most of the cycle is in the

laminar range. Because the energy spectrum obtained by the LDV for this case represents the frequency content of u′ over the entire cycle, it is expected that there will be a higher effect of ambiguity on the energy spectrum than the cases of steady turbulent flow or pulsating flow where the flow is turbulent during the entire cycle.

In summary the LDV is a reliable instrument in measuring both mean velocity and disturbance energy spectra under conditions encountered in this study.

CHAPTER V

RESULTS OF THE IN VITRO EXPERIMENTS

This chapter summarizes the information obtained by applying the disordered flow analysis to in vitro measurements of the centerline velocity downstream from three stenosis models with area reduction of 25, 50, and 75 percent.

The upstream velocity waveform was the same for the three stenoses considered. Figure (5-1) displays this velocity waveform which is sinusoidal function with frequency 1 Hz, minimum and maximum velocities 14 and 68 cm/sec respectively (Reynolds number range from 500-2400).

The results in this chapter demonstrate some of the important fluid mechanics phenomena associated with pulsating flow through partial occlusions, such as vortex shedding and the development of flow instabilities which break down into turbulence and then decay as the fluid moves downstream of the constriction. The results also have implication to clinical applications and the interpretation of the in vivo measurements.

5.1 Results for 25 Percent Occlusion

Figure (5-2) shows the instantaneous velocity at five selected positions downstream of the stenosis, the distance being measured from the throat of the occlusion. It is interesting to notice the existence of periodic fluctuations in the velocity waveform at different phases of the cycle, depending upon the position of measurement. At position X_1

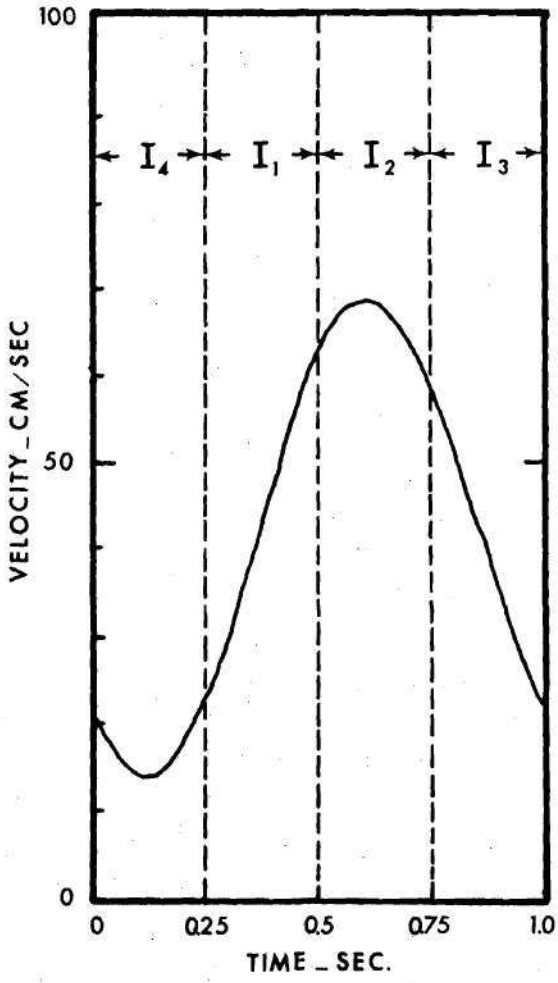

Figure 5-1. The Upstream Waveform and Intervals Used for Analysis of Time-Development of Disorder

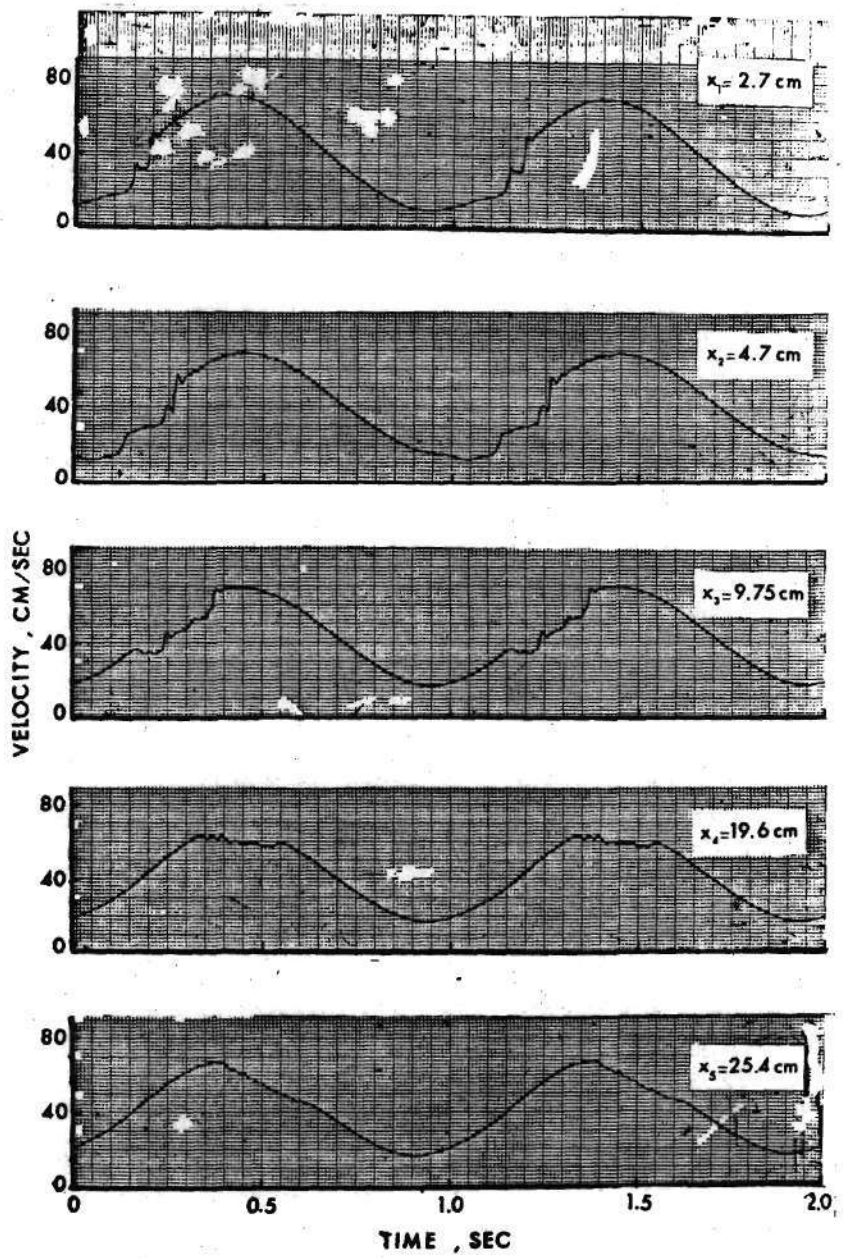

Figure 5-2. Instantaneous Velocity at Different Locations Downstream of 25 Percent Occlusion

these fluctuations are observed in the acceleration phase. At position X_2 they move slightly toward the peak and have a different pattern from that at X_1, but the disturbance is still repeatable in each cycle. The same can be seen for the third position X_3. Position X_4 was chosen such that these periodic fluctuations exist in the peak region. Position X_5 shows the periodic velocity variations in the deceleration phase having much smaller amplitude of fluctuations. Measurements at positions farther downstream showed complete dissipation of these fluctuations.

The instantaneous waveforms do not indicate the existence of any random or turbulent fluctuations. This will be discussed in more detail later in this section.

The observed periodic fluctuations in the velocity waveforms are due to vortex shedding as a result of instability in the boundary of the separation region. This region extends farther downstream while the flow is accelerating and contracts while the flow is decelerating (8). During the deceleration, the Reynolds number increases and several vortices are created in this shear layer. The number shed depends on the Reynolds number range during the acceleration phase, the acceleration time, and both the shape and size of the stenosis. These vortices are convected axially and to some extent radially, with the flow and move with a velocity which depends upon the local instantaneous velocity. Their effect at different locations along the centerline occurs at correspondingly different times in the cycle giving rise to a periodic fluctuating pattern in the velocity waveforms. The vortices decay by viscus dissipation as they move axially. This dissipation mechanism is

different from that of vortices breakup into turbulence after interaction with tube walls (38).

The following presentation and discussion of results obtained by analyzing the instantaneous velocity waveforms will show something of the nature of these vortices, such as the number and speed of travel. It should be emphasized, however, that the measurements were taken only at limited positions and at the centerline of the tube. The full description of the nature of such a flow requires both axial and radial velocity measurements in addition to flow visualization to follow different events occurring at different places in the flow field.

5.1.1 Ensemble Average and Disturbance Velocities

Figures (5-3) show the ensemble average velocity waveforms and the corresponding $u'^2(\tau)$ plots. The ensemble average waveform that was taken five tube diameters upstream of the center of the occlusion is also presented with the corresponding $u'^2(\tau)$ plot. The R.M.S. of the disturbance velocity is less than 0.8 cm/sec (1.2 percent of the corresponding ensemble average velocity) which indicates no substantial flow disturbance upstream of the stenosis. These low values can be attributed to electronic noise, Doppler ambiguity and small phase errors in triggering while sampling the analog velocity output from the LDV.

The results for position X_1 show the ensemble average which exhibits two sharp velocity fluctuations. These are very clearly seen as two spikes in the $u'^2(\tau)$ plot. Theoretically, if a disturbance is precisely periodic, it should not appear in the u'^2 graphs. In practice, however, there are slight irregularities in the periodicity of vortex shedding

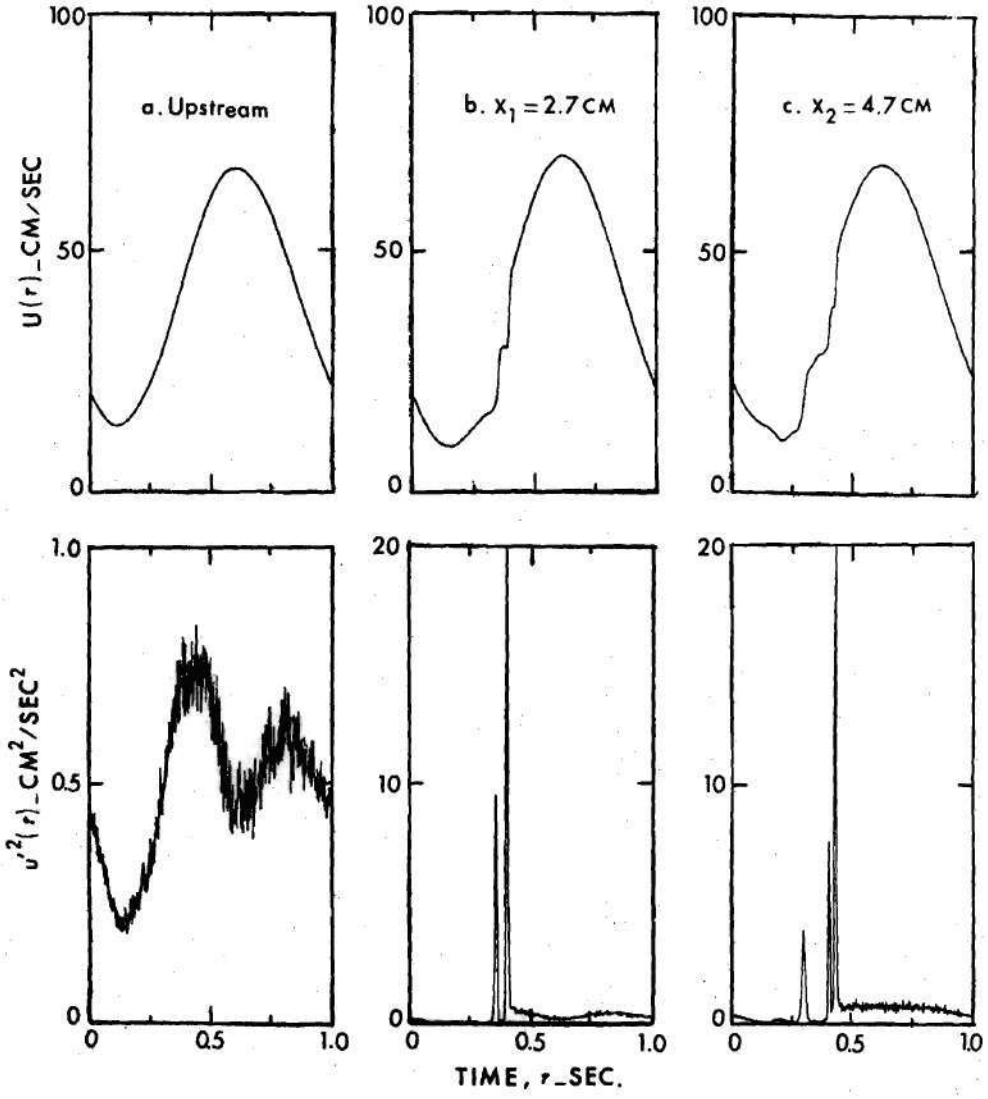

Figure 5-3. Ensemble Average and Disturbance Velocities for the 25 Percent Occlusion

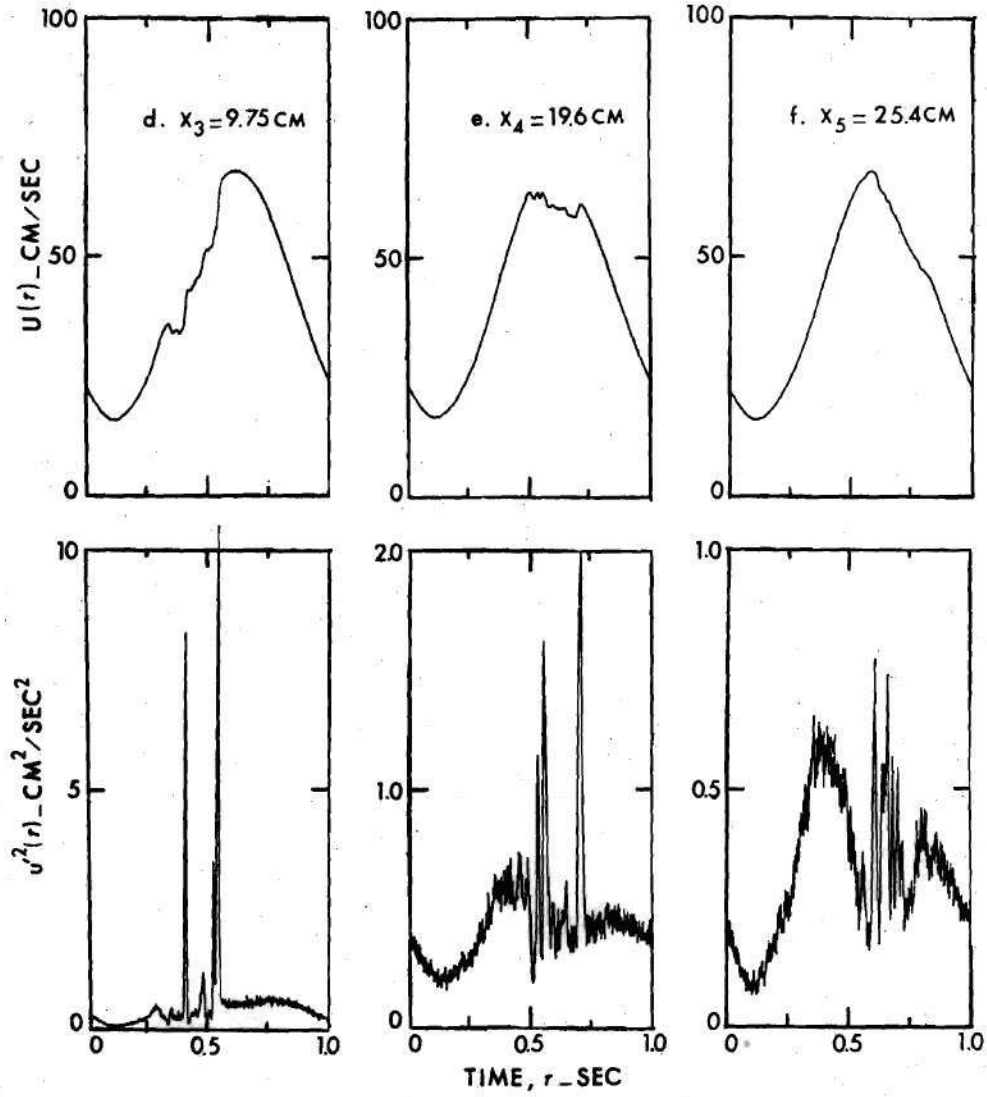

Figure 5-3. (Continued) Ensemble Average and Disturbance Velocities for the 25 Percent Occlusion

and to some extent of the triggering signal which lead to the sharp peaks in the u'^2 curves.

At the position X_2, the two spikes observed in the previous position move farther toward the peak region and are now closer to each other while a new spike is observed to occur early in the acceleration phase. The average speed of travel between X_1 and X_2 for the first vortex is 37 cm/sec and for the second 50 cm/sec, indicating that the second major vortex observed at X_1 is approaching the first one as they move downstream.

Results at position X_3 show that the vortices convected from X_1 continue merging, the average velocity of the first between X_2 and X_3 is 50 cm/sec and that of the second vortex being 52 cm/sec. These velocities are approximately equal to the local instantaneous velocity at the position where the irregularities caused by the vortex are observed. The third vortex first observed at X_2 is traveling with average speed of 31 cm/sec between X_2 and X_3. The $u'^2(\tau)$ curve indicates a fourth vortex that starts to have an effect on the centerline velocity and was not observed in previous positions.

At position X_4, the fluctuations caused by the vortices are shown in the peak region. The amplitudes of these irregularities are very much reduced. Several spikes are observed in u'^2 (τ) plots. Except for these spikes the shape of the curve is similar to the upstream one. Because of the relatively reduced effect of the vortices on the ensemble average and $u'^2(\tau)$ for this position, it is hard to follow the individual vortices.

The last position X_5 shows that the amplitude of the velocity variations is heavily reduced and they exist in the deceleration phase.

Complete dissipation of these vortices is observed at positions farther downstream.

5.1.2 Power Spectra of the Disturbance Velocity

The downstream velocity waveforms show periodic velocity fluctuations due to vortex shedding at a particular phase during the velocity cycle. If vortices passing through the position of measurements are perfectly reproducible, and if there are no electronic noise, Doppler ambiguity and phase error in the triggering process, the disturbance velocity defined by equation (2-4) should be zero. In reality, all these effects are existing and the disturbance velocity in this case is the deviation of the instantaneous velocity from its ensemble average due to the above mentioned factors. Hence, it is expected that the magnitude of the disturbance energy for a given frequency does not have the physical meaning of energy.

However, these disturbance velocities tend to have particular frequencies. These frequencies can be related to the frequency of the velocity fluctuations. It should be clear in mind the physical meaning of the frequency of the velocity fluctuations due to a vortex, which is defined as the fundamental frequency of the velocity variation due to the motion of the vortex relative to the point of measurement. This is explained in detail in Appendix E.

The disturbance energy spectrum E(f) was calculated for the total velocity cycle and the four intervals representing the four phases namely the acceleration (I_1), peak (I_2), deceleration (I_3), and valley (I_4). This was done for the upstream location and the five locations downstream

of the stenosis. Figure (5-1) displays the four phases with respect to the upstream velocity waveform. The four intervals are each defined to be 0.25 seconds in duration with the maximum velocity occurring at the center of the peak phase for the upstream waveform.

Figure (5-4) shows the energy spectrum of u′ calculated for the total velocity cycle at position X_1. The upstream spectrum is drawn in the same plot for reference. It is clear that the spectrum does not show any indication of turbulence. The several peaks observed reflect the sample window problem (see Appendix F). The sample window includes two cycles representing the disturbance velocity variation due to the two vortices passing by this position of measurement. For this reason the energy spectrum shows the fundamental lobe that corresponds to frequency in the neighborhood of 25 Hz and side lobes that have frequencies in the neighborhood of 45, 70, 95, and 120 Hz. The frequency of velocity fluctuation due to vortices as calculated from the instantaneous velocity waveform is 25 Hz, which verifies the fact that the frequency of the fundamental lobe is the frequency of velocity fluctuation. Spectra for other positions show similar behavior.

Because there are no events other than this regular pattern of flow instability caused by the vortex shedding, the energy spectra for the time intervals that do not include the velocity fluctuations do not give any new information over the corresponding upstream ones.

For example at position X_3, Figure (5-5) displays the spectra for the four intervals namely the acceleration (I_1), peak (I_2), deceleration (I_3), and valley (I_4). For interval I_1 the frequency of the velocity

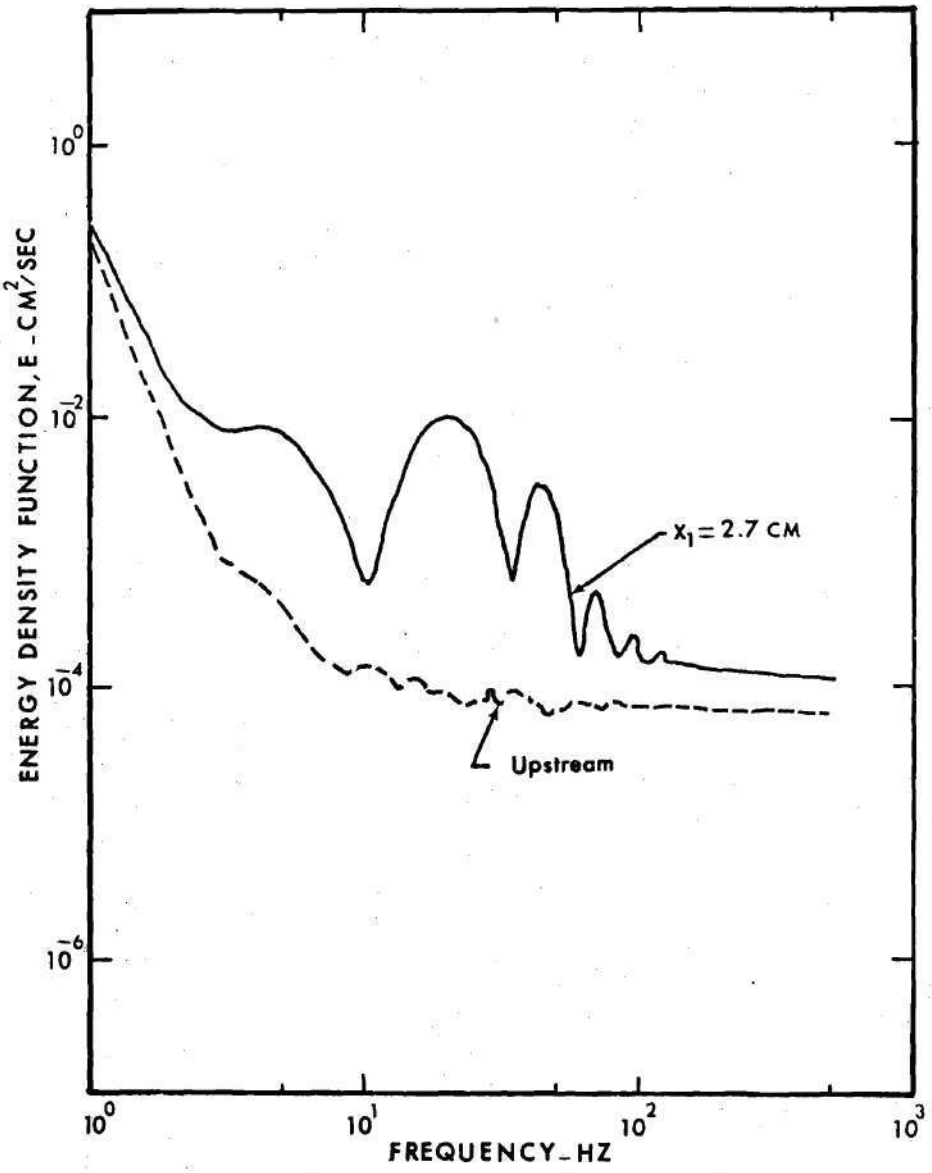

Figure 5-4. Disturbance Energy Spectrum at X/D = 2.1 Distal to 25 Percent Occlusion

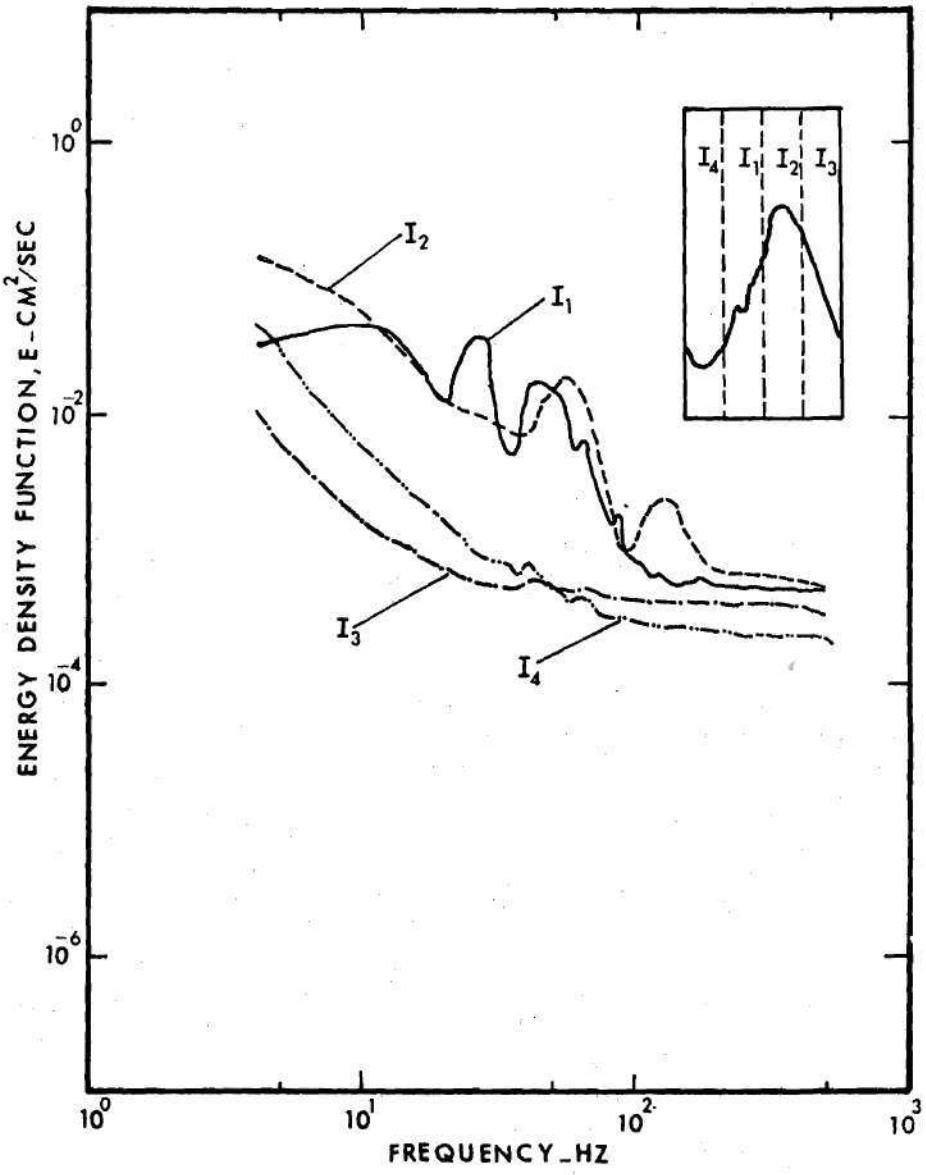

Figure 5-5. Development with Time of the Disturbance Energy Spectrum at Position 3 (X/D = 7.7) Distal to 25 Percent Occlusion

fluctuation corresponds to 25 Hz while that for I_2 is 55 Hz. Spectra for I_3 and I_4 are very similar to the corresponding upstream ones.

5.1.3 The Autocorrelation Functions

Figure (5-6) shows the autocorrelation functions calculated for the disturbance velocity for two axial positions. The results for the autocorrelation function reinforce the conclusion that initial instability is vortex related and that this disturbance never became truly randomized into turbulence. If it is assumed that

$$u(t) = A_o \sin\omega_o t + \sum_{i=1}^{n} A_i \sin\omega_i t \qquad (5\text{-}1)$$

then it can be shown that

$$R(\tau) = \frac{A_o^2}{\sum_{j=0}^{n} A_j^2} \cos\omega_o \tau + \sum_{i=1}^{n} \frac{A_i^2}{\sum_{j=0}^{n} A_j^2} \cos\omega_i \tau \qquad (5\text{-}2)$$

If there is a single dominant frequency ω_o (i.e., $A_o \gg A_i$, $i \neq 0$), then $R(\tau)$ will form a relative maximum at $\tau \cong 2\pi/\omega_o$, provided n is not large and the summation term in equation (5-2) can be neglected. Such is the case at position X_1, as illustrated in Figure (5-6a). The peak at $\tau \cong 0.04$ agrees very well with the dominant velocity fluctuation frequency of 25 Hz obtained from the analog output on the strip chart recorder and the appropriate peak in the energy spectrum. As the frequency ω_o becomes less dominant, other features in the graph $R(\tau)$ appear. This

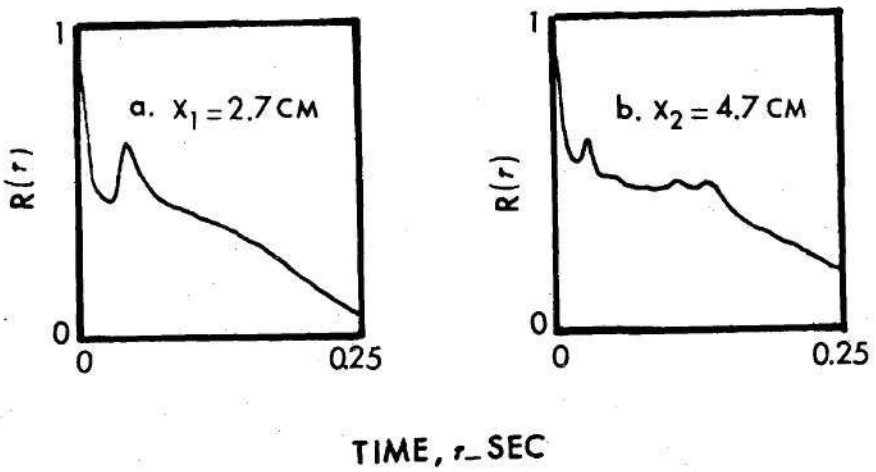

Figure 5-6. Autocorrelation Function at Two Axial Positions Downstream of the 25 Percent Occlusion

can be seen in Figure (5-6b) which gives results for position X_3. Several minor peaks appear as the vortex structure is altered (refer to Figure (5-2)).

5.2 Results for 50 Percent Occlusion

The results presented in this section for pulsating flow downstream of a 50 percent occlusion show an interesting flow field in which there are two periodic phenomena occurring. The first is the vortex shedding mechanism previously observed and discussed for the 25 percent occlusion. The second is that of periodic instabilities that start in the deceleration phase of early positions downstream of the stenosis, but at later axial positions break down into turbulent or random velocity fluctuations. For this reason, measurements were taken at more axial positions to follow both the vortices and turbulence.

Figures (5-7) display the instantaneous velocity waveforms for the upstream position and seven selected downstream positions, namely, 2.7, 4.7, 9.75, 15, 20, 26, and 40 cm measured from the center of the constriction. The first graph for position X_1 shows some periodic velocity fluctuations early in the acceleration phase which may correspond to one pair of vortices. These periodic fluctuations are also observed in the velocity waveform of other axial locations. At positions X_4 and X_5 these primary fluctuations are seen in the peak phase. At position X_6 these fluctuations reach the deceleration phase before complete dissipation. The mechanism of vortices generated and convected with the flow while losing their strength before complete dissipation is similar to that for the case of 25 percent occlusion. It is clear that there are several of

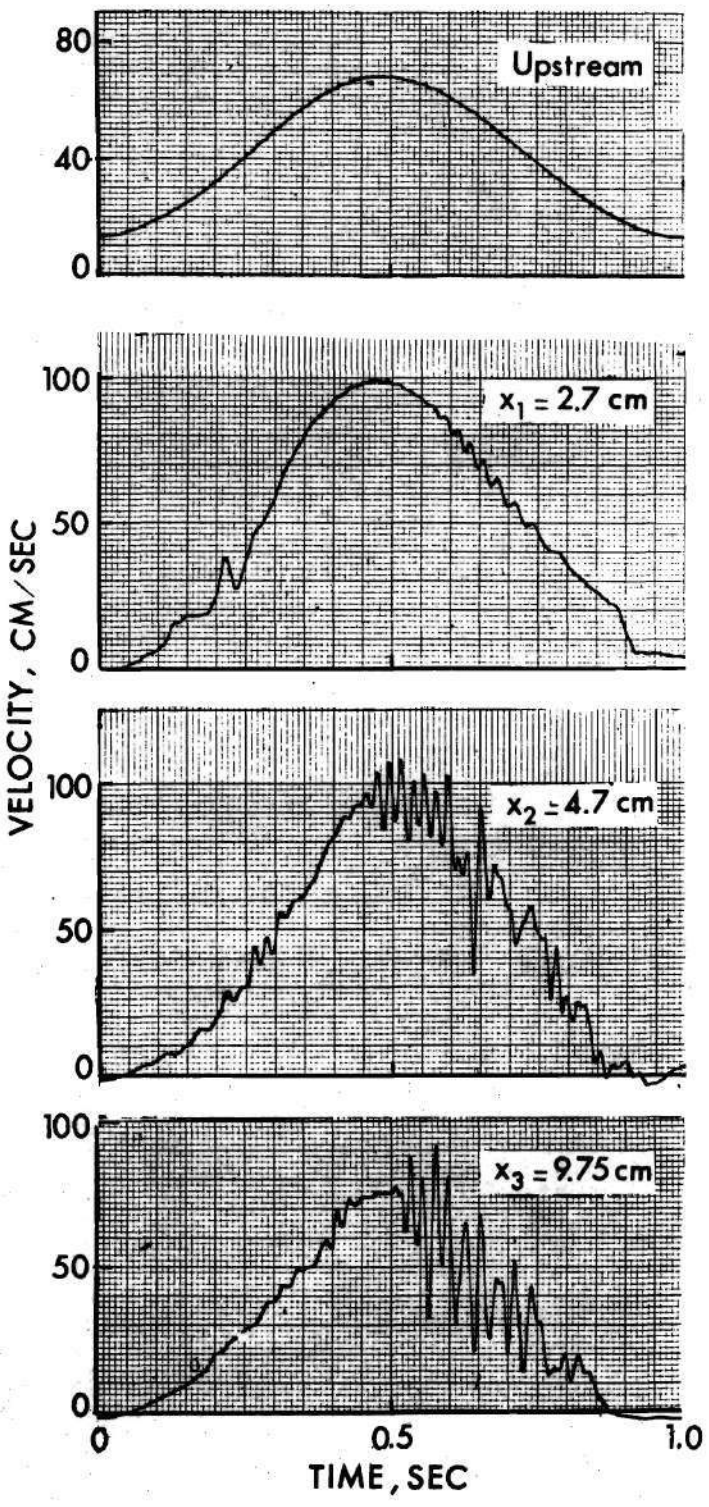

Figure 5-7. Instantaneous Velocity at Different Locations Downstream of 50 Percent Occlusion

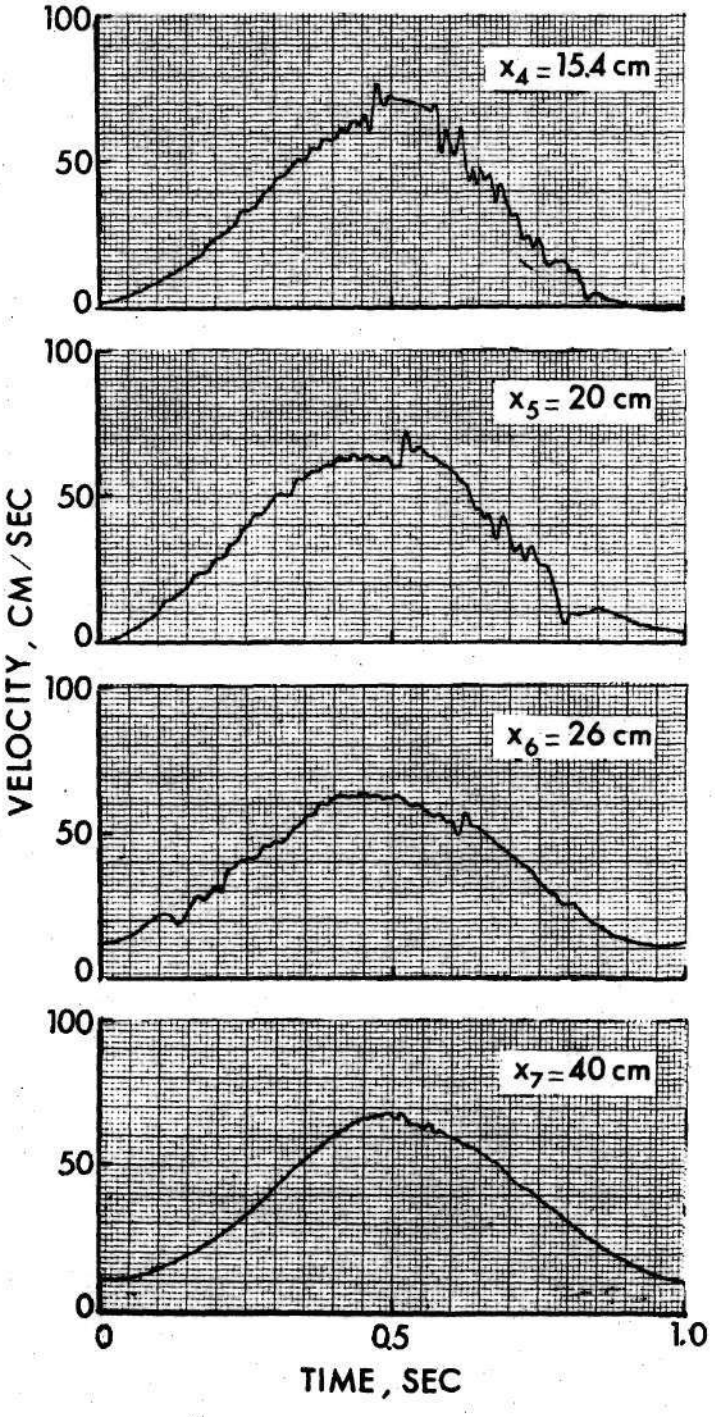

Figure 5-7. (Continued) Instantaneous Velocity at Different Locations Downstream of 50 Percent Occlusion

these velocity fluctuations but they have relatively smaller amplitudes in comparison with the primary ones discussed above. Also some of these velocity fluctuations have irregular patterns.

The same figure also indicates an increase in the peak velocity at X_1 and X_2 to about 100 cm/sec as compared with the pre-stenotic value of 68 cm/sec. Thus, the peak instantaneous Reynolds number at X_1 and X_2 is approximately 3500. This increase tends to destabilize the flow (86) so that the presence of periodic flow instabilities is more likely to lead to a breakdown into turbulence. This occurs at position X_2 and X_3. Because of the expansion of the flow downstream of the stenosis, the increase in the peak velocity is not preserved and the maximum velocity decreases gradually with distance until it reaches the upstream value. Also, production of turbulence is not balancing dissipation, so turbulence decays as the flow moves downstream of the stenosis as indicated by velocity waveforms at positions X_5 to X_7.

The minimum velocity decreases and becomes negative at several of the axial positions before it recovers to the upstream value at position X_7. The instantaneous velocity waveforms at different axial locations and their relative position with respect to the stenosis are displayed in Figure (5-8) as an alternative way of presenting the data.

5.2.1 Ensemble Average and Disturbance Velocities

The ensemble averages presented in Figures (5-9) show only the primary periodic fluctuation discussed in the previous section. The $u'^2(\tau)$ plots show that at position X_1, there are two spikes corresponding to two vortices, the first one is moving faster than the second. By the

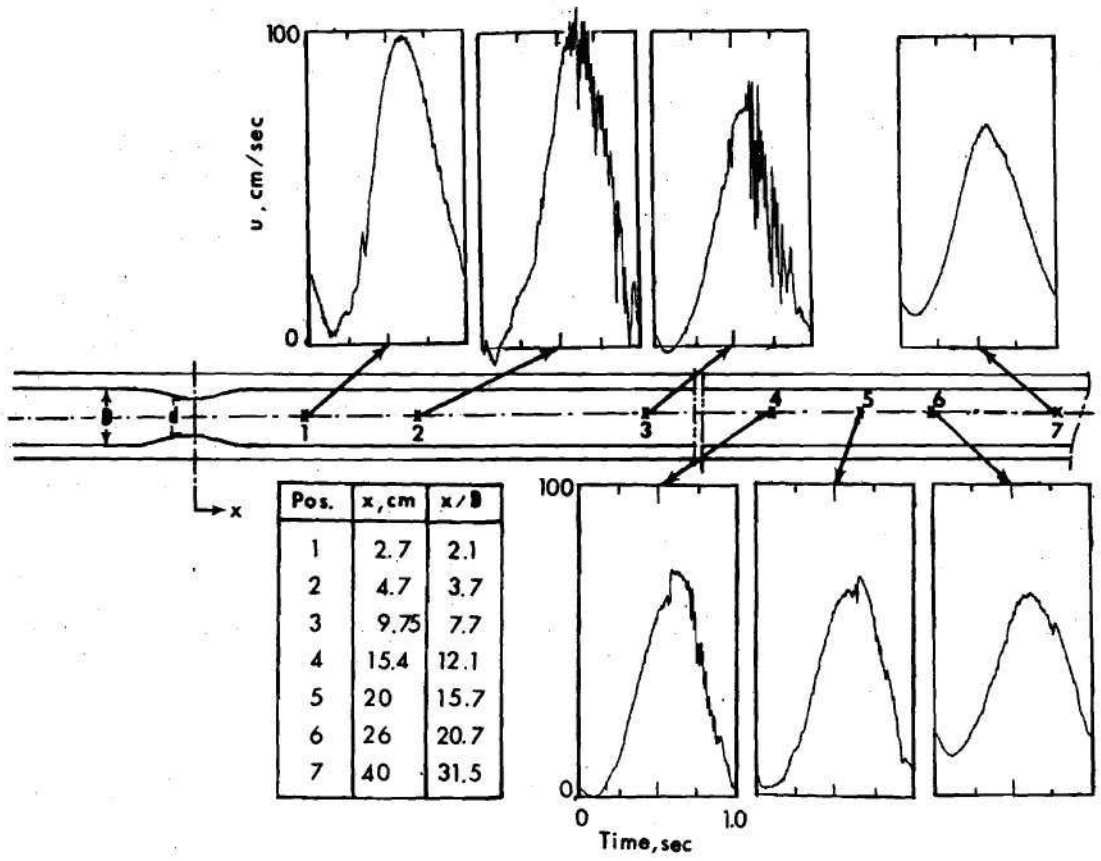

Pos.	x, cm	x/B
1	2.7	2.1
2	4.7	3.7
3	9.75	7.7
4	15.4	12.1
5	20	15.7
6	26	20.7
7	40	31.5

Figure 5-8. Alternative Presentation of Instantaneous Velocity u(t) for Different Axial Positions

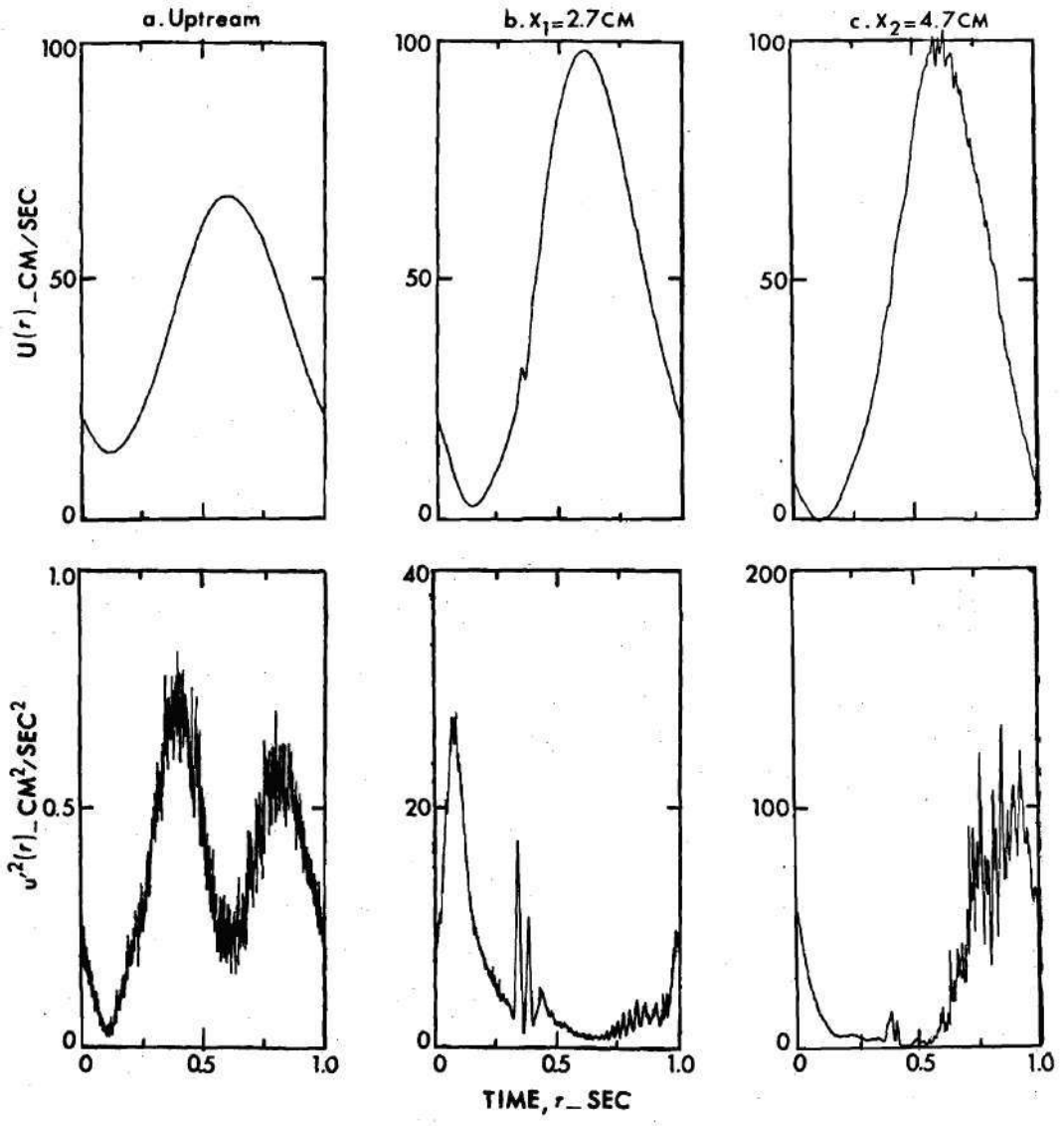

Figure 5-9. Ensemble Average and Disturbance Velocities for the 50 Percent Occlusion

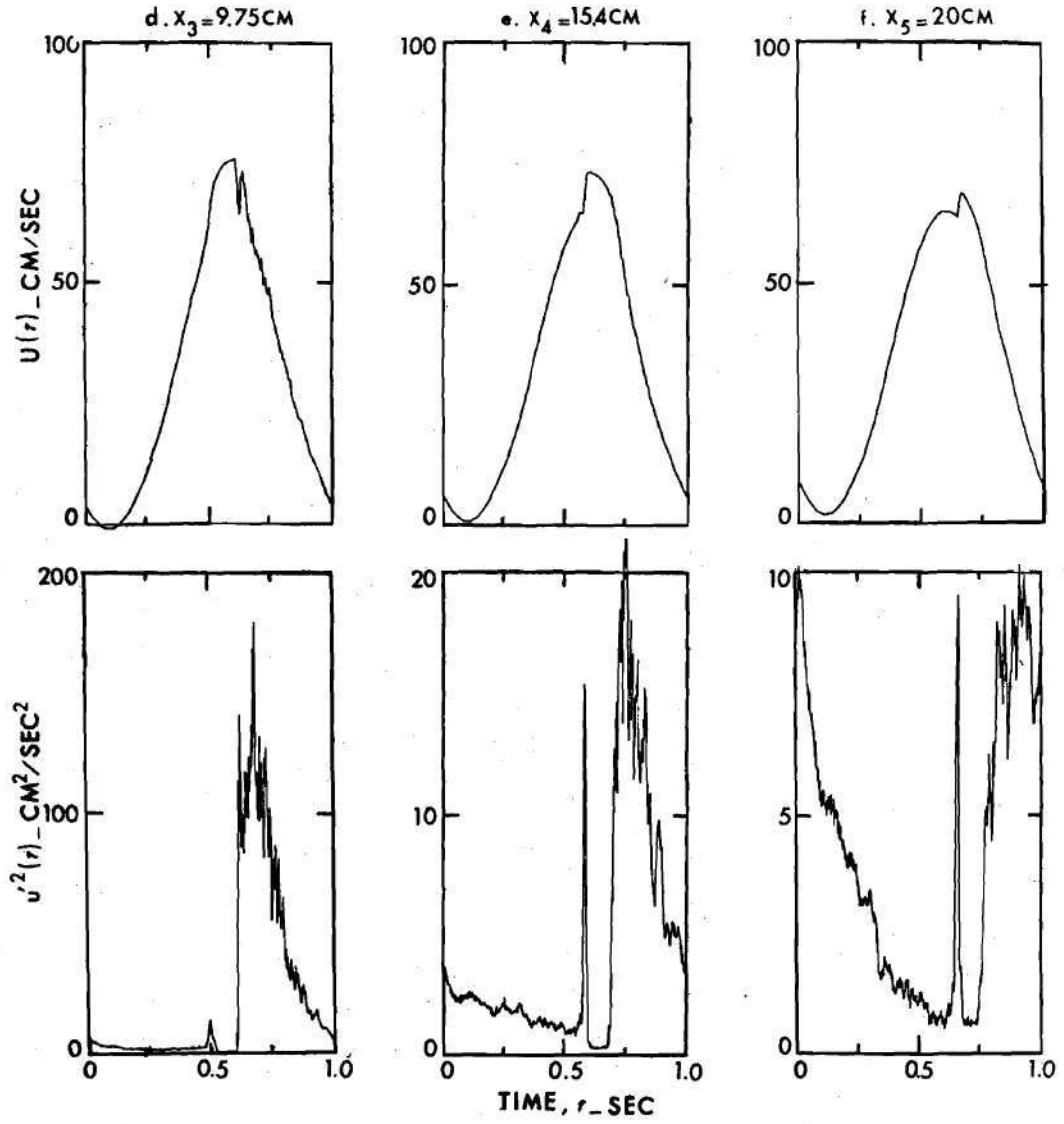

Figure 5-9. (Continued) Ensemble Average and Disturbance Velocity for the 50 Percent Occlusion

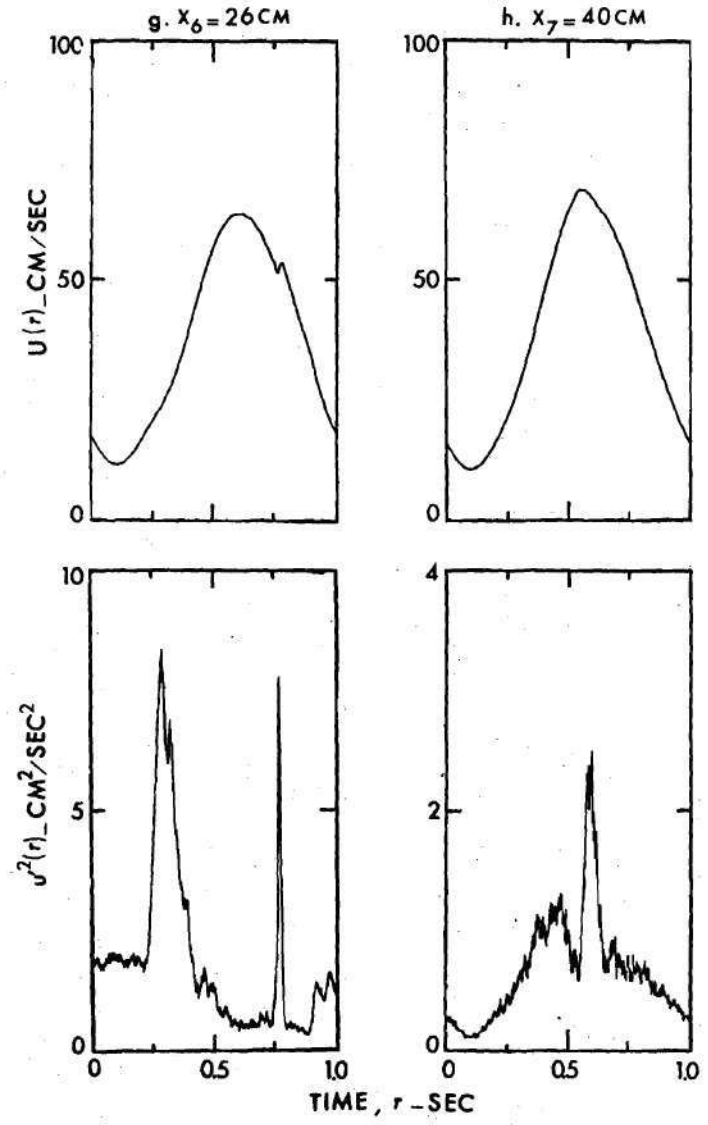

Figure 5-9. (Continued) Ensemble Average and Disturbance Velocities for the 50 Percent Occlusion

time they reach X_3, they merge into each other and they start to move as one vortex. However, at X_3 the instantaneous waveform chart occasionally shows two peaks corresponding to two vortices but in most cases shows only one. This means that the mechanism of merging is not regular, but on the average the two vortices form one periodic velocity fluctuation and not two. At position X_6 the unified vortex reaches the deceleration phase. Later positions indicate complete dissipation of this vortex.

Table (5-1) shows the average convection velocity for the two main vortices as calculated from $u'^2(\tau)$ curves. The values calculated for the average traveling velocities of the vortices are comparable to the local instantaneous velocities at which the periodic fluctuations are observed.

The $u'^2(\tau)$ plots show that turbulence starts in the deceleration phase and probably part of the peak region. The periodic instability that breaks down to turbulence can be seen clearly in the ensemble average for position X_2. The instantaneous waveforms at positions X_1 and X_2 (Figure (5-7)) show that the instability is growing gradually in amplitude and that it has a high frequency which appears to decrease as the flow decelerates. The $u'^2(\tau)$ plots for axial positions X_3, X_4, and X_5 show that the turbulence break up occurs suddenly during the peak phase. This turbulent front or the sharp increase in u'^2 occurs at a well defined time in the peak region and is then followed by a gradual decrease in u'^2 with time. The front is present at different locations in the velocity cycle depending upon the axial location considered.

The method of measurement used in taking the data is Eulerian. Consider the Lagrangian approach by imagining a mass of the fluid moving

Table 5-1. Average Vortex Velocity Between Different Axial Positions

Vortex Number	Average Vortex Velocity, cm/sec				
	$X_1 \rightarrow X_2$	$X_2 \rightarrow X_3$	$X_3 \rightarrow X_4$	$X_4 \rightarrow X_5$	$X_5 \rightarrow X_6$
1	40.4	46.4	67.1	58	55.1
2	57.7	63.7	67.1	58	55.1

Table 5-2. Location and Average Velocity of the Turbulent Front

Axial position	X_3 = 9.75 cm	X_4 = 15.4 cm	X_5 = 20 cm	X_6 = 26 cm	X_7 = 40 cm
Cycle phase	Peak	Peak	Deceleration	Acceleration (next cycle)	Peak (next cycle)
τ_T msec	109	185	257.4	738	1060
V_T cm/sec	73.75		12.5		
		64.1		43.5	

τ_T: time between the beginning of the peak phase and the sharp increase in $u'^2(\tau)$ plot that corresponds to the turbulent front.

V_T: the average velocity of the turbulent front.

in the vicinity of the centerline of the tube. This mass exhibits a periodic instability in the velocity at locations near the exit of the stenosis. This instability associated with the mass of fluid breaks down to turbulence as the mass moves farther downstream. The front end of this mass is the turbulent front. Because the peak velocity decreases and the mass carrying the turbulent fluctuations passes through locations where it starts in the deceleration phase, not in the peak one, turbulence fluctuations decay gradually.

The turbulent front is actually convected at a velocity close to the local instantaneous velocity of the flow. Table (5-2) summarizes the locations of the turbulent front in the velocity cycle and it averages convection velocity.

Finally, the split peak observed in the ensemble average at position X_3, which is similar to some of the in vivo results previously presented in Chapter III, actually corresponds to the beginning of the turbulent fluctuation or the turbulent front. However, the split peaks on the ensemble averages at positions X_4 and X_5 corresponding to the leading vortex. So, both the turbulent front and the vortices can cause this split peak in the ensemble average. It is also noticed that for all positions the moving vortices were leading the turbulent front without coalescing.

5.2.2 Energy Spectra of the Disturbance Velocity

As previously explained, different phenomena occur during different phases of the velocity cycle. For this reason, separate calculations of the energy spectra for these phases should help to isolate the behavior

of the various phenomena with respect to frequency content.

The energy spectra of the disturbance velocity calculated for the four phases I_1, I_2, I_3, and I_4 are displayed in Figures (5-10) for the seven axial locations.

The energy spectra for the acceleration phase (I_1) at different locations (Figure (5-10a)) show several important features. The spectrum for position X_1 has a broad peak at a frequency of about 20 Hz. This corresponds to the frequency of velocity fluctuations due to the primary pair of vortices as observed before (see Figure (5-7b)) and it is re-emphasized that the magnitude has no direct meaning with respect to the magnitude of flow disturbance. The spectrum for location X_2 shows two broad peaks. One of them is at frequency about 24 Hz, which corresponds to velocity fluctuation frequency caused by the main pair of vortices, and the second peak is at frequency about 48 Hz. This appears to be the frequency of the periodic instability that starts with a relatively small amplitude near the end of the acceleration phase or it might be due to the window effect.

The spectrum at X_3 shows that the content at higher frequencies is greater than that of the other positions. By observing the instantaneous velocity waveform (Figure (5-7d)), there are some velocity fluctuations in the acceleration phase. Also Figure (5-9d) shows that part of the spike corresponding to the main vortex pair is actually in the acceleration phase.

The integral of the energy spectrum from zero frequency to infinity gives the total disturbance energy per unit time, provided that this

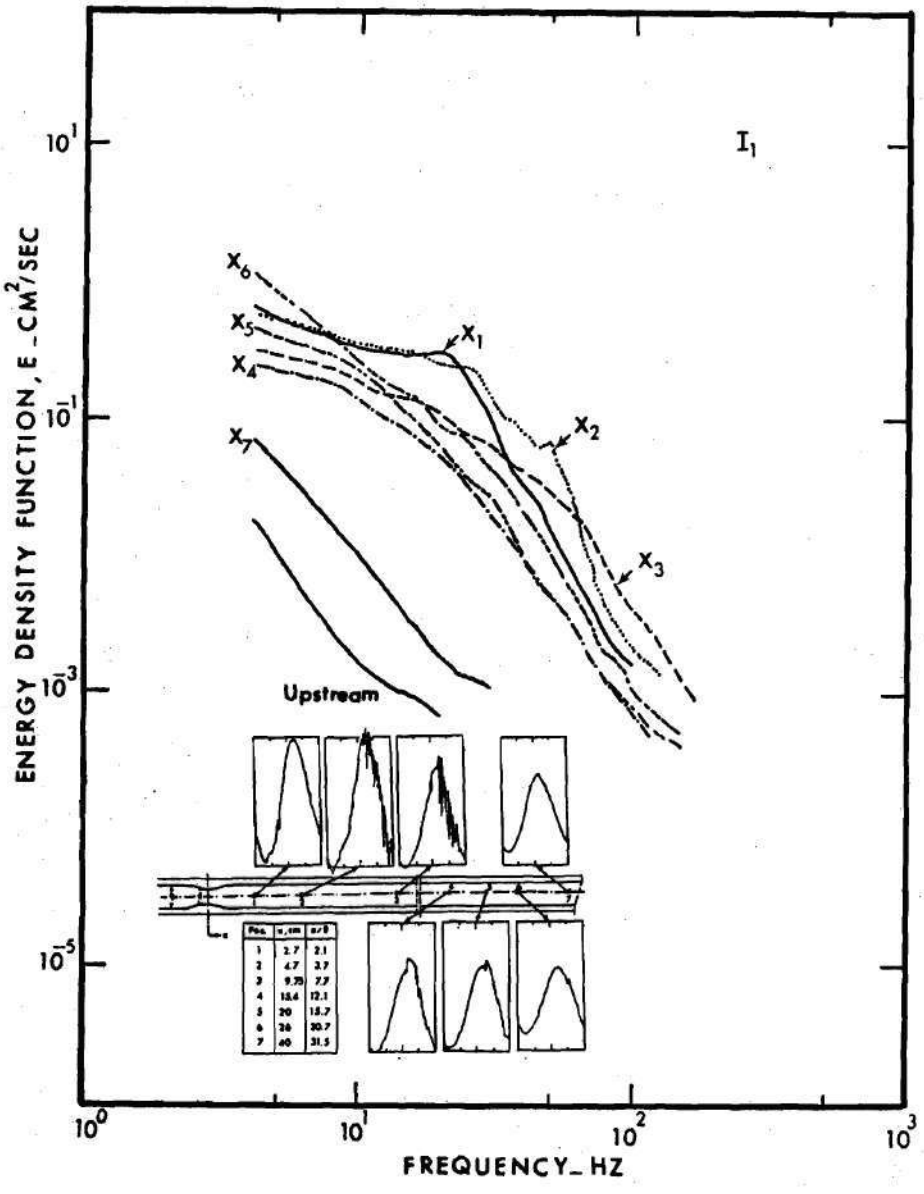

Figure 5-10a. Disturbance Energy Spectra for the Acceleration Phase at Different Axial Positions Distal to 50 Percent Occlusion

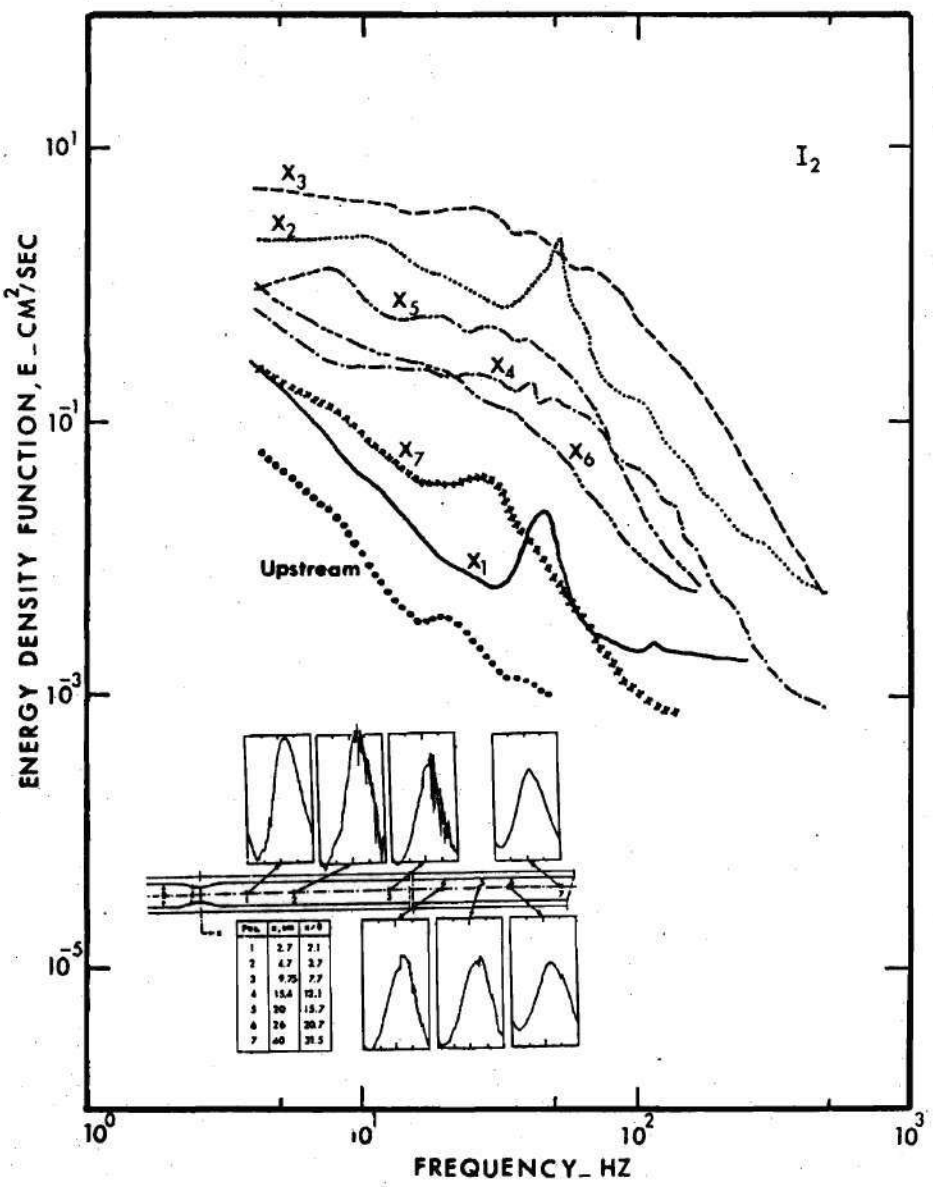

Figure 5-10b. Disturbance Energy Spectra for the Peak Phase at Different Axial Positions Distal to 50 Percent Occlusion

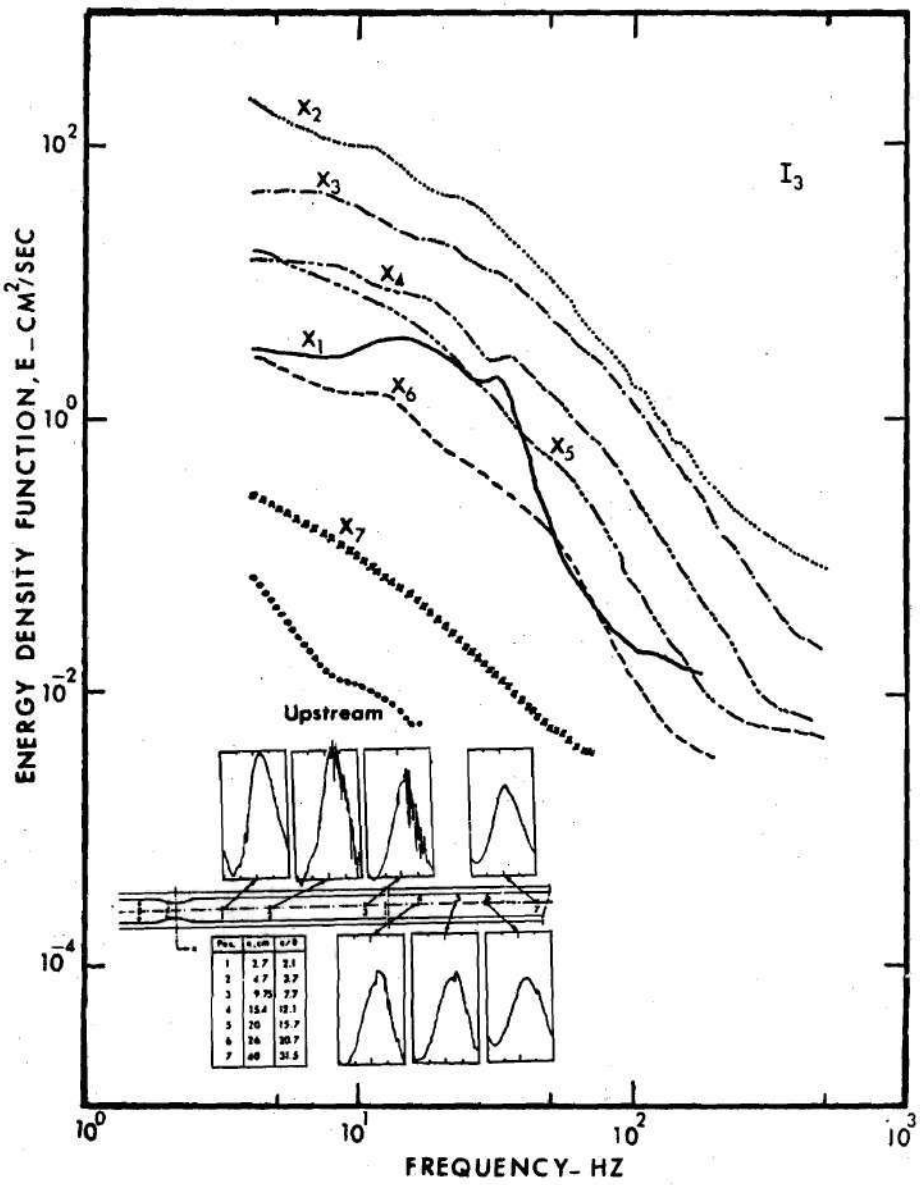

Figure 5-10c. Disturbance Energy Spectra for the Deceleration Phase at Different Axial Positions Distal to 50 Percent Occlusion

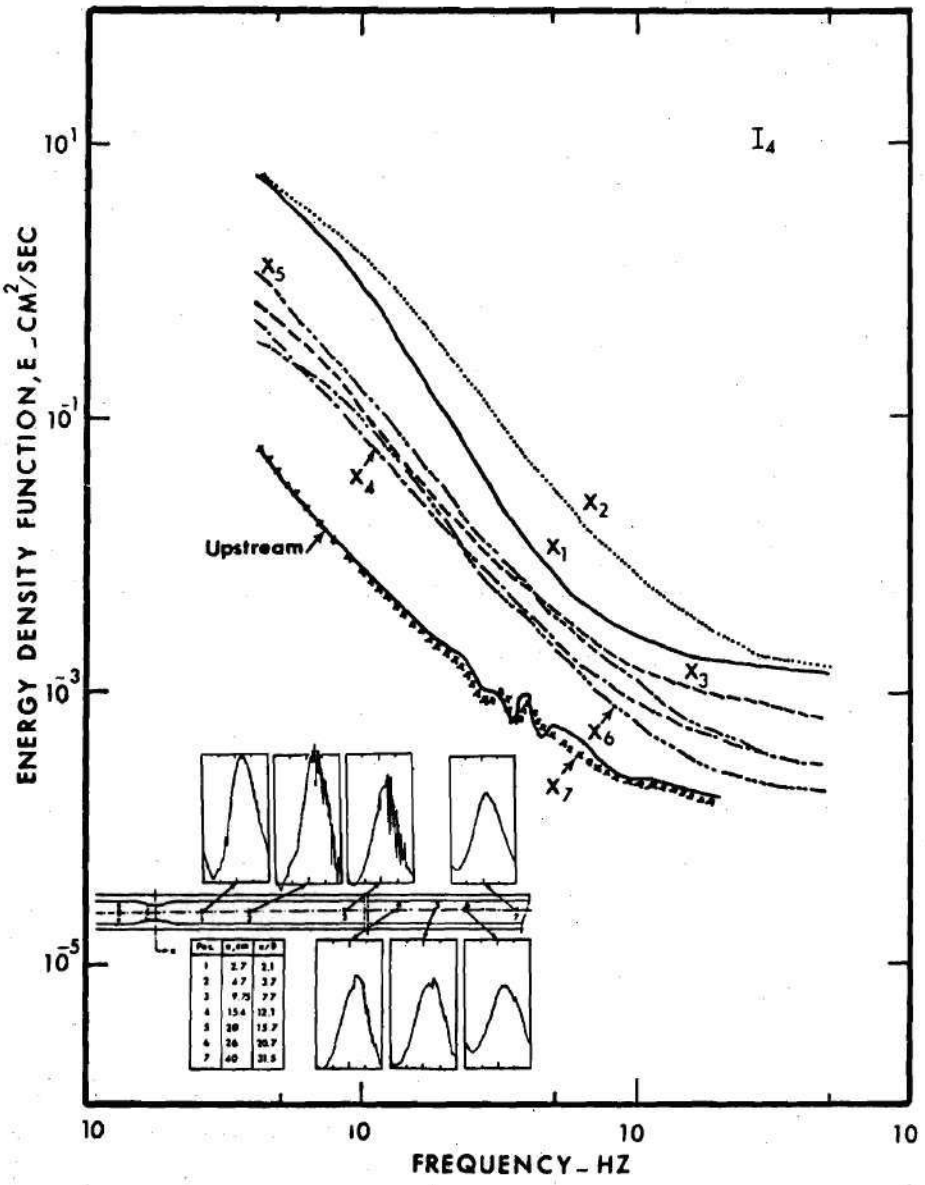

Figure 5-10d. Disturbance Energy Spectra for the Valley Phase at Different Axial Positions Distal to 50 Percent Occlusion

spectrum is not representing periodic phenomena such as the vortex shedding.

Although the spectra for X_3, X_4, X_5, and X_6 have similar shapes, the total disturbance energy for position X_6 is higher than that for X_5. Also, the total disturbance energy for position X_5 is greater than that for position X_4. As previously explained, the turbulent front that breaks up early at position X_2 continues to move downstream while turbulence is decaying. By the time this front reaches locations X_5 and X_6 it shows up in the acceleration phase (see also Table (5-2)). It is clear that the spectral shape of the decaying turbulent front is different from a "typical" turbulent spectrum. It tends to have higher amplitudes at lower frequencies which indicates the laminarization trend. The spectrum for location X_7 is very similar to the upstream one which means that the flow during the acceleration phase at this location is recovering back to the upstream condition.

The disturbance energy spectra for the peak phase (I_2) are presented in Figure (5-10b). The peak in the spectrum of each of locations X_1 and X_2 occurs at frequency about 48 Hz, which corresponds to the periodic instability that breaks down later to turbulent fluctuations. It is noticed also that total disturbance energy at position X_2 is much higher than that at X_1. This can be seen also clearly in the u'^2 plots Figures (5-9a and b). At position X_3 the turbulent front is formed, followed by turbulent fluctuations. At this position as indicated by Figure (5-9c) and Table (5-2), the front occurs in the peak phase. For this reason the spectrum of position X_3 contains the highest level of

disturbance energy. At position X_4 a small part of the turbulent fluctuations occupies part of the peak phase as can be seen by Figure (5-8d). As a result the turbulence level goes down as indicated by the energy spectrum of position X_4. A change in the shape of the energy spectrum is observed at position X_5. The amplitudes at high frequency are less than the corresponding ones at position X_4, because the turbulent front at this position starts in the deceleration phase. The spectra for positions X_5 and X_6 show higher amplitudes for low frequencies than the spectrum at location X_4. This may be due to the existence of velocity fluctuations caused by the moving vortices which pass through this location while flow is in the peak phase. There exist also some small amplitude low frequency fluctuations observed in the instantaneous velocity waveform (Figures (5-7f and g) in the vicinity of the peak phase.

The deceleration phase (I_3), being the most unstable phase in the velocity cycle, should actually contain most of the turbulent or random velocity fluctuations. Figure (5-10c) displays the energy spectra for the seven poststenotic axial locations and the upstream one. The energy spectrum at position X_1 shows that the regular pattern of velocity fluctuations that breaks down to turbulence tends to have lower frequencies than the 48 Hz observed for the spectra of both the acceleration and peak phases. The spectrum for the deceleration phase tends to have a broad peak that corresponds to frequency of about 33 Hz. This is due to the fact that the frequency of oscillation of the instantaneous velocity is decreasing with the passage of time in the deceleration phase. As can be seen in Figure (5-7b) at position X_1 where an estimate of the period of

oscillation at the start of I_3 gives a value of 0.022 sec ($f \cong 45$ Hz), while towards the end of I_3 the period is about 0.03 sec ($f \cong 33$ Hz). Spectra taken farther downstream show a much broader frequency distribution because of the breakup of the periodic disturbance into turbulence and random velocity fluctuations. The maximum disturbance energy level is obtained at position X_2. Then a gradual decrease is observed at other positions downstream until position X_7, since the turbulent fluctuations are decaying as the flow moves downstream. Also, as illustrated in Table (5-2) and Figures (5-9) turbulent front exists in the peak phase at position X_3 and X_4 while turbulent fluctuations extend to the deceleration phase. At position X_5 the front starts in the deceleration phase and at later positions it is not existing in the deceleration phase at all.

The valley phase is the phase during which the minimum velocity is reached. At most of the locations X_1 through X_5, the velocity during this phase is close to zero and sometimes a negative velocity is also observed. The spectral shapes (Figure (5-10d)) show that most of the contributions to the disturbance energy are from the low frequency components. The axial decay of the disturbance energy for phase I_4 is similar to that for phase I_3.

Although the four intervals chosen for this analysis were each carefully defined to be 0.25 seconds in duration with the maximum velocity occurring at the center of the peak phase for the upstream wave form (Figure (5-1)), other possibilities cannot be excluded. For example if the beginning of the deceleration phase for the location X_3 is to be considered the onset of the turbulence fluctuations, "the turbulent front,"

a different spectrum for the disturbance velocity is obtained for the newly defined deceleration phase B (see Figure (5-11)). The contribution from the high frequency components to the total disturbance energy is more than that spectra for I_3. This shows that the end of the deceleration phase I_3 includes low frequency fluctuations and the peak region has higher frequency components of velocity fluctuation . This conclusion was obtained before in discussing spectra for phase I_3. Actually, when seeking turbulence similarity, the $u'^2(\tau)$ plots should be used to locate and define the time intervals in accordance with the position of the turbulent front. Then, by following the turbulent zone with the sample window the spectral evolution of this in a Lagrangian approach can be seen as a function of distance.

The energy spectra for the total velocity cycle provide information of the frequency content of the disturbance energy during the entire cycle without regard to whether it is due to nonreproducibility in the periodic velocity fluctuations caused by a vortex or due to random or turbulent fluctuations. Of course, events which occur in acceleration, deceleration, peak, or the phase of minimum velocity (valley), all are presented on one plot for this case. However, the energy spectrum for the total velocity cycle may give qualitative information of the nature of the disturbance created during the entire velocity cycle at different axial positions which may have some applications in comparing different axial positions for the same degree of occlusion or different degrees of occlusion for certain axial locations. Figure (5-12) displays the energy spectra of the disturbance velocity for the entire velocity cycle. Spectra for

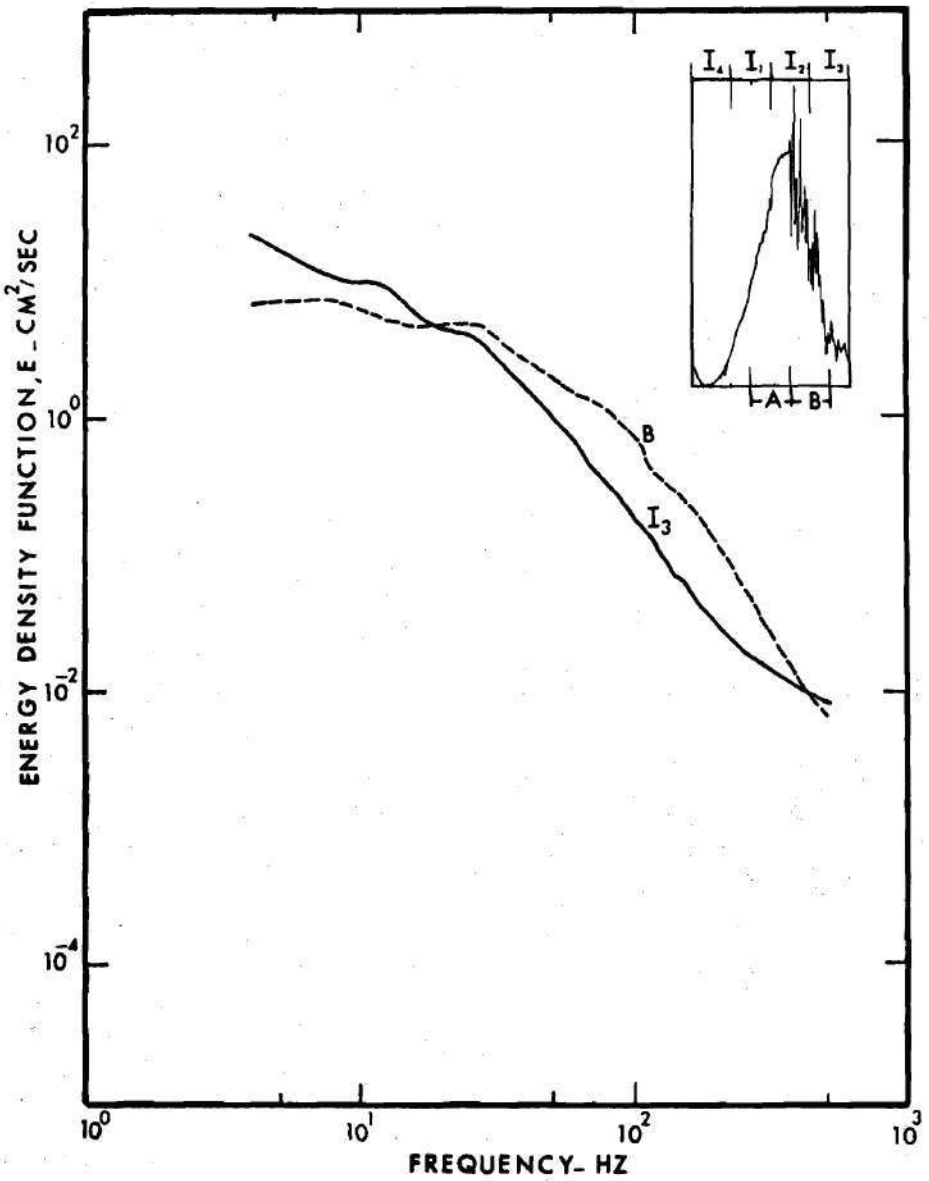

Figure 5-11. Alternative Definition of the Deceleration Phase and the Corresponding Energy Spectrum

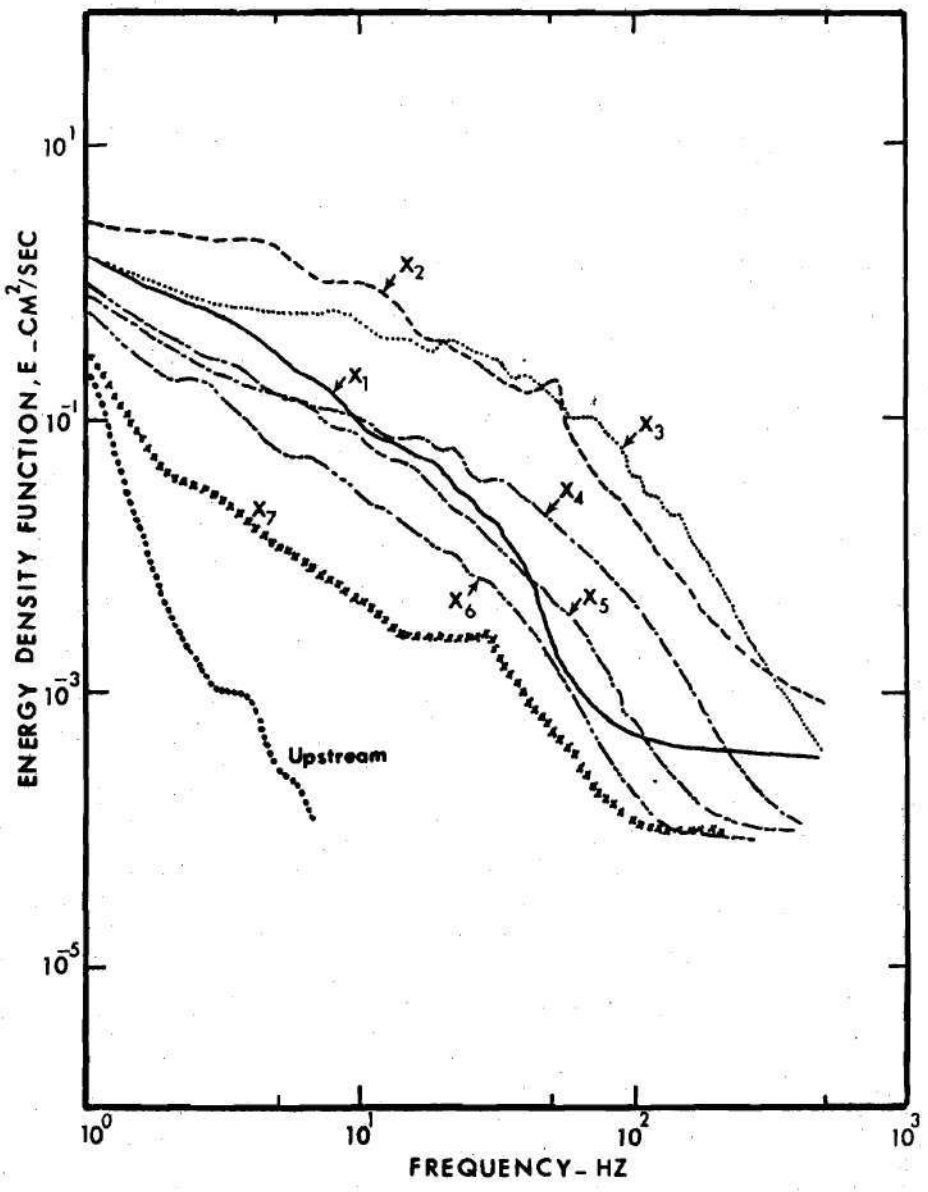

Figure 5-12. Energy Spectra for the Total Velocity Cycle at Different Axial Positions Downstream of 50 Percent Occlusion

different axial positions show the development of periodic instability (position X_1 and X_2), the breakdown to turbulence (position X_3) and then decay of turbulence (position X_4 to X_7).

The possibility of expressing the disturbance energy spectra in terms of similarity parameters has been examined. The approach is to consider each phase separately and to exclude the spectra that correspond to periodic velocity fluctuations such as vortex shedding or the periodic instability that precedes the turbulent fluctuations. The dimensionless parameters considered are the same used to reduce the in vivo data, namely

$$E^* = \frac{F\bar{U}}{2\pi d} \qquad \text{and} \qquad N_s^* = \frac{2\pi f d}{\bar{U}}$$

Since positions considered for this analysis are somewhat distal from the stenosis exit, the unoccluded diameter of the tube is considered to be the characteristic length. The characteristic velocity $\bar{U}$ was defined before by equation (3-4).

There are other different combinations of characteristic length and velocity that could be used for these data. However, there does appear to be a definite, but limited region distal to the stenosis for which the spectral data are reasonably correlated by introducing the above similarity parameters. This is illustrated by Figure (5-13) which shows the similarity plots at different locations for the deceleration phase. For position X_3 the spectrum for the deceleration phase B previously defined in this section was used. The spectrum for the deceleration

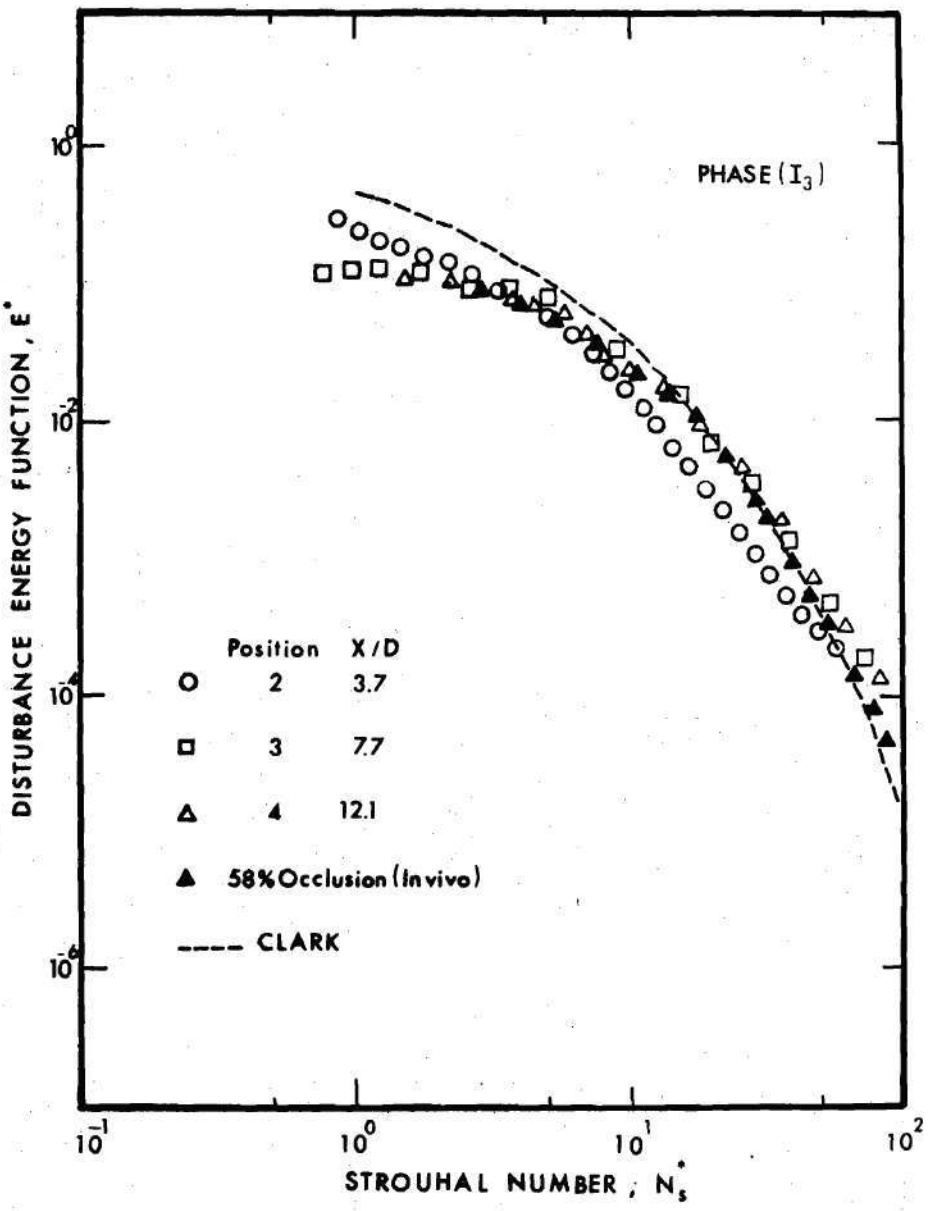

Figure 5-13. Dimensionless Energy Spectra for the Deceleration Phase for the 50 Percent Occlusion

phase I_3 for this position does not correlate well with other data because of the contribution of the low frequency fluctuations at the end of the deceleration phase. Spectra for positions X_3 and X_4 show a very good correlation. In general, spectra for locations X_2 (2.1D) to X_4 (12.1D) fall reasonably well into a single group. Locations X_5, X_6, and X_7 are transitional ones, and the spectra at these locations are different from the others and are not presented in Figure (5-13). So for locations between 4 and 12 times the unoccluded tube diameter, a reasonable correlation was obtained for the similarity parameters chosen provided the "most turbulent" part of the cycle is examined.

Because of the nature of the disturbance velocities for the other phases and for different locations, the correlation among all spectra is not possible. For example, the peak region has different spectral shape after position X_3 because of the vortices passing through it and the displacement of the turbulent front away from this phase.

Care is required in comparing these spectra with a "typical" turbulent energy spectrum, since it is difficult to decide just what spectral shape is typical. As with in vivo experiments, in vitro data for the deceleration phase are compared with that reported by Clark (42). The agreement between these results and the present spectra is reasonably good as can be seen by Figure (5-14). The in vivo data for the deceleration phase for the case of 58 percent stenosis are also presented on the same plot. A very good agreement with the in vitro results is noticed, especially those at locations 3 and 4.

In comparing the spectra for the peak phase with the in vivo results

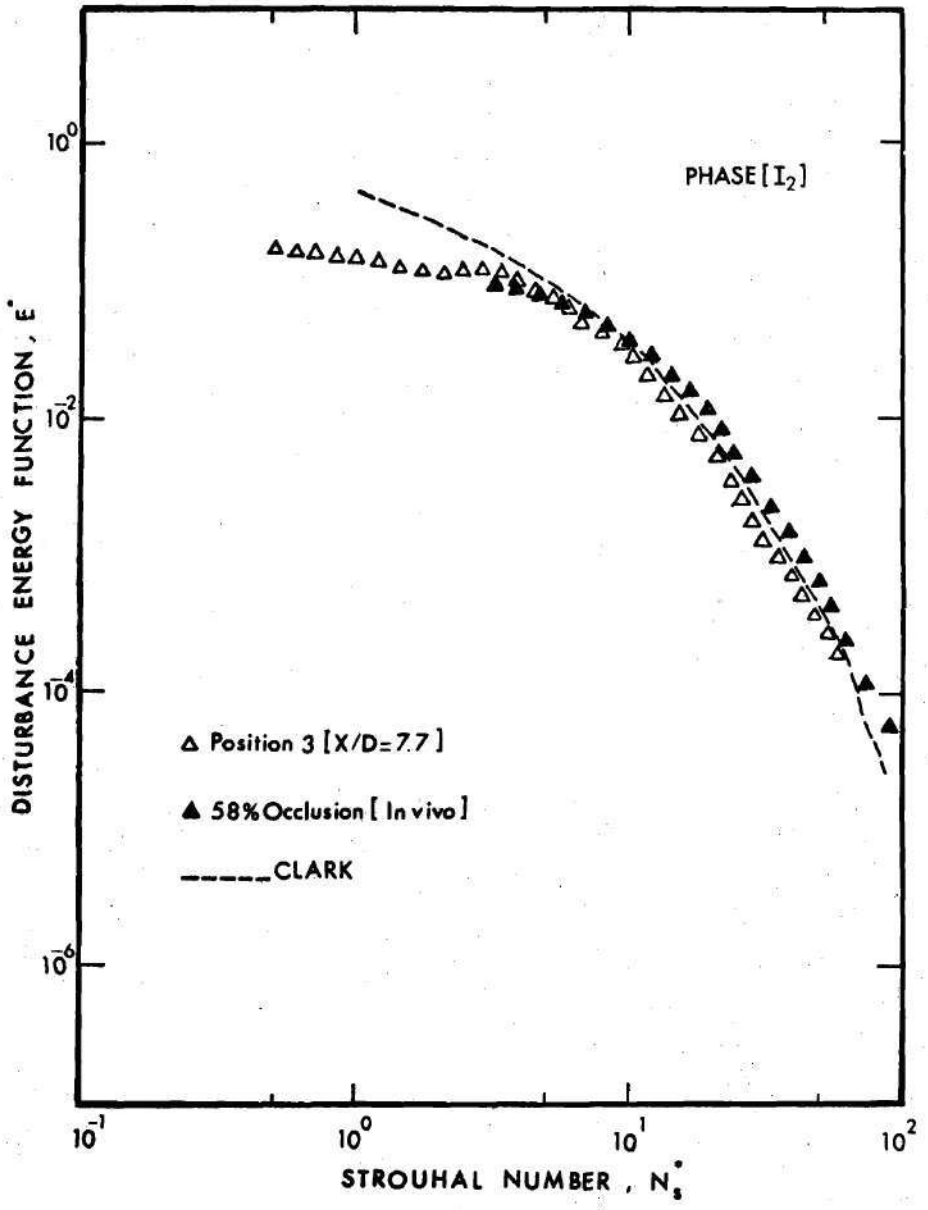

Figure 5-14. Comparison Between the Present Results and Those of Clark and the In Vivo Experiments

and those of Clark, only the spectrum at position X_3 agrees very well with these data (Figure (5-14)). Of course the low frequency components for Clark's spectrum do not agree with other data because this data was filtered for frequencies below 22.4 Hz as previously discussed in Chapter III.

The spectrum for the acceleration phase I, at the first position (X/D = 2.1) was compared to the corresponding phase in the in vivo data (X/D = 1.7). A curve was drawn through the data presented in Figure (3-6a) for occlusions up to 50 percent area reduction for the purpose of this comparison. Figure (5-15) displays the results. These were the only data in which in vivo and in vitro results were similar due to the fact that the spectrum at position X_1 for the acceleration phase is not a turbulent one.

5.2.3 Autocorrelation Functions

The autocorrelation plots are an alternative method of presenting the data. There are several features of interest that the autocorrelation curves can show in the time domain. Such as, the periodic instability that breaks up into turbulence and the turbulent fluctuations. Figure (5-16) displays the autocorrelation curves for the two phases I_2 and I_3 at the first four positions. For the peak phase the periodic instability starts at position X_1 and X_2 before it breaks up to turbulent fluctuations at position X_3 and X_4. The frequency of the periodic instability can be calculated from the autocorrelation curves at X_1 and X_2 and it shows to be 51 Hz which reasonably agrees with the value obtained before from the energy spectra (48 Hz). At position X_3 and X_4 the autocorrelation curves show turbulent random behavior of the disturbance velocity.

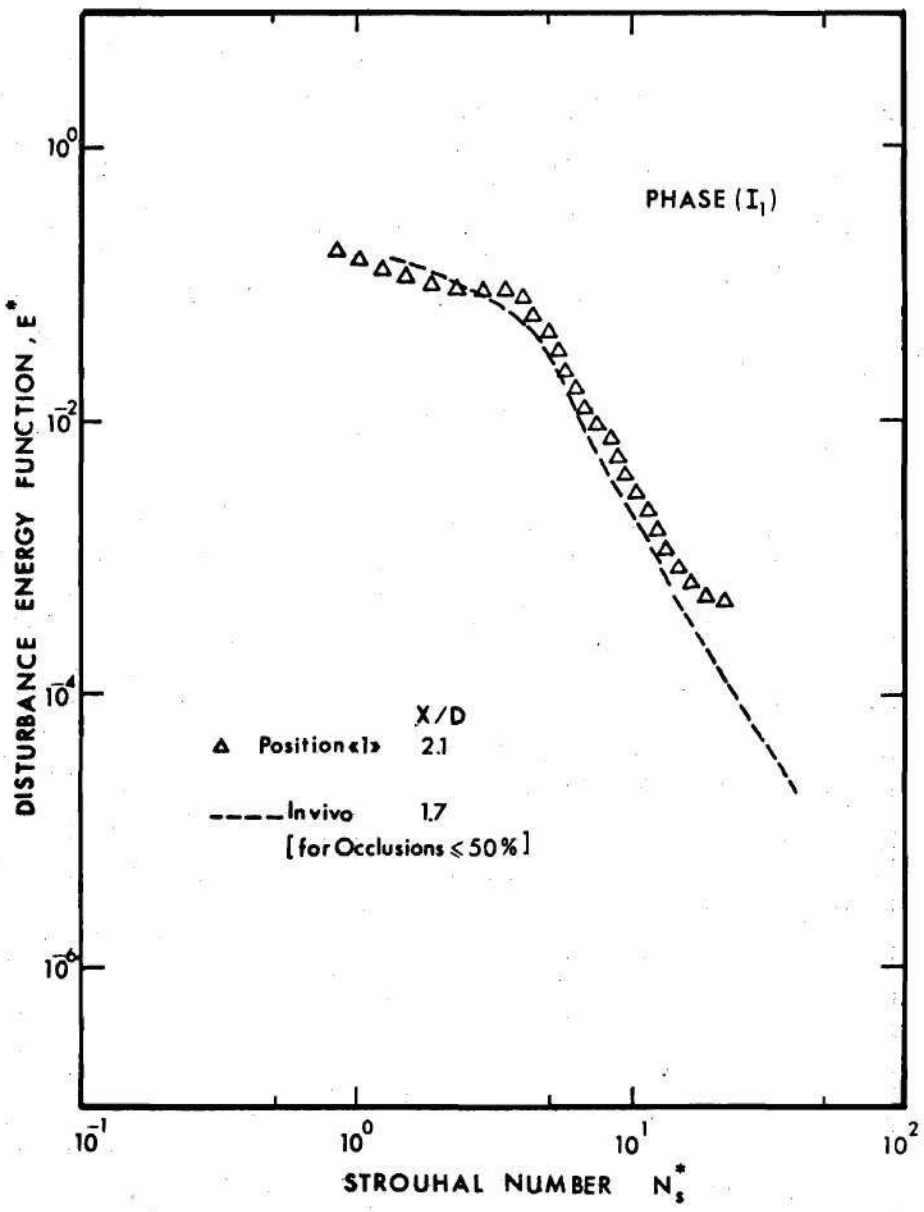

Figure 5-15. Comparison Between In Vitro and In Vivo Results for the Acceleration Phase--50 Percent Occlusion

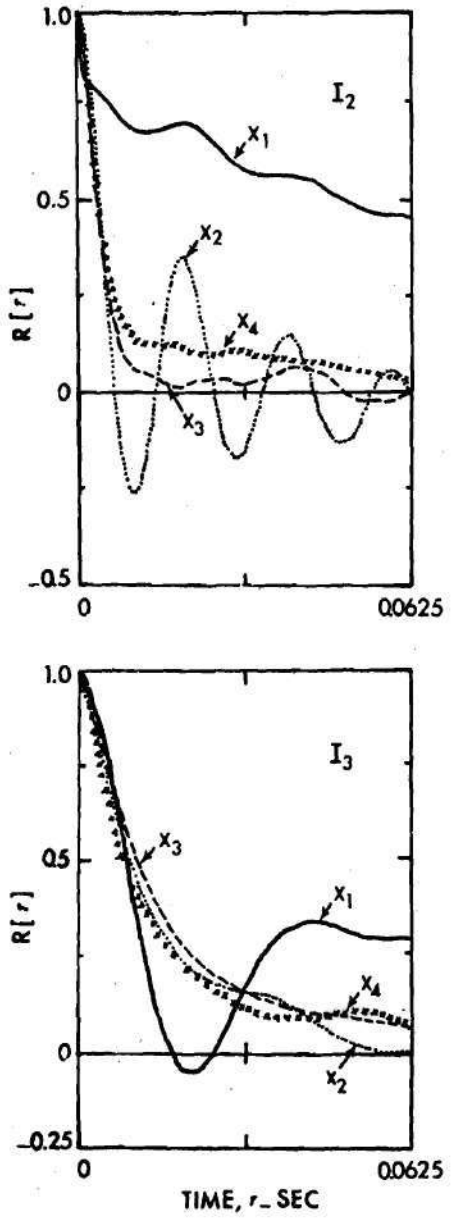

Figure 5-16. Autocorrelation Functions for the Peak and Deceleration Phases--50 Percent Occlusion

For the deceleration phase, the autocorrelation curve at position X_1 shows that the periodic instability has a frequency of (23 Hz) which is lower than the frequency of instabilities observed in the peak phase. This conclusion was obtained also in discussing the energy spectra of the disturbance velocity. Other autocorrelation curves show that the disturbance velocity is random which indicates the breakup of turbulent fluctuations.

5.3 Results of 75 Percent Occlusion

Figure (5-17) illustrates the velocity waveform variation with axial position in the near distal flow field for the 75 percent occlusion. All velocity measurements were taken at the centerline of the tube. The sharp increase in velocity during the acceleration phase for position X_1 is indicative of the passing of a large vortex. A high frequency instability is observed near the end of the acceleration extending over the peak phase and part of the deceleration. The peak velocity is approximately 160 cm/sec compared to 68 cm/sec for the upstream waveform which is the same as that for the 25 and 50 percent occlusion. The waveform for position X_2 shows the breakdown of these instabilities, which are convected with the flow, to random turbulent fluctuations. Although the mean velocities are noticeably lower than the corresponding waveform for position X_1, the amplitudes of the turbulent fluctuations are considerably higher. At position X_3, which is 7.7D downstream of the stenosis center, a substantial decay of turbulence is seen and most of the turbulent fluctuations are existing in the deceleration phase. Further positions downstream show complete decay of turbulence and no indication of any

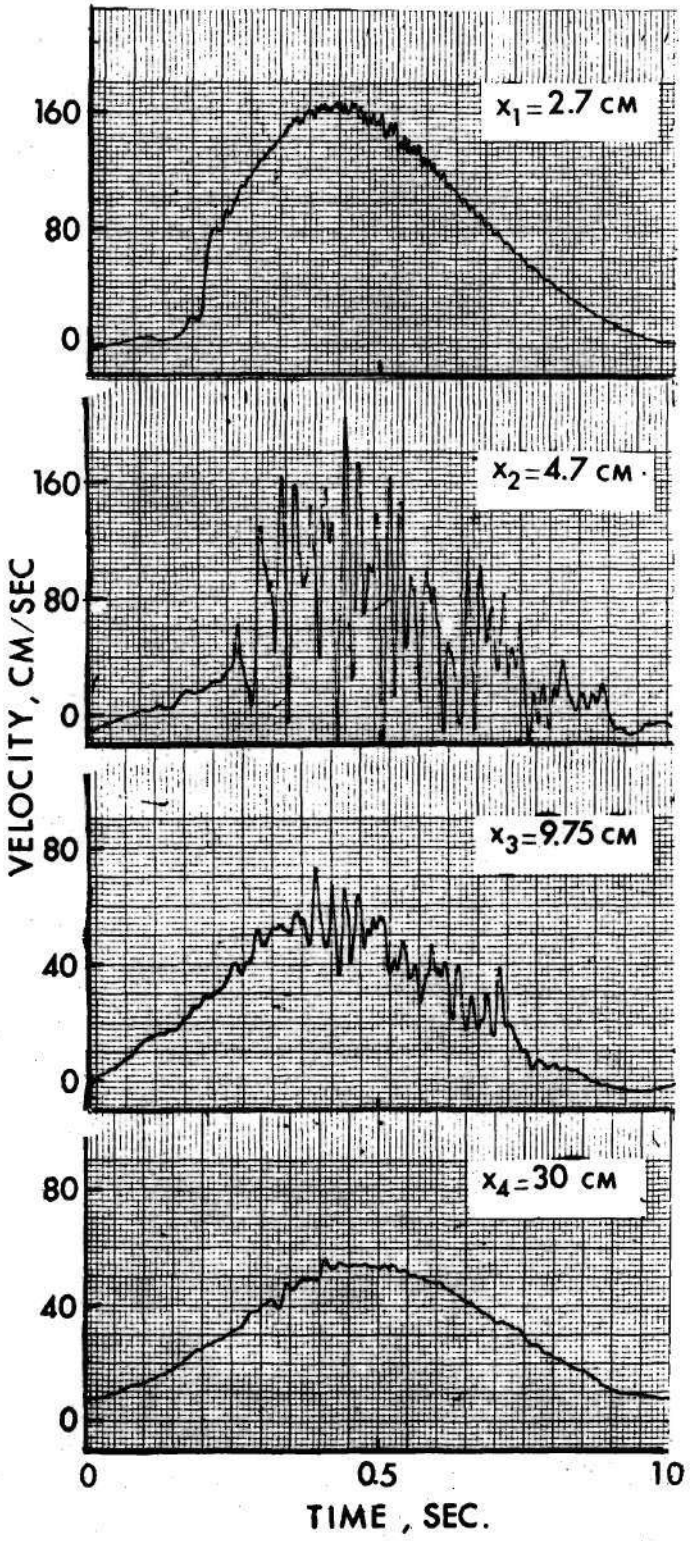

Figure 5-17. Instantaneous Velocity at Different Locations Downstream of 75 Percent Occlusion.

discrete vortices. An example of one of these positions is X_4 at 24D from the center of the occlusion.

In the following sections, analysis of the flow disorder for the three axial locations X_1, X_2, and X_3 is presented.

5.3.1 Ensemble Average and Disturbance Velocities

Ensemble average waveforms are displayed in Figure (5-18) with their corresponding $u'^2(\tau)$ plots. Results at position X_1 show the periodic instability that first appears near the end of the acceleration phase and then develops and grows as it passes through the peak phase, reaching maximum amplitude during the peak phase and decays completely by the end of the deceleration phase (this is clear also in Figure 5-17).

If we consider a mass of the fluid in the vicinity of the centerline moving axially, then as it reaches position X_1 a periodic flow instability with axial distribution similar to that shown by the $u'^2(\tau)$ plot. As this mass moves farther downstream, the instability breaks down to turbulence or random velocity fluctuations creating the turbulent moving front previously discussed for the case of 50 percent occlusion.

A sharp increase in the ensemble average velocity is observed during the acceleration at position X_1 and a corresponding spike is seen in the $u'^2(\tau)$ plot. This indicates the passing of a strong vortex. However, this vortex no longer exists as a separate entity at later positions downstream. As previously explained both the vortices and the turbulent front are moving with an average convection velocity corresponding to the local instantaneous one. The observed vortex is leading the turbulent front but moving with a slower velocity of approximately 15 cm/sec, while

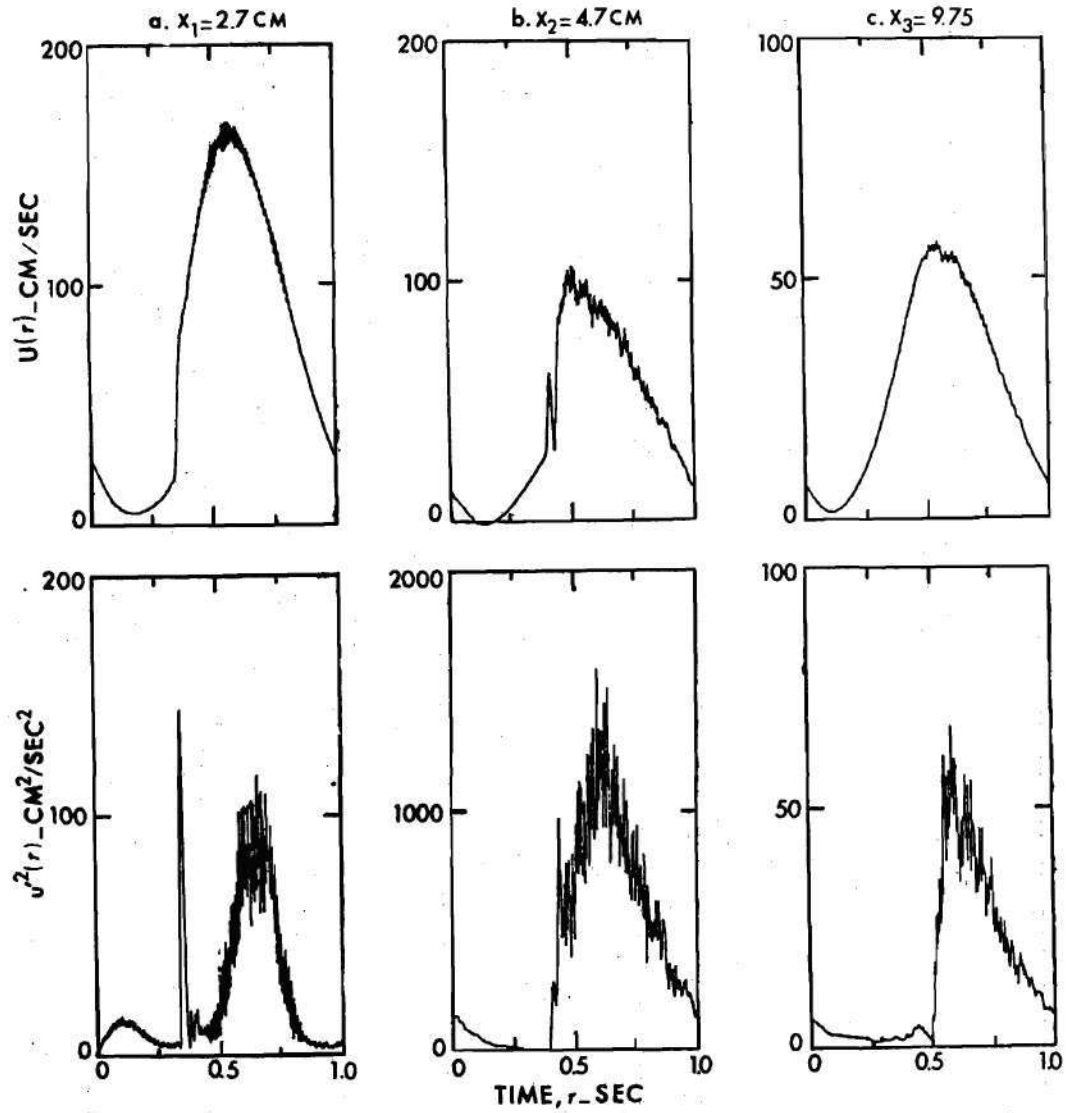

Figure 5-18. Ensemble Average and Disturbance Velocities for the 75 Percent Occlusion

the turbulent front is traveling with average velocity about 150 cm/sec at position X_1. It is then likely that the turbulent front overtakes the vortex before reaching position X_2. For a case like this, the vortex breaks down to very high turbulent fluctuations which are observed in the instantaneous waveform at position X_2. The $u'^2(\tau)$ plot shows that u'_{rms} reaches about 40 cm/sec during the velocity cycle which is comparable to the corresponding ensemble average values. Although the ensemble average has a peak velocity only about 100 cm/sec at position X_2, the instantaneous values are much higher. As with position X_3 in the case of 50 percent occlusion, a split peak is observed in the ensemble average waveform at position X_2 which corresponds to the starting of the turbulent front.

The $u'^2(\tau)$ plot for position X_3 shows that the turbulent front moves with an average velocity of 57 cm/sec between position X_2 and X_3. One might notice that the turbulent front at position X_2 was in the acceleration phase and at position X_3 it starts in the peak phase. For the case of 50 percent occlusion the turbulent front first appears in the peak phase at position X_3. It is noticed also that there is a considerable decay in turbulence at position X_3, because the turbulent production is not balancing dissipation. Measurements at later positions indicate no vortices and complete dissipation of turbulence.

5.3.2 Energy Spectra of Disturbance Velocity

Energy spectra for the four phases at different axial locations are presented in Figures (5-19). The corresponding upstream spectra for each phase is also presented for comparison.

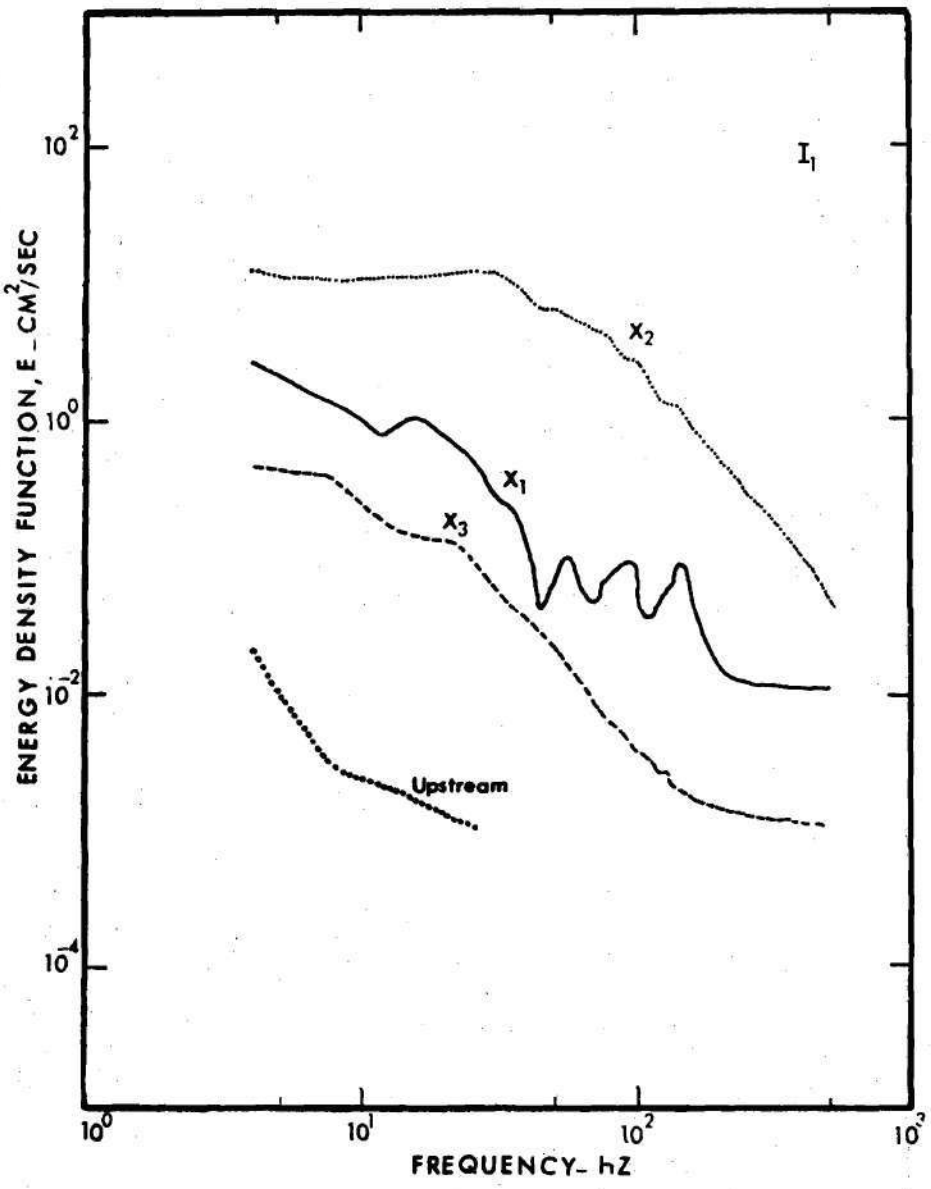

Figure 5-19a. Disturbance Energy Spectra for the Acceleration Phase at Different Axial Positions Distal to 75 Percent Occlusion

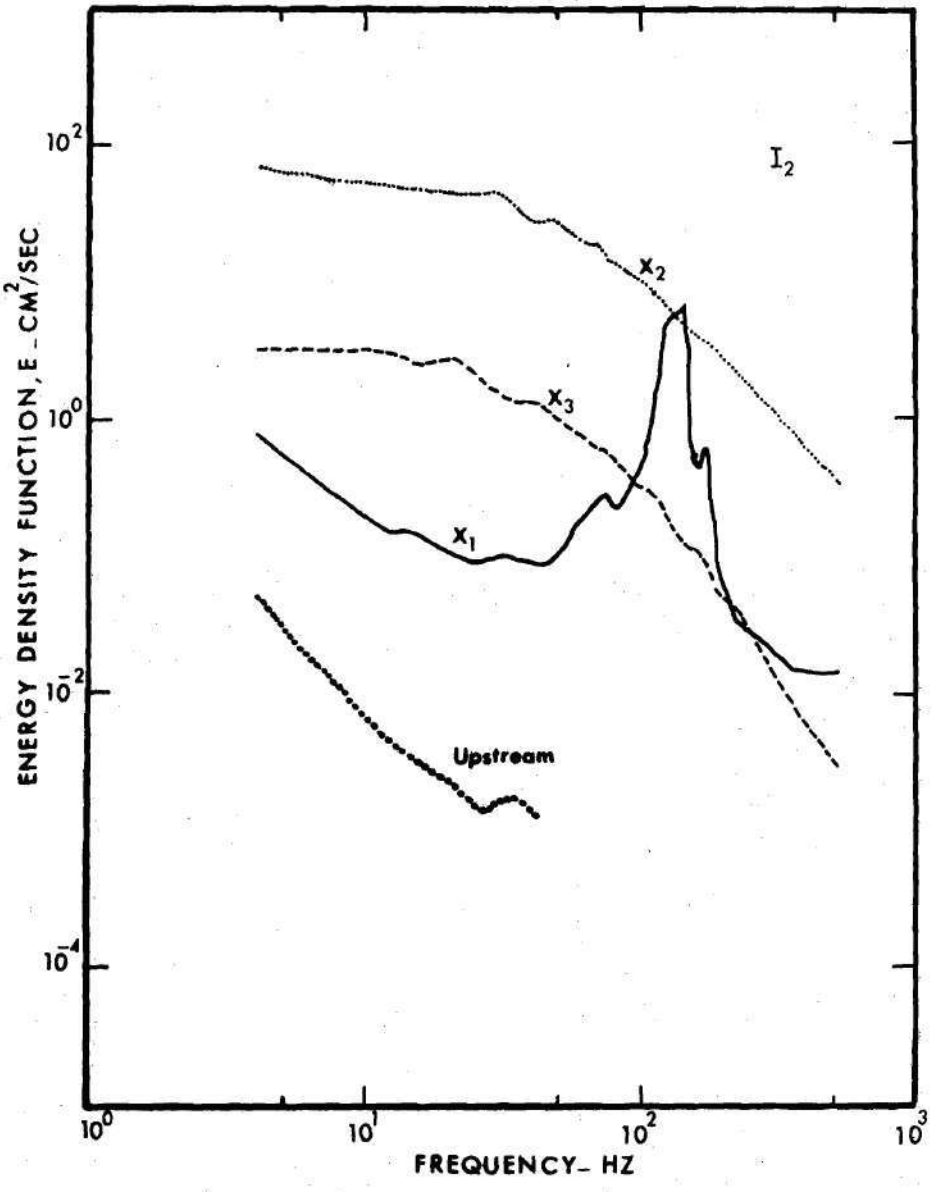

Figure 5-19b. Disturbance Energy Spectra for the Peak Phase at Different Axial Positions Distal to 75 Percent Occlusion

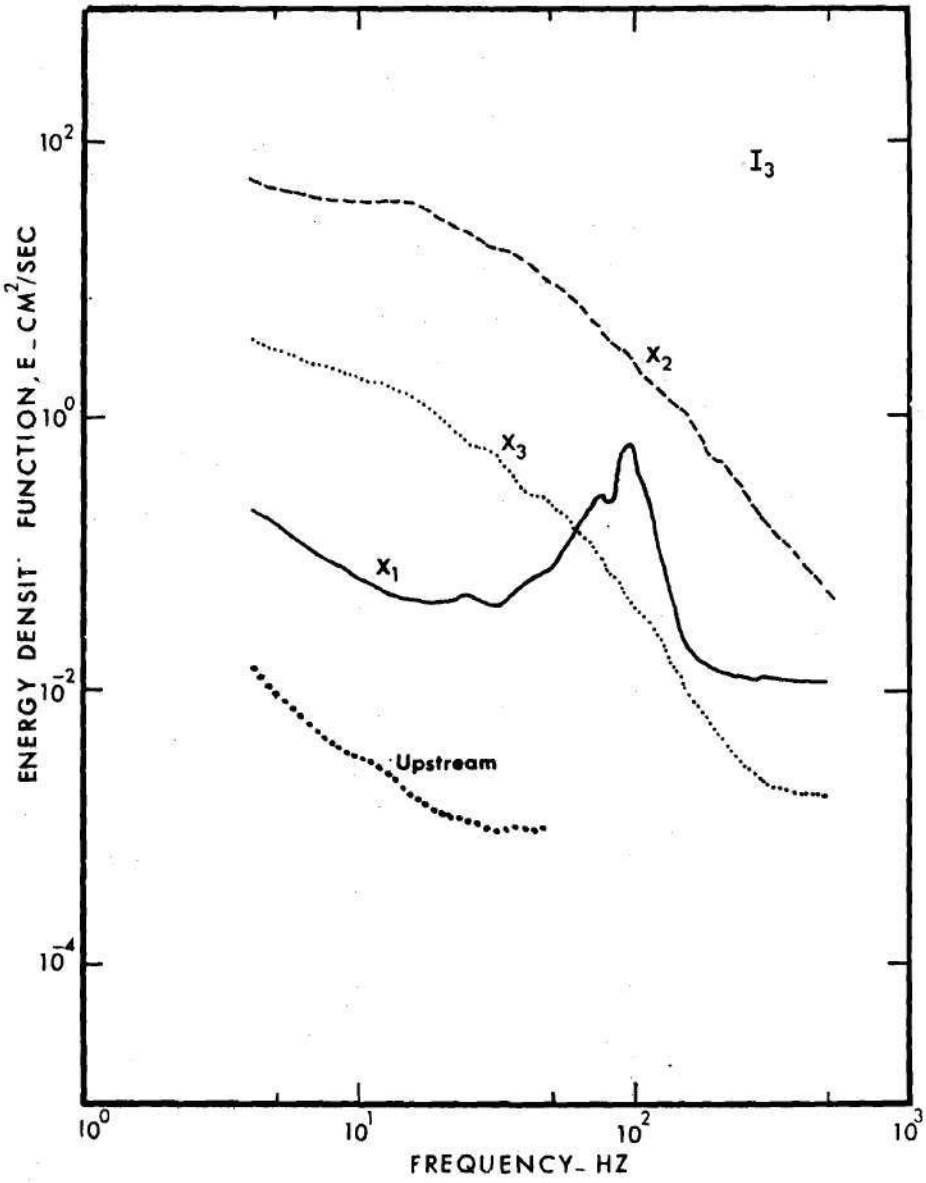

Figure 5-19c. Disturbance Energy Spectra for the Deceleration Phase at Different Axial Positions Distal to 75 Percent Occlusion

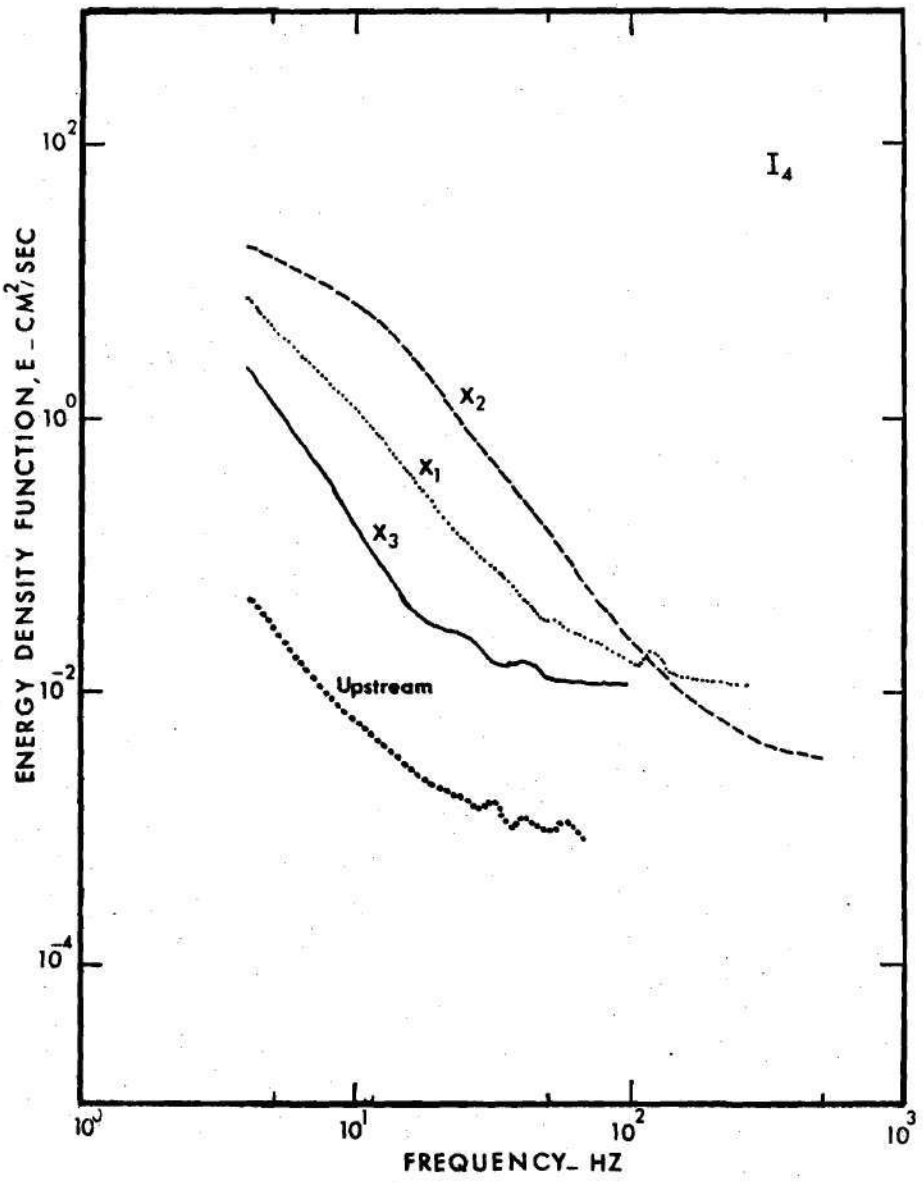

Figure 5-19d. Disturbance Energy Spectra for the Valley Phase at Different Axial Positions Distal to 75 Percent Occlusion

Spectra for the acceleration phase shown in Figure (5-19a) are at least one decade higher than the upstream spectra, which indicates a high level of disturbance energy. The spectrum at position X_1 shows several peaks, the first one is at a frequency of approximately 16 Hz which corresponds to the frequency of the velocity fluctuations due to the passing vortex. The source of other peaks is difficult to specify because they may be due to window effect and/or the part of the periodic instability that starts near the end of the acceleration phase. The spectrum at position X_2 shows the disturbance energy drastically increasing due to the turbulence breakup. Actually, part of the acceleration phase includes these turbulent fluctuations as indicated by Figure (5-18), which shows also that the turbulent front starts in the acceleration phase. Disturbance energy spectra at position X_3 indicates the decay of the disturbance energy in the acceleration phase because the turbulent front is no longer in this phase.

Figure (5-19b) displays the energy spectra at different axial locations for the peak phase. At position X_1 a distinguishable peak at frequency approximately 140 Hz is observed with some spread due to the window effect. This peak is due to the periodic instabilities with a well-defined frequency of 140 Hz. Spectra for positions X_2 and X_3 are characteristic of turbulence. The decay of turbulence is clear at position X_3 but both curves show the same general shape.

At position X_1, the deceleration phase energy spectra shown in

Figure (5-19c) has a peak at a frequency of approximately 90 Hz, which again corresponds to the periodic instability. It is likely then that the instability moving with the flow, which breaks down later to turbulence tends to have axial frequency and amplitude distribution. The leading side of the instability being at high frequency, the core at frequency 140 Hz, and at the tail the frequency is approximately 90 Hz. Again, spectra at positions X_2 and X_3 show the breakdown of these periodic instabilities into turbulence and then gradual decay.

The spectra for the valley phase (I_4) (Figure (5-19d)), which represents the phase of minimum velocity does not show any indication of high frequency components during this period. The level of disturbance energy is maximum at position X_2, while decay for this disturbance is observed at position X_3.

The analysis of the energy spectra was also performed for the total velocity cycle and it is presented in Figure (5-20). It simply summarizes the events at each of the axial locations considered. The two characteristics of the spectra at different phases for position X_1 are shown, namely the periodic fluctuations due to velocity variation at 16 Hz and the periodic instability at 140 Hz. The spectra for positions X_2 and X_3 show turbulent breakup and decay respectively.

As with the 50 percent occlusion analysis, spectral correlations were examined. The data collapses very well for the deceleration phase at the two axial positions X_2 and X_3 as can be seen by Figure (5-21). For the peak phase, there is no good agreement between data at positions X_2 and X_3. However, spectrum for the peak phase at position X_3 agrees

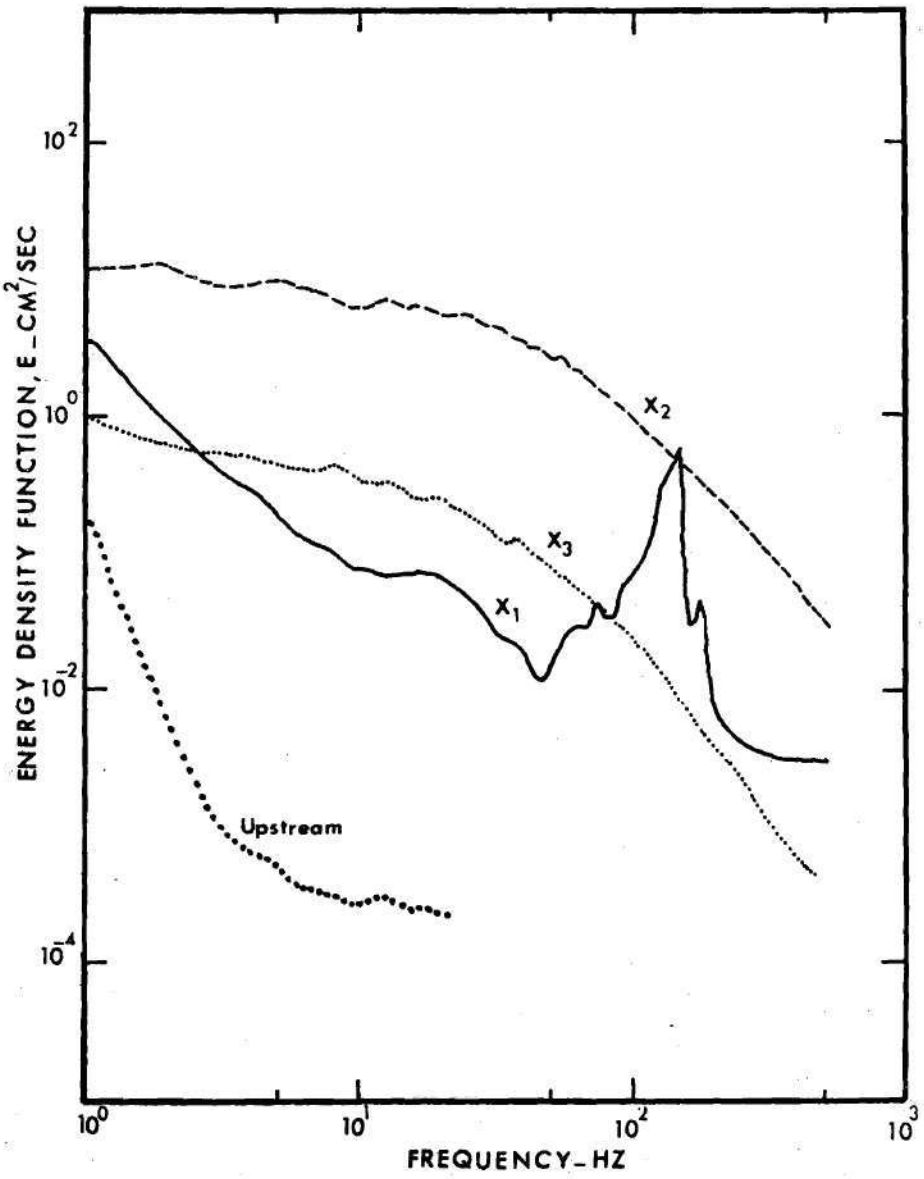

Figure 5-20. Energy Spectra for the Total Velocity Cycle at Different Axial Positions Downstream of the 75 Percent Occlusion

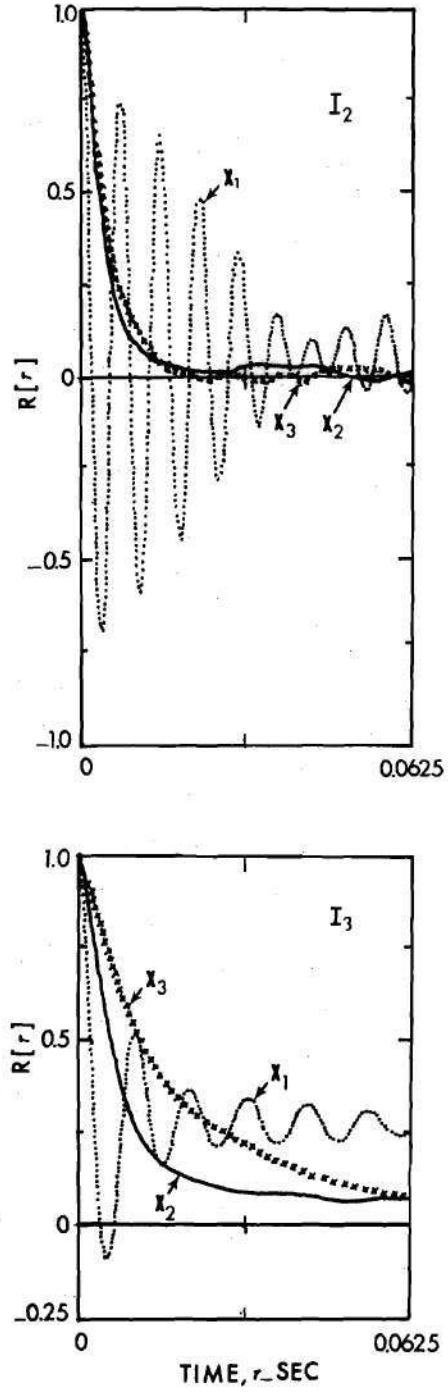

Figure 5-23. Autocorrelation Functions for the Peak and Deceleration Phases with 75 Percent Occlusion

fluid moves further downstream. It was found that each degree of occlusion has its own flow field characteristics. The following is a brief summary of the conclusions for each of the three stenoses.

5.4.1 The 25 Percent Stenosis

The flow field for this mild stenosis is characterized by several vortices being shed during the acceleration phase at the near poststenotic field which then propagate downstream with the local velocity. The number of vortices passing a given station depends upon axial position. After moving a short distance downstream, these vortices begin to interact with each other. This interaction occurs between pairs of vortex rings. Because vortices are shed at different times during the acceleration phase, they move with different velocities. The leading vortex is slower than the trailing one. This brings the two vortices closer together. Each becomes the predominant influence on the motion of the other. Thus, the original vortices lose their identity resulting in one vortex ring. This mechanism is similar to vortex ring formation and interaction in submerged impinging jets (87). As the vortices move downstream they lose their strength and decay by viscous dissipation. The data show no indication of turbulence in the poststenotic flow field distal to this 25 percent occlusion. This is in contrast to the mild stenosis (20 percent area reduction) for the in vivo data presented in Chapter III, where turbulence was observed during the peak and deceleration phases. This might be due to the complex nature of the velocity waveform for the in vivo data. Also, the acceleration phase for in vivo data is 0.05 second compared to 0.25 second for the in vitro one, so that the effective frequency for the

animal studies may be higher.

5.4.2 The 50 Percent Stenosis

The poststenotic flow field for this mild stenosis includes three major classes of disturbances, the shed vortices, the periodic instabilities, and turbulence. The vortices are shed during the acceleration phase at early positions downstream of the stenosis. These vortices are convected with the flow keeping their identity, losing their strength and decaying by viscous dissipation. The mechanism of vortices interacting with each other is also observed to occur at the near poststenotic field. Periodic instabilities are observed to develop during the peak phase and part of the deceleration at positions very close to stenosis exist. These instabilities,which are lead by the shed vortices, are amplified as they move with the flow associating with a mass of the fluid. They have frequency distribution ranging from 33 to 48 Hz. Once breakup has occurred to these instabilities, the turbulent front is formed with a sharp increase in disturbance energy and the convection velocity of this front can be easily followed in the $u'^2(\tau)$ curve.

There appears to be very little far field production of turbulent energy, only dissipation. Hence, turbulence decays as it moves downstream. The phenomena of a turbulent flow region moving with the flow are similar to turbulent "slugs" observed in transitional pipe flow (88). The energy spectra for turbulent regions in the cycle are similar, but a universal correlation is not possible because of the existence of at least three different phenomena which have different spectral characteristics. The in vivo and in vitro studies exhibit some similarities in

behavior and some differences. The split peak previously observed in the ensemble averages of the in vivo data is also observed at some axial locations downstream of the stenosis and corresponds to the beginning of the turbulent front or a passing vortex. Also, similarity in energy spectra between in vivo and in vitro data was clear provided that the most turbulent part of the cycle is examined. On the other hand, the vortex shedding and the turbulent front are not clearly defined in the in vivo data as they are for in vitro studies. This suggests an in vivo set of experiments to be done where several axial locations are considered for each degree of constriction, or an in vitro study at the same "acceleration" rate of the in vivo data.

5.4.3 The 75 Percent Stenosis

The distal flow field for this severe constriction is more violent. Both the vortices and the turbulent front are formed in a similar way to the case of 50 percent occlusion. However, because the turbulent front is moving downstream ten times faster than the leading vortices, it is able to catch up and overtake the vortices breaking them into high amplitude turbulent fluctuations. This region of turbulence is convected downstream led by its turbulent front. As it moves downstream, turbulence decays because production of turbulence is not balancing dissipation and the flow recovers to the upstream condition. Again spectral similarity for turbulent regions in the cycle were obtained and shown to agree very well with the corresponding in vivo results. At position X_2 the ensemble average waveform is similar to the 74 percent occlusion studied in vivo. Both cases show split peaks which are due to the turbulent front.

Care should be considered in trying to generalize the results obtained from this study because:

(1) These results were obtained for a particular upstream waveform, and a different one may lead to different results.

(2) The water glycerol mixture was used as the working fluid. This does not account for the possible effects of cellular elements in blood upon turbulence.

(3) Both the tube and the stenosis were rigid. So the effect of the elasticity of the tube was not studied.

(4) Only the axial velocity component was measured.

The three phenomena observed, namely the vortex shedding, the periodic instability, and the moving turbulent front requires further radial and axial measurements to better define the origin of these flow instabilities and flow visualization would also be helpful.

The implication that measurable disturbance in pulsating flow through modeled stenosis can be detected by analysis methods described here supports the speculation that fluid dynamic studies of flow disorder may be a valuable diagnostic tool to detect vascular disease. Comparison of spectra and ensemble average waveforms obtained proximal to a suspected stenosis site with those obtained distally may lead to the detection of the occlusion.

The results obtained from this study add to the understanding of physiological turbulence, its development and decay. However, further experiments are necessary to extend this work to a full field description and analysis and also by introducing different upstream waveforms and studying the effect of vessel wall extensibility.

CHAPTER VI

THE THEORY OF PULSED DOPPLER ULTRASONIC VELOCIMETER

The application of flow disorder analysis to human biological studies will require a noninvasive measurement technique. The most promising instrument is the pulsed Doppler ultrasonic velocimeter (PD). In this chapter the principle of operation, description, and limitations of the PD system employed in the present study will be explained. A technique to improve the frequency response of this system will also be discussed.

6.1 Principle of Operation

Most ultrasonic flow meters utilize a classic physical phenomenon, the Doppler effect, for their operation. Whenever there is relative motion among a sound source, an observer, and a propagating medium of sound waves, the frequency of the sound waves received by the observer will be different from the source frequency. The difference in frequency is known as the Doppler frequency shift.

If sound scattering particles are present in a moving fluid (in the case of blood, they are erythrocytes) and there are transmitter and a receiver for sound waves, the velocity of the fluid (u) can be detected by measuring the shift in frequency f_d, which is given by

$$f_d = \frac{2uf_o \cos\theta}{C} \qquad (6\text{-}1)$$

where

f_o is the emission frequency of the sound waves

C is the speed of propagation of sound in the medium

θ is the angle between the acoustic beam axis and the velocity vector of the scatterers.

It is assumed that the particle velocity is the same as the fluid velocity. In Appendix B a complete derivation for equation (6-1) is given, together with an estimate of the error involved in having it in this linear form.

Consider the velocity vector $\vec{V}(t)$ in the flow field shown in Figure (6-1), with axial and radial components u(t) and v(t), respectively. These two components can be written, using Reynolds decomposition as

$$u(t) = U + u'(t) \; ; \qquad (6\text{-}2)$$

$$v(t) = V + v'(t)$$

where the primes represent disturbance velocities and U and V are the time average velocities.

If the ultrasonic beam makes an angle θ with respect to the vessel axis, then the components of velocity in the direction of the beam axis and perpendicular to it are denoted by u^* and v^*. A similar decomposition gives

$$u^*(t) = U^* + u^{*\prime}(t) \; , \qquad (6\text{-}3)$$

$$v^*(t) = V^* + v^{*\prime}(t)$$

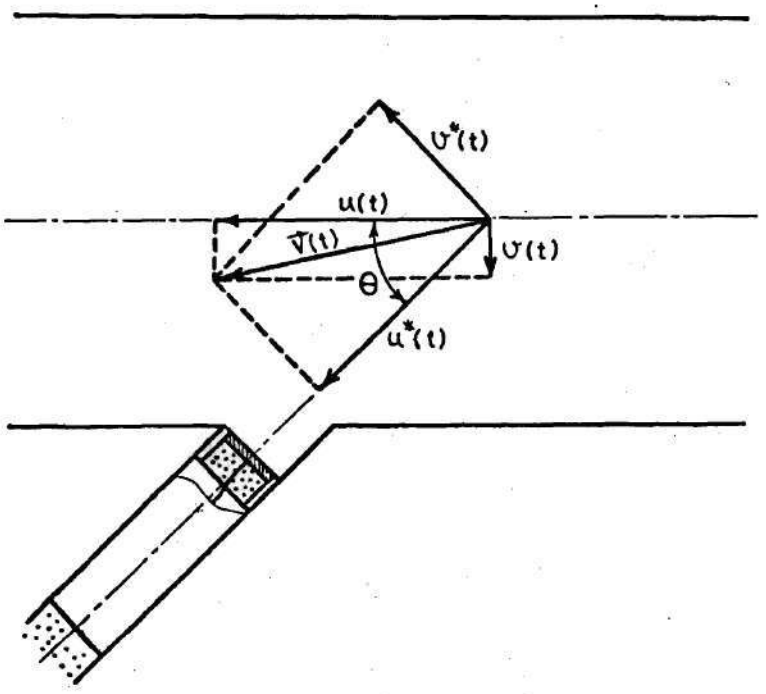

Figure 6-1. Sketch of Instantaneous Velocity Vectors and Components

These components are related to the axial and radial components by the equations

$$u^* = U\cos\theta + u'(t)\cos\theta + V\sin\theta + v'(t)\sin\theta \,, \tag{6-4}$$

$$v^* = V\cos\theta + v'(t)\cos\theta + U\sin\theta + u'(t)\sin\theta$$

Combining equations (6-3) and (6-4), and taking the time average of all quantities,

$$U^* = U\cos\theta + V\sin\theta \tag{6-5}$$

$$V^* = U\sin\theta + V\cos\theta$$

By substitution from equation (6-4)

$$u^{*\prime}(t) = u'(t)\cos\theta + v'(t)\sin\theta \,, \tag{6-6}$$

$$v^{*\prime}(t) = u'(t)\sin\theta + v'(t)\cos\theta$$

By squaring and taking the time average of all quantities

$$\overline{u^{*\prime 2}} = \overline{u'^2}\cos^2\theta + \overline{u'v'}\cos 2\theta + \overline{v'^2}\sin^2\theta \,, \tag{6-7}$$

$$\overline{v^{*\prime 2}} = \overline{u'^2}\sin^2\theta + \overline{u'v'}\cos 2\theta + \overline{v'^2}\cos^2\theta$$

If measurements are to be taken at the centerline of a fully developed pipe flow, there are three simplifications which can be made in these equations.

The assumption of equipartition of turbulence energy among fluctuation components at the center of the flow can be employed. This assumes local isotropy of the turbulence at the centerline for pipe flow, which was shown experimentally by Laufer (89). For this case

$$\overline{u'^2} = \overline{v'^2}$$

2. The mean radial velocity component is zero

$$V = 0$$

3. At the centerline of the tube, the Reynolds stress is zero because of the condition of symmetry, so that

$$\overline{u'v'} = 0$$

By substitution into equation (6-7)

$$\overline{u^{*'2}} = \overline{u'^2} \qquad (6\text{-}8)$$

$$\overline{v^{*'2}} = \overline{v'^2}$$

Ideally, the PD system measures only the component u^*, although the v^*

component may have a small effect due to the finite size of the sample volume which contributes to "geometric broadening" (72). If the above mentioned simplifications are not fulfilled, then equation (6-8) is no longer applicable and equation (6-7) should be used. If either of $\overline{u'^2}$ or $\overline{v'^2}$ are not known, at least the ratio between them should be known, in addition to Reynolds stress. By examining equation (6-7) one can notice that for the cases of flow through tubes where the radial velocity components are not zero (such as the near field distal to a stenosis), using equation (6-8) as a measure of $\overline{u'^2}$ from the PD results for $\overline{u^{*,2}}$ will yield values which are too large, since $\overline{u^{*,2}} \geq \overline{u'^2}$.

6.2 General Description

The basic function of all PD devices is to emit an ultrasonic pulse at a pre-selected interval, receive the backscattered signal and obtain the frequency shift by comparing it with a delayed version of the transmitted pulse. This frequency shift or Doppler frequency should then be processed in a suitable frequency-to-voltage converter to secure an analog output proportional to the velocity measured. Accordingly, the PD device can be divided into three parts. The first is the control circuitry which is responsible for activating the piezo-electric crystal to transmit the ultrasonic pulses and to receive the response of this crystal to the backscattered waves. The output of this circuit is the Doppler frequency which is sometimes called the audio signal since, for the velocities measured in arteries, the corresponding Doppler frequency is in the audible range. The second is the PD probe that supports the piezo electric crystal and is responsible for sending and receiving the

ultrasonic waves. The third part is the audio signal processor which gives an analog output proportional to the velocity. This is often termed the frequency-to-voltage conversion

6.2.1 Block Diagram of the PD Circuits

The PD system employed in this research is a phase-coherent pulsed Doppler type which was designed by F.D. McLeod (57).

The essential requirement of a phase coherent system is that each burst of ultrasound transmitted be derived from a master oscillator so that the basic rate and the related harmonics have a fixed phase relationship. If this is not done, mixing and beating will occur among the pulse repetition rate harmonics and the Doppler audio signal.

The PD system has timing and gating circuits to allow for the measurement of the velocity in a selected range interval along the transmitted beam axis. A short burst of ultrasound is emitted from a piezoelectric transducer into the fluid. Sound reflected from scatterers in the fluid returns to the transducer with a time delay proportional to the range. This range delay time represents the total propagation time

$$\tau = \frac{2R}{C} \qquad (6\text{-}9)$$

where

R is the range distance from the transducer and

C is the velocity of sound in the medium.

The echo from a desired observation range is selected by range-gating the return signal. This is accomplished by having a timing circuit

open the sample gate for a short interval after the selected range delay. By varying range delay and gate period one can select both depth and range of observation.

Resolution or the ability to separate adjacent targets is determined by the duration of the emitted signal, the transducer characteristics, and the gating interval time.

The block diagram of the basic circuit, Figure (6-2), shows a master oscillator which is the heart of the entire system and is the driver of all frequencies in the system. Primarily, it generates the transmission frequency (f_o) and drives the range and gating circuit. This latter circuit produces a square wave with frequency equal to the pulse repetition frequency (f_p). This wave is mixed with the transmission frequency (f_o) to produce a train of emission pulses, each with a certain number of cycles at the emission frequency (f_o). The number of cycles depends upon the controlled duration of the square pulse.

The range and gating circuit is also responsible for generating another square pulse delayed by a variable delay time (τ) which determines the range as previously explained. Again this square pulse is generated at frequency (f_p) and is mixed with the back scattered signal which first passes through an amplifier of variable gain. The output from this mixer will be a train of back scattered signals at frequency (f'), the duration of which depends on the duration time of each square pulse coming from the range gating circuit. This time is known as the listening time and it determines the depth of the sample volume. Thus, the signal coming from mixer (I) should theoretically have frequency ($f' + f_p$), considering

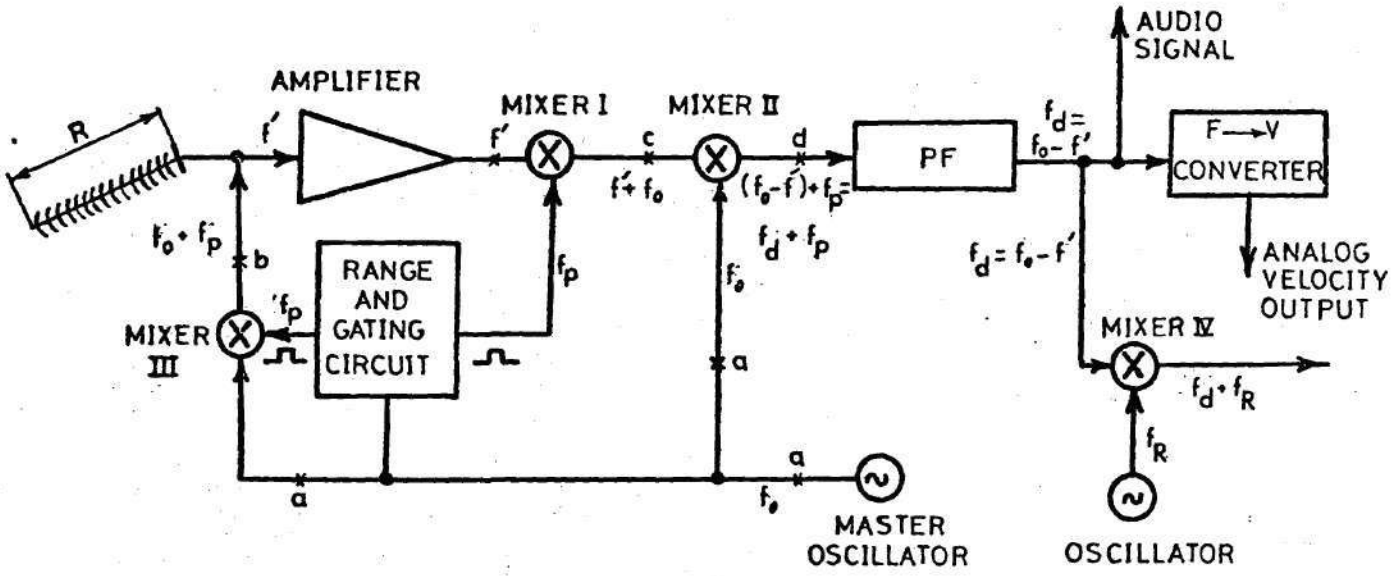

Figure 6-2. Basic Pulsed Doppler Velocimeter Block Diagram

that the emitted signal is only Doppler shifted by a single velocity. This signal then passes through a broadband mixer (II) where it is demodulated by mixing it with the transmission frequency (f_o). This signal is low pass filtered to remove the sum of the input frequency and thus the output from this mixer is a signal that has a frequency equal to the Doppler frequency (f_d) plus the pulse repetition frequency (f_p). The low pass filter is also set to remove the components of the pulse repetition frequency, converting the broadband mixer output to a Doppler-shifted signal in the audible frequency range. This audio signal may then pass to the next step which is frequency-to-voltage conversion to obtain an analog output proportional to the "velocity" of the flow measured. The audio signal may also be mixed with a reference frequency generated by a separate oscillator to have a constant frequency offset (f_R). This will be used later to improve the method of processing of the audio signal. Figure (6-3) shows the output signals at different stages in the circuit.

Principal Data of PD Used

Transmission frequency, f_o = 7.7 MHz

Pulse duration = 4, 8, and 16 cycles of the above frequency

Pulse repetition frequency = f_o/160, 320, and 640

= 48.125, 24.0625, 12.031 kHz

Listening gate time = 0.5 - 3 μsec

Delay time = 0-10 μsec

$f_P = \frac{1}{T_P}$ ..... PULSE REPITITION FREQUENCY

T_S ..... EMISSION OR SENDING TIME

T_L ..... LISTENING OR GATE TIME

τ ..... TIME DELAY, TIME BETWEEN SENDING AND LISTENING

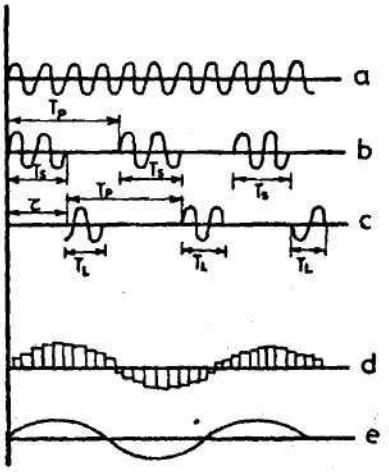

a ..... MASTER OSCILLATOR

b ..... TRANSMITTED BURSTS

c ..... RANGE GATED RECIEVED ECHOES

d ..... OUTPUT OF MIXER II OVER MANY PULSE REPITION FREQUENCY

e ..... THE AUDIO SIGNAL OUTPUT FROM THE LOW PASS FILTER

Figure 6-3. Output Signal at Different Stages in the PD Circuit

6.2.2 Operation of PD

6.2.2.1 Controls. Pulse Repetition Frequency (PRF)--the PRF control allows selection of the pulse repetition frequency. There are three pulse repetition frequencies available: 12, 24, and 48 KHz.

Pulse Cycles--the pulse cycles control selects an emission pulse duration of 4, 8, or 16 cycles of emission frequency f_o.

Delay--the time delay between the emission pulse and the start of the observation period is selected with the time delay potentiometer.

Gate--the gate control potentiometer adjusts the total time during which the sample gate is opened.

Transducer Gain--a gain control is provided to adjust the amplification of the transducer signal. The gain used for a given return signal is found by turning the gain off and then slowly increasing it until no further changes in the wave form output are observed. It should be mentioned that increasing the gain increases both the signal and the noise.

Range Gain (Slope)--the instrument is equipped with a varying range gain to compensate for signal attenuation and spherical scattering of the reflected signal. In principle, the control "equalizes" the signal level when the sample gate is at the near wall or far wall.

6.2.2.2 Calibration. Consider the Doppler equation (6-1). It can be rewritten as:

$$f_d = k_1 u \tag{6-10}$$

where

$$k_1 = \frac{2f_o \cos\theta}{c} \quad .$$

If we let the frequency to voltage conversion factor at the instrument be k_2, then the output voltage from the frequency to voltage converter (V_o) is

$$V_o = k_2 f_d . \tag{6-11}$$

Combining the two equations

$$u = K V_o$$

where

$$K = \frac{1}{k_1 k_2} = \frac{1}{k_2}\left(\frac{c}{2f_o \cos\theta}\right) \tag{6-12}$$

for the PD system used in this research

$$f_o = 7.68 \text{ MHz}$$

$$\theta = 45^o$$

and the speed of sound in water is taken to be C = 1500 m/sec. By substitution into equation (6-12)

$$K = \frac{0.01381}{k_2} \text{ (cm/sec)/Volts}$$

where

k_2 is given in Hz/Volt.

6.2.3 Probe

Figure (6-4) shows the PD probe used in these experiments, which was constructed in the Biomechanics laboratory. This probe consists of:

1. A single transducer acting both as transmitter and receiver. The lead zirconate crystal is 1/16" (1.6 mm) diameter and 0.0157" (0.4 mm) thickness.

2. A plexiglass acoustic insulator to decouple the crystal from the probe casing. It also acts as an electric insulator.

3. Backing block on the rear side of the crystal.

This part of the probe is chiefly responsible for the bandwidth and sensitivity of the transducer. For this case the material used is Devecon F.

4. A brass metal case.

5. A co-axial cable of minimum required length.

6. The RTV filling material.

6.2.4 Processing of the Doppler Signal

Ideally, for laminal flow spectrum the Doppler signal should be an impulse function at frequency f^*, the Doppler frequency defined by equation (6-1). However, because both the sample time and piezo-electric crystal size are finite, the velocity is not measured at a point but rather averaged in some sense over a sample volume, during a finite sampling time. Thus, depending upon the characteristics of the moving stream and the geometry of the sample volume, there may be velocity

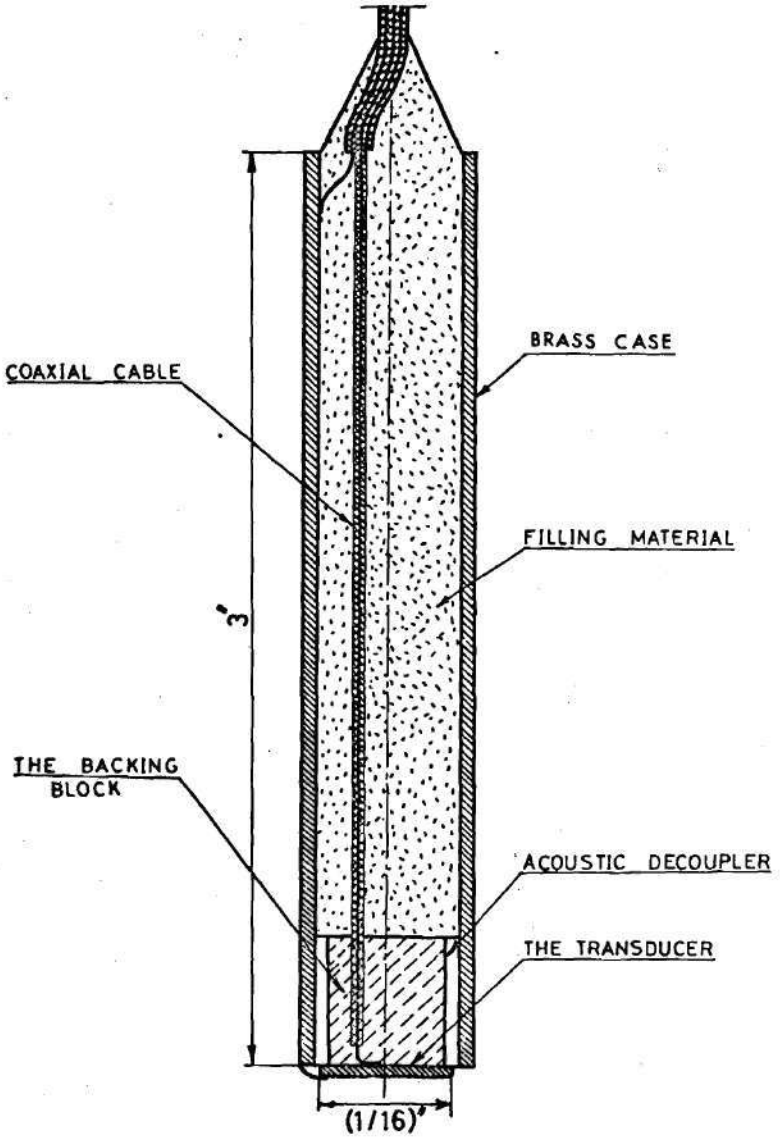

Figure 6-4. PD Probe

present in the region of Doppler sensitivity. Furthermore, the intensity of the back scattered signal depends on the number and velocity of different scattering particles passing through the sample volume. As a result of these phenomena and also the electronic noise in the circuit, the spectrum of the output Doppler audio signal is spread over a range of frequencies. Figure (6-5) illustrates the spectral broadening in the actual audio signal.

The fluid dynamicist would like to relate information contained within the Doppler signal directly to a knowledge of flow velocity within the sample volume. For most pulsed and continuous wave devices available today this is done by means of a zero crossing detector. Rice (90,91) has shown that these detectors measure the rms value of the frequency spectrum rather than the mean value. For small spectral bandwidth these two quantities are close in value but as the bandwidth increases, differences can become quite large. Another method of frequency-to-voltage conversion is the phase-lock loop as discussed in Appendix B.

The DISA tracker employed with the laser Doppler anemometer utilizes a phase-lock loop system and has proven to be very reliable in the turbulence measurements. Although this processor was engineered for laser use, the Doppler principle is the same regardless of the wave source. It is necessary to pre-condition the audio signal, however, before introducing it to the tracker since the frequency ranges for operation were designed around requirements for Doppler-shifted light frequencies rather than Doppler-shifted ultrasound frequencies.

It must be pointed out that prior to this study there exist no

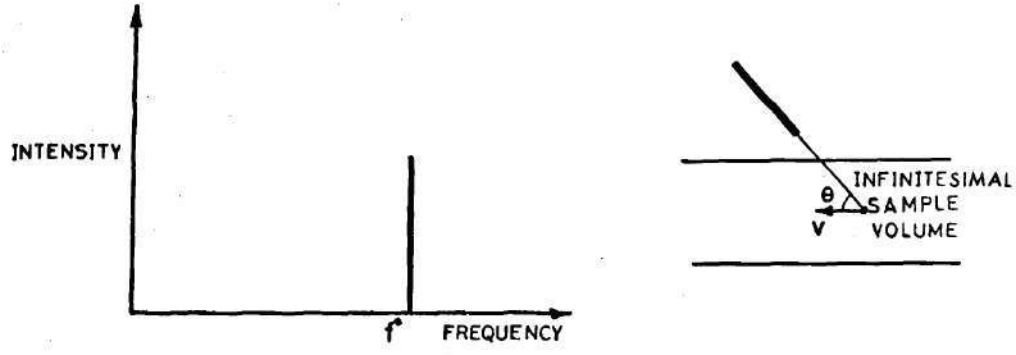

a-IDEAL AUDIO SIGNAL SPECTRUM

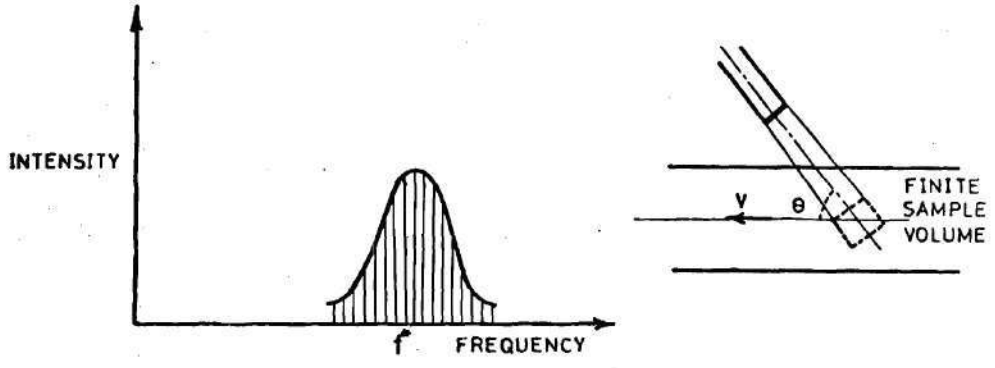

b-REAL AUDIO SIGNAL SPECTRUM

Figure 6-5. Audio Signal Spectrum

reliable turbulence measurements using ultrasound. Therefore, the objective of this phase of the research was to determine whether an existing advanced phase-lock loop processor could be used to improve the measurement of turbulence in a flow system which simulates conditions in a major artery.

Since a feasibility study was the goal, modification of electronic circuits was beyond the scope of this research.

6.3 Sample Volume

In actual measurements using the PD system, the velocity is measured over a finite volume (sample volume). This is analogous to the averaging effect observed when using a pitot tube or hot film anemometer. The size and shape of this sample volume becomes important in relation to the accuracy with which local flow velocity at a point can be measured, for the spectral content of the back scattered signal is greatly affected by the sample volume geometry and dimensions. Basically, there are five reasons that cause the sample volume to be finite and affect its shape:

1. The acoustic beam diverges,
2. The sampling time is finite,
3. Crystal size is finite,
4. The emission time for the ultrasonic waves is finite, and
5. The piezo crystal has certain acoustic characteristics.

Due to the complications involved in dealing with all the factors at one time to estimate the sample volume size, the first three factors will be considered first, then the remaining factors will be discussed.

Figure (6-6) shows the sample volume of PD probe due to finite

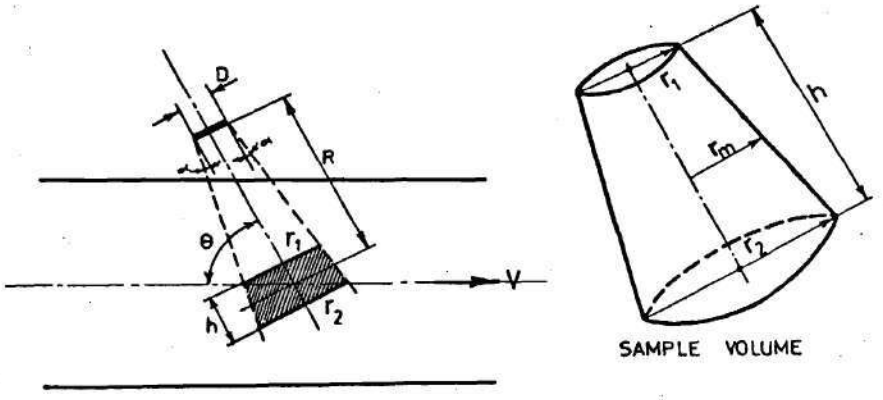

Figure 6-6. Sample Volume Dimensions

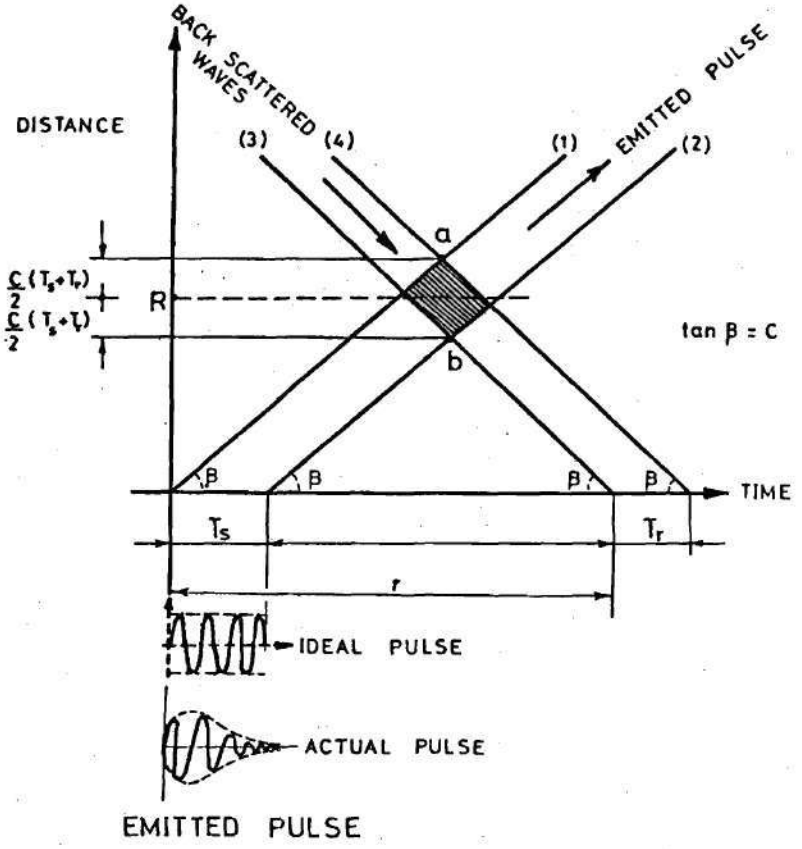

Figure 6-7. Distance Time Curves for the Traveling and Back Scattered Pulses

piezo crystal size, finite sampling time, and acoustic beam spread. The sample volume is shown centered about the tube center line. The acoustic beam dimensions are governed largely by the geometry of the transducer compared to the wavelength of the acoustic radiation. A disc-shaped piezo-electric element can be modeled as a piston radiator, and for this case the radiation pattern has a directional character only when the wavelength λ is much shorter than the piston diameter, D. Then, the beam divergence angle α is roughly equal to $\lambda/2D$ (93). Thus, if smaller transducers are used to decrease beam width, a proportional decrease in radiation wavelength must be kept to maintain directionality. Hence

$$\alpha \cong \tan\alpha \cong \frac{\lambda}{2D} \qquad (6\text{-}13)$$

where

$$\lambda = \frac{C}{f_o}$$

Due to the divergence angle of the acoustic beam the sample volume has the shape of truncated cone with dimensions:

vertical height = h

radius at the top = $r_1 = \frac{D}{2} + (R - \frac{h}{2}) \frac{\lambda}{2D}$

radius at the bottom = $r_2 = \frac{D}{2} + (R + \frac{h}{2}) \frac{\lambda}{2D}$

where

C is the speed of sound

R is the distance from the crystal to the center of the sample volume.

With these, the sample volume can be calculated

$$\text{Sample volume} = \left(\frac{r_1 + r_2}{2}\right)^2 \cdot h \qquad (6\text{-}14)$$

$$= \left(\frac{D}{2} + \frac{R\lambda}{2D}\right)^2 \cdot h$$

with a finite sampling time (T_s), the sample volume height corresponding to an instantaneous listening time (h) can be calculated from the simple relation

$$h = T_S \cdot C \ . \qquad (6\text{-}15)$$

However, a correction is necessary when considering the effect of finite listening time and the piezo crystal characteristics.

Figure (6-7) shows the distance-time curves for the traveling pulses, where (T_s) is the emission time (which equals to the number of emitted cycles multiplied by the emission frequency f_o). Because the pulses are traveling with the speed of sound, lines (1) and (2) represent the envelope of straight lines that give the distance-time relation for the pulse emitted and all these lines have slope equal to the speed of sound (C). While this pulse is traveling, part of its energy is reflected and the back scattered waves that move back towards the crystal follow, on this diagram, lines perpendicular to the two lines (1) and (2). If the gate is opened for listening after delay time (τ), for a period of time (T_r), lines (3) and (4) will represent the envelope of the straight lines representing time-distance relation for the back scattered waves.

It is seen that the total sample volume height is

$$h = (T_s + T_r) \tag{6-16}$$

If the distance (R) is to be measured from the center of the sample volume to the crystal, then the delay time (τ) should be

$$\tau = \frac{T_s - T_r}{2} + \frac{2R}{C} \tag{6-17}$$

It was implicitly assumed that the transmitted pulse is ideal and has uniform geometry and shape, but due to the inertia of the transmitting crystal, the pulse has a tear drop-like shape. Figure (6-8) shows the effect of the piezo crystal characteristics on the transmitted pulse (74). The initial rise corresponds to the transient response of the crystal due to the electric excitation applied to it, and the tapered "tail" is due to the ringing effect when the drystal dissipates stored energy exponentially in free response.

The result of this is distortion in the geometry and intensity distribution within the pulse. The transducer ringing also increases the actual time of the pulse and thus may increase the geometric sample volume.

Intensive analysis and experiments are required to estimate the effect of the piezo crystal response on the sample volume size and velocity measurements. These studies are beyond the scope of the present research.

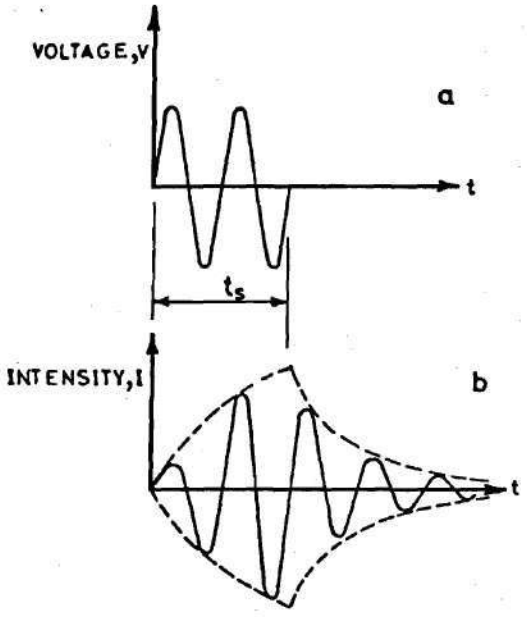

PIEZOCRYSTAL TRANSDUCER RESPONSE
a___DRIVING BURST
b___ACOUSTIC BURST

SCHEMATIC DESCRIPTION OF BEAM AND PULSE GEOMETRY

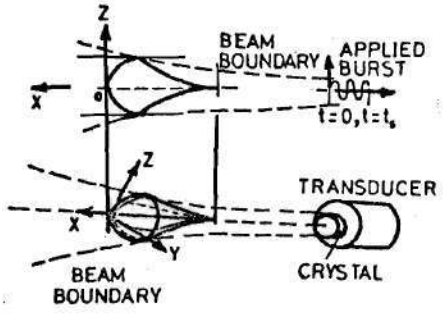

JUXTAPOSITION OF TRANSDUCER AND FLOW SECTION WITH TRANSMITTED PULSE COORDINATE DIRECTIONS SHOWN

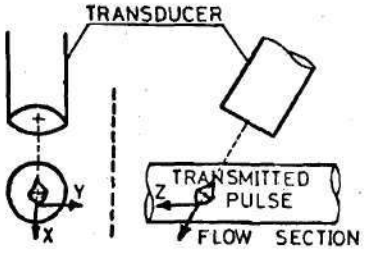

Figure 6-8. The Effect of Piezo Crystal Characteristics on the Transmitted Pulse

6.4 Range-Velocity Limitation

To properly determine the actual Doppler shift frequency (f_d), the measurements must be repeated at a rate (sampling frequency) at least twice that of the maximum frequency shift expected. This requirement comes about in accordance with Shannon's sampling theorem and consequently fixes the minimum transmitting pulse repetition rate, f_p

$$f_p \geq 2\Delta F_{max} = \frac{4f_o V_{max} \cos\theta}{C} \quad . \tag{6-18}$$

Range determination is the other constraint of the pulse repetition frequency. If a maximum acoustic beam range, R_{max} is assumed, then the maximum delay time equals to $2R_{max}/C$ according to equation (6-9). If all significant returns are to be recieved prior to the transmission of a new pulse, the maximum pulse repetition frequency in the absence of the secondary reflections is

$$f_p \leq \frac{c}{2R_{max}} \quad . \tag{6-19}$$

Combining the above two equations (6-18) and (6-19) yields the "range-velocity" constraint,

$$V_{max} R_{max} \leq \frac{C^2}{8f_o \cos\theta} \quad . \tag{6-20}$$

Thus, with a given pulsed ultrasound device, there is only one V_{max} and R_{max} for each pulse repetition frequency. For the PD device

used in the present research the following table gives the values of V_{max} and R_{max} for the pulse repetition frequencies available.

PRF, KHz	R_{max}, cm/sec	V_{max}, cm/sec
12.0313	6.2338	58.59
24.0626	3.1168	117.19
48.1252	1.5584	234.38

6.5 A Modified Technique to Use the DISA Phase Lock Loop for Processing of the PD Audio Signal

A DISA phase-lock loop (PLL) frequency tracker, designed for use with the DISA Mark II Laser Doppler Velocimeter system, has been used in previous LDV flow studies. It has tracking ranges of 15, 50, 150, and 500 KHz and 1.5 and 5 MHz. The frequency range of the typical Doppler ultrasound signals under conditions similar to arterial flow velocities is about -3 to +12 KHz for the aorta and approximately 0-7 KHz for the carotid artery. If the signal is properly preconditioned, it is possible to track the demodulated ultrasound signal with the DISA PLL. The preconditioning required is (1) attenuation, (2) mixing the Doppler signal with a frequency offset signal to shift the result into an appropriate tracking range, and (3) proper balancing of the offset signal amplitude with the amplitude of frequency modulated Doppler signal.

The existing PD system has a constant offset frequency of 6.9 KHz which allows tracking in the first two ranges of the PLL (15 and 50 KHz ranges). The problem with using the frequency offset (f_R) is that the audio signal is not only frequency modulated, it is also amplitude modulated. Thus, if the audio signal decreases sufficiently in amplitude, the tracker may lock on the frequency offset signal and ignore the audio frequency. The solution suggested for this problem is to use the characteristics of the high pass filter to attenuate the frequency offset signal to the degree that the tracker lock on the composite signal, in other words keep proper balancing of the offset signal amplitude with that of the audio. Figure (6-9) shows the basic filter characteristics. If the cut off frequency of the filter (f_c), the amplitude attenuation is gradual. By proper choice of (f_c) the frequency shifted audio signal ($f_R + f_d$) can be high passed in such a way that (f_R) signal is attenuated sufficiently to allow the tracker to follow ($f_R + f_d$) signal even with amplitude modulation of the audio signal. Figure (6-10) shows a sketch for the arrangement used in preconditioning of the audio signal before using the DISA tracker.

One of the problems in phase-lock loop is to maintain "lock" or, in other words, to minimize "drop-out" of the output signal. If the frequency of the input FM signal changes so abruptly as to exceed the stability range for lock, there is a loss of meaningful output signal. The DISA PLL has several bandwidth ranges which trade off stability range for frequency resolution, and it also has a dropout rate, measured as a percentage time of operation out of lock. For reliable turbulence

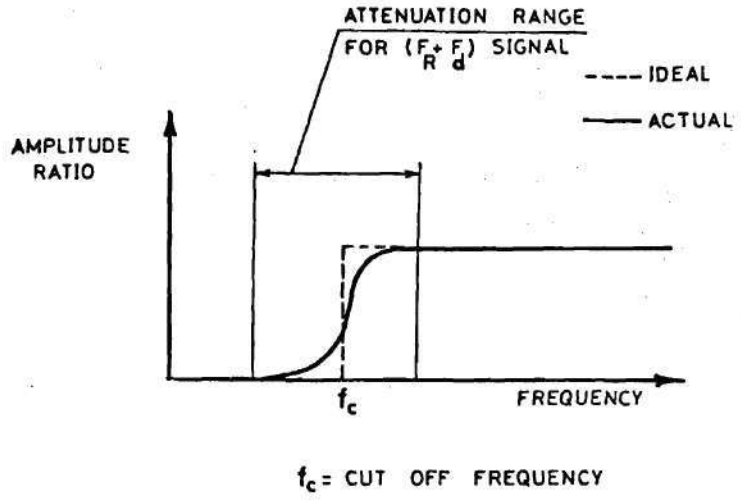

Figure 6-9. Basic High Pass Filter Characteristics

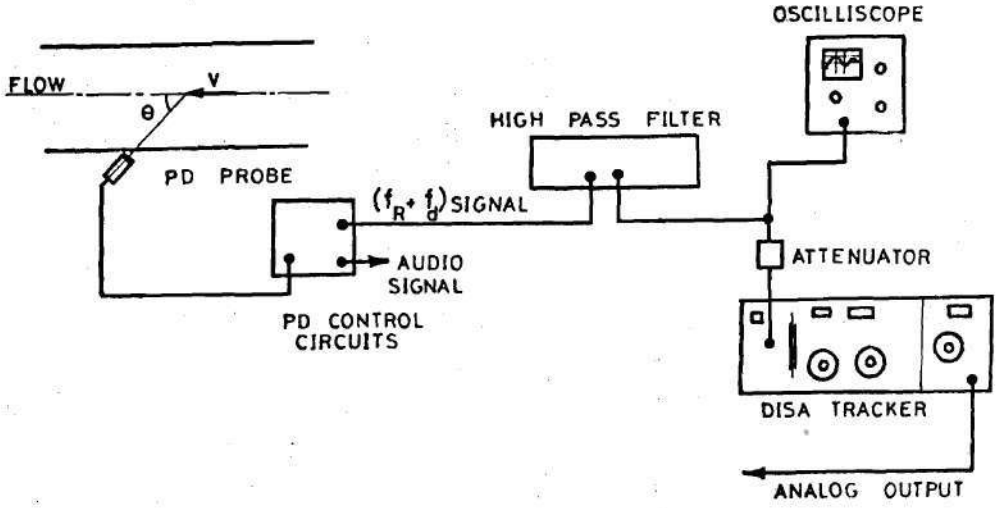

Figure 6-10. Experimental Arrangement to Process the Audio Signal

measurements experience has shown that dropout rates on the order of five percent or less are required.

CHAPTER VII

COMPARISON BETWEEN LASER DOPPLER VELOCIMETER AND PULSED DOPPLER ULTRASONIC VELOCIMETER

A direct comparison between the pulsed Doppler Ultrasonic Velocimeter (PD) and the Laser Doppler Velocimeter (LDV) was conducted in a water flow system for two flow configurations. In one case the centerline velocity was measured by both instruments in a fully developed pipe flow with no constriction. In the other, centerline velocity measurements were made at a fixed position downstream of a stenosis model with 50 percent area reduction.

These experiments serve as a basis for determining the capability and limitations of the present PD system and suggest areas in which further development is required.

7.1 Flow System and Instrumentation

The flow system employed for these experiments is the same one used for the in vitro experiments explained in Chapter V. Both steady and pulsating flows were obtained as previously explained. The working fluid used was water with silicon carbide particles as scatterer.

Several instruments were used for these experiments, primarily:

1. A DISA type 55L-Mark II Laser Doppler Velocimeter (LDV).
2. F.D. Mcleod Pulsed Doppler Ultrasonic Velocimeter (PD).
3. High and low pass filters type Krohn-Hite model 13343.

4. Triggering oscilloscope.

5. Strip chart HP Model 7702B with two channels and HP Model 8802A preamplifiers.

6. HP Model 5451B Fourier Analyzer system.

7. Digital Voltmeter Fluke Model 8000A.

A description of the instrumentation and brief account of the principles of operation have been given in previous chapters.

7.2 Preliminary Studies

The reliability of the procedure and instruments was checked by several experiments. Experience was gained with the LDV by changing frequency range, bandwidth, seeding level, photomultiplier location, and focusing. A slight seeding using silicon carbide particles of 1.5 μm average diameter (specified by manufacturer) was adequate.

A series of preliminary experiments was conducted to compare the LDV and the hot film anemometer in steady and pulsating flow measurements. This was explained earlier in Chapter IV. The LDV proved to be an accurate instrument to measure the velocity with reasonable frequency response.

Experience was also needed with the PD, the high pass filter, and the DISA tracker. Various values of Pulse Repetition Frequency (PRF), gate time (listening time), gain, slope, and the number of emitted pulses were tried. The PRF of 50 KHz showed to be the best for these experiments. An increase in gate time increased the power of the returning signal, but increases also the sample volume depth. So, one micro-second was a good compromise. Gain and slope were set to constant relative

values of 4.0 and 4.0, respectively. These values were chosen such that the zero crossing detector gave no output with the probe unplugged.

To precondition the $(f_R + f_d)$ signal the high pass filter was set at a frequency slightly higher than the reference frequency (f_R = 6.9 kHz). Using an oscilloscope to monitor the $(f_R + f_d)$ signal after being high pass filtered, the preferable range for the cut-off frequency of the high pass filter was obtained. Below this range the tracker locked only on (f_R) signal (the reference frequency signal), while higher values for the cut-off frequency attenuated the $(f_R + f_d)$ signal so much that the tracker lost tracking completely. These cases were observed clearly on the scope.

It was found that the 1.5 μm seeding particles did not provide satisfactory scattering for the ultrasonic pulses. These particles resulted in low signal to noise ratio and the audio signal was too weak to be used. However, with 11 μm silicon carbide particles the audio signal was strong enough and high signal to noise ratio was obtained.

Experience showed also that for most experiments performed the tracker frequency range of 50 KHz was the best and the appropriate bandwidth setting depended primarily on the turbulence level of the flow. Higher turbulent fluctuations require higher bandwidth settings.

7.3 Experimental Procedure

Comparison between LDV and PD included two sets of experiments, namely, zero and 50 percent occlusion measurements. Both steady and pulsating flow conditions were tested in each set.

7.3.1 Zero Occlusion Measurements

The PD and LDV were compared in steady pipe flow for five values of Reynolds number, 6100, 8300, 10800, 12600, and 15000. To assure a more reliable comparison the two laser beams were set to intersect at the centerline of the test section at a position that corresponds to the intersection of the PD probe axis with the test section axis.

A small concentration of the silicon carbide particles (1.5 μm average diameter) was then added in such a way that a good Doppler signal was obtained for the LDV. Using the LDV as the reference measuring instrument and the control valves to change the flow condition, the desired velocity was obtained The Fourier Analyzer was used to perform analysis in both time and frequency domains. One hundred samples, each of one second duration, were used to calculate the average velocity. Another 100 samples of similar duration were employed to calculate the power spectra of the disturbance velocity. With this sampling time, a frequency resolution $\Delta f = 1$ Hz was maintained. For a maximum frequency of 512 Hz a data block of size 1024 was used which means 1024 data points for each sample window of one second duration. The root mean square of the disturbance velocity was calculated directly and by integrating the power spectrum. A teleprinter and an x-y plotter were the output modes employed.

After taking several measurements with the LDV, the silicon carbide particles of 11 μm average size were added with sufficient concentration to secure a good audio signal which was monitored on the oscilloscope. The high pass filter was adjusted to give an acceptable cut-off frequency,

and the DISA tracker was adjusted to yield the minimum drop out. Different bandwidth settings were considered for most of the experiments to study the effect of the bandwidth on the spectral shape. The analog output from the tracker was analyzed in a way similar to that used for the LDV.

For both instruments the analog output was low pass filtered at 512 Hz to avoid aliasing from higher frequencies.

For the pulsating flow only one velocity waveform was considered. This was selected to fall within the limitations of the tracking range of the existing phase lock loop when used for processing the PD Doppler signal. The waveform was sinusoidal with frequency of one Hertz, minimum velocity about 45 cm/sec and maximum velocity about 90 cm/sec. A similar procedure was followed in dealing with the analog output as with steady flow. The only difference was that the driving signal for the pulsating pump was used as triggering signal. This activates a variable delay circuit which was set to give a one micro second pulse at any desired time subsequent to the trigger. This pulse, in turn, was used to initiate the analog to digital conversion process in Fourier Analyzer. In this way, the sampling started each time for a fixed point relative to one complete velocity cycle.

7.3.2 Fifty Percent Occlusion Measurements

With the model M2 of 50 percent area reduction, the measurements of the centerline velocity were taken at a position of one inch downstream of the minimum area or throat of the constriction (X/D = 2). The test procedures for both steady and pulsating flow were similar to those

followed for the zero occlusion measurements.

7.4 Experimental Results

In this section results of experiments for the cases of zero and 50 percent occlusion are presented.

7.4.1 Zero Occlusion Results

7.4.1.1 Steady Flow. Figure (7-1) shows the average velocity measured by the PD plotted versus that measured by LDV. The distribution of points around the bisector of the two axes shows a very good agreement between the two instruments. The percentage difference is less than three percent of the value measured by LDV. Figures (7-2a) to (7-2e) show the energy spectra of the disturbance velocity obtained using LDV and PD for Re = 6100, 8300, 10800, 12600 and 15000, respectively.

As discussed in an earlier section (6.2.4) there are several factors which affect the energy spectra measured with the PD-tracker system. One of these was the tracker bandwidth setting. In all cases of steady flow, the bandwidth value which gave lowest signal dropout rate also yielded best agreement with the LDV results, and they are the data with the lowest dropout which are graphed in Figures (7-2).

Figure (7-2f) illustrates an example of energy spectra for different bandwidth settings of the PD-tracker system. The spectrum for the case of four percent bandwidth corresponds to high signal dropout rate. The case of one percent bandwidth can be shown to filter the frequency components of the signal. The best bandwidth setting with minimum dropout was two percent. A good agreement with the LDV spectrum is observed.

Figures (7-3) and (7-4) show the results for Re = 6100 and 15000

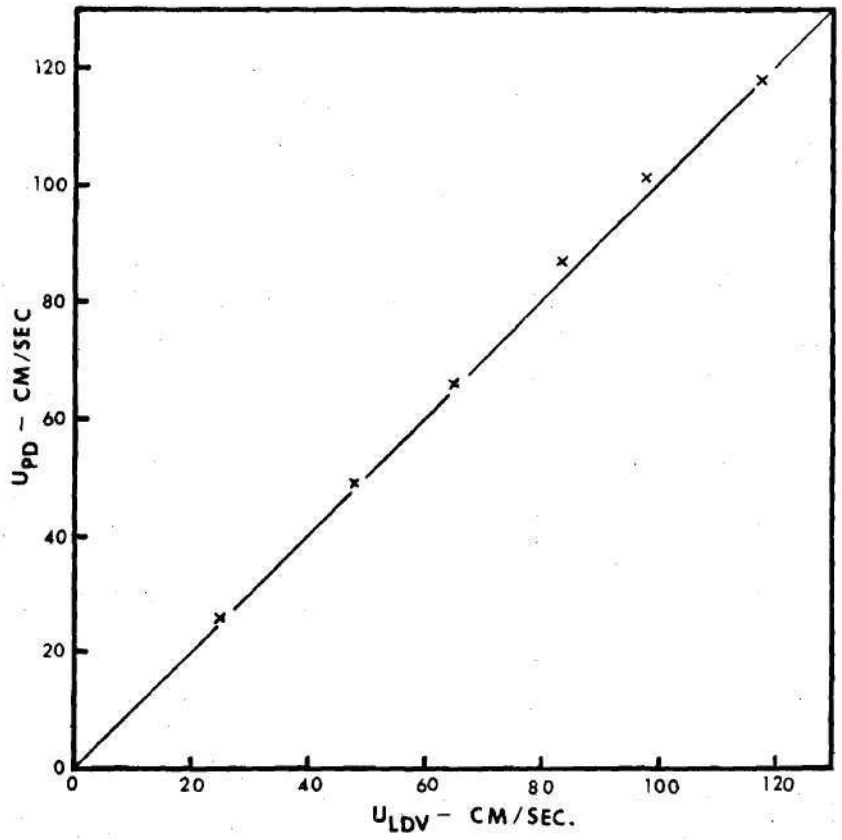

Figure 7-1. Average Velocity Measurements for PD and LDV, Steady Flow

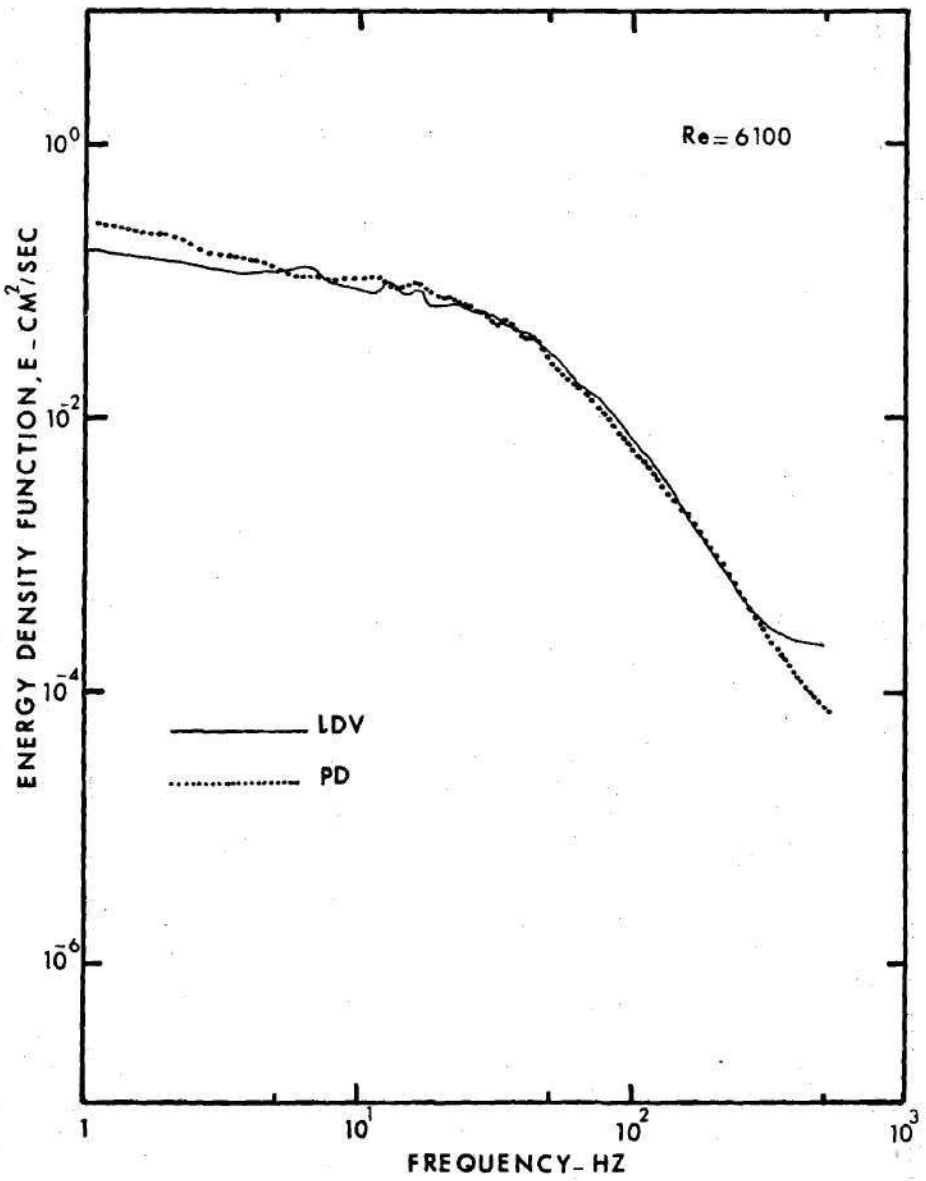

Figure 7-2a. Disturbance Energy Spectra for Re = 6100, Steady Flow

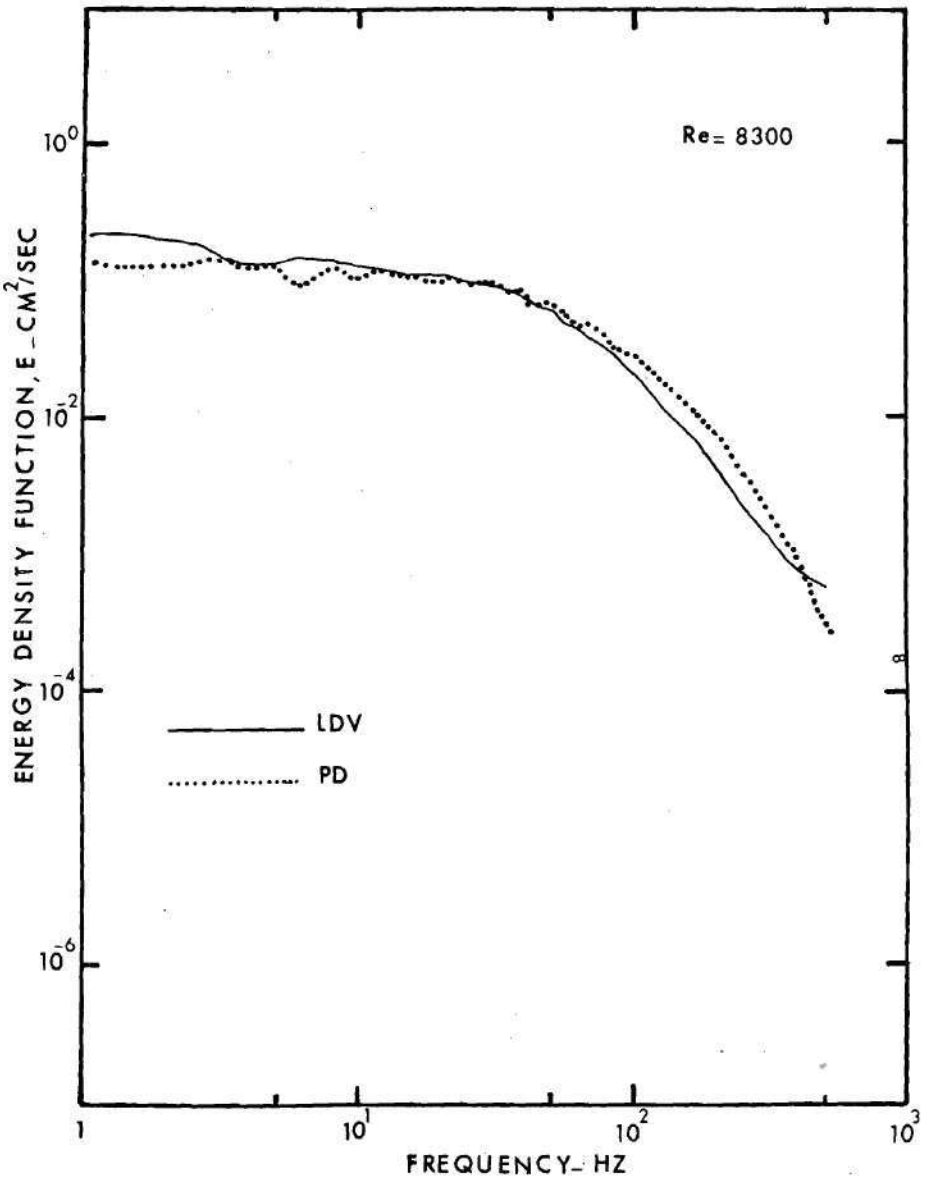

Figure 7-2b. Disturbance Energy Spectra for Re = 8300, Steady Flow

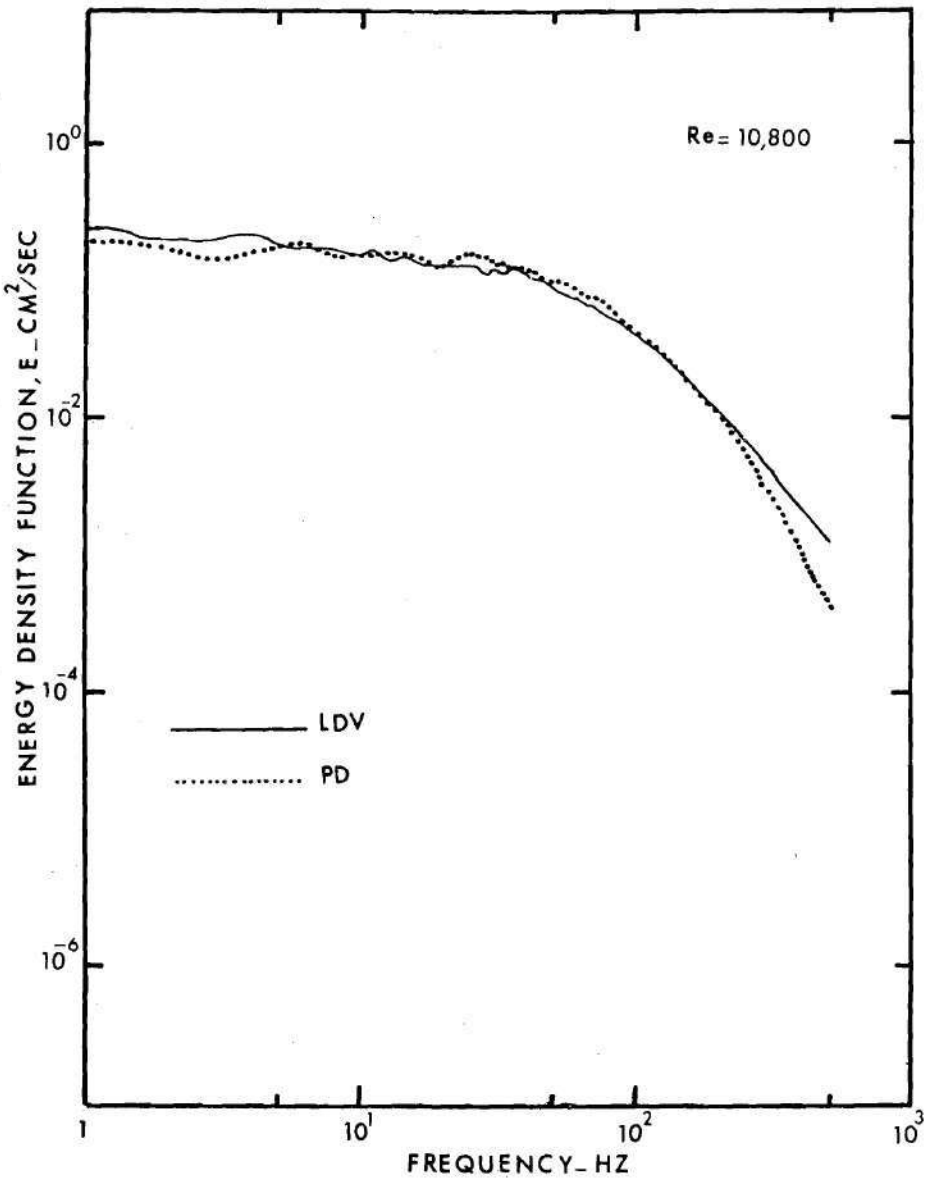

Figure 7-2c. Disturbance Energy Spectra for Re = 10,800, Steady Flow

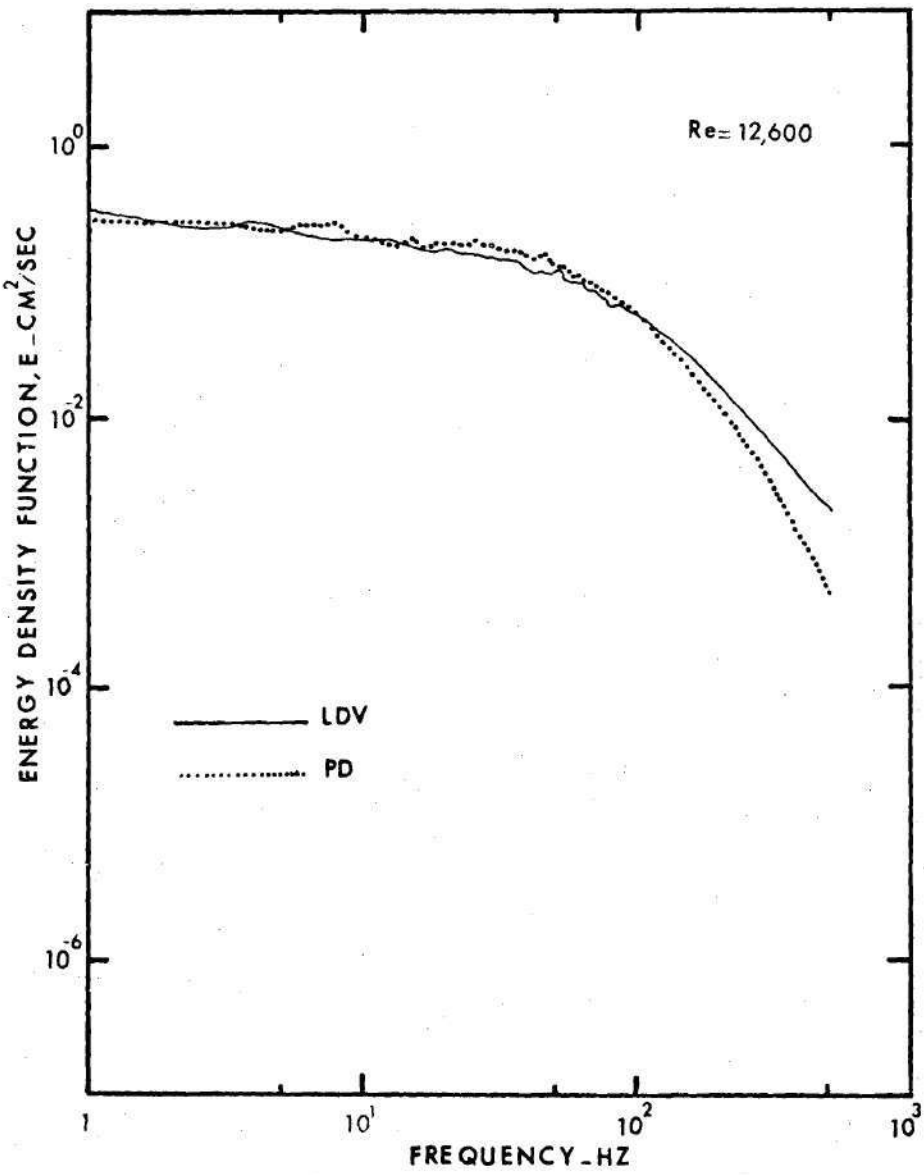

Figure 7-2d. Disturbance Energy Spectra for Re = 12,600, Steady Flow

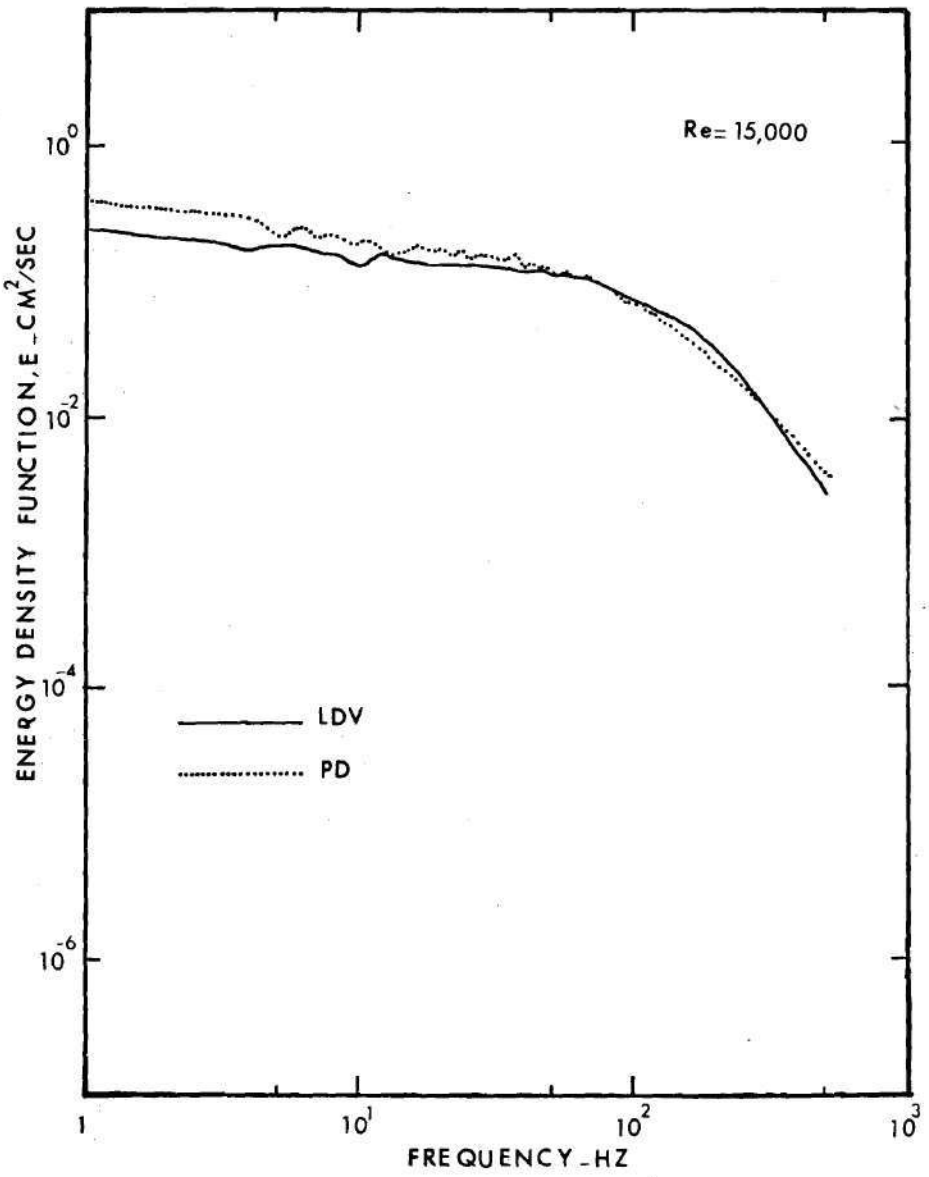

Figure 7-2e. Disturbance Energy Spectra for Re = 15,000, Steady Flow

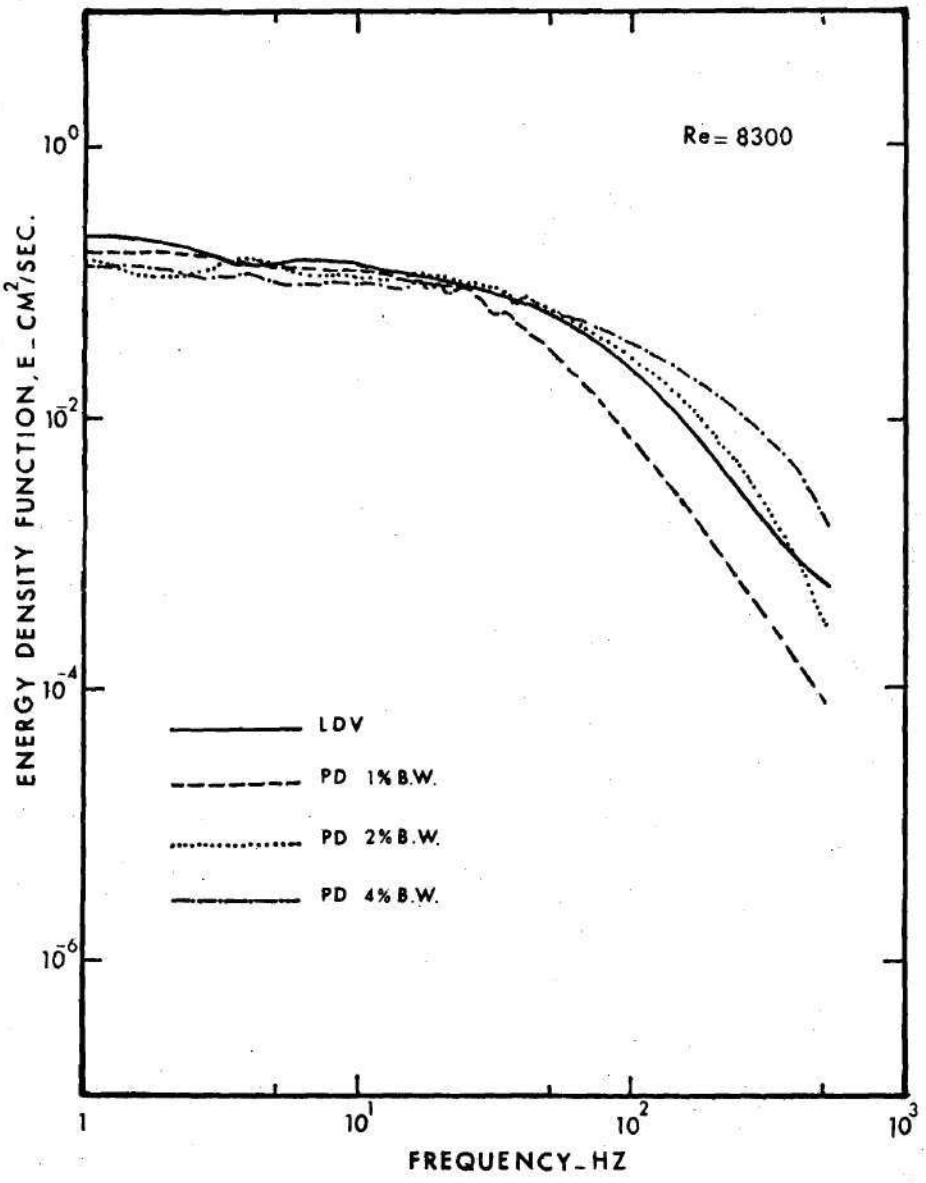

Figure 7-2f. Disturbance Energy Spectra for Different Bandwidth Settings of the PD System

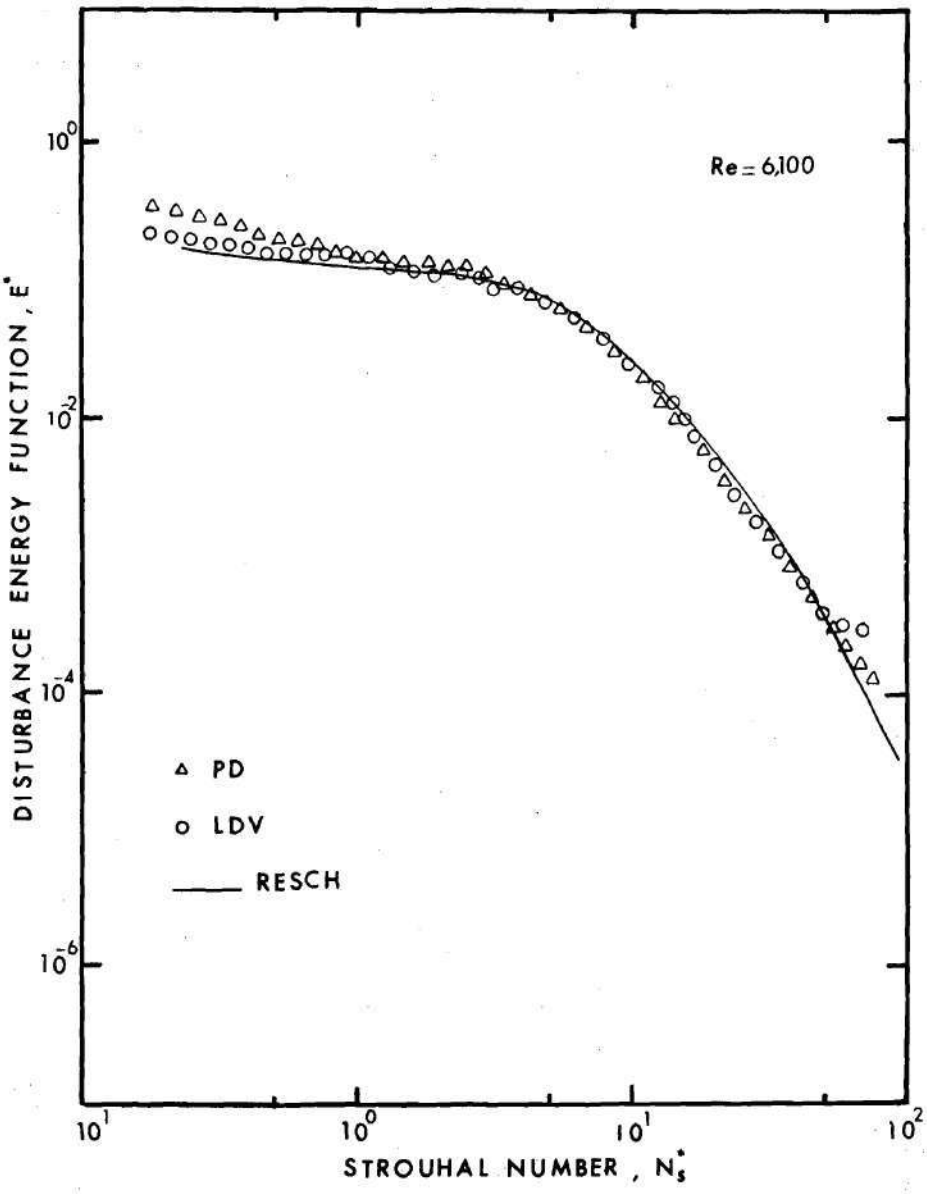

Figure 7-3. Nondimensionalized Energy Spectra for Re = 6100, Steady Flow

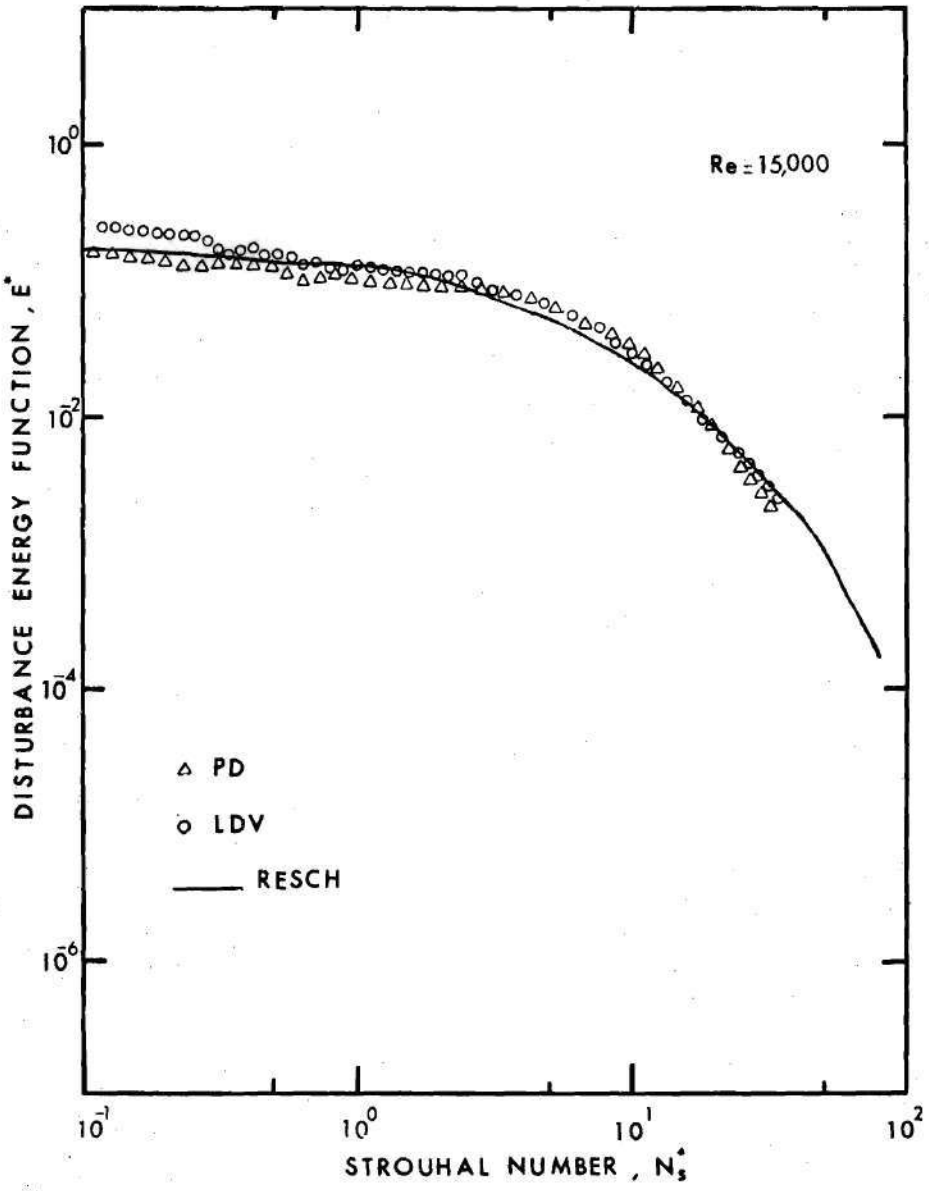

Figure 7-4. Nondimensionalized Energy Spectra for Re = 15,000, Steady Flow

as the dimensionless energy spectrum function, E^* versus dimensionless frequency parameter (Strouhol number), Ns^*. These results were compared with the data measured by Resch (82) using a hot film anemometer. A very good agreement is observed which verifies the accuracy and reliability of the results obtained.

The turbulence intensities were calculated for both instruments and the results are presented in Figure (7-5). The results are compared with the Sanborn (94) and Coantic (95) equations. The range of scatter of the hot film measurements reported in the literature is also indicated on the same graph. A reasonably good agreement is seen in this comparison for both LDV and PD. The turbulent intensities for PD used for this plot are those corresponding to the lowest dropout.

7.4.1.2 Pulsating Flow. For this comparison only one velocity waveform was considered, which varied between 45 and 90 cm/sec. Figure (7-6a) displays the ensemble averages measured by both instruments for a one complete cycle. A good agreement between LDV and PD measurements is observed. The energy spectra of the disturbance velocity for these experiments are shown in Figure (7-7). For frequencies below 60 Hz a good agreement is noticed. However, for higher frequencies the level of the PD spectrum is higher. Some explanation for this can be obtained from the measurement of $u'^2(\tau)$ versus τ. These plots are shown in Figures (7-6b, c, d). It can be seen that $u'^2(\tau)$ values as measured by the PD are higher during the low velocity segment of the cycle than those obtained with the LDV. On the other hand, agreement is quite good in the peak velocity region, which is also the time during which the magnitude

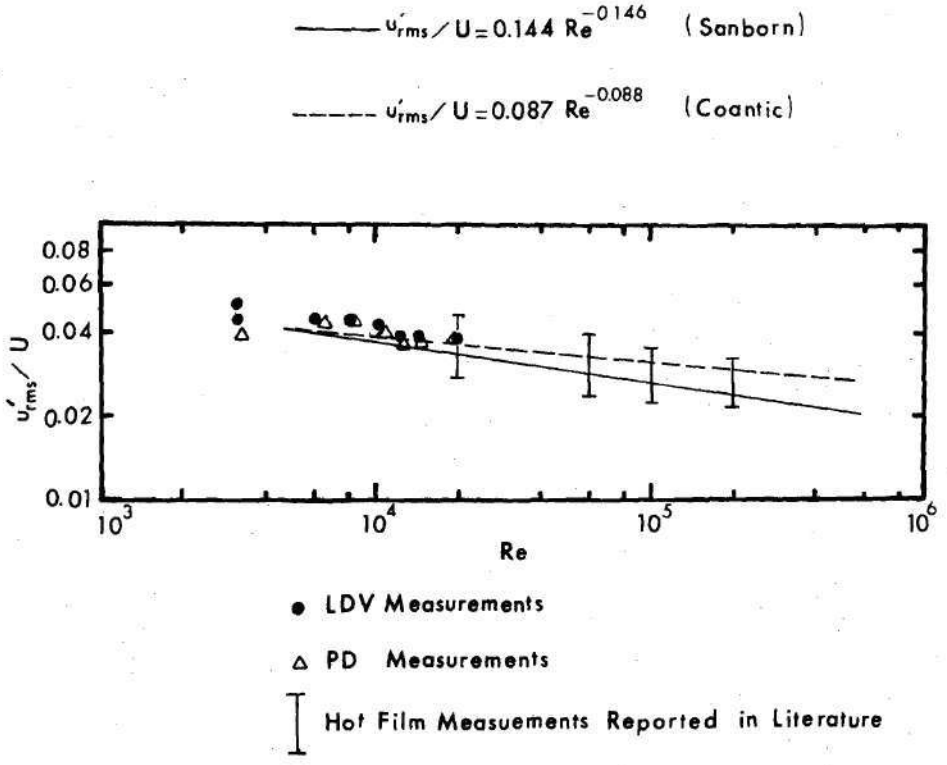

Figure 7-5. Turbulence Intensity Measurements

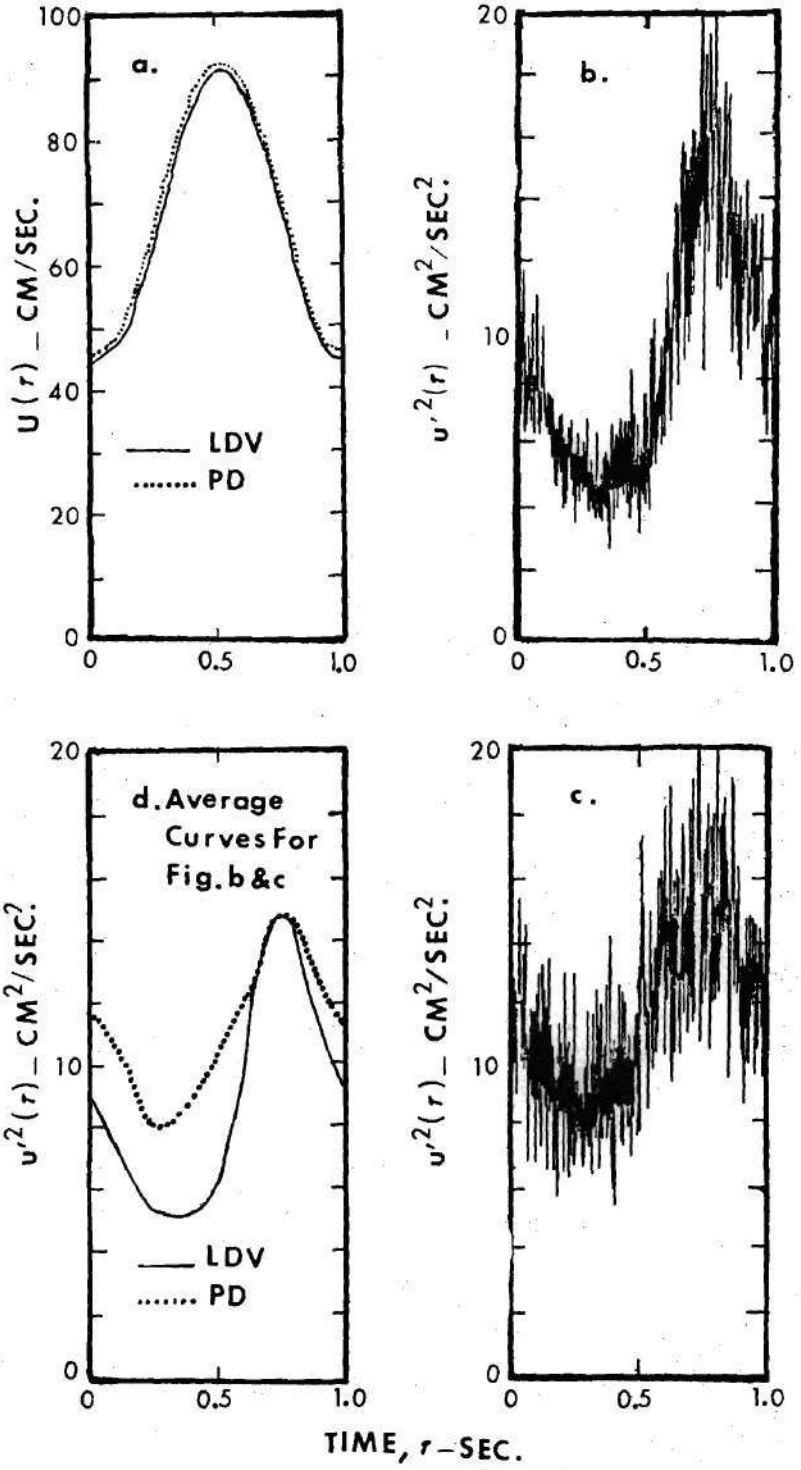

Figure 7-6. Ensemble Average and Disturbance Velocities for Pulsating Flow Measurements

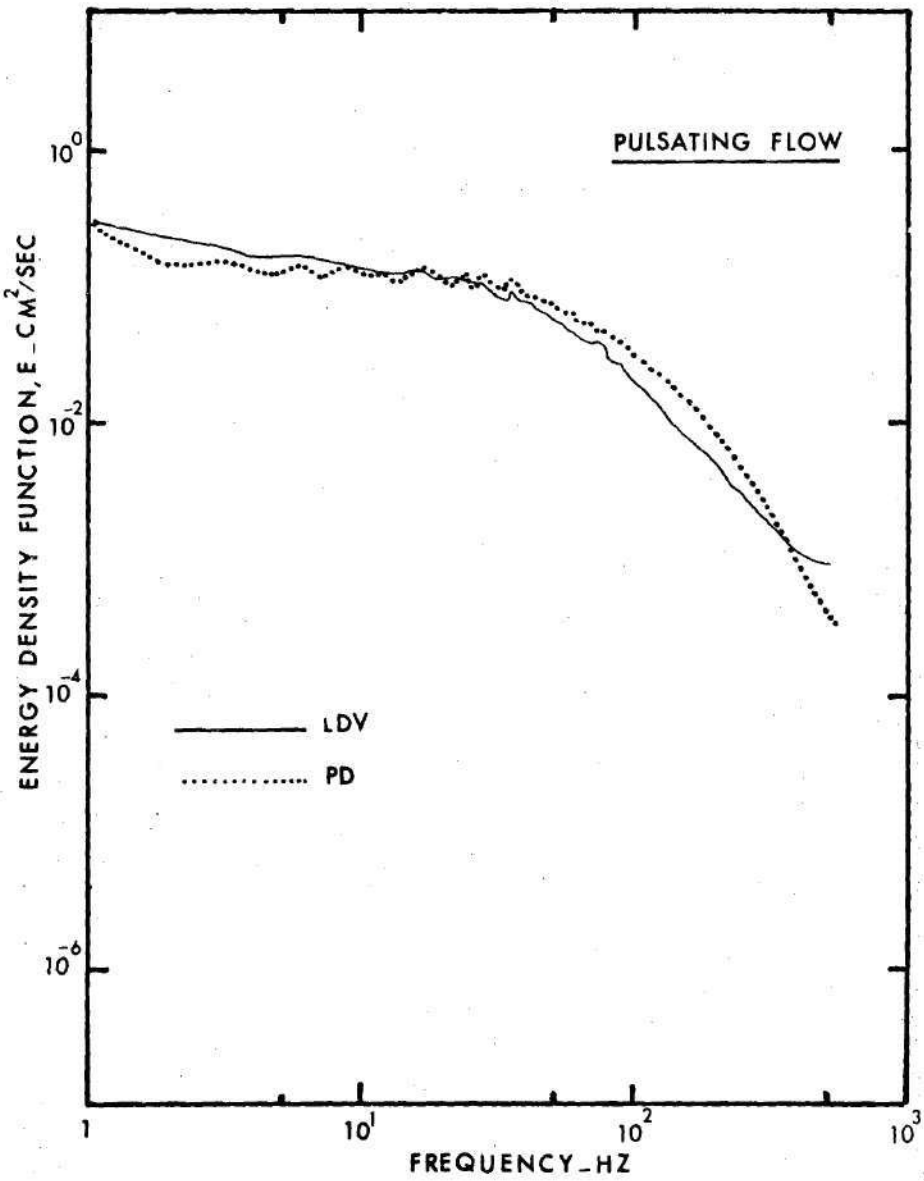

Figure 7-7. Energy Spectra, Pulsating Flow Measurements

of the turbulence fluctuation is greatest. It is believed that this is a consequence of the inability to maintain a sufficiently small PD signal dropout for the duration of the cycle using a single bandwidth setting on the phase lock loop. This suspicion is bolstered by the fact that the dropout indicator on the tracker fluctuates during the cycle, with its minimum occurring near peak flow velocity and maximum occurring near minimum flow velocity. It was also observed that the signal dropout for the LDV is maintained at a small value for the entire cycle. In addition, the tracker provides output of a step function which is activated during signal dropout. This signal is typically of very short duration and gives the appearance of a more or less random series of impulses. If the velocity output signal is assumed to be constant during these periods, this would increase the high frequency contents of the energy spectrum.

7.4.2 Studies with 50 Percent Occlusion

Results presented in the previous section dealt with fully developed turbulent pipe flow, a well defined configuration. For this case the rms turbulence velocities near the centerline are approximately the same, and the Reynolds stress is zero at the axis and varies linearly with the radial coordinate until viscous stress near the wall becomes significant. Thus, as demonstrated by equation (6-8) the ultrasound measurements along a 45^{o} line with respect to the axis are related directly to the laser measurements of the axial velocity component. Such is not the case with a poststenotic flow field. Deshpande (81) has demonstrated extreme nonisotropy in turbulence velocities distal to a

75 percent stenosis and this will occur, although perhaps not as dramatically, in the present case. Furthermore, the shear layer formed in passing through the constriction creates strong peaks in turbulence velocities off-axis as well as larger gradients in the mean velocity profiles than will appear in the pipe flow case. Thus, the effect of the larger sample volume of the PD system and the presence of any asymmetry in either the post stenotic field or the location of the sample volume about the tube centerline may contribute to non zero Reynolds stress. This presents a difficulty in relating the ultrasound measurements at $\theta = 45^{o}$ to those of the laser at $\theta = 0^{o}$, as evidenced by equation (6-7).

In a study aimed primarily at a flow field description without regard to any clinical application, this problem may be circumvented by utilizing a much larger tube radius, by making u' and w' measurements with the LDV, and by careful alignment of the sample volume with the tube axis. However, the clinical application of the ultrasound measurements do not allow these precautions, and an important aspect of this research was to elucidate problems in employing the PD for measurements in vessels of approximately one cm diameter. Thus, a direct comparison of the turbulence velocity component measured by ultrasound with that detected by the laser will not be possible for the case with 50 percent occlusion. The general spectral shapes, however, should be similar and this will serve as a check on the frequency response of the PD-tracker system.

The results of the steady flow measurements downstream of the 50 percent occlusion are presented in (Figures (7-8). The spectral shapes are similar, but the energy level is different being higher for

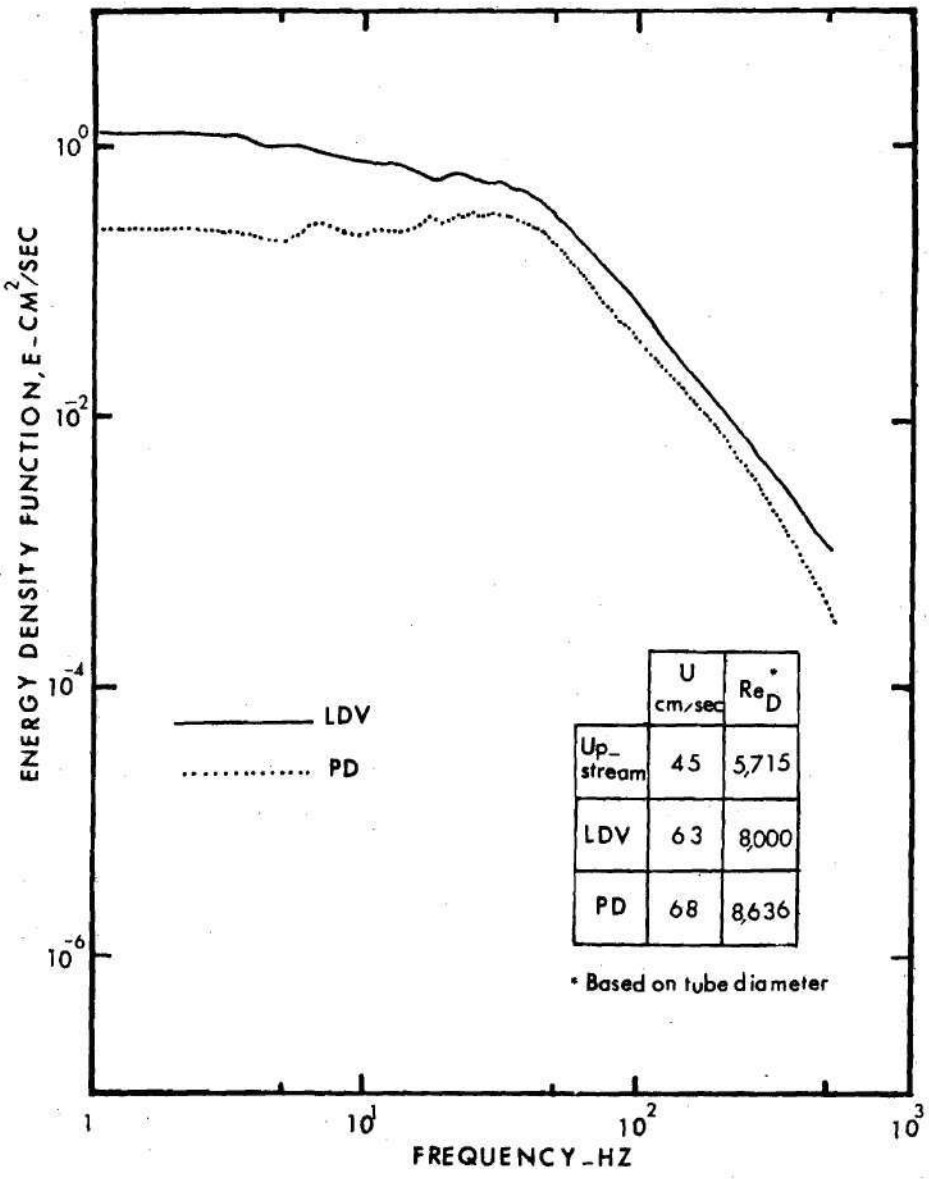

Figure 7-8a. Disturbance Energy Spectra at X/D = 2 Distal to 50 Percent Occlusion, Steady Flow

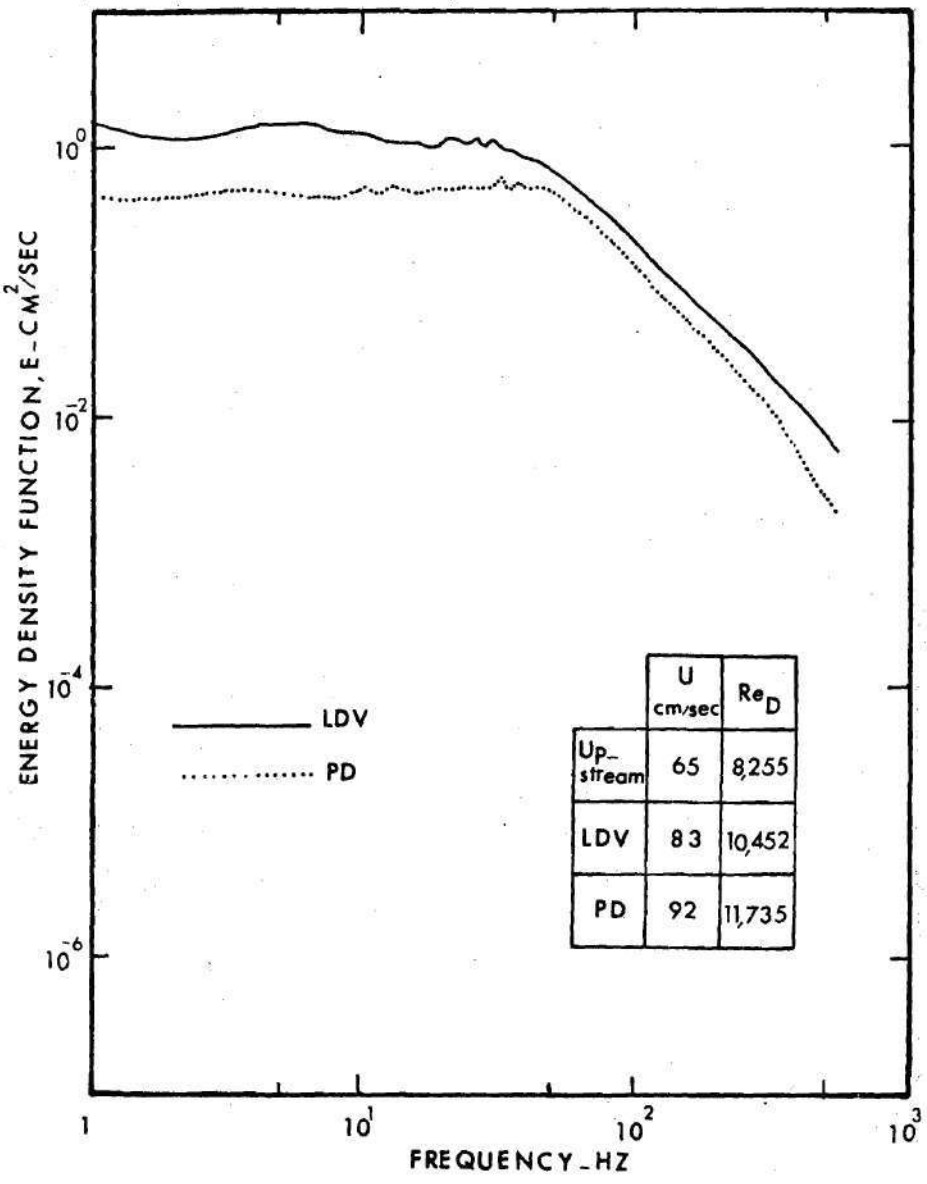

Figure 7-8b. Disturbance Energy Spectra at X/D = 2 Distal to 50 Percent Occlusion, Steady Flow

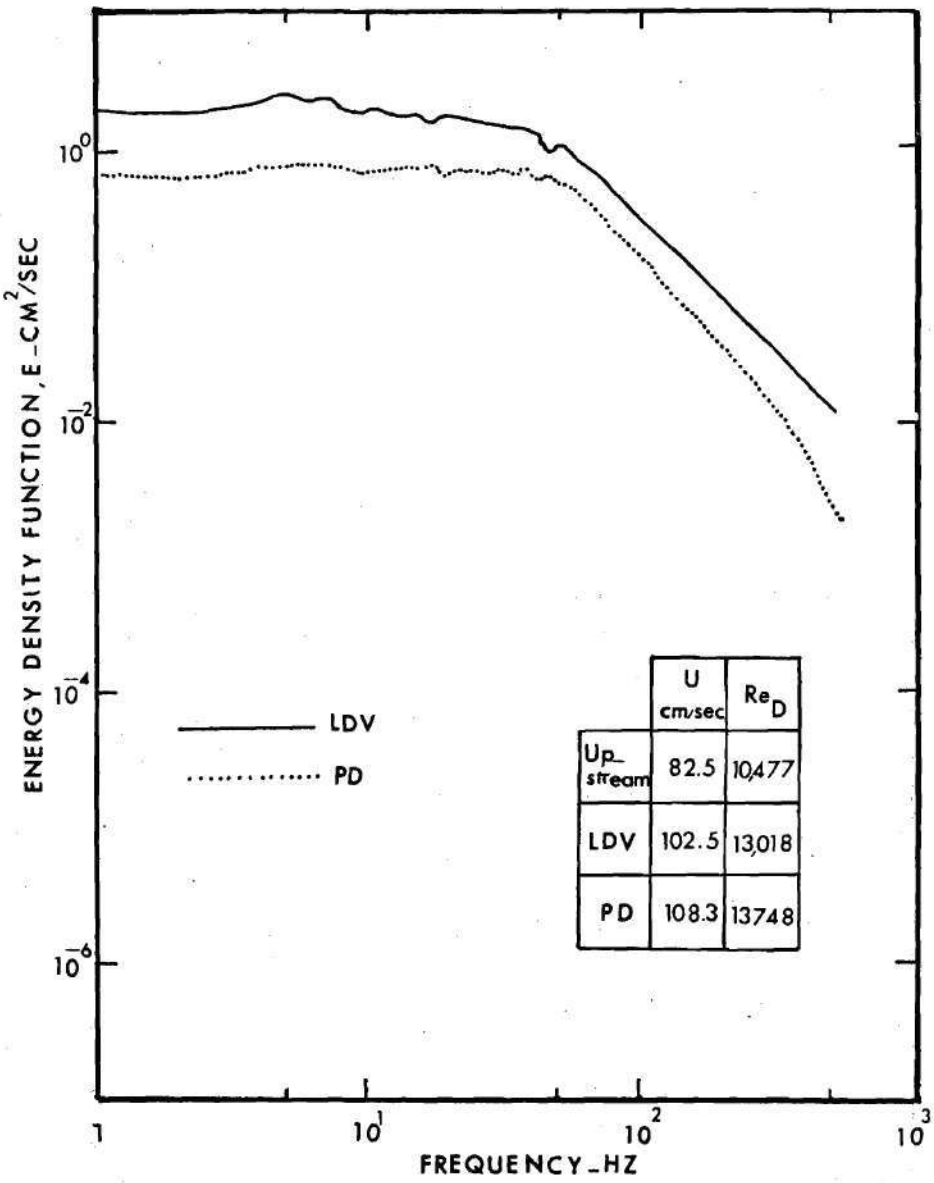

Figure 7-8c. Disturbance Energy Spectra at X/D = 2 Distal to 50 Percent Occlusion, Steady Flow

the LDV as previously explained. The average velocities measured by both instruments show higher values for the PD.

The pulsating flow measurements were only for a case where the upstream waveform was taken similar to that one considered for pulsating flow through the tube with no occlusion. The energy spectra of the disturbance velocity for LDV and PD are displayed in Figure (7-9a). Figure (7-9b) shows the ensemble average waveform for both instruments. Again the spectral shapes look similar; however, there is a difference in the ensemble average measurements between the two instruments, the PD being higher which is the same trend observed in the steady flow measurements.

7.5 Discussion

Turbulence spectra and intensities as measured by the PD Phase Lock Loop (PLL) system in steady turbulent pipe flow agrees very well with data from LDV and hot film instruments. Although precise limits have not yet been defined on the frequency response and Reynolds numbers, it appears that very useful turbulence information may be obtained with ultrasound. The pulsatile flows were more difficult to track, but loss of accuracy in measuring the variation of $u'^2(\tau)$ with time in the cycle could always be associated with increased signal dropout which, in turn, was due to operating beyond the marginal limits of the tracking range during the low velocity phase of the waveform. This may be corrected by varying the offset frequency to a point where $(f_R + f_d)$ is always within a given tracking range of the PLL.

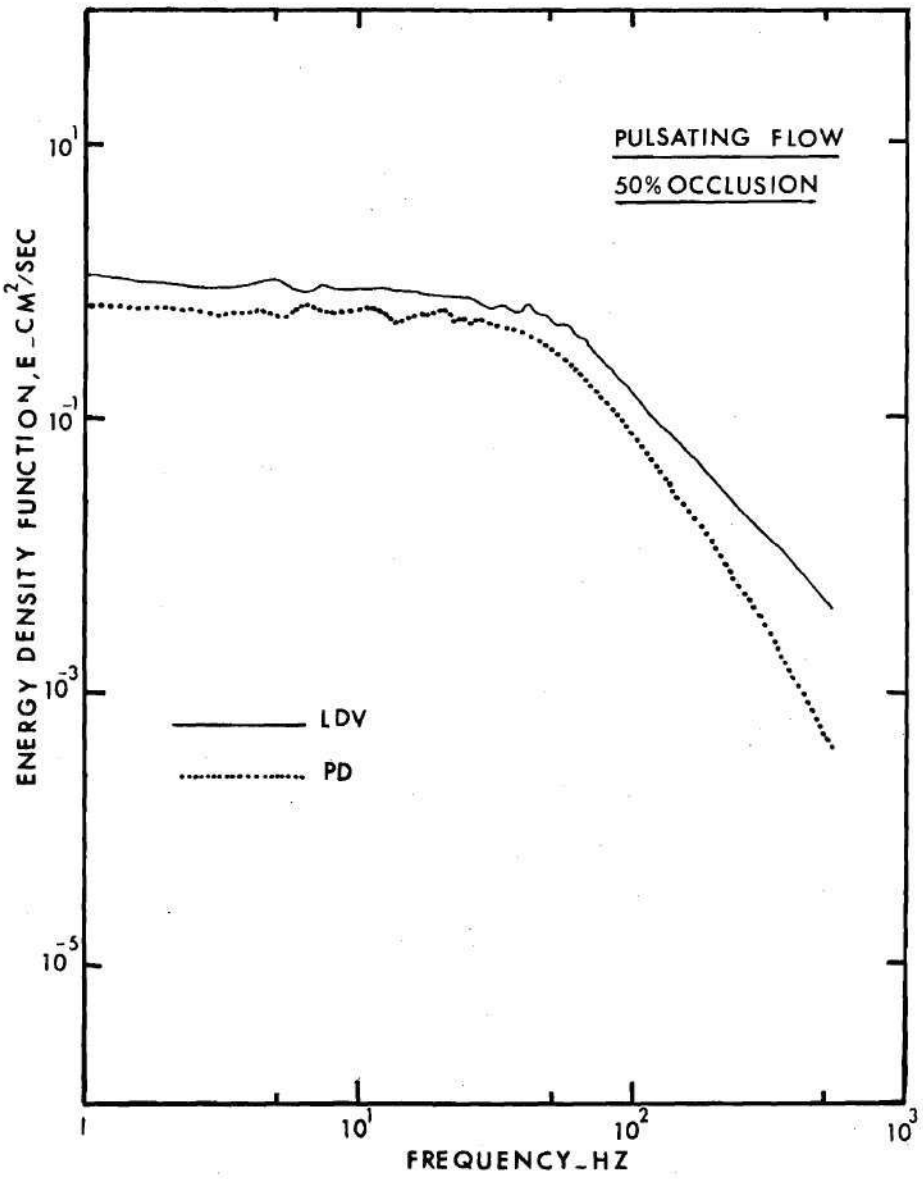

Figure 7-9a. Disturbance Energy Spectra at X/D = 2 Distal to 50 Percent Occlusion, Pulsatile Flow

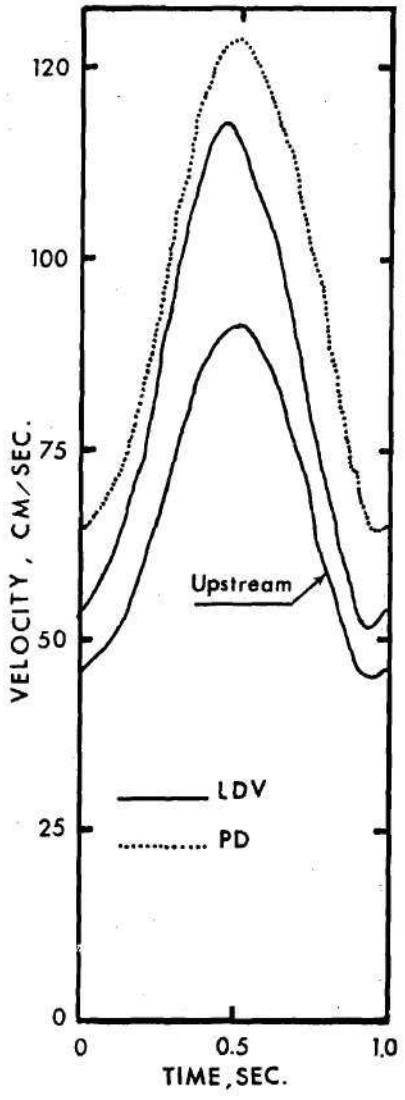

Figure 7-9b. Ensemble Average Velocities at X/D = 2 Distal to 50 Percent Occlusion, Pulsatile Flow

The poststenotic flow measurements of turbulence using the PD/PLL system at an angle to the flow is still difficult due to severe nonisotropy of the turbulent fluctuations.

Factors causing spectral broadening of laser Doppler measurements (George and Lumley (92)) also affect Doppler ultrasound measurements and will limit the response of the instrument to velocity fluctuations of high frequency. Likewise, the size of the sample volume is intimately connected with the size of turbulent eddies which can be resolved.

The PD/PLL system has provided tremendous improvement over the zero crossing detector (ZCD). Efforts to measure turbulence with McLeod's ZCD and with an off-the-shelf model were totally unsuccessful. No meaningful data whatsoever could be obtained. Furthermore, even the ensemble average velocity measurements were of poor quality in comparison with the laser system.

The results illustrated in this chapter represent a significant advancement in the state of the art of velocity measurements with ultrasound. The primary objective is to demonstrate that meaningful turbulence measurements may be obtained with ultrasound under flow conditions similar to those found in the arterial system. The present data indicate that this can be done and that noninvasive detection of blood flow disorder may, therefore, be possible.

CHAPTER VIII

CONCLUSIONS AND RECOMMENDATIONS

A theory for the analysis of disorder in pulsatile flow has been introduced. The motivation was to use the analysis of flow disorder created by arterial stenosis as a diagnostic tool to detect Atherosclerosis noninvasively.

The basis of this theory is to decompose the instantaneous velocity at a certain position in the flow field into a deterministic ensemble average velocity and a disturbance component. Several digital techniques have been suggested to describe the disordered flow which includes computation of the ensemble average waveforms, energy spectra, and autocorrelation functions of the disturbance velocity and determination of the rms values of the disturbance velocity and its variation with time. For situations in which the disturbance exists over only part of the velocity cycle, the temporal development of the disturbance velocity was obtained by dividing the cycle into time intervals that represent the important phases of the flow, such as, the acceleration, peak, and deceleration phases.

The theory has been applied to in vivo hot film measurements and in vitro LDV measurements of the poststenotic field of modeled rigid stenoses, and was employed to compare the pulsed Doppler ultrasonic velocimeter with the laser Doppler velocimeter. The following conclusions were obtained:

1. Flow disorder, as described by this analysis, is a sensitive indicator of the presence of mild constrictions in the vessel under study.

2. The disturbance velocity measured in the in vivo experiments is a nonstationary random variable for mild to moderate stenoses.

3. The flow field distal to modeled stenoses is characterized by the existence of three major classes of disturbances, the shed vortices, the periodic instabilities that break down to turbulence, and the turbulent fluctuations.

4. The existence and interaction among these disturbances depend on the degree of constriction, Reynolds number, and the frequency parameter.

5. Spectral similarity was obtained between in vivo and in vitro data provided that the most turbulent parts of the cycle are examined.

6. The deceleration phase has shown to be the most unstable phase in the entire velocity cycle.

7. The split peak observed in the ensemble average waveform at certain positions downstream of the stenosis can be caused by a vortex or by a turbulent front passing through this position while flow is reaching its maximum velocity.

8. Average velocities, turbulence spectra, and intensities as measured by the PD phase-lock loop system in steady pipe flow agree very well with LDV, which implies that meaningful turbulence measurements may be obtained with ultrasound under flow conditions similar to those found in the arterial system. Detailed conclusions and discussions were previously given at the end of each chapter.

In summary, it has been shown that flow disorder analysis could be used as a powerful diagnostic tool for the noninvasive detection of Atherosclerosis. In addition, basic fluid mechanics studies were presented which add to the knowledge of the nature and characteristics of the poststenotic flow field.

Recommendations for Future Research

There are several directions of further development in the flow disorder studies and ultrasound, such as

1. Further in vitro studies aimed at a more detailed flow field description in the radial coordinates should be performed to elucidate the mechanism of instability formation. This study should include flow field visualization to identify regions of particular interest, and a wide variation of velocity waveform shapes and frequencies should be investigated to determine conditions leading to instability.

2. It would be useful to attempt a more detailed probing of the in vivo poststenotic field that includes a wider range of radial and axial positions and of flow conditions more than what is presently available. These must then be related to the in vitro studies for their similarities and differences before a thoroughly useful clinical understanding is possible.

3. Additional research is needed to carefully define the accuracy and limitations of the pulsed Doppler ultrasound system in an in vivo environment and to relate clinical measurements at an angle with the vessel to the more conventional axial and radial turbulence component measurements in fluid mechanics.

APPENDICES

APPENDIX A

PULSATILE FLOW PUMP

For more realistic modeling of arterial hemodynamics and because it has been shown that flow instabilities are sensitive to the shape of the velocity waveform, the Biofluid Dynamics Laboratory plans the construction of a pulsatile flow pump capable of simulating physiologic in vivo waveforms (83). The pulsatile flow pump shown in Figure (A-1) is designed to introduce a pulsatile velocity waveform into models of stenoses, bifurcations, and elastic tubes. The specified waveform can be as simple as a sinusoidally varying flow or as complex as a physiologically normal waveform. The ability to produce a specified waveform is made possible by a specially designed spool valve which is shown in the same Figure. A steady supply of water, or other liquid, is furnished to the spool valve by a centrifugal pump. The position of the spool determines whether the flow is diverted toward the test section or toward the bypass return to the pump. This valve concept helps to minimize the pump supply pressure and flow fluctuations, thereby reducing overall system oscillations. The valve outlet leading to the flow experiment is smoothly contoured to reduce flow turbulence and valve noise. The movable spool is held in alighment with the valve body by a linear ball bearing which allows very low friction axial movement while reducing the lateral movement and vibration to practically zero. A flexible

bellows mounted from the valve body to the spool shaft makes a water tight, low restriction seal.

The spool position, and hence, the flow pulse wave, is controlled by the driving system consisting of a reference signal generator, power amplifier, and shaker. The desired flow velocity waveform is furnished by the reference signal which can be a sine wave from a signal generator or other waveform shape. The output from this wave generator controls the output of the power amplifier which in turn drives the shaker. The shaker positions the spool to allow the proper amount of flow into the experiment. The desired velocity waveform at the test section can be obtained by controlling the waveform generator (both the amplitude of the waveform and the D.C. offset) and the power amplifier gain.

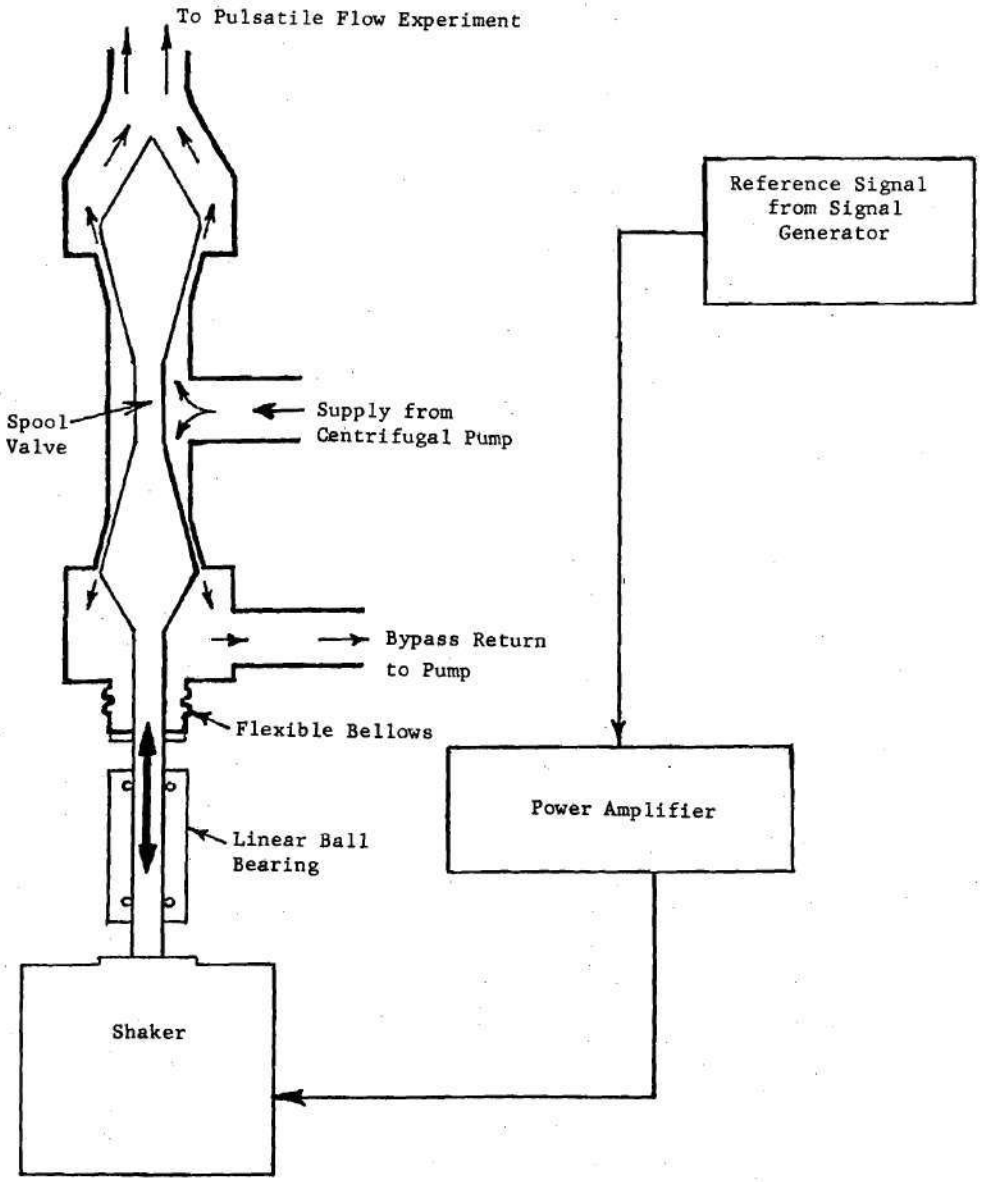

Figure A-1. Detailed Schematic of Pulsed Flow Pump

APPENDIX B

ADDITIONAL INFORMATION ON THE DISA 55L LDV SYSTEM AND THE FREQUENCY TRACKER

The information included in this appendix provides a more in depth explanation of the DISA LDV system. The majority of discussion is based on information found in the DISA operation manual (84) and Carpenter (96).

Basic Concepts

Before any description of the LDV system can be given, several basic concepts dealing with the physics of lasers and electronics must be understood. These concepts include properties of laser light, interference fringes, heterodyning, definition of a Schmitt trigger, integrating circuits, and filters.

Laser Light

The laser is not new to the scientific community. Because of its unique physical properties, it has been utilized in many types of instrumentation. Generally, laser light may be described as having four basic properties:

1. Laser light is very nearly monochromatic, i.e., one wavelength is present.

2. Laser light is highly collimated, i.e., there is very little dispersion of the beam.

3. There is little phase difference present in the beam. The beam is coherent.

4. The laser may be operated in a mode which results in Gaussian variation in intensity across the beam.

Interference Fringes

Because the laser beam is a coherent light source, mixing of two beams will produce interference fringes or lines. The production of these fringes is due to constructive and destructive interference. In the LDV system two beams are focused together at a point. At the intersection of these beams an interference fringe is produced.

If both beams have the same frequency, a stationary fringe pattern will be produced. The distance between fringes is directly related to wave length of the beams and the intersection angle. If, however, one beam is of slightly different wavelength, a moving fringe pattern results. The speed of the fringes will be directly related to the difference in wavelengths (frequency). Because both beams have a Gaussian distribution, the resulting sampling volume (or fringe region) will also have a Gaussian distribution.

Heterodyning

In its simplest terms, heterodyning is the mixing of two signals. If two signals, f and $f + \Delta f$, are mixed, the resultant signal will be comprised of two frequencies, $2f + \Delta f$ and Δf. This may be described mathematically by the equation:

$$\sin((f)t + \emptyset) \cdot \sin((f + \Delta f)t + \beta) = \frac{1}{2} \sin[(2f + \Delta f)t + \emptyset + \beta]$$

$$+ \frac{1}{2} \sin[(\Delta f)t + \emptyset - \beta]$$

where $\emptyset$ and β are phase constants. By using selective filtering either frequency may be obtained. The fringe pattern produced by the mixing of two beams of laser light is the result of optical heterodyning. There are three aspects of electronics which should be discussed before entering the discussion of the tracker itself. These are the Schmitt trigger, a simple integrating circuit, and the voltage controlled oscillator (VCO).

Schmitt Trigger

A Schmitt trigger is an electronic circuit which will produce a pulse of set amplitude and duration when an input voltage increases above a certain threshold value. The trigger will not fire again until the voltage has dropped below and then risen above the threshold value (see Figure (B-1)).

Integration Circuit

In electronic systems, most analog integrators employ some type of resistive capacitive network. The time constant associated with this network is based, in part, on how quickly the capacitor can be charged and discharged ($t = 1/R_c$). This time constant restricts the integration to a certain range of frequencies. This fact required different time constants (e.g., different capacitance values) for accurate integration of different frequencies. Generally, optimum integration is achieved when the network is tuned for an individual frequency.

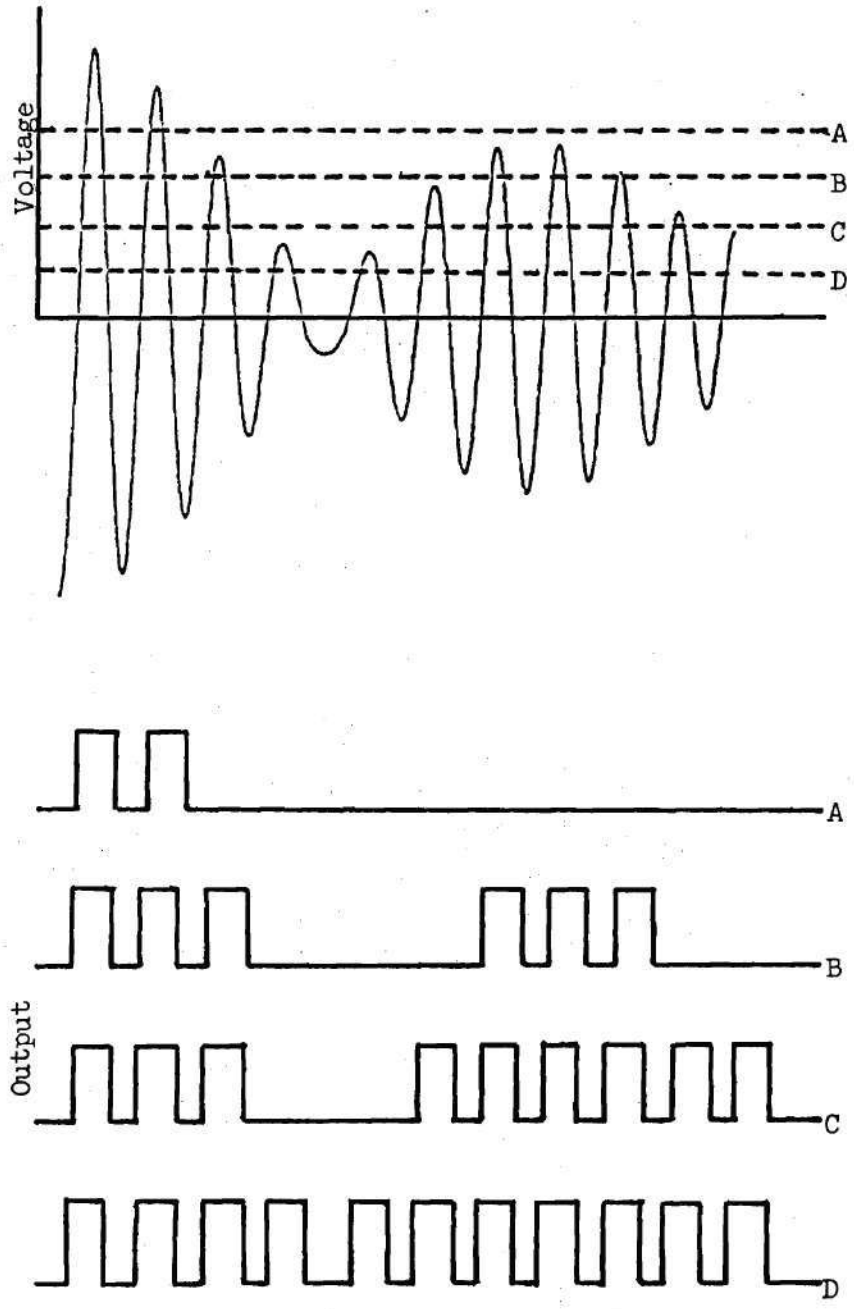

Figure B-1. Pulses from Schmitt Trigger with Various Threshold Values

Voltage Controlled Oscillator

A voltage controlled oscillator or VCO is a device which produces a frequency output which is directly proportional to the voltage applied. The ranges of the VCO used in the DISA trackers may be found in Table B-1.

Basic DISA Tracker Design

The DISA 55L Laser Doppler Anemometer Mark II is built around the earlier Mark I system. For this reason, the Mark I system is discussed first. The system can be separated into two parts, production of the Doppler frequency and tracking or following of the Doppler frequency to produce a velocity signal.

Production of f_D

In the Mark I system, a laser beam passes through a beam splitter to produce two separate beams. The two beams are then focused to a point to form a sampling volume. Since the beams are of equal frequency, the resulting fringe pattern is stationary. As a particle passes through the fringes, the light scattered from the particle varies in amplitude with a frequency of f_D. Where f_D is determined from

$$V = \frac{f_D \times \lambda}{2 \sin \theta/2} \qquad \text{(B-1)}$$

with V being the normal velocity component of the particle passing through the fringe, λ being the wavelength of the laser beam, and θ being the intersection angle of the two beams.

To change the light amplitude variation into an electric signal,

a photomultiplier with receiving optics is used. This signal is both amplitude and frequency modulated. The amplitude modulation is a result of variations in seeding concentration. The frequency modulation is, of course, a result of variations in the velocity component being measured.

Tracking of f_D

The frequency tracker is built aroung an automatically tracking variable oscillator. For use in a wide variety of flows the tracker has been designed to cover Doppler frequencies varying from 2.25 KHz to 15 MHz. To maintain accuracy of lower frequencies, the tracker provides seven overlapping ranges as shown in Table B-1. Each range has a dynamic range of approximately 6:1. By using this system, turbulence variations up to ± 35% about any mean Doppler frequency between 3 KHz and 11 mHz may be followed within one of the ranges.

The tracker or frequency follower is shown in a block diagram in Figure B-2. The Doppler signal is fed into a mixer where the f_D signal is mixed with a second frequency (f_{VCO}) from a voltage controlled oscillator. When tracking, the resulting frequency (f_T) is near f_{IF}. A narrow band filter (IF/A) is then employed to remove as much noise as possible. From there, the signal passes to the first limiter (Limiter I). The limiter consists of a Schmitt trigger with an adjustable threshold level. In this way, the inherent amplitude modulation is removed and a constant amplitude square wave is produced. This signal is then fed to the discriminator which produces a feedback voltage that controls the VCO and maintains the mixed frequency f_T near f_{IF}.

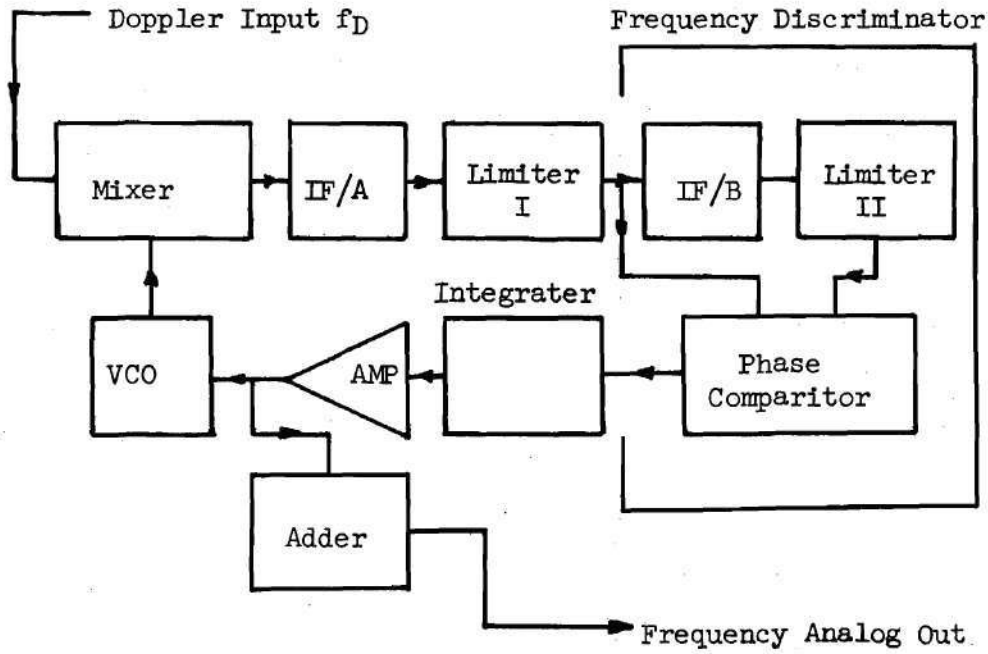

Figure B-2. Block Diagram of LDV Tracker

The discriminator consists of a second narrow band pass filter, a second limiter, and a phase comparator. The signal coming from Limiter I is fed through the second narrow band filter (IF/B also centered at f_{IF}) to remove all the higher harmonics in the signal. The result is a sinusoidal signal. The signal is then passed through Limiter II to produce the second square wave signal at f_{IF}. This second IF stage is designed, however, to produce an output that lags the output of Limiter I by 90^{o} if $f_T = f_{IF}$. The signal lags by less than 90^{o} (to 0^{o}) if $f_T < f_{IF}$ and by more than 90^{o} (to 180^{o}) if $f_T > f_{IF}$. This signal and the signal from Limiter I are then compared by way of a phase comparator. The comparator performs a simple analog multiplication and its output is therefore $2f_{IF}$. The Mark space/time ratio varies with the phase difference of the inputs. This signal is then integrated to produce a dc voltage which varies with phase difference (the difference between f_{IF} and f_T). This correction voltage is amplified and fed to the voltage controlled amplifier. As a result of this feedback, the oscillator frequency tracks that of the Doppler signal with the difference between the oscillator and the Doppler frequency being held nearly constant at f_T.

Restated, f_T is held very nearly equal to f_{IF}. How well f_T equals f_{IF} is dependent on the feedback loop gain. As the loop gain is increased the difference between f_T and f_{IF} is decreased. There is, however, an upper limit to the loop gain, above which the circuit will oscillate. For this reason, the gain is set at a value which will provide close tracking without oscillation.

The correction voltage applied to the voltage controlled oscillator

is by definition directly proportional to f_{VCO}. By monitoring this voltage an analog signal proportional to the Doppler frequency may be obtained. This is accomplished by subtracting the voltage which corresponds to f_{IF} (as constant). The following relations may aid in understanding the basic mixing.

f_D mixed with $f_{VCO} \rightarrow f_T$

f_T compared to $f_{IF} \rightarrow$ correction to VCO

VCO to change f_{VCO} so that $f_T - f_{IF} \sim 0$

$f_{VCO} - f_D = f_T \cong f_{IF} = cst$

$f_{IF} \simeq f_{VCO} - f_D$

$f_D \simeq f_{VCO} - f_{IF}$

f_{VCO} α voltage applied to VCO.

In order to follow different velocity ranges, the center frequencies of both narrow band filters and limiters are set to a new f_{IF}, as in Table B-1. For proper integration, the integration components must also be changed. The total effect of the narrow band filter and the necessary integration factors places a limit on how fast the tracker can follow a signal. The tracking speed can be improved by changing the width of the band pass filters. This is accomplished by changing the position of the percent bandwidth setting. Increasing the bandwidth may, however, reduce the signal to noise ratio of the signal entering into the discriminator section of the tracker. The tracker is equipped with five bandwidth settings (.5, 1, 2, 4, 8 percent of the frequency range).

Table B-1. Frequency Ranges for LDV Tracker

Range	(f_T)	(f_{IF})	(f_{VCO})
15 kHz	2.25 - 15 kHz	1.5 kHz	3.75 - 16.5 kHz
50 kHz	7.50 - 50 kHz	5 kHz	12.5 - 55 kHz
150 kHz	22.5 - 150 kHz	15 kHz	37.5 - 165 kHz
500 kHz	75 - 500 kHz	50 kHz	125 - 550 kHz
1.5 mHz	.225 - 1.5 mHz	150 kHz	.375 - 1.65 mHz
5.0 mHz	.75 - 5 mHz	500 kHz	1.25 - 5.5 mHz
15 mHz	2.25 - 15 mHz	1.5 mHz	3.75 - 16.5 mHz

Present Tracker

The early system had two major drawbacks which restricted its usefulness. The first drawback is that at low velocities only ± 35% of the Doppler frequency could be followed. In most applications this affords no hindrance. However, in recirculation regions, velocities may be quite near zero (on the average) with fluctuations in excess of 100 percent. This would be impossible for the Mark I tracker to follow. The second drawback is a result of the interference fringes produced. Since the fringe is stationary, a particle traveling in a "negative" direction will produce a Doppler frequency equal to that produced by a particle with equal velocity traveling in the positive direction. This effect is known as sign ambiguity (common in heat transfer type anamometers). Although not a serious drawback, treatment of recirculation regions would be more accurate if direction could be determined.

Both drawbacks have been alleviated in the Mark II model system. This was accomplished by producing a moving fringe pattern. To produce a moving fringe pattern, the beams producing the fringe must be of different frequencies. To shift the frequency of one of the beams, an acousto-optic (or Bragg) cell is used. After the laser light has entered the optical package (or transducer) the beam is divided by a beam splitter into two beams. One beam passes through the transducer unaffected. The other beam enters a Bragg cell where the frequency is shifted by a value determined by the acoustic excitement of the cell. The Bragg cell is driven at 40 mHz to produce a beam shifted by + 40 mHz. The frequency detected by the photomultiplier will be greater than 40 mHz for "positive"

flow and less than 40 mHz for "negative" flow.

Because the tracker is designed to operate only in the frequency ranges shown in Table B-1, the signal from the photomultiplier must be processed to give a signal which will be within the range of the tracker. This is accomplished through the use of a range translator. The range translator is a local oscillator capable of producing frequencies from 0 to 50 mHz in steps of 10 kHz. To provide maximum stability the oscillator is driven from the same 40 mHz oscillator used to drive the Bragg cell. The signal produced by the local oscillator (f_{LO}) is mixed with the signal coming from the photomultiplier. The resulting frequency (f_T) is then fed into a tracker system similar to that in the Mark I system. This tracker frequency f_T is defined as:

$$f_T = f_D + f_{LO} - 40 \text{ mHz}$$

If f_{LO} is set equal to 40 mHz, the tracker frequency is equal to the Doppler frequency f_D and the tracker becomes essentially the same as the Mark I system.

In order to track a negative velocity, the photomultiplier signal must be mixed with a local oscillator (range translator) signal which is greater than 40 mHz. This results in a tracker signal f_T within one of the ranges. As now becomes apparent in Table B-1, the versatility of the tracker has been greatly enhanced. By selecting a range which is higher than the range needed to track a signal in the Mark I system and

then translating the signal to a frequency that can be handled by that range, larger fluctuations (greater than 35 percent) in velocity can be followed. Tracking is exactly the same as for the Mark I system except the frequency being tracked is now followed in a higher frequency range, thus allowing for greater frequency fluctuations. Conversely, by mixing the photomultiplier signal with a local oscillator signal less than 40 mHz, a signal of low variation may be tracked in a lower frequency range (compared to the range necessary in the Mark I system). In this way, the frequency ranges originally designed to handle various velocity ranges may now be considered as ranges of variation, lower ranges handling the lower variations in velocity (or f_D) and higher ranges handling higher fluctuations. Of course, there is some danger in increasing the noise entering the system by using the higher frequency range which requires a wider bandpass filter.

Also of consideration is the use of the percent bandwidth setting which can also change the width of the bandpass filter. The choice of which settings to use becomes, at times, a compromise. For example using a frequency range of 500 kHz with an eight percent bandwidth will result in a frequency response of approximately 4 kHz while a frequency range of 5 mHz with a one percent bandwidth will produce a comparable 5 kHz frequency response. The choice of setting to be used would depend largely on the position which allows the optimum tracker response.

Since the tracker is now following some fluctuation f_T, the

signal processing for an analog output must be changed. In the Mark I system the VCO was controlled by a fast servo loop to maintain the difference between f_D and f_{VCO} constant at f_T (which very closely approximated f_{IF}). The same configuration is used in the Mark II system. The difference between f_T and f_{VCO} is held constant at f_T which very closely approximates f_{IF}. The frequency of the bandpass filters may be described by the following equation:

$$f_{IF} = f_{VCO} - f_T = f_{VCO} - f_D - f_{LO} + f_o \qquad \text{(B-2)}$$

where f_{VCO} is the voltage controlled oscillator output, f_D is the Doppler frequency, f_{LO} is the frequency from the range translator and f_o is the 40 mHz shift from the Bragg cell. Since f_{IF}, f_{LO}, and f_o are all constant, f_{VCO} varies only because of the Doppler frequency f_D. In order to simplify processing, the range translator provides a second signal. This signal is the difference between f_o (40 mHz) and the translation frequency f_{CO} given is:

$$f'_{LO} = f_{LO} - f_o \qquad \text{(B-3)}$$

since f_{LO} and f_o are both constant f'_{LO} is also a constant. Using equation (B-3), equation (B-2) may be rewritten as

$$f_{IF} = f_{VCO} - f_T = f_{VCO} - f_D - f'_{LO}$$

or

$$f_D = f_{VCO} - f_{IF} - f'_{LO} \tag{B-4}$$

The three frequencies on the right hand side of equation (B-4) are counted digitally to produce a digital display of the mean velocity. Since f_{IF} and f'_{LO} are constants, the counting time used is constant and independent of the integration time selected. The VCO signal (f_{VCO}), however, is counted for a period of time dependent on the integration time selected. After completion of counting, the digital value is multiplied by the correction factor determined from equation (B-1) and then displayed.

The analog signal is also processed in a manner different from the Mark I system. The Mark II system operates on the basis of equation (B-4). The frequencies f_{VCO} and f'_{LO} are fed into separate frequency to voltage converters and subtracted. Since f_{IF} is constant and does not change with translation as does f'_{LO}, no frequency to voltage converter is necessary. The digital unit provides a dc voltage which is directly proportional to f_{IF}. This voltage is also subtracted. The result is a voltage which is directly proportional to f_D. In order that the analog signal produced be equal to the velocity component of the flow, an adjustable gain amplifier is provided. The resulting signal may then be processed by any method desired.

APPENDIX C

SAMPLE WINDOW PROBLEM

All practical measurements are made over some finite interval of time. A voltmeter probe is touched to a test point long enough to get reasonable voltage reading. An oscilloscope is viewed long enough to obtain the desired waveform parameters. A signal processing system acquires a time segment of a signal, then processes that segment of information. In all of these cases, a time window is used. The view of whatever is being measured is limited to a finite time interval.

For measurements in time, the effects of this time window are generally not apparent or are easily ignored. It is assumed that what is happening outside the window is the same as what is happening inside the window. But, when a windowed signal is Fourier analyzed to gain frequency-domain information, the effects of the window cannot be ignored. This is because a time-domain window can cause a frequency-domain error that is referred to as leakage.

Leakage is a term for the apparent smearing or leaking of energy from one frequency component into adjacent components. To see how this comes about, let us look at the example in Figure (C-1).

A cosine wave is shown in Figure (C-1a). It is represented as both a function of time and as two discrete spectral components in the frequency domain. By virtue of the discreteness of the components, the

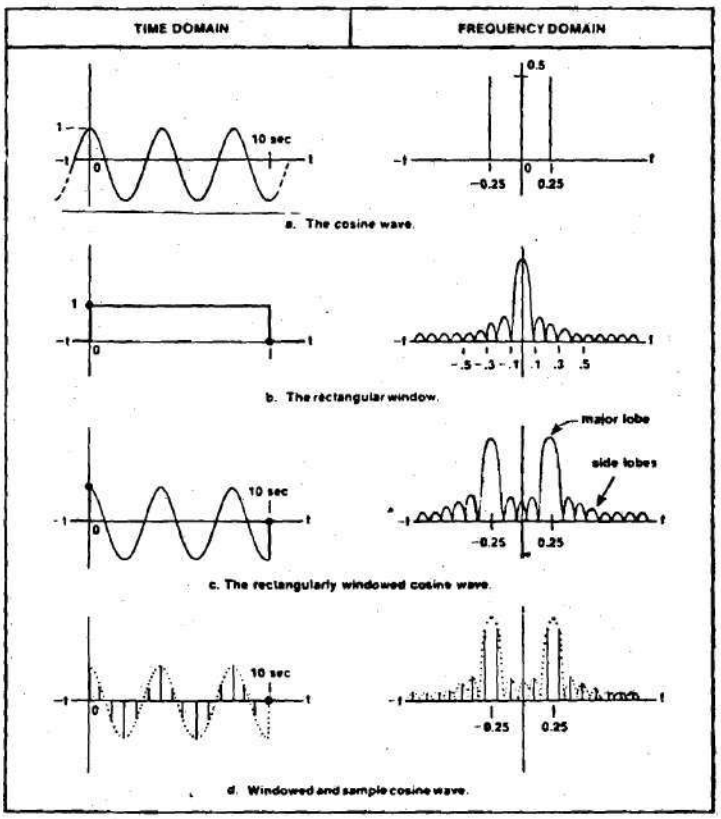

Figure C-1. Leakage Comes from Windowing

time function is assumed to continue throughout all time.

Now, to make any measurement, a reasonable time segment of the cosine wave must be selected. In short, the cosine wave has to be windowed, and the window can be represented by the rectangular pulse in Figure (C-1b).

Signal measurement or acquisition takes place over the duration of the rectangular window. The acquisition process corresponds to time-domain multiplication of the signal by the rectangular window. In the frequency domain, this corresponds to convolving the signal's line spectrum with the rectangular window's $|(\sin f)/f|$ shaped spectrum. The results of both of these operations, the time-domain windowing and the corresponding frequency domain convolution, are shown in Figure (C-1c).

The windowed signal in Figure (C-1c) can be correctly referred to as a gated cosine wave. However, if it is thought of as a representation of the continuous cosine wave, then leakage error occurs in the frequency domain. This leakage error is the spreading of energy from the original line spectrum into the major lobes and side lobes indicated in Figure (C-1c).

In a digital processing system, the acquisition contains an additional step before digitizing takes place. This is shown in Figure (C-1d) and consists of sampling the signal a number of times over the window duration. When the windowed and sampled signal is looked at in the frequency domain, via the fast Fourier Transform (FFT) for example, the corresponding frequency samples outline the envelope of the major lobes and side lobes. So, in digital systems leakage error appears as a roll-off or decay from the major spectral components.

The most common solution for the leakage is to change the window shape, which in turn changes the distribution of the leakage error. Examples of these windows are the cosine (Hanning), Hamming and Parzen windows. The present study did not examine the effects of various windows.

APPENDIX D

SAMPLE PROGRAMS FOR THE IN VITRO DATA ANALYSIS

A sample program is given in Figure (D-1) for the analysis of the total wave form. The program for the temporal analysis of the four intervals is shown in Figure (D-2). These programs are applied to HP Model 5451B Fourier Analyzer system.

```
  1 L        2Ø
  4 BS      1Ø24
  7 MS       31
 1Ø L        21
 13 RA        Ø       Ø
 17 MS       21       Ø
 21 #        21      1ØØ        Ø
 26 ·

 28 L         Ø
 31 BS     1Ø24
 34 CL        Ø
 37 MS       31
 4Ø L         1
 43 MS       11        1
 47 A+        1
 53 D         Ø        4
 54 #         1      1ØØ        Ø
 59 :         Ø      1ØØ
 63 *         Ø      191
 67 X>        2
 7Ø L        1Ø
 73 CL        1
 76 CL        4
 79 CL        6
 82 CL        8
 85 MS       31
 88 L        11
 91 MS       11        Ø
 95 *         Ø      191
 99 A-        2
1Ø2 X>        3
1Ø5 *         3
1Ø8 A+        6
111 X>        6
114 X<        3
117 X>        7
12Ø F
122 SP
124 D         1        4
128 X<        3
131 CL        3        Ø       256
136 CL        3      768      1Ø24
141 CR        3
144 CL        Ø      256       768
149 A+        4
```

Figure D-1. Program for the Total Waveform Analysis

```
152 X>          4
155 X<          7
158 CR          7
161 A+          8
164 X>          8
167 #          11      1ØØ          Ø
172 :           4      1ØØ
176 :           8      1ØØ
18Ø :           6      1ØØ
184 X<          1
187 W           Ø       Ø           5Ø
192 TL
194 ·

196 $           1       1          512
2Ø1 W           1     512
2Ø5 X<          8
2Ø8 X>          9
211 W           Ø       Ø
215 CL          9       1         1Ø24
22Ø $           9
223 :           9
226 ·

228 X<          4
231 W           Ø       Ø
235 X>          5
238 CL          5       1         1Ø24
243 $           5
246 :           5
249 ·

251 X<          6
254 ·

256 $           6
259 :           6    1Ø24
262 W           6    1Ø24
267 X<          2
27Ø $
272 :           Ø    1Ø24
276 W           Ø    1Ø23
28Ø X<
283 ·

285 F
287 *-
289 W           Ø       Ø           1Ø
294 ·
```

Figure D-1. (Continued) Program for the Total Waveform Analysis

```
  1 L        2Ø
  4 BS      1Ø24
  7 MS       31
 1Ø L        21
 13 MS       11       Ø
 17 MS       31      -1        1
 22           Ø     256
 26 MS       21       Ø
 3Ø #        21     1ØØ        Ø
 35 ·

 37 L         Ø
 4Ø CL        Ø
 43 MS       31
 46 BS      256
 49 L         1
 52 MS       11       1
 56 A+        1
 59 D         Ø       4
 63 #         1     1ØØ        Ø
 68 :         Ø     1ØØ
 72 *         Ø
 76 X>        2
 79 CL        1
 82 CL        4
 85 CL        6
 88 CL        8
 91 MS       31
 94 L        11
 97 MS       11       Ø
1Ø1 *         Ø     1ØØ
1Ø5 A-        2
108 X>        3
111 *         3
114 A+        6
117 X>        6
12Ø X<        3
123 X>        7
126 F
128 SP
13Ø D         1       4
134 X<        3
137 CL        3       Ø       64
142 CL        3     192      256
147 CR        3
15Ø CL        Ø      64      192
155 A+        4
158 X>        4
161 X<        7
```

Figure D-2. Program for the Time Intervals Analysis

```
164 CR          7
167 A+          8
17Ø X>          8
173 #          11       1ØØ          Ø
178 :           4       1ØØ
182 :           8       1ØØ
186 :           6       1ØØ
19Ø X<          1
193 W           Ø         Ø         5Ø
198 TL
2ØØ ·

2Ø2 $           1         1        128
2Ø7 W           1       127
211 X<          8
214 X>          9
217 W           Ø         Ø
221 CL          9         1        256
226 $           9
229 :           9
232 ·

234 X<          4
237 W           Ø         Ø
241 X>          5
244 CL          5         1        256
249 $           5
252 :           5
255 ·

257 X<          6
26Ø ·

262 $           6
265 :           6       256
269 W           6       256
273 X<          2
276 $
278 :           Ø       256
282 W           Ø       255
286 X<          2
289 ·

291 F
293 *-
295 W           Ø         Ø         1Ø
```

Figure D-2. (Continued) Program for the Time Intervals Analysis

APPENDIX E

PROOF OF THE DOPPLER SHIFT EQUATION FOR PD

Consider a piezo electric crystal acting as a source of ultrasonic waves and also acting as a receiver for the back scattered waves. Figure (E-1) shows this crystal which sends waves along a line inclined with an angle θ to the velocity vector of a scatterer at distance (L) from the crystal.

The total Doppler shift is the sum of the two parts. The first can be found by noting that to an observer moving with the scatterer at velocity (v), the crystal is moving toward him and its frequency (f_o) appears as a frequency (f_1). To obtain a relation between (f_o) and (f_1), imagine that the crystal sends one complete acoustic wave with a frequency (f_o). Referring to Figure (E-1), the time difference between the two points (a) and (b) in the wave if ($1/f_o$). This will not be the same when received by the scatterer. The time between a_1 and b_1, which corresponds to (a) and (b) as they are received by the scatterer equals to

$$\begin{array}{l}\text{the time for (b) to be received by}\\ \text{the scatterer - the time for (a)}\\ \text{to be received by the moving target}\\ \text{(scatterer)}\end{array} = \left\{\frac{1}{f_o} + \frac{L - v\cos\theta/f_o}{C}\right\} - \frac{L}{C} \qquad \text{(E-1)}$$

This time also equals to ($1/f_1$), hence

$$\frac{1}{f_1} = \frac{1}{f_o}\left[1 - \frac{v}{c}\cos\theta\right]$$

or

$$f_1 = f_o/(1 - \frac{v}{c}\cos\theta) \qquad \text{(E-2)}$$

The second part of the total Doppler shift can be found by observing that the scattering of the sound waves by the moving particles is equivalent to the transmission of a frequency (f_1) from a virtual source moving with the fluid. Thus to an observer fixed at the crystal acting as a receiver, the frequency (f_1) will appear as (f_d) given by:

$$f_d = f_1/(1 - \frac{v}{c}\cos\theta) \qquad \text{(E-3)}$$

Combining equations (E-2) and (E-3), we get

$$f_d = f_s/(1 - \frac{v}{c}\cos\theta)^2 \qquad \text{(E-4)}$$

The total Doppler frequency shift

$$\Delta F = f_d - f_o = \frac{f_o}{(1 - \frac{v}{c}\cos\theta)^2} - f_o$$

$$= f_o\left[1 - \frac{2v\cos\theta}{c} + 3\left(\frac{v\cos\theta}{c}\right)^2 \ldots\right] \qquad \text{(E-5)}$$

The last equation is a nonlinear equation that gives the relation between (ΔF) and the velocity measured (v).

If we consider

$v = 150$ cm/sec

$c = 1.5 \times 10^5$ cm/sec

$\theta = 45^o$

then

$$\frac{v \cos\theta}{c} = 7.07 \times 10^{-4}$$

$$\left(\frac{v \cos\theta}{c}\right)^2 = 5 \times 10^{-7}$$

This shows that the second term is three orders of magnitude less than the first. So, if the infinite series in equation (B-5) is added up to the linear term only the error will be in the order of 0.1 percent. Hence,

$$\Delta F = \frac{2v \cos\theta \, f_o}{c} \qquad \text{(E-6)}$$

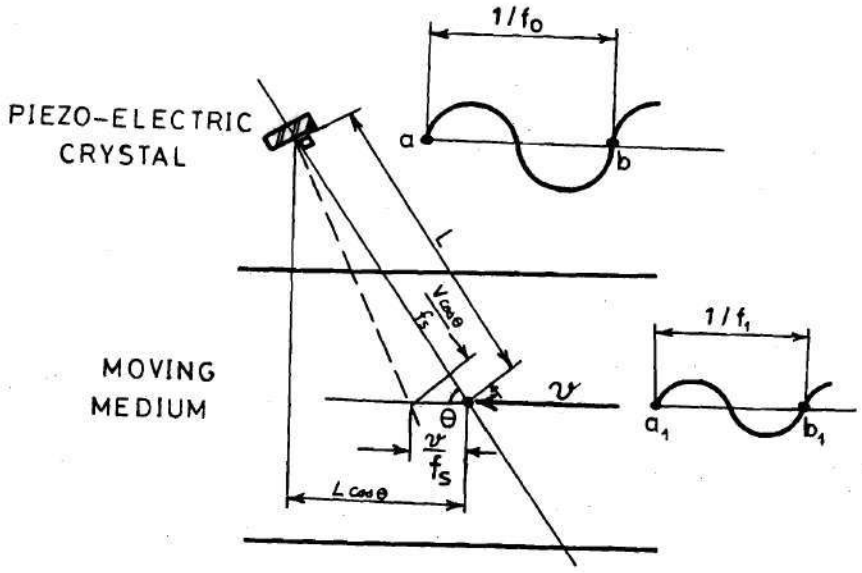

Figure E-1. Proof of the Doppler Equation

APPENDIX F

THE FREQUENCY OF VELOCITY FLUCTUATIONS

Consider a hypothetical case where there are three stationary two-dimensional vortices. These vortices are assumed to be linear and of equal intensity Γ, with centers lying on a straight line and rotating in the same direction. The rotational speeds within the vortex are characteristically inversely proportional to the radius, or, mathematically,

$$v = \frac{\Gamma}{2\pi r} \qquad \text{(F-1)}$$

where

v = the tangential speed cm/sec

r = the radius cm

Γ = the circulation or intensity cm^2/sec

Equation (F-1) shows that as r increases v decreases. Consider that R is the radius at which v is practically "zero." Further, assume that these three vortices are equally spaced, with spacing distance "h" between centers, where

$$h > 2R$$

Let a hot film probe move with velocity u_p toward the vortices, keeping

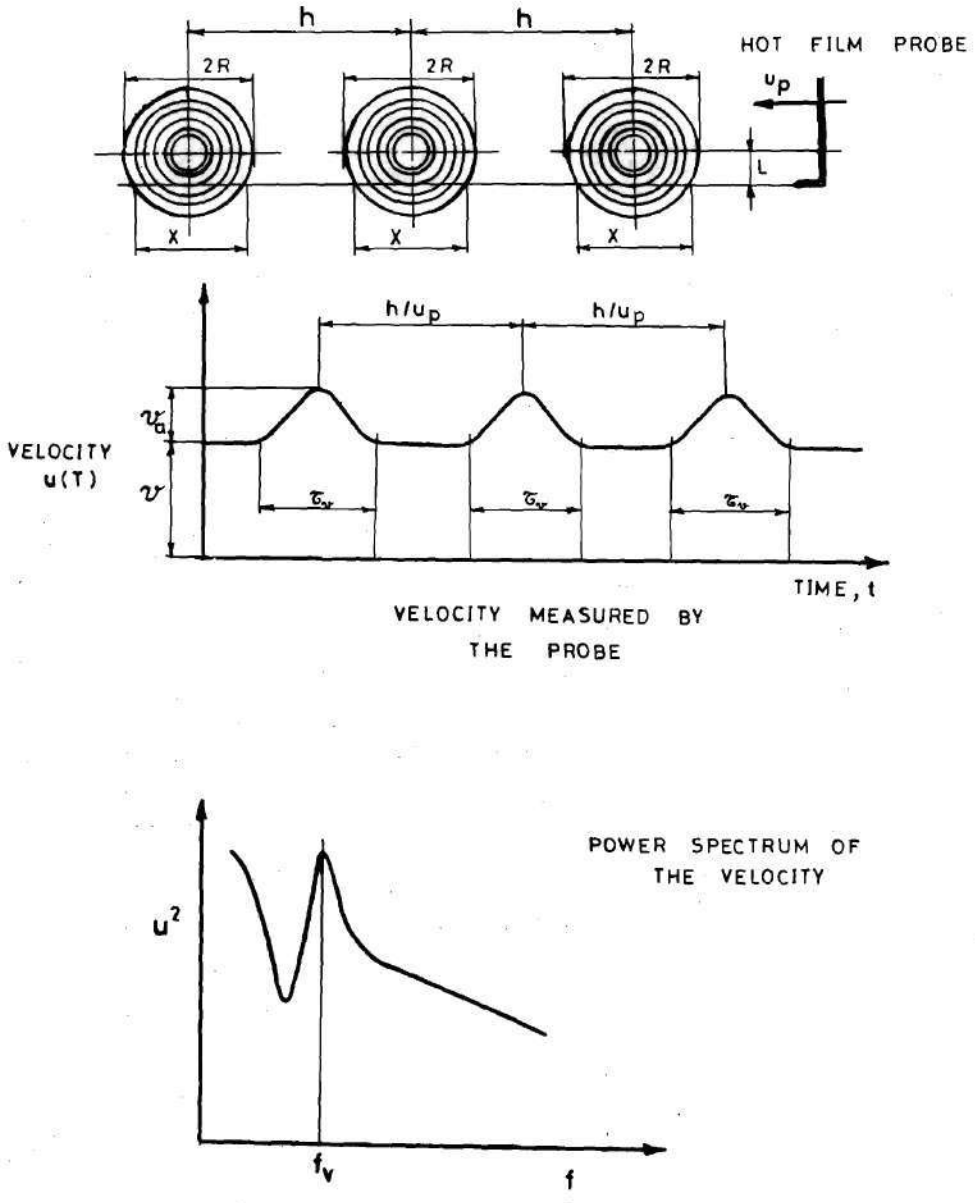

Figure F-1. The Frequency of Velocity Fluctuation

of symmetry of the vortices. The more the distance (L) increases the greater is the frequency f_v observed in the energy spectrum of the measured velocity. If the centerline of the vortices is close to the probe, a peak at low frequency is expected in the energy spectrum and a periodic velocity fluctuation with relatively large amplitude (v_a) is to be seen in the instantaneous velocity versus time plot. The opposite will occur if the probe is far from the centerline of the vortices (but still $L < R$) low amplitude velocity fluctuation will be shown on u(t) plot and a peak at high frequency in the energy spectrum.

Thus, the vortex shedding frequency, f_s, and the vortex fluctuation frequency, f_v (or the fundamental frequency of velocity fluctuation due to motion of a vortex relative to the probe) are not necessarily the same, and this difference depends upon the site of the velocity measurement with respect to the vortex and upon the spacing between the vortex centers.

BIBLIOGRAPHY

1. Boyd, W. (1965) Pathology for the Physician. Seventh Edition, Lea and Febiger Publ. Comp., pp. 104-157.

2. Fry, D. L. (1968) "Acute Vascular Endothelial Changes Associated with Increased Blood Velocity Gradients." Circulation Research, Vol. 22, pp. 165-197.

3. Fry, D. L. (1973) "Response of the Arterial Wall to Certain Physical Factors." Atherogenesis: Initiating factors. A Ciba foundation symposium 12, pp. 93-125 (New series). Elsevier, Excerpta Medica, North Holland, Amsterdam.

4. Caro, C. G., Gerald, J. M. F., and Schroter, R. C. (1971) "Atheroma and Arterial Wall Shear: Observation, Correlation and Proposal of a Shear-dependent Mass Transfer Mechanism for Atherogenesis." Proc. Roy. Soc. (London) B. 177, pp. 109-159.

5. Caro, C. G. (1973) "Transport of Material Between Blood and Wall in Arteries." Atherogenesis: Initiating factors. A Ciba foundation symposium, 12, pp. 127-164 (New series). Elsevier, Excerpta Medica, North Holland, Amsterdam.

6. Lee, J. S. and Fung, Y. C. (1970) "Flow in Locally Constricted Tubes at Low Reynolds Number." J. Appl. Mech., Vol. 37, pp. 9-16.

7. Morgan, B. E. and Young, D. F. (1974) "An Integral Method for the Analysis of Flow in Arterial Stenoses." Bull. Math. Biol., Vol. 36, pp. 39-53.

8. Daly, B. J. (1976) "A Numerical Study of Pulsatile Flow Through Stenosed Canine Femoral Arteries." J. Biomechanics, Vol. 9, pp. 465-475.

9. Kozman, T. A. and Forrester, J. H. (1973) "Pulsatile Flow in a Modelled Stenosis," 26th Annual Conf. on Eng. in Med. & Biol., Vol. 15, p. 307.

10. Deshpande, M. D., Giddens, D. P., and Mabon, R. F. (1976) "Steady Laminar Flow Through Vascular Stenoses," J. Biomechanics, Vol. 9, pp. 165-174.

11. Young, D. F. and Tsai, F. Y. (1973) "Flow Characteristics in Models of Arterial Stenoses -- I. Steady Flow." J. Biomechanics Vol. 6, pp. 395-410.

12. Young, D. F. and Tsai, F. Y. (1973) "Flow Characteristics in Models of Arterial Stenoses -- II. Unsteady Flow." J. Biomechanics, Vol. 6, pp. 547-559.

13. Young, D. F., Cholvin, N. R., and Roth, A. C. (1974) "Some in Vivo Measurements of Pressure Losses Across Arterial Stenoses," 27th Annual Conf. on Eng. in Med. & Biol., Vol. 16, pp. 128.

14. Fox, J. A. and Hugh, A. E. (1966) "Localization of Atheroma: A Theory Based on Boundary Layer Separation." Br. Heart J., Vol. 28, pp. 388-399.

15. Texon, M. (1963) in Atherosclerosis and Its Origin. Edited by M. Sandler and G. H. Bourne, Academic Press, New York, pp. 167-195.

16. Rodbard, S. (1966) "Dynamics of Blood Flow in Stenotic Vascular Lesions." Am. Heart J., Vol. 72, pp. 698-704.

17. Miller, C. W., Histand, M. B., Hokanson, D. F., Mcleod, F. D., and Daigle, R. E. (1973) "Atherosclerosis and Its Effect on Thoracic Aorta Wall Motion and Peripheral Blood Velocity Patterns." IEEE Ultrasound Symp., pp. 77-80.

18. Siegel, M., Olinger, M., and Ho, B. (1975) "Velocity Profiles in the Presence of Obstructions Using a Random Signal Ultrasonic Blood Flow Meter." IEEE Ultrasonics Symp. Proc., pp. 22-24.

19. Bentz, J. C. and Evans, N. A. (1975) "Hemodynamic Flow in the Region of a Simulated Stenosis." ASME paper No. 75-WA/Bio-10.

20. Hagl, S., Messmer, K., Pfau, B., and Meisner, H. (1974) "Influence of Stenosis on the Velocity Profile Analyzed by a Pulsed Doppler Ultrasonic Flow Meter." in Cardiovascular Applications of Ultrasound (Robert S. Reneman Editor), North Holland Publ. Comp., Chapter 17, pp. 216-225.

21. Peronneau, P. A., Hinglais, J. R., Xhaard, M., and Delouche, P. (1974) "The Effect of Curvature and Stenosis on Pulsatile Flow In Vivo and In Vitro." in Cardiovascular Application of Ultrasound (Robert S. Reneman Editor), North Holland Publ. Comp., Chapter 17, pp. 216-225.

22. Roach, M. R. (1972) "Poststenotic Dilatation in Arteries," in Cardiovascular Fluid Dynamics (Berbel Editor), Academic Press, Vol. 2, pp. 111-139.

23. Giddens, D. P., Mabon, R. F., and Cassanova, R. A. (1976) "Measurements of Disordered Flows Distal to Subtotal Vascular Stenoses in the Thoracic Aortas of Dogs." Circulation Research, Vol. 39, pp. 112-119.

24. Bellhouse, B. and Bellhouse, F. (1969) "Fluid Mechanics of Modeled Normal and Stenosed Aortic Valves." Circulation Research, Vol. 25, pp. 693-704.

25. Stein, P. D. and Sabbah, H. N. (1976) "Turbulent Blood Flow in the Ascending Aorta of Humans with Normal and Diseased Aortic Valves." Circulation Research, Vol. 39, pp. 58-65.

26. Bruns, D. L. (1959) "A General Theory of the Causes of Murmurs in the Cardiovascular System." American J. of Medicine, Vol. 27, pp. 360-374.

27. Freuhan, C. T. (1962) "On the Aeolian Theory of Cardiovascular Murmur Generation." New Physician, Vol. 11, pp. 433-438.

28. Socks, A. H., Tickner, E. G., and MacDonald, I. B. (1971) "Criteria for the Onset of Vascular Murmurs." Circulation Research, Vol. 29, pp. 249-256.

29. Tobin, R. J., Chang, I. D., Koutsoyannis, S. P. (1976) "Wall Pressure and Displacement Measurements in a Simulation of Cardiovascular Murmur Generation." SUDAAR Report No. 484, Stanford University.

30. Fredberg, J. J. (1973) "Turbulent Pseudosound Production in Atherosclerotic Arteries." Ph.D. Thesis, Massachusetts Institute of Technology.

31. Lees, R. S. and Dewey, C. F., Jr. (1970) "Phonoangiography: A New Non-invasive Diagnostic Method for Studying Arterial Disease." Proceedings of the National Academy of Science, Vol. 67, No. 2, pp. 935-942.

32. Duncan, G. W., Gruber, J. O., Dewey, C. F., Myers, G. S., and Lees, R. S. (1975) "Evaluation of Carotid Stenosis by Phonoangiography." New England Journal of Medicine, Vol. 293, No. 22, pp. 1124-1128.

33. Giddens, D. P. et al. (1977) "An Investigation of the Flow Disturbances Created by Subtotal Vascular Stenosis." Final Report for National Science Foundation Grant ENG 74-21986.

34. Giddens, D. P., Mabon, R. F., Khalifa, A. M. A., and Cassanova, R. A. (1976) "Measurement of Flow Disorder Created by Mild Stenosis." Fachtagungen Medex 76 Basel/Schweiz. Biomedizinische Technik, Band 21.

35. Giddens, D. P., Cassanova, R. A., Khalifa, A. M. A., and Mabon, R. F. (1976) "Analysis of Disordered Flow Created by Vascular Stenosis." Digest of the 11th International Conference on Medical and Biological Engineering, Ottawa, pp. 330-331.

36. Hinze, J. A. (1975) Turbulence. 2nd Edition, McGraw-Hill Book Co., New York, pp. 50-64.

37. Winter, D. C., Wells, M. K., and Morgan, R. J. (1975) "Detection of Cardiovascular Flow Disturbances Using Autocorrelograms." Paper presented at 28th ACEMB meeting, New Orleans.

38. Cassanova, R. A. (1976) "An Experimental Investigation of Steady and Pulsating Flow Through Partial Occlusions in Rigid Tube." Ph.D. Thesis, Aerospace Engineering, Georgia Institute of Technology.

39. Giddens, D. P., Mabon, R. B., Cassanova, R. A., Menon, R. K., and Chandler, J. (1974) "Experimental Observations of the Velocity Field Distal to Partial Occlusions in Arteries." Recent Advances in Engineering Science (T. S. Chang, Editor) Vol. 6, pp. 47-54.

40. Nerem, R. M., Seed, W. A., and Wood, N. B. (1972) "An Experimental Study of the Velocity Distribution and Transition to Turbulence in the Aorta." J. of Fluid Mechanics, Vol. 52, pp. 127-160.

41. Kim, B. M. and Corcoran, W. H. (1974) "Experimental Measurements of Turbulence Spectra Distal to Stenoses." J. Biomechanics, Vol. 7, pp. 335-342.

42. Clark, C. (1976) "Turbulent Velocity Measurements in a Model of Aortic Stenosis." J. Biomechanics, Vol. 9, pp. 677-687.

43. McEvoy, N. M., Pimmel, R. L., and Nerem, R. M. (1975) "Analysis of High Frequency Disturbances in Aortic Velocity Signals." Paper presented at 28th ACEMB Meeting, New Orleans.

44. Falsetti, H. L., Kiser, K. M., Francis, G. P., and Belmore, E. R. (1972) "Sequential Velocity Development in the Ascending and Descending Aorta of the Dog." Circulation Research, Vol. 21, pp. 328-338.

45. Pawell, H. E. (1974) "Spectral Analysis of Turbulence in Simulated Arterial Flow." (Abstract) in Proceedings of 27th Annual Conference of Engineering in Medicine and Biology. The Alliance of Engineering in Medicine and Biology, Chevy Chase, Md.

46. Parker, K. (1976) "Instability in Arterial Blood Flow." Chapter 16, in Cardiovascular Flow Dynamics and Measurements (Hwang, N. H. C. and Normann, N. A., Editors), University Park Press, Baltimore, Md.

47. Seed, W. A. and Wood, N. B. (1970) "Development and Evaluation of a Hot Film Velocity Probe for Cardiovascular Studies." Cardiovascular Research, Vol. 4, p. 253.

48. Ling, S. C., Atabek, H. G., Fry, D. L., Patel, D. J., and Janicki, J. S. (1968) "Application of Heated-film Velocity and Shear Probes to Hemodynamic Studies." Circulation Research, Vol. 23, p. 789.

49. Satomura, S. and Kaneko, Z. (1960) "Ultrasonic Blood Rheograph." Proceedings of the International Conference on Medical Electronics 3rd London, pp. 239-242.

50. Kaneka, Z., Shiraishi, J., Omizo, H., Kato, K., Motomiya, M., Izumi, T., and Okumura, T. (1965) "An Analysing Method of Ultrasonic Blood-rheograph Sign Sonograph." Digest 6th International Conference on Medical Electronics and Biological Engineering, pp. 286-287.

51. Rushmer, R. F., Baker, D. W., and Stegall, H. F. (1966) "Transcutaneous Doppler-flow Detection as a Non-destructive Technique." J. of Applied Physiology, Vol. 21, pp. 554-566.

52. Strandness, D. E., McCutchen, E. P., and Rushmer, R. F. (1966) "Application of a Transcutaneous Doppler Flowmeter in Evaluation of Occlusive Arterial Disease." Surgery Gynaecology and Obstetrics, Vol. 22, p. 1039.

53. Strandness, J. R., Schultz, R. D., Summer, D. S., and Rushmer, R. F. (1967) "Ultrasonic Flow Detection." American Journal of Surgery, Vol. 113, pp. 311-320.

54. Reid, J. M., Davis, D. L., Phillips, J. B., and Spencer, M. P. (1974) "Transcutaneous Flow Mapping with Continuous Wave Doppler." in Cardiovascular Applications of Ultrasound (Robert S. Reneman, Editor), North Holland Publ. Comp., pp. 244-248.

55. Gosling, R. G., King, D. H., Newman, D. L., and Woodcock, J. P. (1969) "Transcutaneous Measurement of Arterial Blood-velocity by Ultrasound." Ultrasonics for Industry, London, Conference Papers. pp. 16-23.

56. Gosling, R. G. and King, D. H. (1974) "Continuous Wave Ultrasound as an Alternative and Complement to X-ray in Vascular Examinations." in Cardiovascular Applications of Ultrasound (Robert S. Reneman, Editor), North Holland Publ. Comp., pp. 266-282.

57. Mcleod, F. D. (1964) "A Doppler Ultrasonic Physiological Flowmeter." in Digest of 17th Annual Conference on Engineering in Medicine and Biology, Cleveland, Ohio, Vol. 6, pp. 81.

58. Baker, D. W. and Watkins, D. W. (1967) "A Coherent Pulse Doppler System for Cardiovascular Measurements." in 20th Annual Conference on Engineering in Medicine and Biology, Boston, pp. 272.

59. Baker, D. W. (1970) "Pulsed Ultrasonic Doppler Blood Flow Sensing." IEEE Transactions on Sonics in Ultrasonics, Vol. SU-17, No. 3, pp. 170-185.

60. Wells, P. N. T. (1969) "A Rangegated Ultrasonic Doppler System." Medical and Biological Engineering, Vol. 7, pp. 641-652.

61. Peronneau, P. A. and Leger, F. (1969) "Doppler Ultrasonic Pulsed Blood Flowmeter." ith International Conference on Medical and Biological Engineering, Chicago, Ill., pp. 10-11.

62. Mcleod, F. D. (1974) "Multichannel Pulse Doppler Techniques." in Cardiovascular Applications of Ultrasound (Robert S. Reneman, Editor), North Holland Publ. Comp., pp. 85-107.

63. Mcleod, F. D. (1967) " A Directional Doppler Flowmeter." Digest of 7th International Conference on Medical and Biological Engineering, pp. 213.

64. Haase, W. C., Foletta, W. S., and Meidl, J. D. (1973) "A Directional Ratiometric Ultrasonic Blood Flow Meter." Proceedings of IEEE Ultrasonic Symposium, pp. 81-85.

65. Reid, J. M., Sigelmann, R. A., Nasser, M. G., and Baker, D. W. (1969) "The Scattering of Ultrasound by Human Blood." 8th International Conference on Medical and Biological Engineering, 10.7.

66. Thompson, P. D., Schwan, H. P., and Joyner, C. R. (1973) "A Determination of Scattering Plane Longitudinal Ultrasonic Waves from Erythrocytes." 23rd Annual Conference on Engineering in Medicine and Biology, Washington, D. C. 21.5.

67. Brody, W. R. (1971) "Theoretical Analysis of the Ultrasonic Blood Flowmeter." Technical Report #4951-1, Stanford University.

68. Flax, S. W., Webster, J. G., and Updike, S. J. (1969) "Theoretical and Experimental Evaluation of Doppler Blood Flow Information." 8th ICMBE, 10.8.

69. Flax, S. W., Webster, J. G., and Updike, S. J. (1974) "Noise and Functional Limitations of the Doppler Blood Flowmeter." in Cardiovascular Applications of Ultrasound (Robert S. Reneman, Editor), North Holland Publ. Comp., pp. 18-31.

70. Jorgensen, J E., Campau, D. N., and Baker, D. W. (1973) "Physical Characteristics and Mathematical Modeling of Pulsed Ultrasonic Flowmeter." Medical and Biological Engineering, pp. 404-420.

71. Baker, D. W., Jorgensen, J. E., and Campau, D. N. (1971) "The Characteristics of Pulsed Ultrasound Flowmeter." Flow--Its Measurement and Control in Science and Industry, Vol. 1, Part III, Dowdell, Editor, pp. 1389-1400.

72. Baker, D. W. and Yates, W. G. (1973) "Technique for Studying the Sample Volume of Ultrasonic Doppler Devices." Medical and Biological Engineering, Vol. 11, No. 6, pp. 766-770.

73. Jorgensen, J. E., Campau, D. N., Garbini, J. L., and Baker, D. W. (1972) "Analytical Modeling of the Pulsed Ultrasonic Doppler Flowmeter." 25th Annual Conference on Engineering in Medicine and Biology, Florida, pp. 75.

74. Jorgensen, J. E. and Garbini, J. L. (1974) "An Analytical Procedure for the Calibration of the Pulsed Ultrasonic Doppler Flowmeter." Transactions of the American Society of Mechanical Engineers, Vol. 96, pp. 158.

75. Baker, D. W., Johnson, S. L., and Strandness, D. E. (1974) "Prospects for Quantitation of Transcutaneous Pulsed Doppler Techniques in Cardiology and Peripheral Vascular Disease." in Cardiovascular Applications of Ultrasound (Robert S. Reneman, Editor), North Holland Publ. Comp., pp. 108-124.

76. Mcleod, F. D., Giddens, D. P., and Khalifa, A. M. A. (1976) "Measurement of Turbulent Flow with Pulsed Ultrasonic Doppler." 29th Annual Conference on Engineering in Medicine and Biology, Boston, pp. 139.

77. Hussain, A. K. F. and Reynolds, W. C. (1970) "The Mechanics of an Organized Wave in Turbulent Shear Flow." J. Fluid Mechanics, Vol. 41, pp. 241-258.

78. Papoulis, A. (1965) Probability, Random Variables and Stochastic Processes. McGraw-Hill Book Company, pp. 282-301.

79. McDonald, D. A. (1960) Blood Flow in Arteries. Edward Arnold Publishers Ltd., London.

80. Priestley, M. B. (1965) "Evolutionary Spectra and Non-stationary Processes." J. Royal Statistical Society, Vol. B27, pp. 204-237.

81. Deshpande, M. D. (1977) "Steady Laminar and Turbulent Flow through Vascular Stenosis Models." Ph.D. Thesis, School of Aerospace Engineering, Georgia Institute of Technology.

82. Resch, F. J. (1970) "Hot-film Turbulence Measurements in Water Flow." J. Hydraulics Div., Proc. A.S.C.E. HY3, pp. 787-800.

83. Cassanova, R. A. (1977) "Pulsating Flow Facility." personal communication.

84. DISA Type 55L Laser Doppler Anemometer Mark II, Instruction Manual (1974), DISA Electronics, Franklin Lakes, New Jersey.

85. Fourier Analyzer System 5451B Manual (1974) Hewlett-Packard Company, Santa Clara, California 95050.

86. Tritton, D. J. (1977) Physical Fluid Dynamics. Van Nostrand Reinhold Company, pp. 213-229.

87. Anderson, W. M. (1967) "Flow Visualization of Vortex Ring Formation and Interactions in Submerged Impinging Jets." M.Sc. Thesis, Mechanical and Aerospace Engineering, Illinois Institute of Technology.

88. Coles, D. (1962) "Interfaces and Intermittency in Turbulent Shear Flow." Graduate Aeronautical Laboratories California Institute of Technology, Pasadena, Publication No. 541, pp. 230-235.

89. Laufer, J. (1954) National Advisory Committee of Aeronautics, Technical Report No. 1174.

90. Rice, S. O. (1944) "Mathematical Analysis of Random Noise." Bell System Technical Journal, Vol. 23, pp. 282.

91. Rice, S. O. (1945) "Mathematical Analysis of Random Noise." Bell System Technical Journal, Vol. 24, pp. 1.

92. George, W. K. and Lumley, J. L. (1973) "The Laser-Doppler Velocimeter and Its Application to the Measurement of Turbulence," J. Fluid Mechanics, Vol. 60, Part 2, pp. 321-362.

93. Morse, P. M. and Ingard, K. U. (1955) Theoretical Acoustics. McGraw-Hill, 1968.

94. Sandborn, V. A. (1955) "Experimental Evaluation of Momentum Terms in Turbulent Pipe Flow." NACA, T. N. 3266, Washington, D.C.

95. Coantic, M. (1966) "Contribution á l'Etude de la Structure de la Turbulence dans une Conduit de section Circulaire." Thése Doct. es. Sc. Marseille,

96. Carpenter, W. A. (1977) "A Fluid Dynamics Model of Angiographic Injections Possible Improvements Through the Use of Drag Reduction Polymers." Ph.D. Thesis, Aerospace Engineering, Georgia Institute of Technology.

97. Oppenheim, A. V. and Schafer, R. W. (1975) Digital Signal Processing. Prentice-Hall, Inc., pp. 532-549.

98. Drake, A. W. (1967) Fundamentals of Applied Probability Theory. McGraw-Hill Book Company, pp. 212-216.

VITA

Adel Mohamed Ahmed Khalifa was born in Cairo, Egypt, on July 20, 1948. He graduated from El-Orman high school in 1965. He received a Bachelor of Engineering degree in Mechanical Engineering from Cairo University in 1970.

He worked as a teaching assistant at Cairo University, where he continued his graduate education and obtained his Master of Engineering degree in Mechanical Engineering in 1974.

In the fall of 1974 he joined the School of Mechanical Engineering, Georgia Institute of Technology to continue his work in pursuit of the Ph.D. degree.

Mr. Khalifa was married in September 1977 to Amal Omar Mahmoud.